

UC Riverside

UC Riverside Electronic Theses and Dissertations

Title

Condensation, Thermalization and Quantum Macroscopicity in Ultra Cold Quantum Gases

Permalink

<https://escholarship.org/uc/item/5q3444dm>

Author

Kelly, Shane P

Publication Date

2020

Peer reviewed|Thesis/dissertation

UNIVERSITY OF CALIFORNIA
RIVERSIDE

Condensation, Thermalization and Quantum Macroscopicity in Ultra Cold
Quantum Gases

A Dissertation submitted in partial satisfaction
of the requirements for the degree of

Doctor of Philosophy

in

Physics

by

Shane P. Kelly

June 2020

Dissertation Committee:

Professor Shan-Wen Tsai, Co-Chairperson
Doctor Eddy Timmermans, Co-Chairperson
Professor Michael Mulligan
Professor Leonid Pryadko

Copyright by
Shane P. Kelly
2020

The Dissertation of Shane P. Kelly is approved:

Committee Co-Chairperson

Committee Co-Chairperson

University of California, Riverside

Acknowledgments

I am incredibly grateful to my adviser, Shan-Wen Tsai, without whose help, guidance and instruction, I would not be here. My PhD experience has been a wonderful experience due to the great collaborations we formed and the breadth of physics we were able to explore. I am equally grateful to my Los Alamos National Lab mentor, Eddy Timmermans, who has been equally critical to my success and enjoyment of my PhD work. What is presented below would not have been possible without their dedication to my education. They have both put a tremendous amount of effort into training me in both complicated many body physics, and the social complexities of academic life such as grant writing, sharing research, and networking. This training has come in a multitude of forms such as teaching me important many body techniques, critical analysis of my ideas and proposals, and detailed care over my writing. I would not be able to do the calculations I can do now, nor write with any bit of clarity without their help and care.

I am also grateful for the collaborations and discussions with Jamir Marino, Alexis Chacón, Levent Subasi, David Campbell, Jin Zhang, Amir M-Aghaei, Hamed Asasi, Amartya Mitra and Shima Imani. They have all significantly contributed in some way to the knowledge I have presented in this Dissertation. I am particularly thankful to Jamir Marino, who introduced me to disorder physics, guided me through complicated many body techniques and has ensured my continued participation in the physics world.

I am also grateful to the UCR faculty who taught my first and second year classes and provided me with the tools required to perform the research presented below. I am particularly grateful to Leonid Pryadko, Michael Mulligan and Chandra Varma, whose

second year classes on Dissipation, Many Body Field Theory techniques and Topology have been critical to the research and collaborations I have formed.

I dedicate this work to my parents Sheryl Kelly and Robert Kelly, and my friend
Jon Serpico. Their support was necessary for my success.

ABSTRACT OF THE DISSERTATION

Condensation, Thermalization and Quantum Macroscopicity in Ultra Cold
Quantum Gases

by

Shane P. Kelly

Doctor of Philosophy, Graduate Program in Physics
University of California, Riverside, June 2020
Professor Shan-Wen Tsai, Co-Chairperson
Doctor Eddy Timmermans, Co-Chairperson

In this dissertation we proposed and modeled five ultra cold atoms experiments that make use of quantum effects to produce novel macroscopic phenomena. The first of these experiments is a proposal to produce a p-wave superfluid using two different atomic species. The pairing species is trapped in two-dimensions and the other species is allowed to move in three-dimensions and mediates the p-wave pairing interaction. We confirm our predictions using the functional Renormalization Group method.

The next experiment studies how macroscopic cat states can be produced and detected in bosonic interferometers. A bosonic interferometer is composed of ultra-cold bosons that can condense in one of two modes. Tunneling and interactions are the primary contributions to the dynamics and in cooperation can produce highly entangled states such as Schrodinger cat states. We show how the quantum Fisher information, a tool in quantum metrology, can be used to perform a partial state tomography to determine the nature of the superposition in experimental cat states.

In the last three proposals, we study the long time equilibration dynamics of three different proposed experiments. The first proposed experiment takes place in the same bosonic interferometer as discussed in the Schrödinger cat work, and we identify a novel mechanism for the breakdown of thermalization with the slow dynamics of an unstable fixed point in a semi-classical approximation. The second proposed experiment also takes place in the same bosonic model, but involves a periodic kick to the interaction strength. We find that these dynamics can produce a time-crystal-like state where discrete time-translation symmetry is broken in the long time dynamics. Finally, we study the long time dynamics of a clean fermionic chain and a disordered fermionic chain that are coupled by density density interactions. In this proposal, we find that the effects of disorder can be transferred to the clean chain and prevent thermalization.

Contents

List of Figures	xiii
List of Tables	xix
1 Introduction	1
Bibliography	9
2 Weak Three Dimensional Mediators of Two Dimensional Triplet Pairing	11
2.1 Published Abstract	11
2.2 Introduction	12
2.3 2D Interactions via 3D Mediators	15
2.4 Renormalization Group Analysis of Triplet Pairing Instability	20
2.5 Numerical fRG Results	26
2.6 Discussion	32
Bibliography	35
3 Detecting Macroscopic Indefiniteness of Cat States in Bosonic Interferometers	37
3.1 Abstract	37
3.2 Introduction	38
3.3 Interferometers, Cat States and Double Peak Mixed States	42
3.3.1 Phase Encoding, Read-out, Projective Measurement	43
3.3.2 State Preparation: Cat States and Mixed Double-Peak States	46
3.4 Interferometer Sensitivity and Indefiniteness	51
3.5 Results: Detection Of Indefiniteness via Interferometer Sensitivity	56
3.6 Exploring indefiniteness for a Cat State Entangled with an Auxiliary Qubit	62
3.7 Conclusion and Discussion	66
3.8 Appendix	69
3.8.1 Cat States and Measure by Fröwis and Dür	69
3.8.2 Fisher Information for a Cat Entangled with a Qubit	72
3.8.3 Leggett-Garg violation of a Cat State Entangled with a Qubit	73

Bibliography	74
4 Eigenstate Thermalization and Quantum Fisher Information	79
4.1 Quantum Chaos and Random Matrix Theory	81
4.1.1 Random Matrix Elements of Observables	83
4.1.2 Entanglement Entropy of random wave functions	85
4.2 Eigenstate Thermalization	87
4.2.1 Dynamical Fluctuations and KMS relation	88
4.3 Eigenstate Thermalization and Quantum Fisher Information	90
Bibliography	92
5 Thermalization and its Breakdown for a Large Nonlinear Spin	93
5.1 Abstract	93
5.2 Main Text	94
5.3 Supplemental Material	106
5.3.1 Large-J Scalling At Different Energies and for Different Observables	106
5.3.2 Numerical Details of Exact Construction of Micro-Canonical Ensembles	108
5.3.3 ETH for Off Diagonal Elements and Equal Time Observables Without	
Time Averaging	109
5.3.4 Semi-Classical Eigenstates and Eigenstate normalization	111
5.3.5 Eigenstate Overlaps and Saddle Point Approximation	112
5.3.6 Semi-Classical Equilibrium Observables	116
Bibliography	117
6 Period-n Persistent Oscillations in the Kicked LMG Model	121
6.1 Abstract	121
6.2 Introduction	122
6.3 Model and Classical Approximations	125
6.3.1 Classical Dynamics	126
6.4 Perturbative Limit	127
6.5 Islands of Stability and Persistent Oscillations	130
6.6 Conclusion	136
Bibliography	138
7 Exploring many-body localization	
 in quantum systems coupled to an environment	
 via Wegner-Wilson flows	141
7.1 Abstract	141
7.2 Introduction	142
7.2.1 Structure of the paper	145
7.3 Flow Equation Approach For a Single Chain	145
7.4 Flow Equation Approach For Two Chains	148
7.4.1 The model	148

7.4.2	Two Chain Ansatz	149
7.4.3	Second Invariant and Phase Boundary Analysis	151
7.5	Numerical Results For Equal Length Chains	153
7.5.1	MBL Proximity Effect	153
7.5.2	Second Invariant	159
7.6	Truncated Flow Equations and Truncation Error	160
7.6.1	Truncation Error for the MBL Proximity Effect Ansatz	160
7.6.2	Truncated Flow Equations	164
7.7	Engineering the geometry of the inter-chain couplings	167
7.7.1	Separation of Time Scales	169
7.7.2	Effective Hamiltonian at intermediate times: $\tau \lesssim \tau_n$	171
7.7.3	Density-Density interactions between uncoupled clusters	173
7.7.4	Explicit form of the Hamiltonian for $\delta = 3$	174
7.8	Conclusions	178
7.9	Appendix	179
7.9.1	Notation	179
7.9.2	Flow Equation Generators	181
7.9.3	The Flow Equations.	182
7.9.4	Numerical Details	182
	Bibliography	184
	8 Conclusion	189
	A Many Body Quantum Mechanics: an Overview	195
A.1	General Quantum Mechanics	195
A.1.1	Unitary Dynamics	196
A.1.2	Heisenberg Picture, simple BCH	197
A.1.3	Interaction Picture	198
A.1.4	Correlations, Generating Functions, Greens Functions	198
A.1.5	Two time correlations	200
A.1.6	The thermal state and the KMS relation	202
A.2	Quantum Components	204
A.2.1	Spins: Operators	204
A.2.2	Spins: Wave Functions	205
A.2.3	Bosons: Operators	208
A.2.4	Bosons: Wave Functions	210
A.2.5	Spin-Boson Mapping	211
A.3	Composite Systems	213
A.3.1	Fermionic Systems	213
A.3.2	Majorana Fermions	213
A.3.3	Representation Of Operators	214

B	Path Integrals and Classical Approximations	221
B.1	Semi-Classical Analysis	221
B.1.1	Inverse of Canonical Quantization	222
B.2	Path Integrals	224
B.2.1	Bosonic Path integral	226
B.2.2	Fermionic Path Integrals	227
B.2.3	Imaginary Time Correlations at the Gaussian Level	228

List of Figures

2.1	This is a plot of the Fourier transform at various distances for a 2D mediated interaction mediated by 3D lattice fermions. U is the onsite interaction strength, NN is for the nearest neighbour and NNN is for the next nearest neighbour. The y-axis is in units of t_2 and the x-axis is in units of t_3	18
2.2	4 point beta functions. The PP diagram is responsible for pairing instabilities while the PH and PH' diagrams are responsible for density wave instabilities.	22
2.3	Phase diagram suggested by bare interaction. This is for fixed V_3 and for U set to cancel onsite interaction. This probably can be smaller.	24
2.4	As we increase the mediated interaction, the critical scale rises exponentially until we are in the strong coupling limit. The overall interaction strength depends on α which we set to 150.	28
2.5	This plot depicts the instability of p-wave pairing to d-wave pairing upon varying the 2D particle density. This cut is at $\mu_3 = 3.85$, $U_{eff}/t_2 = 1$, $\alpha = 150$ and $g/t_3 = .86$	30
2.6	This plot depicts the dependence of the critical temperature of p-wave pairing on the 3D particle density. This cut as the same interaction parameters as in Fig. 2.5: $U_{eff}/t_2 = 1$, $\alpha = 150$ and $g/t_3 = .86$	31
2.7	As we reduce the onsite contact interaction, the effective onsite interaction becomes negative and s-wave pairing starts to dominate. This cut is at $\mu_3 = 3.85$, $\mu_2 = -1.4$, $\alpha = 150$ and $g/t_3 = .86$	32
3.1	(Color online) Classical trajectories. The separatrix is shown in black (bold) and separates the circular free-oscillation trajectories from the self-trapping ones. The green dots mark the fixed point and the green arrows mark the unstable directions.	45
3.2	Distributions $P(j_z)$ for the state evolved from the π and 0 coherent states (0 temperature) for a time T_π and $1.4T_\pi$ respectively. These states were computed for $N = 200$ or for an SU(2) spin with size $J = 100$, and the x-axis, j_z , are the eigenvalues of the observable J_z	50
3.3	Distributions $P(j_z)$ for the state evolved from the π and 0 states at temperature $10\epsilon_\tau$ for the same time intervals as in Fig. 3.2. As in Fig. 3.2, these states were computed for $N = 200$ or for an SU(2) spin with size $J = 100$.	50

3.4	In this plot, the extensive difference (dashed lines, left axis) and quality of indefiniteness (solid lines, right axis) are plotted versus the time spent during the non linear evolution in step 1 of the interferometric process. The scale of the extensive difference is set by the number of particles $N = 200$, or size of corresponding spin $J = 100$, in the evolving state. These quantities are computed for the 0 state at temperature 0 and $10\epsilon_\tau$. An experimenter, testing these cat states shown, would compute the statistical variance and extensive difference from the double peak distributions shown in Fig. 3.2. They would perform the interferometry process discussed above to compute the bound on Δ_q via the CFI.	56
3.5	Quality of indefiniteness, r_q , its experimental bound r_c , the extensive difference $\Lambda(J_z)$ and the reduced extensive difference $\Lambda(J_z)r(J_z)$ are plotted versus the temperature of the initial state. The solid lines are for the thermal states at π , while the dashed lines are for the thermal states at 0. A quantum to classical crossover is shown between temperatures ϵ_τ and $10\epsilon_\tau$. As in Fig. 3.4, the scale of the extensive difference is set by the number of particles $N = 100$ in the evolving state.	60
3.6	The QFI and its experimental bound for convex uncertainty of J_z versus temperature. These are lower bounds on the Fröwis and Dür measure (Eq. 3.20), which also demonstrate the quantum to classical crossover. The y-axis is shown in units of $\frac{1}{4N}$	61
3.7	This is $F_q(\rho, J(\theta, \phi))/4N$ for the 0(Left) and π (Right) cat states.	70
3.8	These are the Wigner distributions and the probabilities, $P(z)$ and $P(\phi)$, (black lines) for the 0(Left) and π (Right) cat states.	71
4.1	Quantum Chaos in Magnetic Hydrogen. Image from Wikipedia[?]	80
5.1	(Color online) Energy dependence of ensemble expectations values of J_x : The orange line is for the Micro-canonical, while the green dots are for the diagonal ensembles with initial phase $\phi' = 0$ and increasing $\langle J_z \rangle / J = z'(E)$. The energy dependence of the eigenstate expectation values is also shown. These calculations were performed for $ J = 1000$ and $\Lambda = 10$. Notice the strong departure of the diagonal ensemble at $E = 1$ from the micro-canonical ensemble. Classical trajectories(inset): the separatrix is shown in black (bold) and separates the circular free-oscillation trajectories (red) from the self-trapping ones (blue). The red dots mark the unstable fixed point at $(z = 0, \phi = \pm\pi)$ and the green arrows mark the unstable directions.	96
5.2	(color online) Micro-canonical and Diagonal Ensemble Expectation Values as a function of $ J $ and ϕ' for $E = 0.5$ (1st column) and $E = 1$ (second column). The color indicates the initial phase ϕ' where in the second column it ranges from 0(dark blue) to π (bright pink). For $E = 0.5$: when $ J $ increases the energy level spacing decreases, the assumptions A2) and A3) of ETH become more valid, and the dependence of the LTOs on the initial phase is lost. While for $E = 1$, memory of the initial state is maintained. These calculations were done with $\Lambda = 10$	101

5.3	(Color Online) Classical fit to exact numerical calculations of diagonal ensemble. This plot shows the $\sqrt{ J \ln J }$ scaling of $j_x = J_x/J$ for the diagonal ensemble of a set of initial states with energy $E = 1$ and different ϕ' and $ J $. The dots are computed using exact diagonalization and the color indicates the initial ϕ' as in Fig. 5.2. Eq. 5.9 predicts $\sqrt{ J \ln J }$ and the linear dashed lines are given by Eq. 5.9 with $F(\phi')$ fit to match the exact calculations for $ J > 500$	104
5.4	(Color Online) These plots demonstrate the validity of ETH in the self trapping limit for a fixed energy of $E = 3$. The different colors corresponds to different values of ϕ' : blue (darker) $\phi = 0$, pink (lighter) $\phi = \pi$. The dashed line is the for the micro-canonical ensemble.	107
5.5	(Color Online) These plots demonstrate the validity of ETH in the self trapping and free oscillating limit, but it fails on the separatrix ($E=1$).	108
5.6	(Color Online) Dynamics of J_x and J_z for different values of ϕ at energies $E = 3$ (top), $E = 1$ (Middle) and $E = 0.5$ (Bottom).	110
6.1	Classical Poincaré plots for $\Lambda = 10$ and $t_1 = t_2 = 0.01$ (left) and 0.25 (right). The black lines in the background are the classical trajectories determined by hamiltonian $H_{eff}^{(1)}$ and the color corresponds to the initial z used to generate the Poincaré plot. The initial ϕ was 0 . The solid black line depicts the separatrix for the deformed models	128
6.2	Long time Q functions of quantum dynamics for two different initial states $z =$ (left) and $z =$ (right), and for $\Lambda = 10$ and $t_1 = t_2 = 0.25$. This demonstrates that at long times, the dynamics of the kicked LMG model are constrained to the integrable tori defined by the effective hamiltonian H_{eff}	129
6.3	These are the classical Poincaré sections for the dynamics given by: $(t_1, t_2) = (1.1, 0.05)$ Left, $(0.35, 0.2)$ Middle, and $(0.3, 0.1)$ Right. In all three cases t_2 is sufficiently large, ensuring that the non-trivial trajectories are large. The non trivial trajectories occur when period of a near by trajectory is close to an integer multiple of t_1 : $\tau_{LMG}(z_0, \phi_0) \approx nt_1$ For the left figure, the non-trivial trajectory in the free oscillating region is an example of an $n = 2$, and the one in the self trapping region is an $n = 1$. This trajectory is particularly impressive, because the trivial trajectories surrounding have become chaotic while these non-trivial trajectories remain integrable. The middle and right plots show $n = 6$ and $n = 3$ non-trivial trajectories.	130

6.4	The top to figures show two example of $n = 1$ non-trivial trajectories for $(t_1, t_2) = (2.1, 0.005)$ Left and $(0.9, 0.004)$ Right. The black lines in each show the trivial trajectory which exists when $t_2 = 0$. The bottom two plots show $\tau_{LMG}(E)$ in blue for the LMG model corresponding to the U_1 dynamics in the top plots ($\Lambda = 10$). The orange line is t_1 , when $t_1 > \tau(E)$, U_1 moves the spin forward along the trajectory by a time $t_1 - \tau(E)$, while if $t_1 < \tau(E)$, U_1 moves the spin backwards along the trajectory by a time $\tau(E) - t_1$. U_2 kicks connects the forward and backward trajectories by. This is done differently in the two regions of phase space. For the left plot, U_2 always kicks z in the positive direction keeping ϕ constant. While in the right plot, U_2 kicks z in the $\pm z$ direction depending on whether $sign(\phi) = \pm 1$	132
6.5	Period $n = 3$ (Left) and $n = 6$ (Right) Persistent Oscillations. The top panel shows these oscillations last indefinitely, while the bottom shows the shape of the oscillation in more detail.	134
6.6	Floquet phases ϕ_n as a function of $\tau(E)$ where $E = \langle n H_{LMG} n \rangle$. The left plot corresponds to $(t_1, t_2) = (0.9, 0.004)$ with classical trajectories shown in Fig. 6.4, the middle plot is for $(t_1, t_2) = (0.3, 0.1)$ and has trajectories shown in Fig. 6.3 and quantum dynamics shown in Fig. 6.5, and the right plot is for $(t_1, t_2) = (0.35, 0.2)$ and has trajectories shown in Fig. 6.3 and quantum dynamics shown in Fig. 6.5. The middle and right plot corresponding to $n = 3$ and $n = 6$ and show a level spacing $= 2\pi/n$. For the $n = 3$ case, the perturbed trajectories for U'_1 are close to the those of the LMG trajectory so the they all have E close to that the $n = 3$ trajectory. For the $n = 6$ case, U'_1 is much more deformed from the LMG trajectoires and therefore these eigen states with $2\pi/n$ spacing are more spread out in energy E and further from the $\tau(E) = 6t_1$ “bare” resonace.	136
7.1	Cartoon of the model described by the Hamiltonian (7.2). The MBL sector (bottom wire) acts as a source of disorder to induce localization in the clean component (green sites). The two systems are coupled site by site via inter-chain couplings (blue lines) of strength Δ^I	148

7.2	Instances of the MBL proximity effect: the plots show, in logarithmic scale, the spatial decay of the couplings between integrals of motion in the clean sector of the system. We display results for parameters which yield both a large and small change in the second invariant, and distinguish them using triangle and circle makers respectively. The results for parameters that yielded a large change in the second invariant (marked with triangles) do not reflect the true l-bit coupling but are displayed to depict how the MBL proximity effect ansatz breaks down. The final clean-chain density-density couplings $\Delta_{ i-j }^c$ depicted here are averaged over 256 disorder realizations. In the top panel, we plot how the final density-density couplings depend on $W^c = \Delta^I/2J^c$ (J^c fixed) while in the bottom panel we plot their dependence on $\langle n^d \rangle$. In the top panel $\langle n^d \rangle = 0.5$ while in the bottom panel $W^c = 225$ ($\Delta^I = 45$ and $J^c = 0.1$). The remaining Hamiltonian parameters are $W = 60$, $J^d = \Delta^d = 0.1$, $\Delta^c = J^c = 0.1$, $\Theta = 0.3$, and $\langle n^c \rangle = 0.1$. These results are not affected by $\langle n^c \rangle$ since they are uniformly distributed in the reference state ρ and do not have an impact on the disorder of the effective fields.	155
7.3	Regions of parameter space where the MBL proximity effect is established. We focus on an instance of a strongly localized dirty chain ($W = 60$, $\Delta^d = J^d = 0.1$), and on a clean chain with $\Delta^c = J^c = 0.1$. The thin, dashed, black lines delimit a square where the parameters Θ and $\langle n^d \rangle$ have been varied in our numerical trials. The region of parameters space in which the MBL Proximity Effect is established is determined by the region where the second invariant is below a specified threshold $\delta I < \delta I^c = 0.1$. In the figure, we draw three different thick, curved, dashed lines, corresponding to the values of the parameter $W^c = 10$ (gray), 30 (dark green), 200 (bright green). These lines mark the values of Θ and $\langle n^d \rangle$ where we expect the second invariant to equal the threshold value $\delta I(W^c, \langle n^d \rangle, \Theta) = \delta I^c$, and above which we expect $\delta I(W^c, \langle n^d \rangle, \Theta) < \delta I^c$. This analysis demonstrates that the MBL Proximity Effect can be observed for the smaller $\langle n^d \rangle$ and Θ when W^c is larger. . . .	157
7.4	Histograms of the change in the second invariant as $\langle n^d \rangle$ is varied across the transition ($W = 60$, $J^d = \Delta^d = 0.1$, $\Delta^c = J^c = 0.1$, $\Theta = 0.3$, and $\langle n^c \rangle = 0.1$).	158
7.5	Median change in the second invariant as a function of $\langle n^d \rangle$ (right) and of W^c (left). W^c is plotted on a log scale since it varies over two orders of magnitude. The remaining Hamiltonian parameters are $\Delta^I = 45$ ($W^c = 225$), $J^d = \Delta^d = 0.1$, $\Delta^c = J^c = 0.1$, $\Theta = 0.3$, and $\langle n^c \rangle = 0.1$. In the left panel $\langle n^d \rangle = 0.5$, while, on the right panel, $W^c = 225$ ($\Delta^I = 45$).	160
7.6	The dirty chain couples to the clean chain every $\delta = 3$ sites. The emergent integrals of motion are illustrated with different colors: n_k^d (blue), $n_{f,r=0}^c$ (red) and N_f (green).	167

7.7 The flow of J_{ij}^c and Δ_{ij}^c for the geometry depicted in Fig. 7.6. The left panel shows the flow of couplings on the clean-chain sites that are not coupled to the dirty chain. It shows an unsuppressed hopping and diverging density-density coupling at long flow time l . The right panel shows the flow of couplings on the clean chain sites that involve a site coupled to the dirty chain. It shows that the hopping onto the coupled site, $r = 0$ (for any f), are suppressed and the density-density coupling involving a coupled site, remains constant instead. This calculation has been performed using an unmodified generator $\eta = [H_0, V]$; in order to remove the divergences in $\Delta_{f,r,f',r'}^c$, we modify the generator to $\eta = [H_0, V']$, with V' given in Eq. 7.20. 169

List of Tables

7.1 This table lists which terms in the commutator $[\eta, H]$ contribute to the beta function $\beta(\Gamma)$ (highlighted in blue) and which are dropped by our ansatz (not highlighted). The rows are labeled by the terms in the sum for the generator $\eta = \eta_h + \eta_\Delta + \eta_I$, and the columns are labeled by the terms in the sum for the Hamiltonian, Eq. 7.11. The notation for the dropped terms is as follows: correlated hopping (C.H.) have a form $n_k^c c_i^\dagger c_j$, inter-chain correlated hopping operators C.H.I. have a form $n_k^d c_i^\dagger c_j$, full scattering terms F.S. have a form $c_i^\dagger c_j^\dagger c_k c_l$, and 3P terms describing three-body and higher particle scattering. The justification for dropping the contributions to $J_{ij}^{c(d)}$ in the third and forth column is discussed in section 7.6.2. 163

Chapter 1

Introduction

Microscopic theories of matter are the most precise theories created by scientists. Scientists create these theories by identifying sources of uncertainties in measurements and uncertainties in predictions and then finding ways to eliminate them. When scientists pursue this process, they are making an implicit assumption about the nature of reality. This assumption is that there are new measurements that could be made that would provide more complete information about the world. Taking this assumption further, scientists like to believe that if all the information in the world was obtained, then all uncertainty about the performed measurements and predictions could be removed. While obtaining complete information on the world is impossible, this belief is useful in applying microscopic theories to idealized situations where information on the rest of the world is irrelevant. These situations are also never perfectly realized in experiments, but the models can be confirmed within the statistical error allowed by the unknown deviations from the ideal.

Quantum mechanics disrupts this implicit assumption and the processes of identifying and removing uncertainties *ad infinitum*. This is best highlighted with the double slit experiment. In this experiment a beam of particles is allowed to pass through two slits and are then detected as they hit a wall behind the slits. Letting the particles go through both slits, they find “dark spots” on the wall where it does not appear possible for the particles to land after passing through the slits. In an attempt to create a microscopic theory, they block one of the slits to reduce uncertainty, but in doing so the dark spots go away, and the particles are now allowed to land where they couldn’t when they were allowed to pass through two slits. This situation appears bad for the ideal of microscopic theories: not only can the experimenter not explain a phenomenon by obtaining more information about the world, obtaining more information destroys the phenomenon. They are forced to conclude that while that information can be “obtained” and given a definite value by measurement it does not exist before it is measured. The value the property has before measurement must then be considered indefinite.

Fortunately, it has appeared that indefiniteness is restricted to microscopic events and we can assume macroscopic events either definitely occur or definitely don’t. We are therefore justified in identifying and eliminating uncertainty when studying macroscopic events like disease and economic collapse. This occurs due to the miracles of statistical mechanics. Statistical mechanics takes confirmed models of microscopic objects and attempts to construct statistical theories of macroscopic objects that are composed of the microscopic ones. These statistical theories allow for missing information and often rely on the assumption of an unknown environment that interacts with the system being modeled.

By applying these theories to the issue of uncertainties, scientists find that the uncertainties introduced by the environment are usually a lot larger than the uncertainties required by quantum mechanics. Therefore, for macroscopic properties, we are safe in assuming any uncertainty is overwhelmingly due to our lack of knowledge.

Starting in the late 20th century, scientists have started to produce experiments in which the simple assumptions connecting microscopic to macroscopic theories no longer hold, and the conclusions on macroscopic indefiniteness must be questioned. Two ingredients go into producing such experiments: first is the ability to isolate matter from an environment, and second is to cool that matter to close to zero temperature. The first ingredient ensures that uncertainties about an environment can not effect the state or its dynamics, while the second ingredient removes the uncertainty about what physical state appears in the experiment. After cooling, the scientists will have a physical state in which everything up to uncertainties required by quantum mechanics can be known. From this pure state, precise and controlled operations can be done to manipulate it and create states of matter that display new phenomenon made possible by the dominance of quantum mechanical uncertainty over statistical uncertainty.

In this dissertation, I will give five examples of such phenomenon that my advisers and I have proposed could be produced in ultra cold quantum gases. Ultra cold quantum gases are produced by slowing and trapping a beam of particles inside a ultra high vacuum chamber[4]. The beam of particles are often first trapped in a Magneto Optical Trap[13]. In this special type of trap the gas particles only absorb light when approaching the edges of the trap. The absorption of light then prevents their escape by kicking the particles back

toward the center of the trap. Once in the trap, additional lasers can be used to further slow the particles down, and once the majority of particles are slow enough, the remaining hot particles are let free by slightly reducing the trap barrier[11]. This and other more advanced mechanism can cool particles down to nano-kelvin temperature[12] and produce quantum gases close to their ground state.

The nature of this macroscopic ground state depends on the type of quantum statistics the cooled particles obey. For physical particles, there are two distinct possibilities for the statistics: bosonic and fermionic. For weakly interacting bosonic gases, the ground state has almost all of the particles behaving in the same way (i.e. occupying the same single-particle quantum state). This state of matter is known as a Bose-Einstein condensate and was first created in 1995 by two separate groups[2, 6]. For Fermi gases, the particles can not occupy the same single particle quantum state and therefore are forced to occupy the N lowest energy states (if N is the number of particles). For fermions to form a condensate, they need to pair up into composite like particles which act like bosons and then condense. This type of condensate was first observed in 2003 by [14].

Condensates are an exciting form of matter because the uncertainty due to quantum mechanics is the overwhelming contribution to the uncertainty apparent in the macroscopic properties of the whole gas. For example, when the particles (the boson or paired fermions) carry a magnetic moment[15] and the magnetic moments are polarized in one direction, the components of the magnetic moment in the two other perpendicular directions are, because of quantum mechanics, completely uncertain. Since the total magnetization is the sum of the magnetization of each particle, and each particle is doing the same thing,

any fluctuation in the total magnetization is due to the cumulative quantum uncertainty of the individual particles.

Fermionic condensates are particularly exciting because depending on the type of condensation, the spin of the composite particle can contain contributions from the orbital momentum of the pairs. This extra degree of freedom can produce novel spin-textures and allow the production of topologically protected states. P-wave fermionic condensates, in which the orbital state of the paired fermions has p-wave spherical symmetry, are particularly sought after in condensed matter because, they might allow for the creation of topologically protected qu-bits[1]. Chapter 2 is a publication[7] in which Shan-Wen Tsai and myself demonstrate a method of creating p-wave fermionic condensates in a “mixed”-dimensional gas. Mixed-dimensional gases contain two distinct species of particles that are confined to move in different dimensions. We studied a situation where one species of particle is confined to a 2D plane while the other is free to move in three dimensions.

While an impressive demonstration of control, the type of uncertainty displayed by weakly interacting condensates is still only microscopic. The magnitude of the total magnetization grows linearly, but the uncertainty $\sqrt{\Delta M^2} = \sqrt{\sum_i (\Delta m_i)^2}$ grows as the square root in the number of particles. Therefore as you increase the number of particles, the direction of the collective magnetization becomes more precise as $1/\sqrt{N}$ (see Chapter 3). This is in contrast to the macroscopic uncertainty characteristic of Schrödinger’s cat state. In the Schrödinger’s cat thought experiment, a cat ends up in a quantum superposition of being dead and alive. Since the dead and alive states are macroscopically distinct, this is an example of macroscopic quantum uncertainty

While weakly interacting BECs don't have this macroscopic uncertainty, states similar to Schrödinger's cat might be able to be created and observed. Chapter 3 is a paper[9] in which Eddy Timmermans, Shan-Wen Tsai and my self discuss the possibilities of producing and detect such a phenomenon using techniques from quantum interferometry. In this paper, we imagine a Bose-Einstein condensate that condenses into one of the two modes, and the single particle hilbert space is equivalent to that of a spin 1/2. When all N particles are condensed into either of the two modes the effective dynamics can be described by a spin- $N/2$. The hamiltonian that can create a schrödinger cat like state is given by:

$$H = -J_x + \frac{\Lambda}{2} J_z^2 \tag{1.1}$$

where J_α are the components of the large macroscopic spin. The cat state produced is one in which the macroscopic spin is in a superposition of a state with most of the particles pointing up and a state with most of the particles pointing down. This spin- $N/2$ model of Bose Einstein condensates is also used in modeling interferometric processes for sensing magnetic fields[15] and rotational motion[3]. In the paper presented in chapter 3, we find that one can use techniques from the sensitivity analysis of interferometers to detect and quantify the quantum indefiniteness produced by the non linear dynamics of Hamiltonian 1.1

Another interesting possibility from ultra cold atom experiments is to test if quantum uncertainty will mimic environmental uncertainty when the dynamics of closed quantum systems come to equilibrium. In other words, can we model the long time dynamics of an isolated pure quantum experiment by assuming the experiment has comes to equilibrium with a fictitious random environment. Surprisingly, the answer is generically yes. In chapter

4, I explain the reason this is generically expected and discuss briefly the differences between the quantum uncertainty of a thermalized closed quantum system and the statistical uncertainty of system thermalized with a true environment.

In the final three chapters, I present 3 proposals for preventing thermalization in closed quantum systems. The first two describe the dynamics of a large non-linear spin, with the aim of predicting the dynamics of Bose-Einstein condensates that have condensed into one of two modes. Chapter 5 is a paper[10] in which Shan-Wen Tsai, Eddy Timmermans and I study the long time dynamics of the Hamiltonian 1.1. Previously, it was known that this Hamiltonian is integrable and poses a set of conserved quantities that prevent thermalization. This lack of thermalization shows up as a memory of the conserved quantities at long times. Surprisingly, we find that the model is also capable of remembering the dynamical conjugate variable to the conserved quantity. This additional memory is found to be due to a set of localized eigenstates. We explain the localization these eigenstates using a semi-classical method that identifies the slow dynamics of an unstable fixed point as the source of localization.

In the second proposal for preventing thermalization, we again study the dynamics of the hamiltonian 1.1, but this time with the addition of a periodic kick. This model generically displays chaos, and with strong enough kicks, thermalizes to an infinite temperature state. We find that when the period of the kicks is in resonance with the period of classical trajectories of Eq 1.1, an alternating set of fixed and unstable fixed point emerges similar to a phenomenon in standard map[5]. In between the kicks, the hamiltonian Eq.1.1 moves the quantum state between the stable fixed points. Due to the stability of the fixed points,

diffusion of quantum uncertainty is suppressed and thermalization is prevented. The quantum state then, instead of equilibrating to a fictitious infinite temperature bath, oscillates forever by jumping around to each of the stable fixed points. This proposal is presented in Chapter 6.

The final proposal is presented in Chapter 7 and discusses the robustness of the most stable mechanism for preventing thermalization in closed quantum systems: many body localization. In many body localization, a locally disordered interacting model of 1D fermions develops a set of exponentially localized eigenstates and integrals of motion. These localized integrals of motion are capable of remembering the initial density distribution for long times. Chapter 7 is a paper[8] I published with Jamir Marino and Rahul Nandkishore, which studies the ability of a chain of many body localized fermions to localize a neighboring chain of clean fermions via density-density interactions. We find that this is possible and identify mechanisms for which the two chains can be delocalized and thermalize. We also identify the potential existence of a MBL like pre-thermal state that occurs when the dirty chain is coupled every odd site to the clean chain.

I then conclude in Chapter 8 with a brief summary of results and an outline of possible future directions. The appendices contain a set of standard notations and useful results I found helpful in obtaining the results presented in the main chapters.

Bibliography

- [1] Jason Alicea. New directions in the pursuit of Majorana fermions in solid state systems. *Reports on Progress in Physics*, 75(7):076501, jul 2012.
- [2] M. H. Anderson, J. R. Ensher, M. R. Matthews, C. E. Wieman, and E. A. Cornell. Observation of bose-einstein condensation in a dilute atomic vapor. *Science*, 269(5221):198–201, 1995.
- [3] P. Berg, S. Abend, G. Tackmann, C. Schubert, E. Giese, W. P. Schleich, F. A. Narducci, W. Ertmer, and E. M. Rasel. Composite-Light-Pulse Technique for High-Precision Atom Interferometry. *Phys. Rev. Lett.*, 114(6):063002, feb 2015.
- [4] Immanuel Bloch, Jean Dalibard, and Wilhelm Zwerger. Many-body physics with ultracold gases. *Rev. Mod. Phys.*, 80(3):885–964, July 2008.
- [5] Boris V Chirikov. A universal instability of many-dimensional oscillator systems. *Physics Reports*, 52(5):263 – 379, 1979.
- [6] K. B. Davis, M. O. Mewes, M. R. Andrews, N. J. van Druten, D. S. Durfee, D. M. Kurn, and W. Ketterle. Bose-einstein condensation in a gas of sodium atoms. *Phys. Rev. Lett.*, 75:3969–3973, Nov 1995.
- [7] Shane Kelly and S.-W. Tsai. Weak three-dimensional mediators of two-dimensional triplet pairing. *Phys. Rev. B*, 97:024503, Jan 2018.
- [8] Shane P. Kelly, Rahul Nandkishore, and Jamir Marino. Exploring many-body localization in quantum systems coupled to an environment via wegner-wilson flows. *Nuclear Physics B*, 951:114886, 2020.
- [9] Shane P. Kelly, Eddy Timmermans, and S.-W. Tsai. Detecting macroscopic indefiniteness of cat states in bosonic interferometers. *Phys. Rev. A*, 100:032117, Sep 2019.
- [10] Shane P. Kelly, Eddy Timmermans, and S.-W. Tsai. Thermalization and its Breakdown for a Large Nonlinear Spin. *arXiv:1910.03138 [cond-mat, physics:quant-ph]*, October 2019.

- [11] Wolfgang Ketterle and N.J. Van Druten. Evaporative cooling of trapped atoms. volume 37 of *Advances In Atomic, Molecular, and Optical Physics*, pages 181 – 236. Academic Press, 1996.
- [12] William D. Phillips. Nobel lecture: Laser cooling and trapping of neutral atoms. *Rev. Mod. Phys.*, 70:721–741, Jul 1998.
- [13] E. L. Raab, M. Prentiss, Alex Cable, Steven Chu, and D. E. Pritchard. Trapping of neutral sodium atoms with radiation pressure. *Phys. Rev. Lett.*, 59:2631–2634, Dec 1987.
- [14] C. A. Regal, M. Greiner, and D. S. Jin. Observation of resonance condensation of fermionic atom pairs. *Phys. Rev. Lett.*, 92:040403, Jan 2004.
- [15] Helmut Strobel, Wolfgang Muessel, Daniel Linnemann, Tilman Zibold, David B. Hume, Luca Pezzé, Augusto Smerzi, and Markus K. Oberthaler. Fisher information and entanglement of non-Gaussian spin states. *Science*, 345(6195):424–427, 2014.

Chapter 2

Weak Three Dimensional Mediators of Two Dimensional Triplet Pairing

2.1 Published Abstract

Recent experiments demonstrate the ability to construct cold atom mixtures where a fermion species is confined to a two dimensional lattice and another species is confined to a three dimensional lattice. We show that by using an arbitrary number of three dimensional species, we can construct an arbitrary, rotationally symmetric, density-density interaction for the two dimensional particles. This possibility allows us to construct an effective interaction for the two dimensional particles that favors $SU(2)$ symmetric triplet pairing. Using functional Renormalization Group on the two dimensional particles, we derive and

numerically confirm that the critical temperature associated with triplet pairing depends exponentially on the interaction strength. We then analyze how the stability of this phase is affected by the variance in particle densities and the fine tuning of interaction parameters. We conclude by briefly discussing the experimental difficulties and the potential to study Triplet pairing physics, including Majorana fermions.

2.2 Introduction

One of the miracles of quantum mechanics is that many properties of low temperature liquids can be described by a single wave function. This phenomenon, known as superfluidity, can present its self in both fermionic and bosonic systems. In the simplest bosonic system, this wave function has only one degree of freedom associated with the superfluid phase. In fermionic systems where condensation occurs due to pairing, the wave function can have additional degrees of freedom associated with the spin and angular momentum of the pairing state. In the most common case, the odd exchange symmetry for the fermions is satisfied by the singlet spin state. In two dimensions, the remaining orbital degree of freedom is then fixed perpendicular to the plane - again, the degrees of freedom are reduced to one. More complex states are possible when the odd exchange symmetry is satisfied by an odd orbital wave function and the wave function is degenerate in the three triplet states. These states tend to be less common in spin half systems since they carry higher angular momentum than the isotropic s-wave singlet state, and thus tend to be energetically less favourable.

Superfluid ^3He , a fermionic superfluid with p-wave orbital pairing, avoids this tendency by an anisotropic Van der Waals interaction. The spin degree of freedom then gives rise to various interesting spin textures, vortices and other unusual properties[13]. A particular interesting property occurs when breaking the degeneracy of the spin triplet state by spin orbit coupling. In this case, the vortices that arise as the temperature is increased carry an angular momentum with half a flux quantum. These vortices are known to host Majorana fermions that carry non Abelian statistics and have been used in proposals for quantum computing. [22, 1]

These exotic phases and the possibility of quantum computing has lead to a large search for p-wave superfluids and Majorana fermions. One of the earliest examples since ^3He was in the superconducting phase of SrRuO_3 [14]. Cold alkali atoms have a particular lure, because they are highly controllable, and they offer the possibility of studying condensation in a weak coupling limit, where perturbative results apply. Proposals for p-wave superfluidity in cold alkali atoms range in mechanism, including taking advantage of anisotropic effects due to a dipolar interaction [2, 4], using long range interactions due to a bosonic mediator[6] and using p-wave Feshbach resonances.[7, 5, 25]

More recently, species-specific optical lattices [12] have been experimentally implemented [11] and have allowed for systems where 1 species of atom is confined to a plane or a wire, while the other particle is free to explore a 3D trap. This possibility led to the a new set of proposals for p-wave pairing mechanisms in cold atoms systems. Nishida[17] and Wu et. al.[23, 16] use a long range attraction, mediated by the 3D particles, to create pairs of 2D particles. Since they are either only considering one species[17, 16] or an imbalance of

spin species[23], the exchange symmetry can't be satisfied by the singlet states in the $l=0$ orbital mode and is forced in to one of the spin triplet states of the $l=1$ orbital mode.

Okamoto[18] studied a system with an equal density of spin-half species in the 2D plane, where the exchange repulsion doesn't prevent s-wave pairing. Here, they went beyond the mean field analysis of [17, 23, 16] and found a full range of orbital pairing states from s-wave to g-wave pairing. Surprisingly, they found p-wave pairing occupied a negligible part of the fermion mediated phase diagram. This suggests that either the exchange interaction is required to stabilize the p-wave phase in mixed-dimensions or that fluctuations destabilize the phase.

In fact, we find that this is not the case. By a directed investigation into the p-wave phase, we demonstrate the stability of the triplet superfluid phase in a wide range of parameter space and that it is stable to fluctuations. If realized, this system would provide a highly controllable, weak coupling analogue of superfluid helium, where one could explore the full range of spin textures and triplet superfluid properties.

We begin this article by reviewing the physics of mixed dimension mediation and demonstrate the ability to construct an arbitrary potential given many mediator types. In Section 2.4 we review functional Renormalization Group and analytically argue why the p-wave phase is stable in this system. In Section 2.5 we present numerical results that demonstrate the stability of the p-wave phase and highlight the nearby S-wave and D-wave instabilities. Finally, we conclude with a discussion on experimental feasibility and the various p-wave pairing states and vortices.

2.3 2D Interactions via 3D Mediators

The full range of a pairing states proposed in [18] and the possibility of p-wave pairing in mixed dimensional cold atom systems is a product of the tunability of a long range interactions. This tunability comes from the ability to change the properties of the higher dimension particle, which mediates the long range interaction. In this article we, study 3D particles (ϕ_r) which can either be bosons (b_r) or fermions (f_r). The 3D particles mediate interactions between the 2D fermionic particles($\psi_{r,\sigma}$) with spin σ . The mediating interaction is computed in [18] and [17] for fermions and in [23, 16] for bosons. The derivation is repeated here to demonstrate the control over the real space interaction for the 2D fermions and to highlight the similarity between various types of 3D mediators.

The action can be broken into the parts for the two types of particles and a term for their interaction:

$$S = S_2(\psi) + S_3(\phi) + S_I(\phi, \psi) \quad (2.1)$$

The interaction between the two particles is an s-wave contact interaction:

$$S_I(\phi, \psi) = g \sum_r \psi_r^\dagger \psi_r \phi_r^\dagger \phi_r \quad (2.2)$$

The strength and sign of the coupling can be tuned by the scattering length via Freshbach resonance. When Fourier transformed, momentum is only conserved in plane:

$$S_I(\phi, \psi) = \quad (2.3)$$

$$\frac{g}{V\beta} \sum_{\vec{k}', \vec{k}, \vec{q}, \vec{q}', q_z, q'_z} \psi_{\vec{k}'}^\dagger \psi_{\vec{k}} \phi_{\vec{q}', q'_z}^\dagger \phi_{\vec{q}, q_z} \delta(\vec{k}' - \vec{k} + \vec{q}' - \vec{q})$$

where we have assumed the 2D plane is located at the center of the 3D trap at $z = 0$ and the sums over Matsubara frequencies and spins are implicit.

In addition to the 2D and 3D traps, we study a system with an added 2D and 3D periodic lattice potential. This allows us to slow the fermi-velocity of the lattice fermions so the interactions mediated by the 3D particles can be approximated as instantaneous. The action of the 2D fermions is written as:

$$S_2(\psi) = \sum_{k, \omega_n, \sigma} \psi_{k, n, \sigma}^\dagger (\varepsilon_k - i\omega_n) \psi_{k, n, \sigma} + \frac{U_2}{A\beta} \sum_{\vec{q}, k_1, k_2} \psi_{k_1+q}^\dagger \psi_{k_2-q}^\dagger \psi_{k_2} \psi_{k_1} \quad (2.4)$$

Where $\varepsilon_k = 2t_2(\cos(k_x) + \cos(k_y))$ is the lattice dispersion, A is the area of the lattice and ω_n are fermionic Matsubara frequencies. The coupling U parameterizes another contact interaction but also depends on the depth of the 2D lattice.

Integration of the 3D particles modifies the chemical potential of the 2D fermions and generates an additional effective interaction. Thus, from now on the 2D chemical potential, μ_2 will be implicitly understood to contain the modification by the 3D particles. We first integrate the 3D particles as fermions ($\phi_r = f_r$) in a 3D lattice with the action:

$$S_3 = \sum_{k, k_z, \nu_n} f_{\vec{k}, k_z, n}^\dagger f_{\vec{k}, k_z, n} G_3^{-1}(\vec{k}, k_z, \nu_n) \quad (2.5)$$

$$G_3^{-1}(\vec{k}, k_z, \nu_n) = \varepsilon_{\vec{k}, k_z} - i\nu_n$$

Where ν_n are the Matsubara frequencies for the 3D particles, G_3 the propagator for the 3D particles and $\varepsilon_{\vec{k}, k_z} = 2t_3(\cos(k_x) + \cos(k_y) \cos(k_z)) - \mu_3$ the 3D lattice dispersion.

The integration is done perturbatively and yields a one loop particle hole diagram for the effective interaction:

$$V_f(q, \omega_n) = -g^2 \frac{A}{V^2 \beta} \sum_{\vec{k}, k_z, k'_z, \nu_n} G_3(\vec{k}, k_z, \nu_n) G_3(\vec{k} + \vec{q}, k'_z, \nu_n + \omega_n) \quad (2.6)$$

Converting to the continuum and integrating the Matsubara sum, we are left with:

$$\frac{-g^2}{(2\pi)^4} \int d\vec{k} dk_z dk_{z'} \frac{n_f(\varepsilon_{q,q_z}) - n_f(\varepsilon_{q+k,q'_z} - i\omega_n)}{\varepsilon_{q+k,q'_z} - \varepsilon_{q,q_z} - i\omega_n} \quad (2.7)$$

To consider a instantaneous mediated interaction by fast 3D particles we insist that $t_2 \ll t_3$.

The strength of this interaction with respect to the bandwidth of the 2D particles is then $O(\frac{g^2}{2t_2 2t_3}) = O(\frac{\alpha g^2}{4t_3^2})$, with $\alpha \gg 1$. We estimate that α can range from 3 to 190: where at the lower end, we used two similar mass particles, such as Li and Na, in lattices with similar depths; while at the upper end, we are considering two particles with significantly different masses, such as Cs and Li, and that the lattice depth of the 2D particles decreases the tunnelling rate by a factor 10[10]. Thus, at first glance, it appears we need $g/2t_3 < 1/\sqrt{\alpha}$ for perturbation theory to be valid when integrating the 2D fermions.

Despite the lattice dispersion preventing an analytic calculation, we can ignore retardation effects by setting $\omega_n = 0$ and numerically integrate Eq. 2.7. The Fourier transform for various distances is plotted in Fig. 2.1 as a function of 3D chemical potential. A key thing to note are the Friedel oscillations, where the sign of the interaction changes sign at different distances and the nearest neighbour interaction is exponentially smaller than the on-site interaction. This means that, if the on-site contact interaction is strong enough to cancel the on-site mediated interaction, an integration of the effective 2D fermionic action will still be perturbative when $g/2t_3 > 1/\sqrt{\alpha}$. Thus, while Fig. 2.1 depicts a negligible nearest neighbour interaction, it can still be formidable, scaling with α .

This calculation was done for a finite sized lattice in [18] and a similar calculation was done by [17] where the lattice potential is not included. Without the lattice, there is no natural ultraviolet cutoff and regularization is needed to deal with an ultraviolet

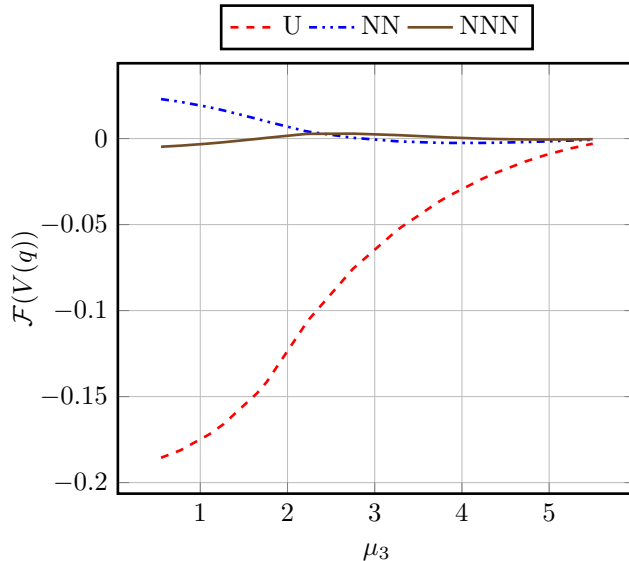


Figure 2.1: This is a plot of the Fourier transform at various distances for a 2D mediated interaction mediated by 3D lattice fermions. U is the onsite interaction strength, NN is for the nearest neighbour and NNN is for the next nearest neighbour. The y-axis is in units of t_2 and the x-axis is in units of t_3 .

divergence. The end result is effectively the same as when the lattice spacing is much smaller than the inter-particle spacing, i.e. at low densities. The difference is at higher densities, where, in the system without the lattice potential, there is no interplay between the lattice spacing and the average particle spacing. For the lattice system, the interaction strength will peak at half filling where the primary mediator switches to lattice hole and the hole density decreases until the band is full and doesn't mediate interactions. While for the system without the lattice potential, the density of states of the scattering mediators is always increasing with the area of the fermi-surface.

For bosonic mediators, we assume the 3D bosonic system has condensed to form a superfluid and interactions are mediated by Bogoliubov particles with dispersion $\omega_q^2 = \varepsilon_0(q)(\varepsilon_0(q) + \Delta)$. Where ε_0 is the dispersion for the free bosons and Δ is the superfluid gap.

The interaction between the 2D fermions and the Bogoliubov quasi-particles is written:

$$S_I(b, \psi) = \frac{g}{V\beta} \sum_{k, q, q_z} \psi_{k+q}^\dagger \psi_k \sqrt{\frac{N_b \varepsilon_0(q)}{\omega_q}} (a_{-q}^\dagger + a_q) \quad (2.8)$$

Where a and a^\dagger are the creation and anihilation operators for the Bogoliouov quasi-particles, and N_b is number of condensed bosons. The action for the quasi particles is now quadratic and can be integrated exactly yielding an effective interaction:

$$V_b(q, \nu) = -\frac{g^2 N_0}{2\pi V} \int dq_z \frac{\varepsilon_0(q)}{\omega_q^2 + \nu^2} \quad (2.9)$$

Fourier Transforming to real space we get:

$$V_b(\delta\vec{r}, \nu) = -\frac{g^2 n_0}{(2\pi)^3} \int dq_z d\vec{q} e^{i\vec{q}\cdot\delta\vec{r}} \frac{\varepsilon_0(q)}{\omega_q^2 + \nu^2} \quad (2.10)$$

where $\delta\vec{r}$ is the distance the two particles and n_0 is the boson density. This interaction is the same as for 3D bosons mediating other 3D particles but with $\delta r_z = 0$. Again we can assume the 3D particles move much faster then the 2D particles and that the interaction potential will be of the Yukawa form with a mass equal to the condensation gap Δ . Thus, with regards to the sign and relative strength of the on-site and nearest neighbour interactions, the bosonic system is the same as the fermi-systems at low density. This means that, in terms of the phase diagram derived from this effective action, the low density lattice fermions, free fermions and free bosons are effectively the same. Of course, this does not mean there aren't great physical differences between these systems. These differences can have great importance related to the feasibility of an experiment. For example, bosonic systems have been show to suffer losses from 3 body Effimov physics and free fermions can have larger fermi-velocities then their low-density lattice counterparts.

We reproduce these calculations here to demonstrate the ability to arbitrarily control the effective on-site and nearest neighbour interaction. For a single mediator, the knobs are the coupling strengths g and U , the mediator density via μ_3 and the tunnelling rate $1/t$. For lattice fermions in 3D, μ_3 allows one to choose the sign of the nearest neighbour. The tunnelling rate controls the overall strength of the mediated interaction while the on-site coupling U can adjust the overall on-site interaction strength to a desired value.

While experimentally infeasible, it is entertaining to note that this process could theoretically be extended to arbitrary control of the effective interaction strength of n^{th} next nearest neighbour sites. In this generalization, there are n free parameters from the n 3D particle densities which can be used to tune the interaction at n different interaction distances. Then, the on-site coupling strength, U , can correct whatever on-site interaction is left over.

2.4 Renormalization Group Analysis of Triplet Pairing Instability

The versatility of this interaction gives a wide range of control over the pairing instability. In this section, we demonstrate that the pairing instability is of the Triplet p-wave type and dominates a significant region of parameter space. To this end, we will work with an explicitly 2D action in the weak coupling limit and consider fluctuations directly via the functional Renormalization Group (fRG)[15].

fRG is a broad class of RG schemes that specifies the dependence of some functional on some parameter via the flow equations. When this functional is the effective action at

a given length scale, one can obtain Wilsonian like RG equations for the various n -point functions [15]. In this paper, we consider a 2D effective action which depends on spin. In a perturbative expansion one can focus only on the small n n -point functions. We write the effective action for the 2D fermions as:

$$\Gamma^\Lambda(\psi) = \sum_i \Gamma_2^\Lambda \psi_i^\dagger \psi_i + \sum_{i,i',j,j'} \Gamma_4^\Lambda(i,i',j,j') \psi_i^\dagger \psi_{j'}^\dagger \psi_i \psi_j \quad (2.11)$$

where i, j , etc. are field variables that carry momentum, spin and Matsubara frequency: $(\vec{k}_i, \omega_{n_i}, \sigma_i)$. For the initial conditions at $\Lambda = 2t$, the effective action is given as the bare 2D action (Eq. 2.4) with a modified interaction, $\Gamma_4^{2t_2} = \frac{U_2 + V_f(\vec{q}, 0)}{A\beta}$. Where $V_f(\vec{q}, 0)$ and U_2 are defined in Eq. 2.4 and Eq. 2.6 correspondingly. We will discuss the generalization to other 3D mediators at the end of this section.

Our analysis on the relevant couplings focuses on the flow of two particle scattering or the 4 point function, Γ_4^Λ . At one loop order, one can ignore the flow of the 2-point function when considering the flow equations for the 4-point function. The flow of the 4-point function, Γ_4 , obtains contributions from the three diagrams shown in Fig. 2.2. The integral for β_{PP} is written:

$$\begin{aligned} \beta_{PP}(\Gamma_4^\Lambda(i, i', j, j')) = & \quad (2.12) \\ & \frac{1}{2} \sum_q \Gamma_4^\Lambda(i, q, j, i+j-q) \Gamma_4^\Lambda(q, i', i+j-q, j') * \\ & \frac{\Theta(\varepsilon_{q'} - \Lambda) \delta(\varepsilon_q - \Lambda) + q \leftrightarrow q'}{(\varepsilon_q - iq_0)(\varepsilon_{q'} - iq'_0)} \end{aligned}$$

where $q' = i + j - q$ and Θ is the step function.

All three beta functions have two internal legs. One internal leg is restricted to an equal energy surface, while the other is restricted to the momentum above the cutoff

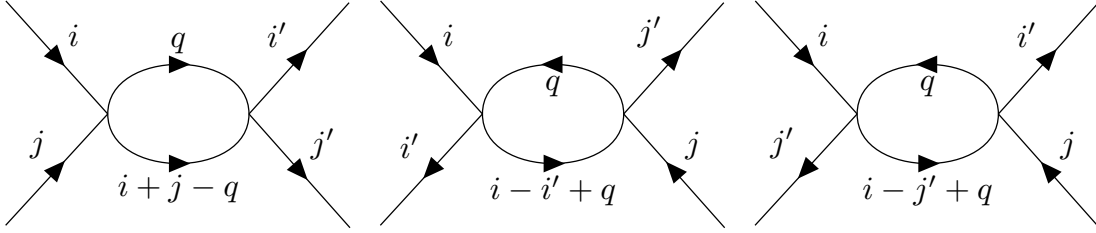


Figure 2.2: 4 point beta functions. The PP diagram is responsible for pairing instabilities while the PH and PH' diagrams are responsible for density wave instabilities.

and determined by momentum conservation. The magnitudes of the beta functions are inversely proportional to the energy of the two internal legs. This causes the diagrams, where the momentum conserved leg is guaranteed to also be on the cutoff energy surface, to flow the strongest. Furthermore, couplings on the fermi-surface will always be flowing, while couplings above the cutoff won't. Therefore the couplings on the fermi-surface that satisfy the momentum conserving condition will be most relevant. In fact it can be shown that all other couplings are irrelevant[21, 20]. The condition for a relevant coupling from the PP diagram is then:

$$\varepsilon_{i+j-q} = \Lambda \quad (2.13)$$

and the condition for the PH contribution is

$$\varepsilon_{i-i'+q} = \Lambda \quad (2.14)$$

These conditions, along with momentum conservation and the restriction of relevant scattering to the fermi-surface, reduce the parameterization of the relevant scatterings to two angles, and the spin dependence: $\Gamma_{PP}^\Lambda(\sigma, \theta_1, \theta_1')$ and $\Gamma_{PH}^\Lambda(\sigma, \theta_1, \theta_2)$. Given SU(2) symmetry the spin dependence breaks down into singlet and triplet scattering, $\sigma = S, T$.

When the effective chemical density of the 2D fermions, μ_2 , is away from half filling, the relevant fermi-surface scatterings don't satisfy Eq. 2.14. On the other hand, the fermi-surface at all fillings obeys inversion symmetry and thus the PP condition Eq. 2.13 is satisfied yielding relevant $\Gamma_{PP}^\Lambda(\theta_1, \theta_{1'})$ couplings. When μ_2 is close to the bandwidth, the energy levels close to the fermi-surface are circular and the frequency integral in Eq. 2.15 can be evaluated at 0 temperature directly yielding[21]:

$$-2t_2\Lambda \frac{d}{d\Lambda} \Gamma_{PP}^\Lambda(\theta_1, \theta_{1'}) = -\frac{1}{8\pi^2} \int \frac{d\theta}{2\pi} \Gamma_{PP}^\Lambda(\theta_1, \theta) \Gamma_{PP}^\Lambda(\theta, \theta_{1'}) \quad (2.15)$$

This equation can be decomposed into angular momentum modes and the resulting set of differential equations solved by:

$$\Gamma_l^\Lambda = \frac{\Gamma_l^{2t_2}}{1 + \ln\left(\frac{\Lambda}{2t_2}\right) \frac{\Gamma_l^{2t_2}}{4\pi}} \quad (2.16)$$

Where, $\Gamma_l^{2t_2}$ is the decomposition of the PP 4-point function, Γ_{PP}^Λ , at the bandwidth scale $\Lambda = 2t$. When $\Gamma_l^{2t_2}$ is attractive, Eq. 2.16 has a divergence at a critical scale,

$$\Lambda_c = 2t_2 \exp\left(-\left|\frac{1}{\Gamma_l^{2t_2}}\right|\right) \quad (2.17)$$

indicating that the system flowed to a new fixed point. For finite temperatures, the singularity in Eq. 2.15 is smoothed and for temperatures above the critical scale, the couplings stay near the free (Fermi liquid) fixed point. For temperatures below the critical scale, the couplings diverge and the flow can not be continued to the new fixed point. A guess with a mean field analysis must be used to determine the properties of the new fixed point. For the PP divergences, mean field suggests a pairing state describes the new fixed point, where the angular momentum and the spin state of pairs are determined by leading Γ_l^Λ .

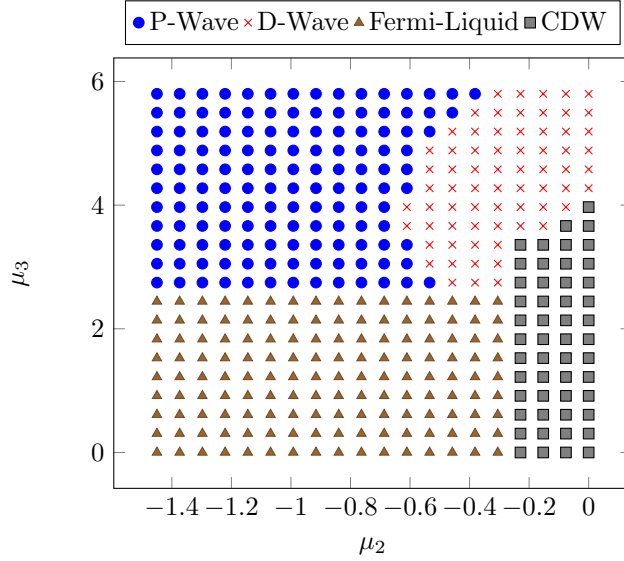


Figure 2.3: Phase diagram suggested by bare interaction. This is for fixed V_3 and for U set to cancel onsite interaction. This probably can be smaller.

Eq. 2.16 indicates the leading divergence will correspond to the mode with largest $\Gamma_l^{2t_2}$. Therefore, we will have triplet pairing when the largest $\Gamma_l^{2t_2}$ has an odd l . On-site, local interactions have a flat Fourier transform and thus only contribute to s-wave interaction. Nearest neighbour interactions, on the other hand, have 4 sites to modify the rotational symmetry and therefore can contribute to $l = 1$ (p-wave) or $l = 2$ (d-wave) modes. So given the tunability of 3D mediators, triplet pairing can be induced by an attractive, long-range, effective action. The condition for this in terms of Γ_l^{2t} is: $\Gamma_1^{2t_2} < 0$ and $|\Gamma_1^{2t_2}| > |\Gamma_l^{2t_2}|$.

This requires that the nearest neighbour attraction be stronger than the on-site attraction, otherwise s-wave pairing will dominate. In spin-less or spin-imbalanced systems, the exchange repulsion guarantees that this is the case. For SU(2) symmetric systems, the mediated on-site attraction, found in Fig. 2.1 and Eq. 2.10, needs to be compensated by a repulsive contact interaction between the 2D particles.

This compensation still leaves the possibility of d-wave pairing and we check this numerically. This calculation begins by breaking the two angles in the relevant couplings, $\Gamma_{PP}^{2t_2}(\sigma, \theta_1, \theta_{1'})$, into 16 patches. We then compute the eigen-vectors and eigen-values of the matrices $\Gamma_{PP}^{2t_2}(\sigma, i, j)$. The number of 0s in the eigen-vector determine the angular momentum, l , and the eigen-value gives us $V_l(2t_2)$. To satisfy the 2π boundary condition, $\Gamma_{PP}^{2t_2}(\sigma, i, j)$ must have eigen-vectors with $2n$ zeros. To satisfy exchange symmetry, matrices with $\sigma = T$ will have odd n , while those with $\sigma = S$ will have even n . For energy levels away from the circular fermi-surface, the decomposition of the beta functions for the relevant couplings will depend on the shape of the fermi-surface, but the general feature that negative eigen-values diverge at a given scale will remain. This is because there is still inversion symmetry and the PP graph is still relevant. This way we can still guess what fix point the RG equations will flow to by decomposing the initial 4-point function $\Gamma_{PP}^{2t_2}(\sigma, \theta_1, \theta_{1'})$.

In search of the $l = 1$ Triplet mode, we consider the μ_2, μ_3 plane where we have fixed the on-site contact interaction to compensate the mediated on-site interaction by $U_{eff}/t = 1$. The overall strength of the mediated interaction will determine the critical scale but won't effect which pairing state appears. For this, we set the over all strength of the contact interaction between the 3D and 2D gasses to be $\alpha g^2/t_3^2=100$. The phases predicted by the decomposition of the initial 4-point function is shown in Fig. 2.3. For $\mu_3 < 2.2$, the nearest neighbour interaction is also repulsive, so the only potential relevant coupling flows to 0. Thus, we predict that this part of the phase diagram will be a fermi-liquid at all relevant energy scales. For $\mu_3 > 2.2$ the nearest neighbour interaction is attractive and we expect pairing. For $\mu_2 < -0.6$ p-wave pairing dominates but for $\mu_2 > -0.6$, the symmetry

of the fermi-surface favours D-wave pairing. For $\mu_2 = 0$ the Fermi surface is nested and we expect the PH couplings to diverge first and the system to favour a CDW.

We suspect similar results for free fermion and bosonic mediators. Given that the on-site contact interaction cancels the on-site mediated interaction, a higher angular momentum pairing state will dominate at low temperatures. Which pairing state will then depend on the geometry of the fermi-surface, and as the 2D fermions approach half filling, a p-wave instability will become a d-wave one. The CDW will continue to persist at half filling due to the nesting of the fermi-surface. The primary difference is that the bosons and fermions don't acquire a repulsive nearest neighbour interaction and destabilize the p-wave phase at a specific doping.

Similar results are also expected to hold in the spinless systems studied with mean field by Nishida and Wu [17, 23, 16]. In this system, the effective interaction, Γ_4^{2t} , is the same as the triple component of the SU(2) symmetric system. The PP instability is still present, but the exchange symmetry only allows odd l . Thus, the negative initial-eigen-value for $l = 1$ will still be dominant, but it won't have to compete with s or d-wave. Furthermore, in the system with fermionic mediators on a lattice, the transition to a fermi-liquid at higher densities will still occur as the $l = 1$ initial-eigen-value changes sign.

2.5 Numerical fRG Results

The results above give our analytic expectation for when the 2D effective action flows to a triplet pairing fixed point. In this section, we numerically solve the RG flow equations, with the intent to directly consider anisotropic effects of the fermi-surface and

the interaction between different pairing instabilities. To this end, we use a different fRG functional, the Wick ordered effective action, $W^\Lambda(\psi)$ which generates wick ordered n-point functions [15, 20, 8]. This functional directly reproduces the effective action as $\Lambda \rightarrow 0$ and has the numerically appealing feature that its flow equations are local in the cutoff.[8] Since the \mathcal{W}^Λ only reproduces the effective interaction in the 0 cutoff off limit, we predict the low energy phases by tracking how correlation functions diverge as the cutoff is lowered. This is because above the critical temperature, \mathcal{W}^Λ doesn't have any divergences and correctly gives the correlation functions. As one approaches the critical temperature, critical fluctuations lead to divergences in the correlation functions. This will again be captured by \mathcal{W}^Λ and will continue to diverge in the same way as we reduce the temperature. This is because we are still starting from the free fixed point.

Therefore, we can use which correlation diverges first to determine the low energy phase.[8] We consider particle-particle correlations to identifying pairing phases:

$$\mathcal{X}_{PP}^\Lambda(f, s) = \left\langle \left| \int d\theta f(\theta) s_{\sigma, \sigma'} \psi_\sigma(k_f, \theta) \psi_{\sigma'}(k_f, -\theta) \right|^2 \right\rangle^\Lambda \quad (2.18)$$

where the expectations are computed at a cutoff Λ using \mathcal{W}^Λ , $f(\theta)$ determines the pairing symmetry, and $s_{\sigma, \sigma'}$ determines whether the system is in a singlet or triplet pairing state.

Similarly, particle-hole correlations are used to identify density wave phases:

$$\mathcal{X}_{PH}^\Lambda(s) = \left\langle \left| \int dk s_{\sigma, \sigma'} \psi_\sigma^\dagger(\vec{k}) \psi_{\sigma'}(\vec{k} + \vec{q}) \right|^2 \right\rangle^\Lambda \quad (2.19)$$

Here $s_{\sigma, \sigma'}$ determines if we are considering spin or charge density waves. At the beginning of the flow these correlations are $O(1)$. As we approach the critical scale, the correlations will diverge, and we can approximate the critical scale for a given correlation as the scale when that correlation is $O(100)$.

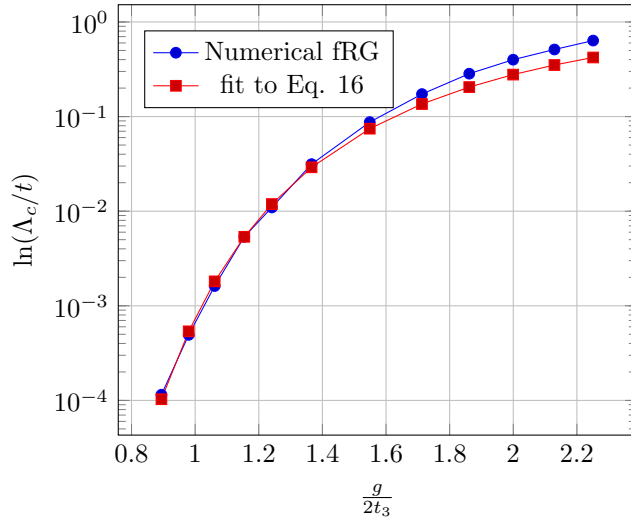


Figure 2.4: As we increase the mediated interaction, the critical scale rises exponentially until we are in the strong coupling limit. The overall interaction strength depends on α which we set to 150.

As is standard with numerical fRG calculations [8, 19, 24, 9, 3], we flow a finite number of couplings by projecting the momentum to a finite number of patches on the fermi-surface. These patches are identified by their angle, θ_i for $i \in (1, m)$. Since the 4th momentum is specified by momentum conservation, there are m^3 couplings and m^3 coupled differential equations to be solved for each $\Gamma^\Lambda(i, j, k)$. Due to this computation complexity we work with $m = 16$, and do not explore the full four dimensional parameter space (μ_2, μ_3, U, g) . Instead, we focus on specific cuts to confirm the above picture and understand the stability of the triplet pairing phase.

First, we test the estimation given by Eq. 2.17, which gives critical temperatures as a function of $|\frac{1}{\Gamma_l^{2t_2}}|$. To this end, we make the first cut deep within the expected triplet pairing phase at $\mu_2 = -1.4$ and $\mu_3 = 3.85$. As before, we set the on-site contact interaction such that the effective on-site interaction at $\Lambda = 2t_2$ is $U_{eff}/t_2 = 1$, and S-wave pairing is

suppressed. We confirmed that the p-wave triplet $\mathcal{X}_{\bar{p}p}^\Lambda(p, T)$ correlation diverged first, and in Fig. 2.4, we plotted the dependence of the critical scale on the magnitude of the coupling strength, $g/2t_3$.

We then fit this to the prediction of Eq. 2.17. This fit has one free parameter, β defined as $\Gamma_1^{2t_2} = \beta\alpha(\frac{g}{2t_3})^2$. β then gives the fraction of the interaction that is contained in the $l = 1$ scattering mode. Despite the non trivial geometry of the fermi-surface and the inclusion of the particle-hole beta functions, the scaling is well described by Eq. 2.17. We find that $\beta = 0.8 * 10^{-3}$. This compares well with our expectation that the $l = 1$ mode is coming from the effective nearest neighbour attraction, which is approximately $2 * 10^{-3}$ at $\mu_3 = 3.85$. A possible source of error is the method we estimate the cut-off. Since we can not numerically compute the location of the asymptote exactly, we have to estimate it by a max correlation strength.

At large $g/2t_3$, the perturbative integration of the effective interaction may be called into question. This can be resolved by increasing α : allowing the effective nearest neighbour strength to still be large, but $g/2t_3$ to still be perturbative. There is still a question on the validity of the one-loop fRG equations, because the effective nearest neighbour interaction still needs to be close to the 2D bandwidth for the critical temperature to be 10% of the bandwidth. This is resolved by an argument by Shankar[21], which states that the fRG calculations can be understood as a type of Large N expansion, where N grows as the cutoff is lowered. This interplay between a high critical temperature and perturbative validity will be discussed further in the Section 7.8.

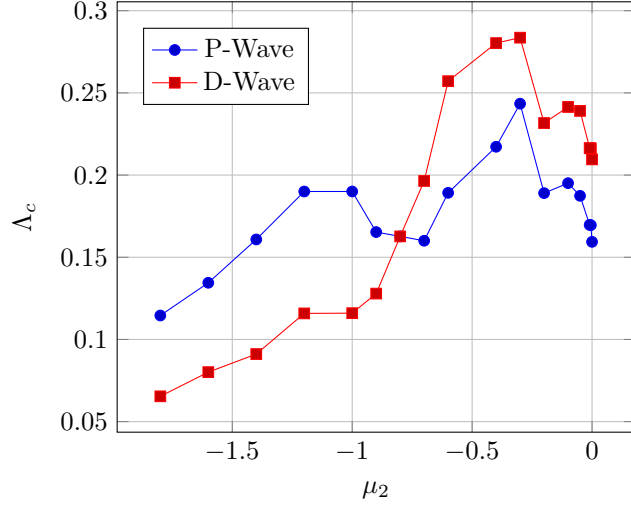


Figure 2.5: This plot depicts the instability of p-wave pairing to d-wave pairing upon varying the 2D particle density. This cut is at $\mu_3 = 3.85$, $U_{eff}/t_2 = 1$, $\alpha = 150$ and $g/t_3 = .86$

In the previous section, we predicted that as we decreased the doping of the 2D fermions, we would transition from triplet pairing to d-wave singlet pairing. This transition was confirmed numerically and is depicted in Fig. 2.5. This figure shows the transition to d-wave at $\mu_2 = -0.8$. Away from the transition the difference between the two critical scales is relatively the same. This is a failure of perturbative fRG equations: when the scatterings responsible for the leading correlation function starts to diverge, it also drives the divergence of non-leading correlation functions. It is worth pointing out that we don't see any exponential scaling in the p-wave interaction because the relative strength of the $l = 1$ interaction doesn't change as we vary μ_2 .

Next, we consider doping in the 3D lattice fermions with a cut at $\mu_2 = -1.4$. Our results are plotted in Fig. 2.6 and confirm our expectations from the previous section. At low 3D particle density, there are few particles to mediate interactions and the system

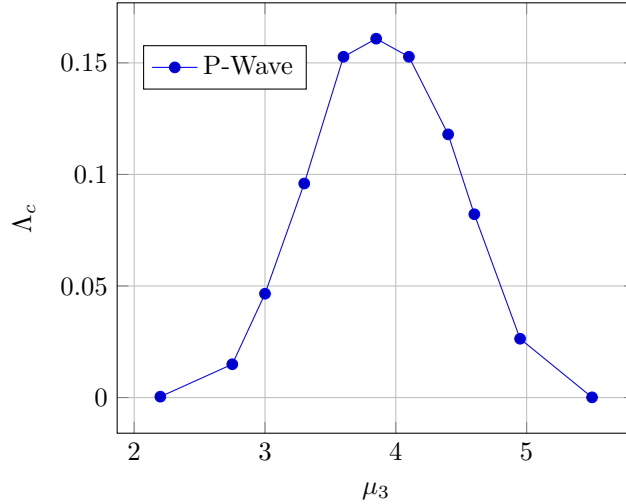


Figure 2.6: This plot depicts the dependence of the critical temperature of p-wave pairing on the 3D particle density. This cut as the same interaction parameters as in Fig. 2.5: $U_{eff}/t_2 = 1$, $\alpha = 150$ and $g/t_3 = .86$

remains a fermi-liquid to lower temperatures. As the 3D particles approach half filling, the nearest neighbour interaction becomes repulsive and the p-wave instability disappears. While at intermediate doping $\mu_3 = 3.85$ the p-wave instability reaches its maximum value.

Finally, we consider the stability of the p-wave phase to the strength of the on-site contact interaction. In Sec. 2.4, we pointed out that it is required to be strong enough to cancel the on site attraction due to the mediated particles. In the previous cuts we always set the contact interaction so the effective on-site interaction was $U_{eff}/t = 1$. In Fig. 2.7, we plot a cut where all parameters are fixed at their optimal values for p-wave pairing, and we vary the on-site contact interaction. Once the effective onsite interaction becomes more attractive than the initial $l = 1$ pairing strength, the s-wave critical scale begins to grow until it over comes the p-wave pairing. The transition point happens below 0 because the

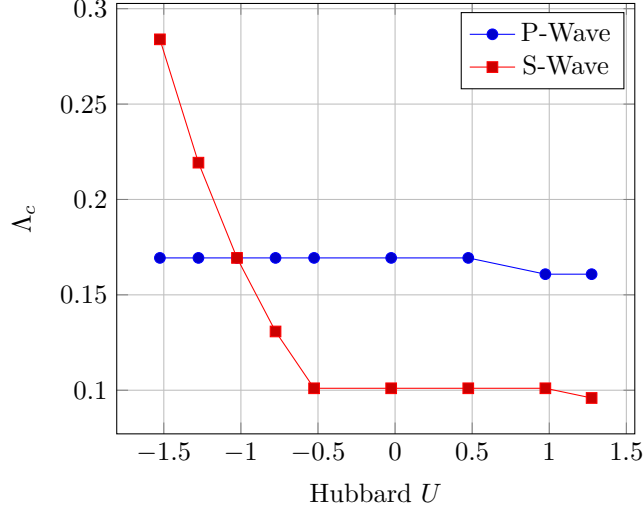


Figure 2.7: As we reduce the onsite contact interaction, the effective onsite interaction becomes negative and s-wave pairing starts to dominate. This cut is at $\mu_3 = 3.85$, $\mu_2 = -1.4$, $\alpha = 150$ and $g/t_3 = .86$

$l = 1$ component still dominates. As we decrease the $l = 1$ component, by changing μ_3 or reducing g/t_3 , the transition point will increase to 0.

2.6 Discussion

The main experimental barrier to realizing this system is cooling. In the weak coupling limit, fRG analysis clearly demonstrates that: at low enough temperatures, the fermi-liquid phase is unstable to triplet pairing. Furthermore, if the next nearest neighbour interaction is close to, but less than, the bandwidth, the critical temperature will be about 10% the bandwidth (an experimentally accessible temperature). The trouble is reaching this interaction strength without invalidating the perturbation theory that derived the mediated interaction. This is achieved by increasing α , i.e. using particles with significantly different masses and increasing the lattice depth of the 2D particles. While this maybe infeasible,

one can still push g/t_3 beyond the perturbative limit. In this limit, one still expects inter-species interactions to mediate some form of long range attraction and a mean field analysis in similar systems has suggested a triplet instability[17, 23, 16]. Thus, despite possible troubles with cooling, our results suggest that fluctuations are compatible with the mean field analysis of previous studies and this system has a p-wave pairing instability.

This work goes beyond previous studies of p-wave pairing in mixed dimension by demonstrating a system with $SU(2)$ spin symmetry is also unstable to triplet pairing. Therefore, if implemented, this system could be used as a test bed for a wider range of triplet pairing physics. In this system, the triplet pairing state is degenerate, and, unlike the singlet counter part, the paramagnetic instability will be the same as the uncondensate state [13]. With the addition of perturbations, such as spin orbit coupling or introducing an imbalance in species, one can explore the full range of possible spin textures and vortices. Maybe most excitingly, if one adds spin orbit coupling, vortices with half a quantum flux will appear and will host Majorana fermions[1].

In this work, we have studied 2D fermions that have a long range attraction which can be mediated by three different types of 3D particles. Focusing on 3D fermions in a lattice, we have shown that an $SU(2)$ symmetric, triplet, p-wave pairing instability is dominant in a wide range of parameter space. We then argued that this phase will extend to the two other types of mediators. We have also argued that the previous mean field results hold for spinless systems in the weak coupling limit where fluctuations dominate the physics. Finally, we have identified nearby s-wave and d-wave, singlet pairing phases and identified the critical energy scale for the transition from the fermi-liquid phase to

the pairing phases. This work demonstrates that systems that don't rely on the exchange repulsion to suppress s-wave pairing are capable of triplet superfluidity, and thus it opens the possibility of exploring the full range of triplet-pairing physics observed in He^3 and similar systems.

Bibliography

- [1] Jason Alicea. New directions in the pursuit of Majorana fermions in solid state systems. *Reports on Progress in Physics*, 75(7):076501, jul 2012.
- [2] M. A. Baranov, M. S. Mar’enko, Val. S. Rychkov, and G. V. Shlyapnikov. Superfluid pairing in a polarized dipolar Fermi gas. *Physical Review A*, 66(1):013606, jul 2002.
- [3] S G Bhongale, L Mathey, Shan Wen Tsai, Charles W Clark, and Erhai Zhao. Bond order solid of two-dimensional dipolar fermions. *Physical Review Letters*, 108(14):145301, apr 2012.
- [4] G. M. Bruun and E. Taylor. Quantum phases of a two-dimensional dipolar fermi gas. *Physical Review Letters*, 101(24):245301, dec 2008.
- [5] Chi-Ho Cheng and S.-K. Yip. Anisotropic Fermi Superfluid via p -Wave Feshbach Resonance. *Physical Review Letters*, 95(7):070404, aug 2005.
- [6] D. V. Efremov and L. Viverit. p -wave Cooper pairing of fermions in mixtures of dilute Fermi and Bose gases. *Physical Review B*, 65(13):134519, mar 2002.
- [7] V. Gurarie, L. Radzihovsky, and A. V. Andreev. Quantum Phase Transitions across a p -Wave Feshbach Resonance. *Physical Review Letters*, 94(23):230403, jun 2005.
- [8] Christoph J Halboth and Walter Metzner. Renormalization-group analysis of the two-dimensional Hubbard model. *Physical Review B*, 61(11):7364–7377, mar 2000.
- [9] Wen-Min Huang, Chen-Yen Lai, Chuntai Shi, and Shan-Wen Tsai. Unconventional superconducting phases for the two-dimensional extended Hubbard model on a square lattice. *Physical Review B*, 88(5):054504, aug 2013.
- [10] D. Jaksch, C. Bruder, J. I. Cirac, C. W. Gardiner, and P. Zoller. Cold Bosonic Atoms in Optical Lattices. *Physical Review Letters*, 81(15):3108–3111, 1998.
- [11] G. Lamporesi, J. Catani, G. Barontini, Y. Nishida, M. Inguscio, and F. Minardi. Scattering in Mixed Dimensions with Ultracold Gases. *Physical Review Letters*, 104(15):153202, apr 2010.

- [12] L. J. Leblanc and J. H. Thywissen. Species-specific optical lattices. *Physical Review A - Atomic, Molecular, and Optical Physics*, 75(5):053612, may 2007.
- [13] Anthony J Leggett. A theoretical description of the new phases of liquid ^3He . *Reviews of Modern Physics*, 47(2):331–414, apr 1975.
- [14] Yoshiteru Maeno, Shunichiro Kittaka, Takuji Nomura, Shingo Yonezawa, and Kenji Ishida. Evaluation of Spin-Triplet Superconductivity in Sr_2RuO_4 . *Journal of the Physical Society of Japan*, 81(1):011009, jan 2012.
- [15] Walter Metzner, Manfred Salmhofer, Carsten Honerkamp, Volker Meden, and Kurt Schonhammer. Functional renormalization group approach to correlated fermion systems. *Reviews of Modern Physics*, 84(1):299–352, mar 2012.
- [16] Jonatan Melkr Midtgaard, Zhigang Wu, and G.M. Bruun. Topological superfluidity of lattice fermions inside a Bose-Einstein condensate. *Physical Review A*, 94(6):063631, dec 2016.
- [17] Yusuke Nishida. Induced p-wave superfluidity in two dimensions: Brane world in cold atoms and nonrelativistic defect CFTs. *Annals of Physics*, 324(4):897–919, 2009.
- [18] Junichi Okamoto, Ludwig Mathey, and Wen-Min Huang. Fermion pairing in mixed-dimensional atomic mixtures. *Physical Review A*, 95(5):053633, may 2017.
- [19] C Platt, W Hanke, and R Thomale. Functional renormalization group for multi-orbital Fermi surface instabilities. *Advances in Physics*, 62(4-6):453–562, nov 2013.
- [20] Manfred Salmhofer. *Renormalization: An Introduction*. Heidelberg, 1999.
- [21] R. Shankar. Renormalization-group approach to interacting fermions. *Reviews of Modern Physics*, 66(1):129–192, 1994.
- [22] Sumanta Tewari, S. Das Sarma, Chetan Nayak, Chuanwei Zhang, and P. Zoller. Quantum Computation using Vortices and Majorana Zero Modes of a $p_x + ip_y$ Superfluid of Fermionic Cold Atoms. *Physical Review Letters*, 98(1):010506, jan 2007.
- [23] Zhigang Wu and G.M. Bruun. Topological Superfluid in a Fermi-Bose Mixture with a High Critical Temperature. *Physical Review Letters*, 117(24):245302, dec 2016.
- [24] D. Zanchi and H. Schulz. Weakly correlated electrons on a square lattice: Renormalization-group theory. *Physical Review B*, 61(20):13609–13632, 2000.
- [25] Chuanwei Zhang, Sumanta Tewari, Roman M. Lutchyn, and S. Das Sarma. $p_x + ip_y$ superfluid from s-wave interactions of fermionic cold atoms. *Physical Review Letters*, 101(16):160401, oct 2008.

Chapter 3

Detecting Macroscopic Indefiniteness of Cat States in Bosonic Interferometers

3.1 Abstract

The paradigm of Schrödinger’s cat illustrates how quantum states preclude the assignment of definite properties to a macroscopic object (realism). In this work we develop a method to investigate the indefiniteness of cat states using currently available cold atom technology. The method we propose uses the observation of a statistical distribution to demonstrate the macroscopic distinction between dead and alive states, and uses the determination of the interferometric sensitivity (Fisher information) to detect the indefiniteness of the cat’s vital status. We show how combining the two observations can provide infor-

mation about the structure of the quantum state without the need for full quantum state tomography, and propose a measure of the indefiniteness based on this structure. We test this method using a cat state proposed by Gordon and Savage [Phys. Rev. A 59, 4623 (1999)] which is dynamically produced from a coherent state. As a control, we consider a set of states produced using the same dynamical procedure acting on an initial thermal distribution. Numerically simulating our proposed method, we show that as the temperature of this initial state is increased, the produced state undergoes a quantum to classical crossover where the indefiniteness of the cat's vital status is lost, while the macroscopic distinction between dead and alive states of the cat is maintained.

3.2 Introduction

Superposition is at the heart of the many predictions made by quantum mechanics that clash with everyday intuition. It allows for the possibility of an experiment in which we must conclude that some property of an object can not be prescribed a definite value before measurement. Instead, this indefiniteness of a property must be modelled by a superposition of possible values and implies a statistical uncertainty that can not be reduced by obtaining more knowledge about the universe. While plausible for microscopic properties, this possibility directly conflicts with our everyday intuition for macroscopic objects. The characteristic example is the Schrödinger's cat thought experiment[55], where a cat ends up in a superposition of alive and dead by entangling with the decayed or excited state of a radioactive source.

When investigating these macroscopic states in an experiment, we are naturally led to two questions: 1) How do we know the cat's life was an indefinite property before measurement? 2) How do we quantify the macroscopicity of the cat and thus, the extent to which it conflicts with our intuition about the macroscopic world? The first question is answered by Leggett-Garg[38], who constructed a set of inequalities on a set of different-time correlation functions that would only be violated if the cat was in an indefinite state at some intermediate time. The second question has been answered by constructing measures of macroscopicity in two general ways[18]: either by focusing on the structure of a macroscopic cat state[36, 37, 14, 5, 29, 42, 56] or generalizing to any macroscopic quantum state[57, 10, 35, 16, 47, 62, 32, 31]. For many of these measures, a state is declared macroscopic based on how the measures scale with the number, N , of constituent particles. The experimental observation of these measures often leads to a way to answer the first question[17, 10, 31].

In this paper we will work with a measure that is a combination of the one proposed by Leggett[36, 37] and the one proposed by Fröwis and Dür[16]. The measure proposed by Leggett is quantified by two numbers: the extensive difference, Λ , which is the difference of the expectation value for some observable A between the dead and alive states of the cat, and the disconnectivity, a quantity based on the entanglement entropy. The extensive difference describes how macroscopically different the dead and alive cats are, while the disconnectivity quantifies how indefinite the vital status of the cat is. The measure of Fröwis and Dür[16], N_{eff} , is applicable to general quantum states and is based on the experimentally quantifiable, quantum Fisher information (QFI). The QFI has been interpreted as a measure of entanglement[27], and has stimulated a variety of work studying this type of

entanglement[49, 27, 16, 33, 24, 15, 58, 44]. The QFI has also been shown to be connected with the resource theory of coherence[59] and to be the maximum quantifier for the resource theory of quantum invasiveness[45]. Inspired by the measure of Fröwis and Dür, and by recent insights relating the QFI to the convex-roof of uncertainty[61, 63](see Section II), we replace the disconnectivity in Leggett’s measure by a function of the QFI and statistical variance.

This choice is further motivated by the fact that the extensive difference and the QFI are both experimentally accessible in bosonic interferometer experiments. The kind of bosonic interferometer experiments discussed here[49, 46, 58, 65, 52, 1, 21, 28, 2, 4, 54, 13, 46, 4, 54, 13] can be understood as a way to estimate a phase encoded onto a macroscopic spin by a projective measurement. The maximum sensitivity of the interferometer to the encoded phase is given by the classical Fisher information (CFI) via the Cramer-Rao bound[11, 51] and is restricted by the phase encoding method and the chosen projective measurement. The QFI quantifies the sensitivity of the interferometer when the best projective measurement is used and is bounded from below by the CFI. The CFI and other measures of sensitivity can be measured by experiments[58, 40] and many proposals exist to optimize the bound the CFI puts on the QFI[44, 20, 17]. The extensive difference can also be obtained in an experiment from the counting statistics of a single-particle observable[40, 58].

Various types of macroscopic states have been produced in these systems, ranging from squeezed states[24, 15] to non-Gaussian entangled states[58]. There also exists many proposals to create macroscopic cat states in bosonic interferometers[33, 25, 41, 43, 34, 7, 26, 23, 19, 8]. In this article we work with a cat state first proposed by Gordon

and Savage[23]. The method for creating this state can be understood from the classical dynamics of the effective collective spin. As we explain in Section I, the classical dynamics exhibit two different kinds of trajectories separated in phase space by the separatrix. As pointed out by Micheli *et al.*[43], the cat state is prepared by creating an initial coherent state with a Wigner distribution that spans the phase space region crossing the separatrix. The quantum dynamics then separates the components from either side of the separatrix into the macroscopically distinct alive (free oscillation) and dead (self-trapping) components of the cat. They prove this by semi-classically evolving the Wigner function and finding it produces a double peak distribution in the z-component of the macroscopic spin.

Similar arguments can be applied to mixed states, and we show that initial thermal distributions also evolve into a double peak state. We show that the higher the temperature the less indefiniteness the state displays, and we describe how an experimenter can observe this transition. These high temperature states are particularly appealing because, despite increasing the temperature, it is still possible to identify the dead and alive states of the cat. Thus, as temperature increases, the vital status of the cat becomes definite before the distinction between dead and alive is lost.

Previous work has suggested the detection of indefinite properties for similar states by using generalized Leggett-Garg inequalities[53] or observation of many-body correlation functions[48], but these methods rely on experimental tools that have yet to be implemented. In this article, we study the possibility of currently available cold atom technology to experimentally detect the macroscopic indefiniteness of these cat states, and distinguish them from the classical uncertainty of the high temperature mixed states. The method we

propose uses the observation of a statistical distribution to demonstrate the macroscopic distinction (extensive difference) between dead and alive states and uses the interferometric sensitivity (QFI) to detect the indefinite vital status of the cat. We show how these two types of observations provide information about the nature of the possible pure states which make up the density matrix, and how this information is useful in observing the crossover from a cat that is in a superposition of dead and alive to a cat that is either dead or alive. Next, we numerically simulate the method for the Gordon and Savage cat state and demonstrate the quantum to classical crossover. Inspired by the Schrödinger's cat thought experiment, we conclude by considering a cat state which is entangled with an auxiliary qubit (representing the radioactive source) and show that such a quantum to classical crossover is controlled by the strength of entanglement with the auxiliary qubit.

3.3 Interferometers, Cat States and Double Peak Mixed States

Interferometry in Bose Einstein condensates has led to new measurement techniques for magnetic fields[46], gravitational fields[54, 13] and rotational motion[4]. In the kind of interferometry that we are considering, the experiment consists of the following four steps[44, 49]:

(1) *State preparation:* In the first step the state, described by a density matrix ρ , is prepared. This step often involves condensing particles into a single wave function and performing entangling operations to allow sensing at higher accuracy.

(2) *Phase encoding:* The unitary evolution of the interferometer encodes a phase onto the state prepared in the first step: $\rho \rightarrow \rho_\psi = U_{\psi,\Omega}^\dagger \rho U_{\psi,\Omega}$. The Hamiltonian of this unitary evolution is proportional to the parameter to be measured, such as the magnetic field strength. ψ is the phase encoded, and Ω represents the additional parameters of the unitary transform.

(3) *Read-out:* An additional unitary evolution U_r is applied to the state to prepare for an effective measurement of an observable R .

(4) *Projective measurement:* A destructive measurement of an observable X is modelled as a projection onto the eigenvector $|x\rangle$ with measurement value x : $\langle x|U_r^\dagger U_{\psi,\Omega}^\dagger \rho U_{\psi,\Omega} U_r|x\rangle$. Repeating this measurement multiple times produces a distribution:

$$p(r, \psi, \Omega) = \langle r|U_{\psi,\Omega}^\dagger \rho U_{\psi,\Omega}|r\rangle \quad (3.1)$$

with $|r\rangle = U_r|x\rangle$.

For simple set-ups, the expectation value of R is directly proportional to the phase encoded and Hamiltonian parameter being estimated. In this paper, instead of using the last 3 steps to estimate the phase, they are used to verify the indefiniteness of some property of the initial state ρ .

3.3.1 Phase Encoding, Read-out, Projective Measurement

A simple form of interferometry involves two quantization modes that can interfere. These modes can be external kinetic modes in which bosons move in two different guides, or the modes can be identified with the two sites of a double well potential[4, 54, 13, 1, 21, 28, 2, 30]. These modes could also be associated with two different internal states of

the boson particles (e.g. hyperfine states of the bosonic atoms[46, 58, 65, 52] that can be coupled by lasers). A highly successful approximation[50, 43, 39, 22] assumes that the bosons only occupy these two modes. This limits the Hilbert space to that spanned by the Fock-states of the two modes: $|m_1, m_2\rangle$, where m_1 and m_2 are the number of bosons in the first and second modes. Counting the particles in the two modes constitutes the projective measurement of step 4: $|x\rangle = |m_1, m_2\rangle$

A single particle in two modes has a two dimensional Hilbert space and is described by a spin half operator, $\mathbf{J} = \sigma/2$. The single particle observable in 2 modes, for a system with N particles are described by linear combination of $SU(2)$ generators of a $N/2$ spin, $\mathbf{J} = \sum_{i=1}^N \sigma_i/2$:

$$J(\theta, \phi) = J_z \cos \theta + J_x \sin \theta \cos \phi + J_y \sin \theta \sin \phi \quad (3.2)$$

where these Cartesian components, J_z, J_x and J_y , satisfy the standard commutation relations: $[J_i, J_j] = i\epsilon_{i,j,k}J_k$. By mapping the sum, $m_1+m_2 = 2j$, and difference, $m_1-m_2 = 2j_z$, onto the magnitude and z-projection of a collective spin, one can connect the Fock representation with this well-known $SU(2)$ algebra for describing rotations. The particle number difference is then mapped to J_z and tunnelling between the two modes is described by J_x (more generally $J(\pi/2, \phi)$).

For internal modes, a Hamiltonian J_z can be created by applying a magnetic field to split the hyperfine states and a Hamiltonian J_x can be created by applying a Rabi-coupling laser field. For external kinetic modes, these Hamiltonians are controlled by shaping the external potential.

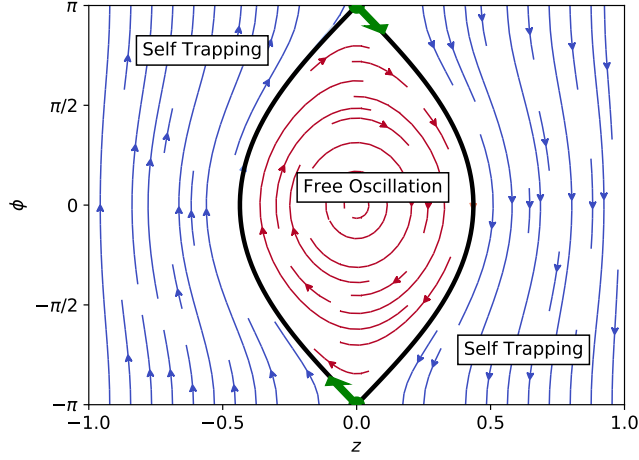


Figure 3.1: (Color online) Classical trajectories. The separatrix is shown in black (bold) and separates the circular free-oscillation trajectories from the self-trapping ones. The green dots mark the fixed point and the green arrows mark the unstable directions.

The phase encoding and read-out operations, $U_{\psi,\Omega}$ and U_r discussed in this paper, are all linear single-particle operations:

$$U(\alpha, \theta, \phi) = e^{-i\alpha J(\theta, \phi)} \quad (3.3)$$

where $U_r = U(T_r \epsilon_r / \hbar, \theta_r, \phi_r)$ and $U_{\psi,\Omega} = U(\psi, \theta_\Omega, \phi_\Omega)$ and ϵ is the energy scale of the Hamiltonian. The collective spin picture maps a projective two-mode number difference measurement, $m_1 - m_2$, to a measurement of the J_z observable. For single-particle read-out, the combined steps 3 and 4 becomes equivalent to an effective measurement on the spin in a new direction: $J_z \rightarrow J_{z'} = U_r^\dagger J_z U_r$. For example, a read-out rotation around the x-axis ($T_r = \frac{\pi \hbar}{2\epsilon_r}$, $\theta_r = \pi/2$, $\phi_r = 0$. *i.e.* $J(\theta_r, \phi_r) = J_x$) produces an effective measurement of J_y .

3.3.2 State Preparation: Cat States and Mixed Double-Peak States

In this paper, the state prepared in the first step of interferometry is the Gordon and Savage cat state[23] or a mixed state with a similar distinction between dead and alive states. In this section, we describe these states and how they can be prepared. In the next section we describe how the last 3 steps can be used to verify indefinite properties of this state.

In bosonic interferometry, state preparation begins with condensation into the ground state of some Hamiltonian $\epsilon_\tau J(\theta, \phi)$. In this paper, we will describe partial condensation using a thermal state:

$$\rho(\beta, z, \phi) = e^{\beta \epsilon_\tau J(\cos^{-1}(z), \phi)}, \quad (3.4)$$

where we have introduced the scaled difference: $z = j_z/j = [m_1 - m_2]/N = \cos(\theta)$. States of this form have been produced for kinetic modes for the Hamiltonian J_x by Gross *et al.*[21], and thermal states of any other Hamiltonian of the form $J(\cos^{-1}(z), \phi)$, can be produced by rotations of the form in Eq. 3.3. For this paper, we will focus on the states $\rho(\beta, 0 = z_c(\pi), \pi)$ and $\rho(\beta, |z_c(0)|, 0)$ which we refer to as the π and 0 state at temperature β^{-1} . The critical imbalance, $z_c(\phi)$, is given by the solid black line in Fig. 5.1.

Following (partial) condensation, cat states can be prepared by the method mentioned above by Gordon and Savage. We will describe this method using the explanation provided by Micheli *et al.*[43]. There they explain how the twist-and-turn[49] Hamiltonian:

$$H = tJ_x + \frac{U}{2}J_z^2 \quad (3.5)$$

produces cat states via a semi classical analysis. The classical analysis assumes a set of variational states which are the ground state of the Hamiltonian $J(\cos^{-1}(z), \phi)$. The classical equations of motion describe the dynamics of imbalance of particles between the two modes (projection onto the axis), z and its conjugate variable ϕ .

The classical equations of motion have been solved analytically[50] and have two fixed points for all parameters, t and U . Dynamical creation of a cat state takes place at larger coupling strength ($U > 4t/N$), where one of the classical fixed points is unstable. The classical trajectories for $2J = N = 200$, $U = 0.1$ and $t = 1$ are shown in Fig. 5.1 and demonstrates a critical line, $\pm z_c(\phi)$, separating two distinct dynamical behaviours. Along one set of trajectories the effective spin rotates around the x-axis so that the variation of the azimuthal (ϕ)-angle is confined to a finite interval. These trajectories, confined to the middle region in Fig. 5.1, correspond to the Josephson oscillations[64, 50, 1] observed in condensed matter Josephson junctions and we refer to them as free oscillations. Along another set of trajectories, the spin rotates around the z-axis so that the ϕ -variable increases indefinitely. Along the latter type of trajectories the particle imbalance (z) does not change sign and the corresponding dynamics is known as self-trapping dynamics. The phase-space (ϕ, z)-regions of the two types of trajectories are separated by a critical line, $z_c(\phi)$, called the separatrix, indicated by the thick black line in Fig.(1). This line is the classical trajectory of both the π and 0 states in the classical analysis. The π state starts on the unstable fixed point, while the 0 starts at $(z_c(0), \phi = 0)$. All numerical calculations presented in this paper have been carried out for the parameters used in Fig. 5.1: $2J = N = 200$, $U = 0.1$ and $t = 1$.

Focusing on pure states ($\beta^{-1} = 0$), the first quantum approximation in a semiclassical analysis treats the initial pure state as a finite width Gaussian probability distribution. In the classical dynamics, the paths of the free oscillation and self-trapping trajectories diverge near the unstable fixed point ($\phi = \pi, z = 0$). In the quantum mechanical evolution of the π and 0 states, the trajectories of the Wigner-distribution amplitudes part ways near the same phase space coordinate. After a time interval during which the z-coordinates of the classically evolving systems on either side of the separatrix have separated maximally (a time $T_\pi = \log(8N)\hbar/[NU]$ for the π -state and $1.4T_\pi$ for the 0-state), the quantum state evolves into a superposition of two macroscopically separated (specified below) states. The corresponding self-trapping and free oscillation components are the dead and alive components of the cat state. In the case of the pure state described above, we a priori know that the vital status is indefinite.

For the case in which the initial state is at a high temperature, the classical dynamics are the same, but uncertainty in the evolved probability distribution reflects our lack of knowledge about the classical phase-space position as opposed to the indefiniteness of the quantum state. As we show below, the measure that we propose indicates that the thermal states are definite.

We numerically compute both the thermal and pure states using exact diagonalization of Eq. 3.5 followed by a time evolution of the states $\rho(\beta, z, \phi)$. The probability distributions for the J_z observable are shown in Fig. 3.2 for the pure states and Fig. 3.3 for the high temperature states. Both the pure states and the thermal states demonstrate a double peak suggestive of a dead and alive labelling. We make this labelling precise for a

pure state $|k\rangle$ by decomposing it into a dead and alive state $|k\rangle = (|alive\rangle + |dead\rangle)/\sqrt{2}$:

$$\begin{aligned} |alive\rangle &= \frac{1}{\sqrt{N_L}} \sum_{j_z} |j_z\rangle \langle j_z|k\rangle \Theta(\langle J_z\rangle - j_z) \\ |dead\rangle &= \frac{1}{\sqrt{N_R}} \sum_{j_z} |j_z\rangle \langle j_z|k\rangle \Theta(j_z - \langle J_z\rangle) \end{aligned} \quad (3.6)$$

Where N_R and N_L , are defined so the alive and dead states are properly normalized. While this decomposition is always possible, it only make sense to call the pure state $|k\rangle$ a cat state if the dead and alive states are macroscopically distinct. In other words, the extensive difference $\Lambda(A) = \langle A\rangle_{alive} - \langle A\rangle_{dead}$ should scale with the number of particles. For the decomposition above, the extensive difference for the observable J_z can then be computed by:

$$\Lambda(J_z) = \sum_{j_z} (P_L(j_z) - P_R(j_z))j_z \quad (3.7)$$

where $P_L(j_z)$ are the re-normalized distributions corresponding to the dead and alive states:

$$\begin{aligned} P_L(j_z) &= \frac{1}{N_L} P(j_z) \Theta(\langle J_z\rangle - j_z) \\ P_R(j_z) &= \frac{1}{N_R} P(j_z) \Theta(j_z - \langle J_z\rangle) \end{aligned} \quad (3.8)$$

where $\Theta(x)$ is the Heaviside-step function which is 1 for $x > 0$ and 0 for $x < 0$.

Thus, any double peak distribution where the peaks are macroscopically separated will have an extensive difference scaling with the number of particles. This is true for the pure states in Fig. 3.2, where the extensive difference is $65 \approx 200/3 = N/3$. Eq. 3.7 can also be applied to the mixed states in Fig. 3.3 and gives a similar extensive difference $\approx N/3$. Experimentally, counting statistics provide the distributions $P(j_z)$ and Eq. 3.7 can be used to determine if the observed state can be meaningfully separated into macroscopically

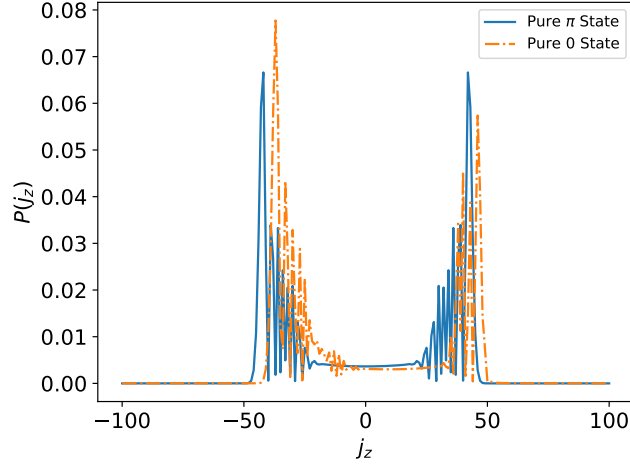


Figure 3.2: Distributions $P(j_z)$ for the state evolved from the π and 0 coherent states (0 temperature) for a time T_π and $1.4T_\pi$ respectively. These states were computed for $N = 200$ or for an $SU(2)$ spin with size $J = 100$, and the x-axis, j_z , are the eigenvalues of the observable J_z .

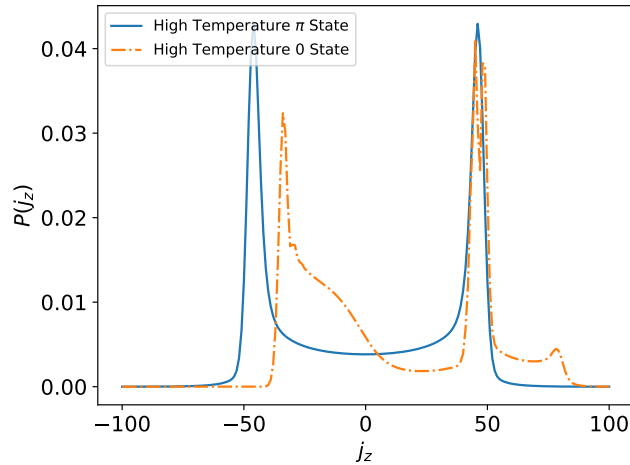


Figure 3.3: Distributions $P(j_z)$ for the state evolved from the π and 0 states at temperature $10\epsilon_\tau$ for the same time intervals as in Fig. 3.2. As in Fig. 3.2, these states were computed for $N = 200$ or for an $SU(2)$ spin with size $J = 100$.

distinct dead and alive cats. The next section describes how to determine the vital status of the cat.

3.4 Interferometer Sensitivity and Indefiniteness

To quantify how indefinite the vital status of the cat is, we use the interferometer sensitivity quantified by the quantum and classical Fisher information (QFI and CFI). In this section, we introduce the interferometer sensitivity, convex roof of the variance, and explain how an experiment can quantify the indefiniteness and obtain information about possible pure states which make up the density matrix.

In the interferometry experiment discussed above, a phase $\psi = \frac{\epsilon\Delta t}{\hbar}$, is encoded on to a state via time evolution by a Hamiltonian, $H_\Omega = \epsilon J(\theta_\Omega, \Phi_\Omega)$, for a time Δt . The sensitivity to the phase ψ is given by the CFI:

$$F_c(R, \rho_\psi, \Omega) = \sum_r p(r, \psi, \Omega) [\partial_\psi \log(p(r, \psi, \Omega))]^2 \quad (3.9)$$

where $p(r, \psi, \Omega) = \langle r | U_{\psi, \Omega}^\dagger \rho U_{\psi, \Omega} | r \rangle$ (Eq. 3.1). The primary use of the CFI, F_c , is that its value provides an upper bound on the estimated phase ψ via the Cramer-Rao bound[11, 51]:

$$\Delta\psi \geq \frac{1}{\sqrt{F_c(R, \rho_\psi, \Omega)}} \quad (3.10)$$

The CFI, $F_c(R, \rho_{\psi=0}, \Omega)$, can be measured in experiments[58]: repeating the four-step process to obtain measurements of $p(r, 0 + \delta, \Omega)$ for a range of small δ allows the construction of the derivative with respect to ψ evaluated at $\psi = 0$ and a direct use of Eq. 3.9. Other methods exist to get more accurate values [44, 20, 17].

A pure state with larger uncertainty, $\Delta J(\theta_\Omega, \phi_\Omega)$, (implying, since the state is pure, a larger indefiniteness in the observable $J(\theta_\Omega, \phi_\Omega)$), responds on a faster time scale, $\omega^{-1} = \hbar(\epsilon\Delta J(\theta_\Omega, \phi_\Omega))^{-1}$ and may have a larger CFI. Whether or not the CFI is larger depends on the observable R in step 3 of the 4 step process: the dependence on the phase (ψ) cancels out if the $\{|r\rangle\}$ basis consists of eigenstates of $J(\theta_\Omega, \phi_\Omega)$. To characterize the sensitivity of the quantum state, independent of the choice of the observable R , one must optimize over all Hermitian operators R . The result of this optimization procedure is the QFI[6, 60, 16]:

$$F_q(\rho_\psi, \Omega) = \max_R F_c(R, \rho_\psi, \Omega) \quad (3.11)$$

Since the Cramer-Rao uncertainty bound on $\Delta\psi$ of Eq.(10) is valid for every choice of the measurement observable, R , the tightest bound on $\Delta\psi$ is obtainable from the QFI:

$$\Delta\psi = \frac{\epsilon\Delta t}{\hbar} \geq \frac{1}{\sqrt{F_q(\rho_\psi, \Omega)}}. \quad (3.12)$$

For a pure state system, $\rho = |k\rangle\langle k|$, it was shown[6] that

$$F_q(\rho_\psi = |k\rangle\langle k|, \Omega) = 4\langle k|(\Delta J(\theta_\Omega, \Phi_\Omega))^2|k\rangle \quad (3.13)$$

where

$$\langle k|(\Delta J)^2|k\rangle = \langle k|J^2|k\rangle - \langle k|J|k\rangle^2 \quad (3.14)$$

With $\Delta\psi = (\epsilon\Delta t)/\hbar$, and $\epsilon\Delta J = \Delta H_\Omega$, the pure state Cramer-Rao bound on the phase can be written as

$$\Delta t \sqrt{\langle k|(\Delta H_\Omega)^2|k\rangle} \geq \hbar \quad (3.15)$$

in agreement with the Heisenberg energy-time inequality.

Here we have chosen to consider the sensitivity of the state $\rho_{\psi=0}$ with 0 phase encoded because we are interested in properties of the state evolved after the first-step, not a different state with phase encoded onto it.

Since the state is pure, we know that any uncertainty in an observed property of the state directly corresponds to a quantum phenomenon of indefinite properties. For a mixed state ensemble, it is not immediately clear that the QFI generalizes the statistical variance as a quantification of indefiniteness. To address this, S. Yu[63] and Toth *et al.*[61] proved the following illuminating expression for the QFI:

$$F_q(\rho_{\psi=0}, \Omega) = \min_e \sum_k P_{k_e} F_q(|k_e\rangle \langle k_e|, \Omega) \quad (3.16)$$

where the optimization over e is over all decomposition of a density matrix, $\rho_{\psi=0}$, into an ensemble of pure states $\rho_{\psi=0} = \sum_k P_{k_e} |k_e\rangle \langle k_e|$, where the $\{|k\rangle\}$ -states of this decomposition are not necessarily orthogonal. This decomposition is not unique because in the vector space of density matrices, the set of all pure state density matrices form an over-complete basis. Thus, e represents one of these non-unique decompositions and k_e labels the pure states which make up that decomposition. The right hand side of Eq. 3.16 is known as the convex-roof of the variance[3, 63, 61].

Cast as a generalization of the concept of statistical variance, the QFI, F_q , can be seen to provide a valid measure of indefiniteness. Indeed, the minimization in the space of density matrices implies that a portion of the sum, $\sum_k P_{k_e} |k_e\rangle \langle k_e|$, of significant P_{k_e} -weight involves pure states, $|k_e\rangle$, with a statistical variance $\langle k_e | (\Delta J(\theta_\Omega, \Phi_\Omega))^2 | k_e \rangle$ that is comparable to the convex uncertainty:

$$\Delta_q J(\theta_\Omega, \phi_\Omega) = \frac{1}{2} \sqrt{F_q(\rho_{\psi=0}, \Omega)} \quad (3.17)$$

This implies that, if we were given full knowledge of the universe, and were able to sort the results based on which pure state, $|k_e\rangle$, was produced by the experimental apparatus, the majority of the distributions, $P_{k_e}(j) = |\langle j(\theta_\Omega, \phi_\Omega) | k_e \rangle|^2$, would have a statistical uncertainty larger than $\Delta_q J(\theta_\Omega, \phi_\Omega)$. Since this uncertainty can not be reduced by obtaining more information, it must be due to the indefiniteness of the observed property $J(\theta_\Omega, \phi_\Omega)$.

Thus a measurement of large sensitivity, $F_q(\rho_{\psi=0}, \Omega)$, implies a large indefiniteness of the phase encoding Hamiltonian $\epsilon J(\theta_\Omega, \phi_\Omega)$ in the initial state ρ . This was pointed out by Fröwis and Dür[16], and was used to construct a measure of indefiniteness ‘ N_{eff} ’ (defined below in Eq. 3.20) by the way $\max_\Omega F_q(\rho_{\psi=0}, \Omega)$ scales with the number of particles. As discussed in the Appendix 3.8.1, this optimization over observables Ω can lead to misleading results when considering the indefiniteness associated with the superposition of two macroscopically distinct states. Instead, we use the extensive difference for an observable J_Ω as a measure of the size of the cat, and we introduce the comparison of the convex uncertainty with the statistical uncertainty

$$r_q(\Omega) = \frac{\Delta_q(J_\Omega)}{\Delta_s(J_\Omega)} = \frac{\Delta_q(J_\Omega)}{\sqrt{\text{Tr}[J_\Omega^2 \rho] - \text{Tr}[J_\Omega \rho]^2}} \quad (3.18)$$

as a measure of the quality of indefiniteness. Since the statistical uncertainty is always greater than the convex uncertainty, $r(\Omega)$ ranges from 0 to 1. When $r_q(\Omega)$ is 1, any observed statistical uncertainty is due to indefiniteness, while for smaller r_q , only a fraction of the uncertainty is due to indefiniteness. The statistical uncertainty can be obtained as part of the same interferometry experiment: if the interferometric procedure is repeated with $\psi = 0$, and with the effective observable as $R = J_\Omega$, the statistical uncertainty follows from counting the p_r -distributions obtained after these steps.

We use $r(\Omega)$ and $\Lambda(J_\Omega)$ because, with the additional knowledge of a double peak distribution in the observable J_Ω , qualitative arguments can be made about the amplitudes of pure states which could make up a representative density matrix ensemble, $e = \{P_{k_e}, |k_e\rangle\}$. If the convex and statistical uncertainties are approximately equal to each other, $\Delta_s/\Delta_q \approx 1$, we know the density-matrix ensemble is, on average, composed of pure states with uncertainty similar to that of the observed statistical distribution. In addition, since different pure states in the ensemble can not destructively interfere with each other, we know that the pure states in the density matrix have small amplitude for the basis states that have small probability of occurrence in the full statistical ensemble. Thus with the additional observation of a double peak, we can conclude that any representation of the density matrix is mostly composed of cat states with extensive difference similar to the observed one.

What can be said when r_q is not very close to 1, but still significant (*e.g.* $r_q > 0.1$)? To answer this question we introduce the product Λr_q as the “reduced extensive difference”, where the extensive difference Λ is given by Eq. 3.7. As long as the individual peaks have narrow width (similar to the pure cat states, see Fig. 3.2) and the reduced extensive difference is significantly larger than the peak width, we can again qualitatively argue that there exists pure states in the density matrix ensemble with extensive difference similar to that of the observed extensive difference Λ . If the reduced extensive difference is significantly larger than the width of the peak, there must exist pure states, $|k_e\rangle$ with variance significantly larger than the width of the peaks and are realized with significant probability P_{k_e} . Since the peaks are narrow and there is very low probability between the

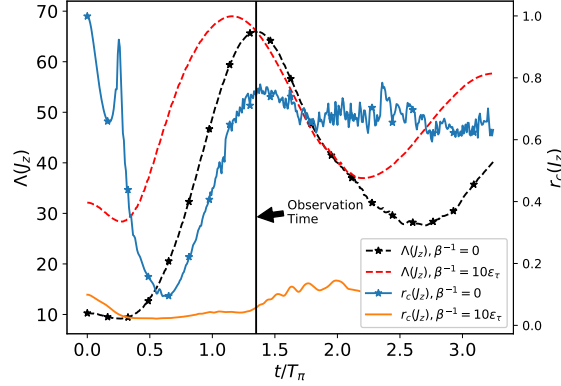


Figure 3.4: In this plot, the extensive difference (dashed lines, left axis) and quality of indefiniteness (solid lines, right axis) are plotted versus the time spent during the non linear evolution in step 1 of the interferometric process. The scale of the extensive difference is set by the number of particles $N = 200$, or size of corresponding spin $J = 100$, in the evolving state. These quantities are computed for the 0 state at temperature 0 and $10\epsilon_\tau$. An experimenter, testing these cat states shown, would compute the statistical variance and extensive difference from the double peak distributions shown in Fig. 3.2. They would perform the interferometry process discussed above to compute the bound on Δ_q via the CFI.

two peaks, the only form these states can take is one with double peak amplitudes similar to the observed distribution. Thus, we know the density matrix contains a significant off diagonal contribution $\langle m|k_e\rangle \langle k_e|m'\rangle P_{k_e}$ for $|m - m'| \approx \Lambda(J_z)$, despite an imperfect quality of indefiniteness, $r_1 < 1$. This makes a connection with the work done by Opanchuk *et al.*[48], who put bounds on $\langle m|\rho|m'\rangle$ using multi-particle correlation functions.

3.5 Results: Detection Of Indefiniteness via Interferometer Sensitivity

In this section, we describe how an experiment would observe the measures discussed in the previous section and what they would observe for the Gordon-Savage cat

state and the mixed states discussed in Section I. The simplest step in such an experiment requires measuring the probability distributions in Fig. 3.2. This requires the state preparation described in Section I, followed by the projective measurement without any phase encoding or read-out. Repeating this reconstructs the distributions for the observable J_z . The extensive difference can then be computed by Eq. 3.7.

For completeness, we have plotted (Fig. 3.4) the dependence of the extensive difference for the 0 thermal state at $\beta^{-1} = 0$ and $\beta^{-1} = 10\epsilon_\tau$ versus the time spent during the non linear evolution that creates the cat. The extensive difference reaches a maximum at a time $1.4 * T_\pi = 1.4 \log(8N)\hbar/NU$ ($\beta^{-1} = 0$) and $1.1T_\pi$ ($\beta^{-1} = 10\epsilon_\tau$). The probability distributions $P(j_z)$ at these times are shown in Fig. 3.2. An experimenter interested in a specific cat does not need to measure the extensive difference at all times. Rather, they can do measurements at time $1.4T_\pi$ for the 0 states or T_π for the π states[43].

This calculation shows that, for the parameters considered ($N = 200$, $U = 0.1t$), the extensive difference of the 0 state is expected to peak at $1.4T_\pi$, and thus suggests $1.4T_\pi$ as a good time to end state creation (step 1) and begin the statistical and interferometric measurements (steps 2-4). Measuring the distribution $P(j_z)$ at this time, they will find an extensive difference of $65 \approx 200/3 = N/3$ particles (Fig. 3.4). For an experiment performed for a fixed particle number, the difference in expectation values between the dead and alive cats (i.e. the extensive difference Λ) would be on the same order of magnitude as the number of particles. An experiment could then be repeated for different number of particles, and

would find the extensive difference scales with N^1 , suggesting that if the trends continue, a macroscopic number of particles would yield a macroscopic cat state.

The second step is to verify the indefiniteness of the cat's vital status. Here, one should compare the statistical and convex uncertainty of the observable J_z , because this was the observable which demonstrated the macroscopic difference ($\Lambda(J_z)$) between the dead and alive cats. The statistical uncertainty can be computed directly from the distributions in Fig. 3.2. The convex uncertainty (computed from the QFI using Eq. 3.17) for J_z is bounded by measuring the sensitivity (CFI) of a probability distribution for some observable J_r to a phase encoding operation $J_{\theta_\Omega, \phi_\Omega} = J_z$. The single-particle observables that provide the best bounds will be the ones that respond most to rotations around the z-axis: any spin pointing in the x-y plane. We use $J_r = J_y$, since rotations around the x-axis are easily implemented, as described in Section I. Experimentally, the interferometric process is repeated with $J_r = J_y$, $J_\Omega = J_z$ and $T_r = \frac{\pi\hbar}{2\epsilon_r}$ for multiple small $\psi_{\epsilon_\Omega} = 0 + \delta$, such that the distribution $p(j_y, 0, J_z)$ and its derivative can be computed and used in the expression for the CFI(Eq. 3.9). With a measurement of the CFI, one can bound the convex uncertainty and quality of indefiniteness via Eq. 3.11:

$$r_q(J_z) = \frac{\Delta_q(J_z)}{\Delta_s(J_z)} > r_c(J_z) = \frac{\frac{1}{2}\sqrt{F_c(R = J_y, \rho, J_z)}}{\Delta_s(J_z)} \quad (3.19)$$

Using the statistical distribution for Δ_s , and:

$$F_c(R, \rho_\psi, \Omega) = - \sum_r \frac{1}{p(r, \psi)} \langle r | [\rho_\psi, \epsilon J(\theta_\Omega, \phi_\Omega)] | r \rangle^2$$

¹We directly confirmed this numerically by computing the π and 0 states for $N = 200 \dots 800$ and found a linear scaling of the extensive difference with the number of particles as $N/3.1$. The semi-classical approach also predicts a linear in N scaling[43]

for the CFI², we numerically compute (and plot in Fig. 3.4) $r_c(J_z)$ for the 0 thermal state at $\beta^{-1} = 0$ and $\beta^{-1} = 10\epsilon_\tau$ versus the time spent during the non linear evolution which creates the cat. For the pure state ($\beta^{-1} = 0$), $r_q = 1$, and $r_c < 1$ reflects the imperfect bound the choice of the observable $R = J_y$ puts on the QFI. For the cat state produced after a non linear evolution for $t = 1.4T_\pi$, the quality of indefiniteness measured by an experiment is about 0.75(see Fig. 3.4). Furthermore, the reduced extensive difference, $\Lambda r_c \approx N/4 = 50$ is significantly larger than the width of the peaks (approximately $N/20 = 10$). Thus, in good faith, an experimenter can believe that the density-matrix ensemble which they are observing is mostly composed of pure states with double peak amplitudes. Furthermore, since $r_q = 1$, one can expect to be able to account for 100% of the quantum variance by using a more optimal observable R [44, 20, 17, 40].

For the state evolved (at $t = 1.1T_\pi$) from the high temperature distribution ($\beta^{-1} = 10\epsilon_\tau$), the quality of indefiniteness is 5% and the reduced extensive difference is $\Lambda r_q = 3 = O(1)$. This is smaller than width of the peak. We must therefore conclude that there is no indefiniteness and that the cat is not dead and alive at the same time. Even with the ideal bound (see Fig. 3.5), the reduced extensive difference is still on the same size as the peak width ($\Lambda r_q = 10$).

In the remainder of this section, we show how these experiments are capable of detecting the crossover to a classical mixture as the temperature of the initial state is increased. Fig. 3.5 demonstrates that the quality of indefiniteness, r_q , and its experimental bound r_c decay to 0 as the temperature is increased. The quantum to classical crossover

²This expression can be obtained by expanding the unitaries in Eq. 3.1 around perturbations about ψ , and substituting into Eq 3.9.

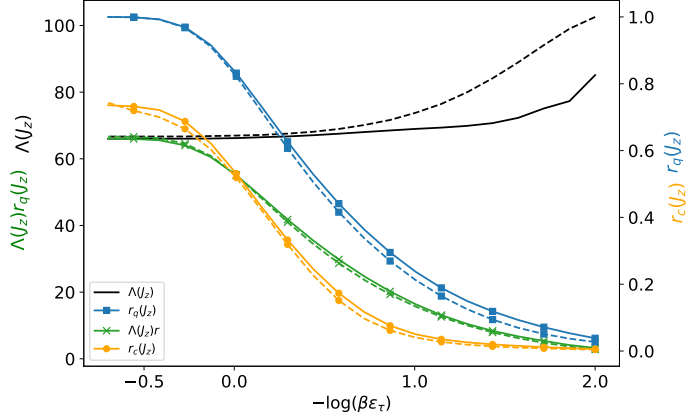


Figure 3.5: Quality of indefiniteness, r_q , its experimental bound r_c , the extensive difference $\Lambda(J_z)$ and the reduced extensive difference $\Lambda(J_z)r(J_z)$ are plotted versus the temperature of the initial state. The solid lines are for the thermal states at π , while the dashed lines are for the thermal states at 0. A quantum to classical crossover is shown between temperatures ϵ_τ and $10\epsilon_\tau$. As in Fig. 3.4, the scale of the extensive difference is set by the number of particles $N = 100$ in the evolving state.

occurs slowly between $\beta^{-1} = \epsilon_\tau$ and $10\epsilon_\tau$, where ϵ_τ sets the energy-scale of the spin Hamiltonian as in Eq. 3.3. For $\beta^{-1} \ll \epsilon_\tau$, the initial state condenses into the pure state and the quantum variance plateaus at its pure state value. This system is particularly interesting, in that the live and dead cat are still macroscopically different ($\Lambda = O(N)$) even at high temperature. Since the extensive difference remains constant, the difference between the dead and alive states is still macroscopic, and there are still two macroscopically distinct states which can be labelled dead and alive. We can then interpret the decay of the quality of indefiniteness to 0 when temperature is increased as a crossover from a cat being dead and alive at the same time to a cat being either dead or alive.

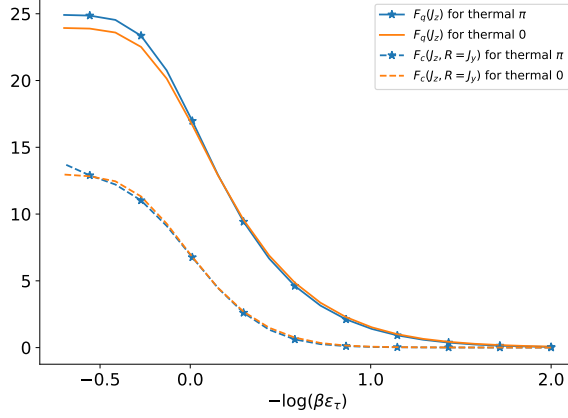


Figure 3.6: The QFI and its experimental bound for convex uncertainty of J_z versus temperature. These are lower bounds on the Fröwis and Dür measure (Eq. 3.20), which also demonstrate the quantum to classical crossover. The y-axis is shown in units of $\frac{1}{4N}$.

The metric for quantum macroscopicity proposed by Fröwis and Dür[16], also shows this quantum-classical crossover. This metric is given by:

$$N_{eff} = \frac{1}{4N} \max_{\Omega} F_q(\rho, \Omega) \quad (3.20)$$

In addition to other methods[44, 17, 20], this can be experimentally bounded from below using the CFI as done above for r_q (using r_c). The bound provided by $F_q(J_z)$ and its experimental bound $F_c(R = J_y, J_z)$ are plotted in Fig. 3.6. The crossover region is the same for Fröwis and Dür's as for the measures above (r_q and Λr_q) because the statistical variance Δ_s and extensive difference Λ is relatively constant through the crossover region. Thus, the main difference is the size of the cat each quantify: both are macroscopic in that they are $O(N)$, but the extensive difference is roughly twice as large. The difference stems from the difference in motivation of the two measures. The extensive difference attempts to describe the difference between the dead and live cat, while the measure by Fröwis and Dür aim to quantify a relative improvement in sensitivity from unentangled states (such as

those in Eq. 3.4). Furthermore, by focusing on the indefiniteness in a specific observable J_z , the extensive difference, $\Lambda(J_z)$, and the quality of indefiniteness, $r(J_z)$, provide additional information about the stability of the dead and alive states as the temperature is increased.

Using this lower bound for N_{eff} , a similar conclusion about quality of indefiniteness is reached, but improving the bound on N_{eff} could lead to different conclusions. In the appendix we show that the dead and alive states of the cat have macroscopic indefiniteness independent of their superposition. We can therefore imagine a situation where N_{eff} is large, but the superposition between the dead and alive states is decohered and the vital status of the cat is definite. This complication was known to Fröwis and Dür[16], so they constructed the relative Fisher information to identify macroscopic superposition. The relative Fisher information involves finding N_{eff} for the dead and alive states, and therefore requires a complicated projective measurement that may not be experimentally feasible.

3.6 Exploring indefiniteness for a Cat State Entangled with an Auxiliary Qubit

In the above sections, we proposed, motivated and tested a new measure for macroscopicity and indefiniteness on the Gordon-Savage cat state. The choice of the Gordon-Savage cat was made due to its potential relevance for ultra-cold atom experiment. However, we note that the strategy of combining the extensive difference Λ with the quality of indefiniteness r_q is applicable to a broader class of cat states. We demonstrate this by considering a cat state which is conceptually more similar to Schrödinger’s cat in which the

dead and alive states are entangled with the decayed and excited states of a radioactive source.

Here, we imagine a cat state entangled with an auxiliary qubit in which the entanglement with the qubit is controlled by a parameter η in the following way:

$$\frac{1}{\sqrt{2}} \{ |a\rangle |\uparrow\rangle + |d\rangle [|\uparrow\rangle \cos(\eta) + |\downarrow\rangle \sin(\eta)] \} \quad (3.21)$$

where $|a\rangle$ and $|d\rangle$ are the dead and alive states, and are assumed to be 1) symmetric such that $\langle j_z | a \rangle = \langle -j_z | d \rangle$ and 2) orthogonal with respect to the identity and J_z : $\langle a | d \rangle = \langle a | J_z | d \rangle = 0$. In the limit $\cos(\eta) = 1$, tracing out the qubit results in an indefinite, pure, cat-state, while in the opposite limit, $\cos(\eta) = 0$, the trace results in a classical ensemble of definite alive and dead states.

Performing the analysis of indefiniteness discussed in the previous section, we compute the QFI. While the state in Eq. 3.21 is a pure state, we suppose we do not have access to the qubit and can only perform measurements on the cat's Hilbert space. Therefore, we must trace out the qubit and use the general formula for the QFI of mixed states[6, 60]:

$$F_q[\rho, \epsilon J_z] = 2 \sum_{l, l'} \frac{(p_l - p_{l'})^2}{p_l + p_{l'}} |\langle l | J_z | l' \rangle|^2 \quad (3.22)$$

where $|l\rangle$ and p_l are the eigenvectors and eigenvalues of the reduced density matrix respectively. Using this expression, one obtains the QFI (see Appendix 3.8.3) as:

$$F_q(\rho_{\psi=0}, J_z) = \Lambda (J_z)^2 \cos^2(\eta) + PW^2 \quad (3.23)$$

and a reduced extensive difference as:

$$\Lambda r_q = \Lambda \sqrt{\frac{1 + \alpha^2 \cos^2(\eta)}{1 + \alpha^2}} \quad (3.24)$$

where PW is the peak width of the dead or alive (assumed to be the same) states: $PW = 2\sqrt{\langle a|J_z^2|a\rangle - \langle a|J_z|a\rangle^2}$, and $\alpha = \frac{\Lambda}{PW} > 1$ is the ratio of the extensive difference to the peak width.

Here we see that when the cat and qubit are not entangled, the quality of indefiniteness, r_q , quantifies a phenomenon of perfect indefiniteness, $r_q = 1$, and when it is partially entangled there is imperfect indefiniteness, $r_q < 1$. In Section 3.4, we argued that when $r_q < 1$, and not too small, a state can be classified as indefinite if the reduced extensive difference is greater than the peak width. For the state in Eq. 3.21, we find this to be the case when $\cos(\eta) > \cos(\eta_c) = \alpha^{-2}$. If an experiment can provide a good bound using the CFI and r_q is “significant”, it will observe a quantum to classical crossover when $\eta \approx \eta_c$, in which the indefinite vital status of the cat becomes definite.

We may now consider the approximate location of the crossover, $\eta_c = \arccos(\alpha^{-2})$ in two limits: 1) when $\alpha = O(1)$ and 2) when $\alpha \gg 1$. In the first limit, the crossover occurs for arbitrarily small values of η as $\alpha \rightarrow 1$. Comparing with the Leggett-Garg experiment discussed in Appendix 3.8.3, the Leggett-Garg inequality is violated for $\cos(\eta) > \frac{2}{3}$. Therefore, the Leggett-Garg experiment is better at detecting the indefiniteness of the partially entangled state for $\alpha < \sqrt{\frac{3}{2}}$. This implies that, in this limit, the projective measurement onto a dead or alive cat done in a Leggett-Garg experiment obtains more information about the mixed cat state than the Fisher Information measurement does.

The opposite is true when $\alpha \gg 1$: by making α arbitrarily large, we can push the approximate location of the crossover to an arbitrarily amount of entanglement with the auxiliary qubit. To make sense of this result we consider a thought experiment where

the auxiliary qubit is measured and the result ignored before performing the sensitivity analysis. In the strongly entangled limit, $\cos(\eta) \ll 1$, the result of this measurement is to produce a dead state 50% of the time and a superposition state, $|\psi_s\rangle \approx |a\rangle + \cos(\eta) |d\rangle$, in which the amplitude for the dead state is small with $\langle d|\psi_s\rangle \approx \cos(\eta)$, the other 50% of the time. In this limit, a simple application of the indefiniteness condition $\Lambda r_q > PW$ suggest that this method is capable of detecting a phenomenon of indefiniteness even when the superposition produced has very little amplitude in the dead state. A more careful consideration would note that the quality of indefiniteness is unreasonably small (not $O(0.1)$ as discussed in Section 3.4) and its ability to restrict the possible state which could make up a representative ensemble is severely limited.

Therefore, as noted above, we must set a bound on the quality of indefiniteness. One way to get an intuition at what such a bound might be, is by analogy to this large α cat state entangled with an auxiliary qubit. If we specify that we are only confident of a phenomenon of indefiniteness when the amplitude of the dead cat in the superposition state, $\langle d|\psi_s\rangle \approx \cos(\eta) \approx r_q$, is greater than 0.1, then we can set the threshold as $r_q > 0.1$. One could also set a more conservative threshold on the quality of indefinites by comparison with the Leggett-Garg experiment in Appendix 3.8.3. There, the Leggett-Garg experiment would fail to witness indefiniteness when $\cos(\eta) = \frac{2}{3}$ and our analogous bound would be $r_q > \frac{2}{3}$.

3.7 Conclusion and Discussion

We have examined how the standard interferometric process can be used to quantify the indefiniteness of cats produced by the two-mode Hamiltonian Eq. 3.5. First, we showed that states with a large extensive difference can be produced for high temperatures initial states. This allows an experimenter to prepare a state which, similar to Schrödinger's cat, has uncertainty between two macroscopically different states without worrying about coherence. We then described a possible experiment to determine the source of this uncertainty and quantify the quality of indefiniteness. We showed how the results of this experiment can be used to infer the possible form of the pure states which could make up a possible density matrix ensemble. This turned out to be particularly useful when describing a quantum to classical crossover where the indefinite superposition of a cat, in two macroscopically distinct states, undergoes a crossover to the definite occupation of either dead or alive. We then finished by demonstrating the general applicability of the method to a model for which the quantum to classical crossover is controlled by the amount of entanglement with an auxiliary qubit.

The experiment described above involves bounding the QFI by the experimentally observable CFI and is thus fallible to the same loopholes other Fisher Information based methods are. In general, these loopholes can not be tightened in the same way loopholes in Bell experiment can because there is no assumption of causally separated events: events in an experiment that measure Fisher information could feasibly affect each other without violating special relativity. Instead one must make reasonable assumptions based on previous experiments, a control experiment, or a comparison with simulation.

For example, in the bosonic interferometer experiment described above, the measurement of the CFI relies on the assumption that the Hamiltonian during the phase encoding process (step 2) is proportional to the single particle Hamiltonian encoding the phase (J_z in the example considered in this paper). If this assumption was violated and the dynamics during the phase encoding process were highly non-linear (*e.g.* J_z^4, J_x^8), a stronger response, mimicking the effects of an indefinite state, could be observed in the distribution $p(r, \psi, \Omega)$. This assumption can not be checked by a causality type argument, but instead must rely on comparison with simulation or the consistency of previous experiments using bosonic interferometer. Without the assumption of linearity, the results of high precision measurements[9, 12] that use the same interferometers could not be accepted. One could also check the assumption of linearity by directly simulating, as done above, the predicted change in distributions $p(r, \psi, \Omega)$ and comparing with the experimental distributions. The tighter they match, the harder it would be to come up with a non-linear Hamiltonian that reproduces the exact same $p(r, \psi, \Omega)$. These simulations would also verify the assumptions made during the interferometry steps (3) and (4) after the phase has been encoded and in which further loopholes may occur.

While simulations and references to previous experiments do not rule out peculiar possibilities in the same way the assumption of causally separated events does for Bell experiments, they do make it hard to imagine simple explanations alternative to the given assumptions. Thus, the combined observation of a high quality of indefiniteness ($r_q \approx 1$) and a double peak distribution provides reasonable evidence that a cat state, which could violate a Leggett-Garg inequality, is produced by the apparatus. In addition, these measures

can be acquired with current cold-atom technology and avoids the complications of the other measures discussed above.

The interpretation of the reduced extensive difference $\Lambda(J_z)r_q(J_z)$ and the arguments inferring the form of the pure states which could make up a representative density matrix ensemble can also be questioned when r_q is small. If r_q is measured very close to one, then the observation of the probability distributions in Fig. 3.2 can be interpreted as observing the amplitudes of a pure state because r_q is equal to 1 only for pure states. On the other hand, when $r_q < 1$, it is a qualitative judgement when comparing Λr_q with the peak width. In Section IV, we discussed one possible way to make such a qualitative judgement, but it may be interesting for future work to more rigorously investigate to what extent the combined observation of r_q and the probability distribution $P(j_z)$ limit the possible states in a density matrix ensemble. Such future work may find it useful to consider the relationship between the QFI and the resource theory of quantum invasiveness[45] which is closely connected to violations of the Leggett-Garg inequalities. Future work will also include a study of the effects of a thermal bath and loss mechanism to identify requirements on loss, tunnelling and interaction rates for producing a cat state.

Acknowledgements: This work was supported in part by the NSF under Grant No. DMR-1411345, S. P. K. acknowledges financial support from the UC Office of the President through the UC Laboratory Fees Research Program, Award Number LGF-17-476883. The research of E. T. in the work presented in this manuscript was supported by the Laboratory Directed Research and Development program of Los Alamos National Laboratory under project number 20180045DR.

Los Alamos National Laboratory is managed by Triad National Security, LLC, for the National Nuclear Security Administration of the U.S. Department of Energy under Contract No. 89233218CNA000001

3.8 Appendix

3.8.1 Cat States and Measure by Fröwis and Dür

In this section we discuss the subtleties of using the measure by Fröwis and Dür, N_{eff} . As defined in Eq. 3.20, N_{eff} is defined by maximizing the quantum Fisher information over all single particle generators of the phase encoding step 2 (labelled by Ω in Eq. 3.20). A naive application of this formula may lead to a wrong assessment of the indefiniteness of cat's vital status. This is because the indefiniteness of the cat's vital status is in a specific observable (J_z above), and the state of the system could have a larger QFI for a different observable. If the conclusions were drawn directly from N_{eff} one may mistakenly conclude the vital status of the cat is indefinite, while, in fact, it is a different property of the cat that is indefinite.

This possibility is manifested in the Gordon-Savage cat discussed in this paper. In Fig. 3.7 we have plotted the QFI for all single particle observables labelled by $\Omega = (\phi, \theta)$. Here we see that the QFI is maximum for spin pointing in the xy-plane. $F_q(J_z)$ still indicates that the cat is indefinite, but if one were to measure N_{eff} they would observe the sensitivity to rotations around a vector perpendicular to J_z (J_y for the π state), and it would tell them nothing about the indefiniteness of the cat's vital status. It would instead

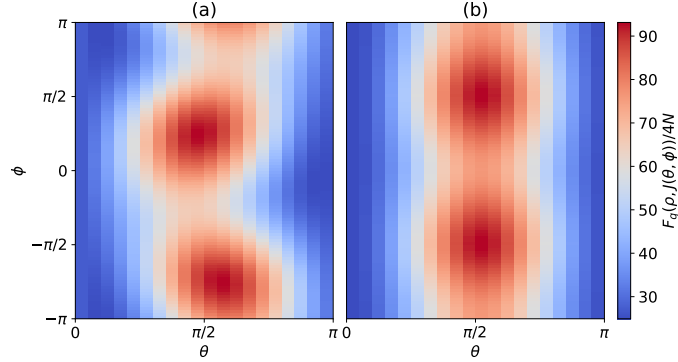


Figure 3.7: This is $F_q(\rho, J(\theta, \phi))/4N$ for the 0 (Left) and π (Right) cat states.

tell them they had a macroscopic quantum state, but the macroscopic indefiniteness would not be in a property with clear dead and alive states distinguishable.

To see how this arises, we consider the Wigner distribution of the 0 and π cats., The Wigner distribution, $W(z, \phi)$, is the quasi-probability distribution function representing a quantum state, $|\psi\rangle$:

$$W(z, \phi) = \sum_n^{N \frac{1-z}{4}} e^{i\phi n} \langle N \frac{z+1}{2} + 2n | \psi \rangle \langle \psi | N \frac{z+1}{2} \rangle, \quad (3.25)$$

where $|N \frac{z+1}{2}\rangle$ are the Fock states $|m_1, m_2\rangle$ with $m_1 = N \frac{z+1}{2}$ $m_2 = N - m_1$. The Wigner distribution has the useful property that the partial integration of one variable gives the probability distribution for the other (e.g. $P(z) = \frac{1}{2\pi} \int_{-\pi}^{\pi} d\phi W(z, \phi)$). By considering the Wigner distributions for the 0 and π states (see Fig. 3.8), we can understand the structure of the quantum state and why N_{eff} may give misleading results. The probability distributions $P(z)$ shown at the bottom of the figures indicate that the two bright red lines highlight what might be called the dead and alive cats. The red lines individually have

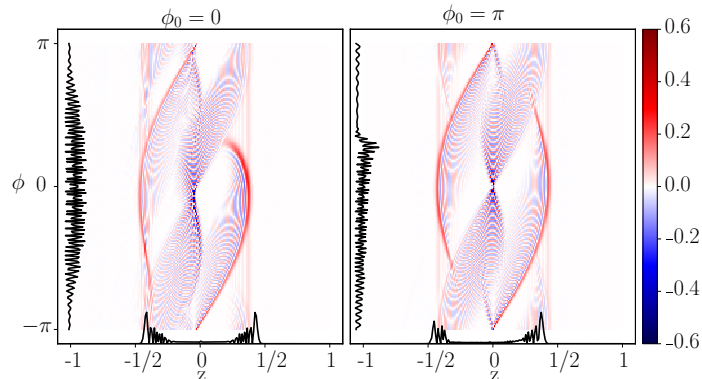


Figure 3.8: These are the Wigner distributions and the probabilities, $P(z)$ and $P(\phi)$, (black lines) for the 0(Left) and π (Right) cat states.

macroscopic uncertainty in ϕ and thus the xy-plane. This implies that the dead and alive cat states are individually macroscopic quantum states.

One can now easily imagine a situation where the coherence between the dead and alive states is lost, but the dead and alive states themselves still have a large value for N_{eff} . Thus if an experiment measured $F_q(J_x)$, it would find the macroscopic indefiniteness of the dead or alive cats. One might then wrongly conclude that the vital status of the cat is indefinite when it is not. This complication was known to Fröwis and Dür[16], so they constructed the relative Fisher information to identify macroscopic superposition. The relative Fisher information involves finding N_{eff} for the dead and alive states, and therefore requires a complicated projective measurement that may not be experimentally feasible.

3.8.2 Fisher Information for a Cat Entangled with a Qubit

In this section we derive the expressions for the QFI of a cat entangled with a qubit discussed in the text. The cat state entangled with a qubit is written as:

$$\frac{1}{\sqrt{2}} (|a\rangle |\uparrow\rangle + |d\rangle (|\uparrow\rangle \cos(\eta) + |\downarrow\rangle \sin(\eta))) \quad (3.26)$$

the dead and alive states are assumed to be 1) symmetric such that $\langle j_z | a \rangle = \langle -j_z | d \rangle$ and 2) orthogonal with respect to the identity and J_z : $\langle a | d \rangle = \langle a | J_z | d \rangle = 0$. These two assumptions imply $\langle a | J_z | a \rangle = -\langle d | J_z | d \rangle$ and $\langle a | J_z^2 | a \rangle = \langle d | J_z^2 | d \rangle$. From these assumptions we derive a relationship between the variance of a (anti-)symmetric cat state, the extensive difference and the peak width as:

$$PW^2 + \Lambda^2 = 4 \langle c_{\pm} | J_z^2 | c_{\pm} \rangle \quad (3.27)$$

and can also write the extensive difference as:

$$\Lambda^2 = 4 |\langle c_{\pm} | J_z | c_{\mp} \rangle|^2. \quad (3.28)$$

We can then derive the QFI from the following expression[6, 60]:

$$F_q[\rho, \epsilon J_z] = 2 \sum_{l, l'} \frac{(p_l - p_{l'})^2}{p_l + p_{l'}} |\langle l | J_z | l' \rangle|^2 \quad (3.29)$$

where $|l\rangle$ are the eigenvectors of the reduced density matrix and p_l are the eigenvalues. When tracing out the qubit we get two non-zero eigenvalues as $\frac{1}{2}(1 \pm \cos(\eta))$ which we will label $l = \pm$ for the symmetric and anti-symmetric cat states and $N - 1$ zero eigenvalues for the spin states orthogonal to the two cat states. If $l = \pm$ and $l' = \mp$ the sum yields $\cos^2(\eta) |\langle c_{\pm} | J_z | c_{\mp} \rangle|^2$. If $l = \pm$ and $l' \neq \pm$ we can insert an identity and obtain $\frac{1 \pm \cos(\eta)}{2} (\langle J_z^2 \rangle_{\pm} - |\langle c_{\pm} | J_z | c_{\mp} \rangle|^2)$.

Putting everything together with Eq. 3.28 and Eq. 3.27: we get

$$F(J_z) = \Lambda(J_z)^2 \cos^2(\eta) + PW^2 \quad (3.30)$$

This gives us an r_q :

$$r_q^2 = \frac{\Lambda(J_z)^2 \cos^2(\eta) + PW^2}{PW^2 + \Lambda^2} \quad (3.31)$$

3.8.3 Leggett-Garg violation of a Cat State Entangled with a Qubit

We imagine an Leggett-Garg experiment in which an initial state is evolved with respect to a Hamiltonian $\frac{H}{\hbar} = |a\rangle\langle a| - |d\rangle\langle d|$, and a measurement of whether the cat is alive or dead is made at $t_1 = 0$, $t_2 = \frac{2\pi}{3}$, and $t_3 = \frac{4\pi}{3}$. From these measurements, correlation functions of the form $K_{ij} = \langle H_i H_j \rangle$ are calculated and if the inequality:

$$1 + K_{12} + K_{23} + K_{13} > 0 \quad (3.32)$$

is violated then the state must have been indefinite at some time between $t = t_1$ and $t = t_3$ [38]. If the initial state is the symmetric cat, $\frac{1}{\sqrt{2}}(|a\rangle + |d\rangle)$, then the violation is -0.5 , while if the initial state is the partially entangled state in Eq. 3.21, the violation is $1 - \frac{3}{2} \cos(\eta)$. Thus the Leggett-Garg experiment is not capable of witnessing the indefiniteness of the entangled state for $\cos(\eta) < 2/3$.

Bibliography

- [1] Michael Albiez, Rudolf Gati, Jonas Fölling, Stefan Hunsmann, Matteo Cristiani, and Markus K. Oberthaler. Direct observation of tunneling and nonlinear self-trapping in a single bosonic josephson junction. *Phys. Rev. Lett.*, 95:010402, Jun 2005.
- [2] K. Baumann, R. Mottl, F. Brennecke, and T. Esslinger. Exploring symmetry breaking at the Dicke quantum phase transition. *Phys. Rev. Lett.*, 107(14):140402, 2011.
- [3] Ingemar Bengtsson and Karol Zyczkowski. *Geometry of Quantum States: An Introduction to Quantum Entanglement*. Cambridge University Press, 2006.
- [4] P. Berg, S. Abend, G. Tackmann, C. Schubert, E. Giese, W. P. Schleich, F. A. Narducci, W. Ertmer, and E. M. Rasel. Composite-Light-Pulse Technique for High-Precision Atom Interferometry. *Phys. Rev. Lett.*, 114(6):063002, feb 2015.
- [5] Gunnar Bjrk and Piero G Luca Mana. A size criterion for macroscopic superposition states. *J. Opt. B*, 6(11):429, 2004.
- [6] Samuel L. Braunstein and Carlton M. Caves. Statistical distance and the geometry of quantum states. *Phys. Rev. Lett.*, 72:3439–3443, May 1994.
- [7] L. D. Carr, D. R. Dounas-Frazer, and M. A. Garcia-March. Dynamical realization of macroscopic superposition states of cold bosons in a tilted double well. *EPL*, 90(1):0–6, 2010.
- [8] L. D. Carr, D. R. Dounas-Frazer, and M. A. Garcia-March. Dynamical realization of macroscopic superposition states of cold bosons in a tilted double well. *EPL*, 90(1):10005, apr 2010.
- [9] Kayleigh Cassella, Eric Copenhaver, Brian Estey, Yanying Feng, Chen Lai, and Holger Müller. Recoil-sensitive lithium interferometer without a subrecoil sample. *Phys. Rev. Lett.*, 118:233201, Jun 2017.
- [10] E. G. Cavalcanti and M. D. Reid. Signatures for generalized macroscopic superpositions. *Phys. Rev. Lett.*, 97:170405, Oct 2006.
- [11] Harald Cramér. *Mathematical methods of statistics*. Princeton University Press, Princeton, 1945.

- [12] M de Angelis, A Bertoldi, L Cacciapuoti, A Giorgini, G Lamporesi, M Prevedelli, G Saccorotti, F Sorrentino, and G M Tino. Precision gravimetry with atomic sensors. *Measurement Science and Technology*, 20(2):022001, dec 2008.
- [13] J. E. Debs, P. A. Altin, T. H. Barter, D. Döring, G. R. Dennis, G. McDonald, R. P. Anderson, J. D. Close, and N. P. Robins. Cold-atom gravimetry with a Bose-Einstein condensate. *Phys. Rev. A*, 84(3):033610, sep 2011.
- [14] Wolfgang Dür, Christoph Simon, and J. Ignacio Cirac. Effective size of certain macroscopic quantum superpositions. *Phys. Rev. Lett.*, 89:210402, Oct 2002.
- [15] J. Estève, C Gross, A Weller, S Giovanazzi, and M K Oberthaler. Squeezing and entanglement in a Bose-Einstein condensate. *Nature*, 455(7217):1216–1219, 2008.
- [16] Florian Fröwis and Wolfgang Dür. Measures of macroscopicity for quantum spin systems. *New J. of Phys.*, 14(9):093039, sep 2012.
- [17] Florian Fröwis, Pavel Sekatski, and Wolfgang Dür. Detecting Large Quantum Fisher Information with Finite Measurement Precision. *Phys. Rev. Lett.*, 116(9):090801, 2016.
- [18] Florian Fröwis, Pavel Sekatski, Wolfgang Dür, Nicolas Gisin, and Nicolas Sangouard. Macroscopic quantum states: Measures, fragility, and implementations. *Rev. Mod. Phys.*, 90:025004, May 2018.
- [19] M. A. García-March, D. R. Dounas-Frazer, and L. D. Carr. Macroscopic superposition of ultracold atoms with orbital degrees of freedom. *Phys. Rev. A*, 83(4):043612, apr 2011.
- [20] Martin Gärttner, Philipp Hauke, and Ana Maria Rey. Relating out-of-time-order correlations to entanglement via multiple-quantum coherences. *Phys. Rev. Lett.*, 120:040402, Jan 2018.
- [21] R. Gati, J. Esteve, B. Hemmerling, T. B. Ottenstein, J. Appmeier, A. Weller, and M. K. Oberthaler. A primary noise thermometer for ultracold Bose gases. *New J. Phys.*, 8:189–189, 2006.
- [22] R Gati and M K Oberthaler. A bosonic josephson junction. *J. of Phys. B*, 40(10):R61, 2007.
- [23] D Gordon and C. M. Savage. Creating macroscopic quantum superpositions with Bose-Einstein condensates. *Phys. Rev. A*, 59(6):4623–4629, 1999.
- [24] C. Gross, T. Zibold, E. Nicklas, J. Estève, and M K Oberthaler. Nonlinear atom interferometer surpasses classical precision limit. *Nature*, 464(7292):1165–1169, 2010.
- [25] Takuya Hatomura. Shortcuts to adiabatic cat-state generation in bosonic Josephson junctions. *New J. Phys.*, 20(1):015010, jan 2018.

- [26] Y. P. Huang and M. G. Moore. Creation, detection, and decoherence of macroscopic quantum superposition states in double-well Bose-Einstein condensates. *Phys. Rev. A*, 73(2):023606, feb 2006.
- [27] Philipp Hyllus, Wiesław Laskowski, Roland Krischek, Christian Schwemmer, Witlef Wieczorek, Harald Weinfurter, Luca Pezzé, and Augusto Smerzi. Fisher information and multiparticle entanglement. *Phys. Rev. A*, 85:022321, Feb 2012.
- [28] B. Juliá-Díaz, T. Zibold, M. K. Oberthaler, M. Melé-Messeguer, J. Martorell, and A. Polls. Dynamic generation of spin-squeezed states in bosonic Josephson junctions. *Phys. Rev. A*, 86(2):023615, aug 2012.
- [29] Jan Ivar Korsbakken, K. Birgitta Whaley, Jonathan Dubois, and J. Ignacio Cirac. Measurement-based measure of the size of macroscopic quantum superpositions. *Phys. Rev. A*, 75:042106, Apr 2007.
- [30] T. Kovachy, P. Asenbaum, C. Overstreet, C. A. Donnelly, S. M. Dickerson, A. Sugarbaker, J. M. Hogan, and M. A. Kasevich. Quantum superposition at the half-metre scale. *Nature*, 528:530 EP –, Dec 2015.
- [31] Hyukjoon Kwon, Chae-Yeun Park, Kok Chuan Tan, and Hyunseok Jeong. Disturbance-based measure of macroscopic coherence. *New J. Phys.*, 19(4):043024, 2017.
- [32] Amine Laghaout, Jonas S. Neergaard-Nielsen, and Ulrik L. Andersen. Assessments of macroscopicity for quantum optical states. *Opt. Commun.*, 337:96 – 101, 2015.
- [33] M. Lapert, G. Ferrini, and D. Sugny. Optimal control of quantum superpositions in a bosonic Josephson junction. *Phys. Rev. A*, 85(2):023611, 2012.
- [34] Hon Wai Lau, Zachary Dutton, Tian Wang, and Christoph Simon. Proposal for the creation and optical detection of spin cat states in bose-einstein condensates. *Phys. Rev. Lett.*, 113:090401, Aug 2014.
- [35] Chang-Woo Lee and Hyunseok Jeong. Quantification of macroscopic quantum superpositions within phase space. *Phys. Rev. Lett.*, 106:220401, May 2011.
- [36] A. J. Leggett. Macroscopic quantum systems and the quantum theory of measurement. *Prog. Theor. Phys.*, 69:80–100, 1980.
- [37] A J Leggett. Testing the limits of quantum mechanics: motivation, state of play, prospects. *J. Phys. Condens. Matter*, 14(15):R415, 2002.
- [38] A. J. Leggett and Anupam Garg. Quantum mechanics versus macroscopic realism: Is the flux there when nobody looks? *Phys. Rev. Lett.*, 54:857–860, Mar 1985.
- [39] Anthony J. Leggett. Bose-Einstein condensation in the alkali gases: Some fundamental concepts. *Rev. Mod. Phys.*, 73(2):307–356, apr 2001.

- [40] D. Linnemann, H. Strobel, W. Muessel, J. Schulz, R. J. Lewis-Swan, K. V. Kheruntsyan, and M. K. Oberthaler. Quantum-enhanced sensing based on time reversal of nonlinear dynamics. *Phys. Rev. Lett.*, 117:013001, Jun 2016.
- [41] Khan W. Mahmud, Heidi Perry, and William P. Reinhardt. Quantum phase-space picture of Bose-Einstein condensates in a double well. *Phys. Rev. A*, 71(2):023615, feb 2005.
- [42] Florian Marquardt, Benjamin Abel, and Jan von Delft. Measuring the size of a quantum superposition of many-body states. *Phys. Rev. A*, 78:012109, Jul 2008.
- [43] A. Micheli, D. Jaksch, J. I. Cirac, and P. Zoller. Many-particle entanglement in two-component Bose-Einstein condensates. *Phys. Rev. A*, 67(1):013607, jan 2003.
- [44] Safoura S. Mirkhalaf, Samuel P. Nolan, and Simon A. Haine. Robustifying twist-and-turn entanglement with interaction-based readout. *Phys. Rev. A*, 97:053618, May 2018.
- [45] Saulo V. Moreira and Marcelo Terra Cunha. Quantifying quantum invasiveness. *Phys. Rev. A*, 99:022124, Feb 2019.
- [46] W. Muessel, H. Strobel, D. Linnemann, D. B. Hume, and M. K. Oberthaler. Scalable Spin Squeezing for Quantum-Enhanced Magnetometry with Bose-Einstein Condensates. *Phys. Rev. Lett.*, 113(10):103004, sep 2014.
- [47] Stefan Nimmrichter and Klaus Hornberger. Macroscopicity of mechanical quantum superposition states. *Phys. Rev. Lett.*, 110:160403, Apr 2013.
- [48] B Opanchuk, L Rosales-Zárate, R Y Teh, and M D Reid. Quantifying the mesoscopic quantum coherence of approximate NOON states and spin-squeezed two-mode Bose-Einstein condensates. *Phys. Rev. A*, 94(6):062125, dec 2016.
- [49] Luca Pezzè, Augusto Smerzi, Markus K. Oberthaler, Roman Schmied, and Philipp Treutlein. Quantum metrology with nonclassical states of atomic ensembles. *Rev. Mod. Phys.*, 90:035005, Sep 2018.
- [50] S. Raghavan, A. Smerzi, S. Fantoni, and S. R. Shenoy. Coherent oscillations between two weakly coupled Bose-Einstein condensates: Josephson effects, oscillations, and macroscopic quantum self-trapping. *Phys. Rev. A*, 59(1):620–633, jan 1999.
- [51] C. Radhakrishna Rao. Information and the accuracy attainable in the estimation of statistical parameters. *Bull. Calcutta Math. Soc.*, 37:81, 1945.
- [52] Max F Riedel, Pascal Böhi, Yun Li, Theodor W. Hänsch, Alice Sinatra, and Philipp Treutlein. Atom-chip-based generation of entanglement for quantum metrology. *Nature*, 464(7292):1170–1173, 2010.
- [53] L. Rosales-Zárate, B. Opanchuk, Q. Y. He, and M. D. Reid. Leggett-garg tests of macrorealism for bosonic systems including double-well bose-einstein condensates and atom interferometers. *Phys. Rev. A*, 97:042114, Apr 2018.

- [54] G. Rosi, L. Cacciapuoti, F. Sorrentino, M. Menchetti, M. Prevedelli, and G. M. Tino. Measurement of the Gravity-Field Curvature by Atom Interferometry. *Phys. Rev. Lett.*, 114(1):013001, jan 2015.
- [55] Erwin Schrödinger. Die gegenwärtige situation in der quantenmechanik. *Naturwissenschaften*, 23(49):823–828, 1935.
- [56] Pavel Sekatski, Nicolas Gisin, and Nicolas Sangouard. How difficult is it to prove the quantumness of macroscopic states? *Phys. Rev. Lett.*, 113:090403, Aug 2014.
- [57] Akira Shimizu and Takayuki Miyadera. Stability of quantum states of finite macroscopic systems against classical noises, perturbations from environments, and local measurements. *Phys. Rev. Lett.*, 89:270403, Dec 2002.
- [58] Helmut Strobel, Wolfgang Muessel, Daniel Linnemann, Tilman Zibold, David B. Hume, Luca Pezzé, Augusto Smerzi, and Markus K. Oberthaler. Fisher information and entanglement of non-Gaussian spin states. *Science*, 345(6195):424–427, 2014.
- [59] Kok Chuan Tan, Seongjeon Choi, Hyukjoon Kwon, and Hyunseok Jeong. Coherence, quantum fisher information, superradiance, and entanglement as interconvertible resources. *Phys. Rev. A*, 97:052304, May 2018.
- [60] Géza Tóth and Iagoba Apellaniz. Quantum metrology from a quantum information science perspective. *J. Phys. A: Math. Theor.*, 47(42):424006, oct 2014.
- [61] Géza Tóth and Dénes Petz. Extremal properties of the variance and the quantum fisher information. *Phys. Rev. A*, 87:032324, Mar 2013.
- [62] Benjamin Yadin and Vlatko Vedral. Quantum macroscopicity versus distillation of macroscopic superpositions. *Phys. Rev. A*, 92:022356, Aug 2015.
- [63] Sixia Yu. Quantum fisher information as the convex roof of variance. *arXiv:1302.5311*, 2013.
- [64] Ivar Zapata, Fernando Sols, and Anthony J. Leggett. Josephson effect between trapped bose-einstein condensates. *Phys. Rev. A*, 57:R28–R31, Jan 1998.
- [65] Tilman Zibold, Eike Nicklas, Christian Gross, and Markus K. Oberthaler. Classical Bifurcation at the Transition from Rabi to Josephson Dynamics. *Phys. Rev. Lett.*, 105(20):204101, nov 2010.

Chapter 4

Eigenstate Thermalization and Quantum Fisher Information

To describe equilibrium matter, scientists make a few simple assumptions so they can easily construct statistical ensembles that only depend on a few parameters such as energy and volume. The most basic of these assumptions is ergodicity: once the system has equilibrated, time averages equal phase space averages along equal energy contours. This assumption relies on chaos to spread the initial state probability distribution evenly across the energy contour and allows the construction of the micro-canonical ensemble. With the additional assumption of an environment that the system can exchange energy with, a macro-canonical ensemble can be constructed.

In closed quantum systems, such as ultra cold atomic gases, neither of these assumptions hold. There is no environment which can thermalize the system, and the ergodic hypothesis apparently fails due to the linearity of quantum mechanics. That is because,

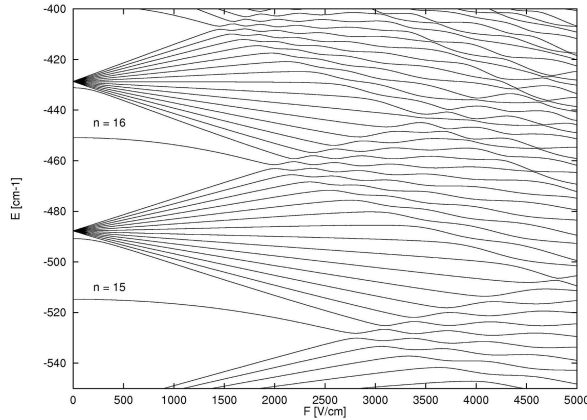


Figure 4.1: Quantum Chaos in Magnetic Hydrogen. Image from Wikipedia[4]

phase space in quantum mechanics is a Hilbert space and dynamics are linear instead of chaotic. Despite this, both these ensembles can often be used to give accurate descriptions of ultra cold atomic gases. In this chapter, I outline our current understanding of why.

My presentation of this will follow a condensed version of the presentation in[2]. I will begin by discussing how, in a quantum model with a well defined chaotic classical limit, chaos presents itself in the matrix elements of the hamiltonian, observables and entanglement entropy. I will then use the results from this discussion to motivate the Eigenstate Thermalization Hypothesis (ETH), which aims to explain why micro and macro canonical ensembles described the long time dynamics of closed quantum systems. I will then show how ETH reproduces the observables and response functions of canonical ensembles. I will then conclude this chapter with a short discussion on the quantum Fisher information, and entanglement for closed quantum systems.

4.1 Quantum Chaos and Random Matrix Theory

To understand how classical chaos appears in the quantum limit, start by imagining the hydrogen atom. Classically, this is a two body system in which space translation symmetry and rotational symmetry sufficiently constrain the dynamics and produce a classically integrable model. This classical integrability allows for the simple identification of the quantum numbers of the hydrogen atom. Upon applying a magnetic field, rotational symmetry is broken and the model becomes chaotic. Classically, for weak magnetic fields, the KAM theorem [1] identifies an approximate set of conserved quantities associated with invariant tori. Quantum mechanically, this translates into the validity of perturbation theory at weak magnetic fields. As the magnetic field strength is increased, the energy levels continue to move away from their unperturbed values until two energy levels meet. Degenerate perturbation theory shows that when the two energy levels get close, hybridization occurs and the two energy levels repel.

The energy levels of the hydrogen atom v.s. the magnetic field strength appears in Fig. 4.1. Imagining each energy level as a particle with a position E and a time B , it appears as if the energy levels act as a 1D classical gas of strongly repulsive particles. After “time” has evolved for many “collisions”, the positions of the “particles” appear random and uncorrelated with their initial positions. This led Wigner [3] to hypothesize that the energy levels at high magnetic fields are essentially random with a distribution determined by a random matrix.

To check this, we can determine the level spacing of a random matrix, and compare with the level spacing obtained from experimental spectra. To do this, we will start with a

two dimensional random matrix:

$$\begin{bmatrix} \epsilon_1 & 2V \\ 2V^* & \epsilon_2 \end{bmatrix} \quad (4.1)$$

which gives eigenvalues:

$$\frac{\epsilon_1 + \epsilon_2}{2} \pm \frac{1}{2} \sqrt{(\epsilon_1 - \epsilon_2)^2 + 4|V|^2} \quad (4.2)$$

If we assume the matrix elements ϵ_i and V are independent Gaussian random variables with variance 1, we can compute the level spacing statistics as:

$$P(\omega) = \left(\frac{1}{\sqrt{2\pi}}\right)^{\beta+2} \int d\epsilon_1 d\epsilon_2 DV_\beta e^{-\frac{\epsilon_1^2 + \epsilon_2^2 + |V|^2}{2}} \delta\left(\omega - \frac{1}{2} \sqrt{(\epsilon_1 - \epsilon_2)^2 + 4|V|^2}\right) \quad (4.3)$$

where $DV_\beta = dV$ when $\beta = 1$ and V is assumed real while $DV_\beta = dRV dIV$ when $\beta = 2$ and V is complex. Here the Dyson parameter, β , is introduced to capture the difference when the off diagonal matrix element is complex v.s. real: at this point in the calculation, it only changes the integration measure. Making the change of coordinates:

$$\epsilon_1 = x + y \quad (4.4)$$

$$\epsilon_2 = x - y \quad (4.5)$$

makes the integral:

$$\begin{aligned} P(\omega) &= \left(\frac{1}{\sqrt{2\pi}}\right)^{\beta+2} \int dx dy DV_\beta e^{-\frac{x^2 + y^2 + |V|^2}{2}} \delta\left(\omega - \sqrt{y^2 + |V|^2}\right) \\ &= \left(\frac{1}{\sqrt{2\pi}}\right)^{\beta+1} \int dy DV_\beta e^{-\frac{y^2 + |V|^2}{2}} \delta\left(\omega - \sqrt{y^2 + |V|^2}\right) \\ &= \left(\frac{1}{\sqrt{2\pi}}\right)^{\beta+1} \int dV e^{-\frac{r^2}{2}} \delta(\omega - r) \\ &= \left(\frac{S_\beta}{\sqrt{2\pi}}\right)^{\beta+1} \omega^\beta e^{-\frac{\omega^2}{2}} \end{aligned} \quad (4.6)$$

where $S_{\beta=1} = \pi$ and $S_{\beta=2} = \frac{3}{4}\pi$. The ω^β term captures the level repulsion and depends on β because of the difference in the volume elements on the third line of Eq. 4.6 when V is restricted to be real or allowed to be complex. The above calculation suggests the following geometrical interpretation of level repulsion. First we see that a two dimensional matrix lives in a $2 + \beta$ dimensional space. After the first coordinate transformations we find that one of these dimensions, x , sets the average energy. The last coordinate transform to spherical coordinates shows that fixing the level spacing to ω fixes the matrix to live on a sphere of radius ω in the remaining $1 + \beta$ dimensions. Level repulsion therefore reflects the fact that the surface area of this sphere shrinks to 0 at a rate $\sim \omega^\beta$ determined by the dimension the sphere lives in: $1 + \beta$.

Surprisingly, these statistics hold for random matrices of higher dimensions. A random orthogonal (real and symmetric) matrix has level statistics given by Eq. 4.6 with $\beta = 1$ and a random hermitian matrix (with off diagonals allowed to be complex) has level statistics given by $\beta = 2$. Furthermore, exact diagonalization has confirmed that hamiltonians with chaotic classical limits also demonstrate these statistics.

4.1.1 Random Matrix Elements of Observables

Since sufficient chaos in the classical limit leads to long time observables becoming ergodic and obeying a micro-canonical ensemble, we expect the long time observables of a quantum hamiltonian with a chaotic classical limit also to obey a micro-canonical ensemble. Lets see if we can use the random matrix hypothesis to test this. Given an initial state ρ , the eigenstates of the random matrix $|n\rangle$ and an observable O , we expect the long time

expectation value to be:

$$O(t) = \sum_{nm} \rho_{nm} e^{i(E_n - E_m)t} O_{nm} \quad (4.7)$$

Where the frequencies $(E_n - E_m)^{-1}$ are randomly distributed according to $P(\omega)$. Due to the random frequencies, we expect that the random phases cancel out at long times and we are left with:

$$\lim_{t \rightarrow \infty} O(t) = \sum_n \rho_{nn} O_{nn} \quad (4.8)$$

To check if this approaches a micro-canonical ensemble, we need to compare with:

$$\sum_n \delta(E_n - E) O_{nn} \quad (4.9)$$

Where E is the energy of the initial state. To check this we compute the properties of the matrix elements of O_{nn} for the eigenstates of a random matrix. If the eigenstates of O are labeled by i , the matrix elements O_{nm} are given as:

$$O_{nm} = \sum_i O_i \langle n|i \rangle \langle i|n \rangle \quad (4.10)$$

The eigenstate wave functions of a random matrix $\psi_n(i) = \langle i|n \rangle$ are given as independent random variables with variance constrained by the normalization:

$$\begin{aligned} \overline{\psi_n(i)} &= 0 \\ \overline{\psi_n(i)\psi_m(j)} &= \delta_{nm}\delta_{ij} \frac{1}{N} \end{aligned} \quad (4.11)$$

where N is the dimension of the Hilbert space. The mean of the matrix elements O_{nm} is then given as:

$$\overline{O_{nm}} = \bar{O} \delta_{nm} \quad (4.12)$$

with $\bar{O} = \sum_n O_{nn} \frac{1}{N}$ the infinite temperature average of the observable O . The fluctuations can also be calculated as

$$\overline{O_{nm}O_{nm}} - \overline{O_{nm}}^2 = \bar{O}^2 \frac{1}{N}. \quad (4.13)$$

Inserting this result into Eq. 4.8, we get:

$$\lim_{t \rightarrow \infty} O(t) = \bar{O} \quad (4.14)$$

Which, being the infinite temperature expectation value, is definitely not the micro-canonical expectation. The issue is that the eigenstate wave functions do not capture any information about energy conservation. The eigenstate thermalization hypothesis will fix this by hypothesizing a statistics for matrix elements of O in the hamiltonian eigenstate basis. This is partially captured by assuming O_{nm} are random variables with mean $\bar{O}(E)\delta_{nm}$ and variance $\sigma(E, n - m) \frac{1}{N}$ both dependent on the energy of the initial state. Before doing this we need to identify what \mathcal{N} should be, as it is the generalization of the normalization of the wave function.

4.1.2 Entanglement Entropy of random wave functions

To identify the generalized \mathcal{N} , we will show that it must be related to entanglement entropy. To do so we will assume the random matrix under study is a tensor product of two subsystems (A and B) and compute the second Rényi entropy. After tracing over subsystem A to obtain the reduced density matrix: $\rho_A = \text{tr}[\psi \langle \psi |]_A$, one computes the second Rényi entropy as:

$$R_2 = -\text{Log}(\text{tr}[\rho_A^2]_B) \quad (4.15)$$

We write the wave functions with basis states a and b of subsystem A and B as $\psi(a, b)$.

The reduced density matrix is then:

$$\rho_A = \sum_a \psi(a, b)\psi^*(a, b) \quad (4.16)$$

and the second Rényi entropy is:

$$e^{-R_2} = \sum_{b, a, a', c} \psi(a, b)\psi^*(a, c)\psi(a', c)\psi^*(a', b) \quad (4.17)$$

If we assume $\psi(a, b)$ is a random wave function with normalization $\sqrt{N_a N_b}$, then:

$$\overline{e^{-R_2}} = \sum_{b, a, a', c} \overline{\psi(a, b)\psi^*(a, c)\psi(a', c)\psi^*(a', b)} \quad (4.18)$$

which can be evaluated using Wicks theorem. The contractions restrict at least one of the sums. Taking only the contributions where one sum is restricted, we find the second Rényi entropy to be:

$$-\ln\left(\frac{1}{N_A} + \frac{1}{N_B}\right) \quad (4.19)$$

In the limit that one of subsystem acts like a bath and is much larger than the other we get:

$$R_2 = \ln(N_A) \quad (4.20)$$

Similar approximation (picking the largest contraction assuming $N_A < N_B$) can lead to an average n th Rényi entropy as:

$$(n - 1)\ln(N_A) \quad (4.21)$$

which gives the Shannon entanglement entropy as:

$$\ln(N_A) = S \quad (4.22)$$

4.2 Eigenstate Thermalization

We are now in a position to generalize the results of the previous section, and construct an ansatz for the energy eigenstate matrix elements for observables:

$$O_{nm} = \bar{O}(E_n)\delta_{nm} + \sqrt{\frac{\sigma(E, \omega)}{\mathcal{N}}} R_{nm} \quad (4.23)$$

where R_{nm} is a random variable with zero mean and unit variance, $E = \frac{E_n + E_m}{2}$, and $\omega = E_n - E_m$. From the previous section, we showed that the log of \mathcal{N} is the entanglement entropy, so we will make a hypothesis that it is the log of the thermodynamic entropy. Redefining $\sqrt{\sigma} = f$ we can write the ansatz as:

$$O_{nm} = \bar{O}(E_n)\delta_{nm} + f(E, \omega)e^{-S(E)/2} R_{nm} \quad (4.24)$$

where the functions of E and ω must be smooth. This constraint becomes apparently required when we evaluate long time observables. Inserting this result into Eq. 4.8, we get:

$$\lim_{t \rightarrow \infty} \langle O(t) \rangle = \sum_n \rho_{nn} \bar{O}(E_n) \quad (4.25)$$

which we compare with, $\sum_n \delta(E - E_n) \bar{O}(E_n)$ for the micro canonical or $\sum_n \frac{e^{-\beta E_n}}{Z} \bar{O}(E_n)$ for the macro canonical ensemble. Now if $\bar{O}(E)$ changes sufficiently slowly with E , and the ensemble under consideration ρ is sufficiently narrow in E , all three expressions will be approximately the same. This can be checked by expanding $\bar{O}(E_n)$ around $\langle H \rangle = \bar{E}$. Doing so results

$$\begin{aligned} \lim_{t \rightarrow \infty} \langle O(t) \rangle &= \sum_n \rho_{nn} \left[O(\bar{E}) + (E_n - \bar{E}) \frac{dO}{dE} + \frac{1}{2} (E_n - \bar{E})^2 \frac{d^2 O}{dE^2} \right] \\ &= O(\bar{E}) + \frac{1}{2} (\delta E)^2 \frac{d^2 O}{dE^2} \end{aligned} \quad (4.26)$$

where δE is the variance of energy. Similar expressions can be obtained for the micro and diagonal ensemble and the only difference will be in the differences in the variance of energy. Since energy is extensive, and the uncertainty is sub extensive for the micro and macro canonical ensemble, then all initial states with sub extensive energy uncertainty will have long time observables well approximated by micro and macro canonical ensembles.

This expansion and argument will generically fail when $\bar{O}(E_n)$ is not analytic in E_n . This occurs in integrable models, where local conserved charges can change discontinuously from eigenstate to eigenstate.

4.2.1 Dynamical Fluctuations and KMS relation

The above showed, that if the observables within an eigenstate are well behaved, and the initial state has sub extensive energy uncertainty, then expectations for individual eigenstates will reproduce expectations from canonical ensembles. We will now check this for the long time dynamical fluctuations. The dynamical fluctuations of an observable in an eigenstate are given as:

$$\begin{aligned} G(t) &= \langle n|O(t)O|n\rangle - \langle n|O(t)|n\rangle\langle n|O|n\rangle = \sum_{m \neq n} e^{i(E_n - E_m)t} |O_{nm}|^2 \\ &= \sum_{m \neq n} e^{i\omega t} e^{-S(E)} |f(E, \omega)|^2 |R_{nm}|^2 \end{aligned} \quad (4.27)$$

where $E = \frac{E_n + E_m}{2}$ and $\omega = E_n - E_m$. Rewriting in terms of E_m the sum variable and writing the sum as an integral:

$$\sum_m F(E_m) = \int d\omega f(E_n - \omega) \sum_m \delta(E_n - \omega - E_m) = \int d\omega f(E_n - \omega) \Omega(E - 2\omega) \quad (4.28)$$

where $\Omega(x)$ counts the number of states at energy density x . This gives us:

$$\begin{aligned}
G(t) &= \int d\omega e^{i\omega t} e^{-S(E_n - \omega/2)} |f(E_n - \omega/2, \omega)|^2 \sum_m \delta(E_n - \omega - E_m) |R_{nm}|^2 \quad (4.29) \\
&= \int d\omega e^{i\omega t} e^{-S(E_n - \omega/2)} |f(E_n - \omega/2, \omega)|^2 \Omega(E_n - \omega) = \\
&= \int d\omega e^{i\omega t} e^{S(E_n - \omega) - S(E_n - \omega/2)} |f(E_n - \omega/2, \omega)|^2
\end{aligned}$$

If O is a local operator, we suspect that it can only make transitions between eigenstates with sub extensive energy differences. This means we can expand about a small omega:

$$G(t) = \int d\omega e^{i\omega t} e^{-\beta\omega/2} |f(E_n - \omega/2, \omega)|^2 \quad (4.30)$$

From which we can we can derive the KMS relationship as:

$$\begin{aligned}
G_{>}(t - i\beta) &= \int d\omega e^{i\omega t} e^{\beta\omega/2} |f(E_n - \omega/2, \omega)|^2 \quad (4.31) \\
&= \int d\omega e^{-i\omega t} e^{-\beta\omega/2} |f(E_n + \omega/2, -\omega)|^2 \\
&= \int d\omega e^{-i\omega t} e^{-\beta\omega/2} |f(E_n + \omega/2, \omega)|^2 \\
&\approx \int d\omega e^{-i\omega t} e^{-\beta\omega/2} |f(E_n - \omega/2, \omega)|^2 \\
&= \langle n | OO(t) | n \rangle - \langle n | O^2 | n \rangle = G_{<}(t)
\end{aligned}$$

where in the second inequality we used the fact that the integral goes $-\infty$ to ∞ , in the second we used the hermeticity of the observable O , and in the approximation we again assume ω is small and that f varies smoothly in E .

4.3 Eigenstate Thermalization and Quantum Fisher Information

As discussed in chapter 3, the quantum Fisher information of observables of the form $O = \sum_i O_i$ where O_i is local, is a measure of entanglement entropy. For a pure state or the equilibrium state of a closed quantum system, the QFI, F_q is given the variance of O .

$$F_1(O) = 4(\langle O^2 \rangle - \langle O \rangle^2) \quad (4.32)$$

while for a Gibbs state, the quantum Fisher information is given by the spectral response function:

$$F_2(T, O) = \frac{4}{\pi} \int_0^\infty \tanh(\omega/2T) X''(\omega, T) d\omega \quad (4.33)$$

where $X''(\omega, T) = \mathcal{I} \int dt e^{i\omega t} \langle [O(t), O] \rangle$. Since a Gibbs state is not pure, we must have $F_1 \geq F_2$ given the expectation values, assuming the expectation values in both expressions are taken with respect to the Gibbs ensemble. If $F_1 \approx F_2$, then we have the interesting possibility that a thermal state almost saturates the entanglement bound.

If $F_1 > F_2$, then the measurement of the QFI for the closed ETH-valid quantum system will not match the corresponding measurement for a thermal state. This measurement would then detect that the closed ETH-valid quantum system is not truly thermalized.

This is likely not to occur because ETH is valid near the middle of the spectrum at reasonably high temperatures. Therefore, both F_1 and F_2 will be sub extensive and the fact a Gibbs state saturates its entanglement bound $F_1 \approx F_2$ is not surprising. In this case, the thermalized closed quantum system has volume law entanglement, but all of this

entanglement does not effect the fluctuations of local observables. It is not a macroscopic quantum state and can not be used for quantum enhanced interferometry.

Bibliography

- [1] L. Chierchia and J. N. Mather. Kolmogorov-Arnold-Moser theory. *Scholarpedia*, 5(9):2123, 2010. revision #91405.
- [2] Luca D'Alessio, Yariv Kafri, Anatoli Polkovnikov, and Marcos Rigol. From quantum chaos and eigenstate thermalization to statistical mechanics and thermodynamics. *Advances in Physics*, 65(3):239–362, May 2016.
- [3] Eugene P. Wigner. Characteristic vectors of bordered matrices with infinite dimensions. *Annals of Mathematics*, 62(3):548–564, 1955.
- [4] Wikipedia contributors. Stark effect — Wikipedia, the free encyclopedia, 2019. [Online; accessed 11-May-2020].

Chapter 5

Thermalization and its Breakdown for a Large Nonlinear Spin

5.1 Abstract

By developing a semi-classical analysis based on the Eigenstate Thermalization Hypothesis, we determine the long time behavior of a large spin evolving with a nonlinear Hamiltonian. Despite integrable classical dynamics, we find the Eigenstate Thermalization Hypothesis for the diagonal matrix elements of observables is satisfied in the majority of eigenstates, and thermalization of long time averaged observables is generic. The exception is a novel mechanism for the breakdown of thermalization based on an unstable fixed point in the classical dynamics. Using the semi-classical analysis we derive how the equilibrium values of observables encode properties of the initial state. We conclude with a discussion

of relevant experiments and the potential generality of this mechanism for the breakdown of thermalization.

5.2 Main Text

In recent years, experiments on ultra cold atoms and trapped ions[10, 28, 43, 47] have succeeded in producing quantum systems that, on relevant time scales, are completely isolated from an environment. Surprisingly, many of these experiments find long time behavior that mimics a system coupled to an environment. These experiments prompt the question of thermalization: Given an initial state $|\psi(t=0)\rangle$, a Hamiltonian $H = \sum_n E_n |n\rangle \langle n|$, and an observable O , when and why does the long time average of O :

$$O(t, T) = \frac{1}{T} \int_t^{t+T} d\tau \langle \psi(\tau) | O | \psi(\tau) \rangle \quad (5.1)$$

lose memory of its initial state? In other words, when does $O(t, T)$, at long time t , depend only on the energy of the initial state?

The eigenstate thermalization hypothesis (ETH)[14, 44, 42, 13, 15, 20, 33] attempts to answer this question. Briefly, it states that if A1) $\langle n | O | n \rangle$ changes very little between eigenstates with similar energy; A2) the level spacings, $E_n - E_{n+1}$, are sufficiently small; and A3) the energy uncertainty of the initial state is sufficiently small, then an eigenstate, randomly selected from a micro-canonical ensemble at the energy of the initial state, will describe the long time average observable (LTO): $O(t, T) \approx \langle n | O | n \rangle$ for large t and T .

ETH was originally discussed[14, 44] in classically chaotic systems where the eigenstates behave similar to random matrices and allows one to hypothesize additional structure on the off diagonal matrix elements of observables, $\langle n | O | m \rangle$. While this stronger version

of ETH allows one to predict relaxation times and response functions[13], we will focus on the weaker version presented above and only focus on the long time memory apparent in time averages.

In extended systems, the standard mechanism for the breakdown of thermalization is the emergence of an extensive set of conserved charges due to underlying integrability[39, 7, 11] or a random disorder potential[19, 35, 1]. In few mode bosonic systems, thermalization has been predicted from semi-classical chaos[46, 6, 23, 24, 3, 4, 5, 36], and it was recently shown that thermalization could fail when an oscillatory drive produced a time crystal[37].

In this letter, we explore a similar phenomenon for the long time behavior of a quantum evolution, but for a system which is not extended nor classically chaotic. The model we study is that of an SU(2) spin with large fixed size $|J| > 50$ and evolving with respect to the Hamiltonian $H = -J_x + \frac{\Lambda}{2|J|} J_z^2$, where J_x, J_z and J_y are the canonical SU(2) spin operators, and we assume $\Lambda > 1$. We formulate the question of thermalization for this system by asking: 1) for which initial states do LTOs thermalize and approach a micro-canonical ensemble, and 2) for states that do not thermalize, what is the mechanism that maintains information about the initial state. We focus our analysis on the time averages, $T \gg 1$, of observables $O = J_x$ and $O = J_z$, and refer to the Supplemental Material (SM) for other observables and for a discussion of $T \rightarrow 0$.

This spin Hamiltonian is expected to describe boson tunneling experiments[47, 45], and the theory community has explored its dynamics[41, 31, 29, 12, 18, 25, 22, 27, 30, 21]. Particularly relevant results are those relating to a semi-classical analysis[41, 31, 29, 38, 12, 22, 27, 30, 32, 17], and describe the classical trajectories shown in Fig. 5.1. These

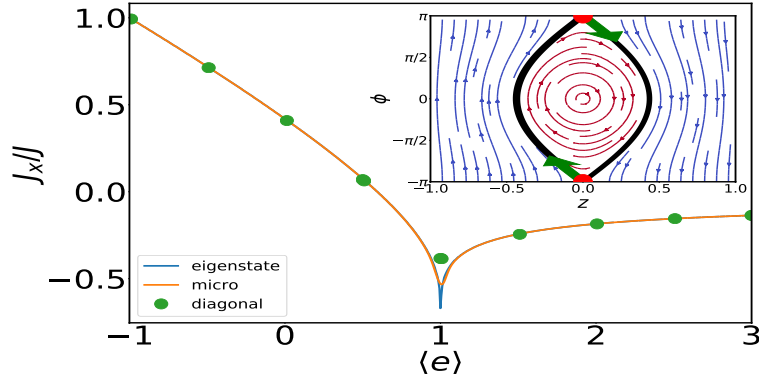


Figure 5.1: (Color online) Energy dependence of ensemble expectations values of J_x : The orange line is for the Micro-canonical, while the green dots are for the diagonal ensembles with initial phase $\phi' = 0$ and increasing $\langle J_z \rangle / J = z'(E)$. The energy dependence of the eigenstate expectation values is also shown. These calculations were performed for $|J| = 1000$ and $\Lambda = 10$. Notice the strong departure of the diagonal ensemble at $E = 1$ from the micro-canonical ensemble. Classical trajectories (inset): the separatrix is shown in black (bold) and separates the circular free-oscillation trajectories (red) from the self-trapping ones (blue). The red dots mark the unstable fixed point at $(z = 0, \phi = \pm\pi)$ and the green arrows mark the unstable directions.

trajectories, and corresponding eigenstates, have two distinct behaviors known as Josephson oscillation and self trapping, and are separated by a separatrix at $E = 1$. Unlike the few-mode boson models, these trajectories are not chaotic and relaxation occurs through quantum effects[22]. Thus, to consider the question of thermalization, we use the correspondence between periodic classical trajectories and eigenstates[16] to access the assumptions required by ETH and answer the questions posed above. We find that 1) for initial states with energy sufficiently different from the energy of the separatrix, $E = 1$, the assumptions of ETH are obeyed (similar to results in [32]) and observables come to an equilibrium described by a micro-canonical ensemble; and 2) for initial states with energy on the separatrix, the assumptions of ETH do not hold and LTO do not thermalize. We find that the breakdown of thermalization is due to the $E \approx 1$ eigenstates becoming localized in classical

phase space. As first pointed out in [17], the semi-classical analysis finds that the localization is due to the asymptotically slow classical dynamics near the unstable fixed point shown in Fig. 5.1. The ubiquity of this semi-classical feature suggests that this mechanism for the breakdown of thermalization is a general phenomenon present in other models.

Semi-Classical Picture and ETH: We first consider the case when the assumptions of ETH are valid and the large spin thermalizes. To do so it will be useful to first consider why assumptions of ETH generally imply thermalization. First consider the eigenstate decomposition of the initial state density matrix, $\sum_{nm} c_n c_m |n\rangle \langle m|$. At long times, t and for sufficiently large T , we can expect that only the diagonal terms of the density matrix contribute to observables[13, 22]:

$$O(t, T) \approx \sum_m |c_m|^2 \langle m| O |m\rangle. \quad (5.2)$$

If A3) of ETH is true, then $|c_m|^2$ is non zero only in a small energy window. Furthermore, if A1) of ETH holds, then $\langle m| O |m\rangle$ is approximately constant over the eigenstates with significant probability $|c_m|^2$. Finally A2) ensures there are multiple eigenstates in the micro-canonical ensemble which can be sampled, and we can conclude that a representative eigenstate $\langle n| O |n\rangle$ can be chosen to factor out of the average in Eq. 5.2 yielding: $O(t, T) \approx \langle n| O |n\rangle$.

We now use a semi-classical analysis to determine when these three assumptions of ETH hold for the nonlinear spin Hamiltonian. The semi-classical analysis is based on a Wigner-function formalism in which states and operators are represented as functions, $W(z, \phi)$ and $O(z, \phi)$, of z , the eigenvalue of $J_z/|J|$, and its conjugate momentum ϕ . In this formalism, the observables J_z and J_x are given by $|J|z$ and $|J|\sqrt{1-z^2} \cos(\phi)$ respectively,

and the Hamiltonian is written as[41]:

$$\frac{H(z, \phi)}{|J|} = \frac{\Lambda}{2} z^2 - \sqrt{1 - z^2} \cos(\phi) \quad (5.3)$$

The expectation values of a state $W(z, \phi)$ with an observable $O(z, \phi)$ is computed with:

$$\langle \psi | O | \psi \rangle = \frac{1}{4\pi} \int_{-1}^1 \int_{-\pi}^{\pi} dz d\phi W(z, \phi) O(z, \phi). \quad (5.4)$$

We use the set of spin coherent states as our initial states because they are regularly created in experiments[47, 45]. In the Wigner-function formalism these states are represented by Gaussian distributions that become more localized around a mean z' and a mean ϕ' as the size of the spin, $|J|$, is increased. Since a state which is more local around a specific z' and ϕ' has smaller energy uncertainty, assumption A3) of ETH is satisfied when $|J|$ is sufficiently large.

We now consider when assumptions A1) and A2) hold by constructing the Wigner functions of the eigenstates via a semi-classical analysis. The zeroth order classical analysis treats Eq. 5.3 as a classical Hamiltonian which yields the periodic trajectories depicted in Fig. 5.1. Fig. 5.1 shows two distinct types of periodic trajectories depending on the energy: for $E < 1$, the trajectories known as Josephson oscillation[41] occur in which z and ϕ periodically oscillates around a stable fixed point at $(z, \phi) = (0, 0)$, while for $E > 1$ trajectories called self trapping[2] occur in which z does not change sign, and ϕ monotonically increases ($z < 0$) or decreases ($z > 0$) depending on the sign of z . At $E = 1$, there is a separatrix separating the two dynamical behaviors.

Using the correspondence between classical periodic trajectories and eigenstates[16], the eigenstate Wigner-functions (EWF) with energy E can be written as $\rho_E(z, \phi) = w(E)\delta(H(z, \phi) -$

E), where $w(E)$ is the normalization of the eigenstate with energy E . The quantized energy levels, $E = E_n$, are then determined by the rule[12] stating that the area swept out by the eigenstate trajectories is quantized to $2\pi/|J|$. Thus, the energy difference between the eigenstate trajectories goes to 0 as $|J|$ is increased, and assumption A2) of ETH holds true.

Considering assumption A1), we first identify that the Hamiltonian in Eq. 5.3 has two distinct types of eigenstates corresponding to the Josephson oscillation and the self trapping trajectories. The self trapping eigenstates are further structured because, for a given energy $E > 1$, there are two disconnected trajectories depending on the initial sign of z . These two trajectories will be identified with the sign of z and their associated EWFs are calculated by selecting the correct trajectory when inverting $H(z, \phi)$:

$$\rho_{E\pm}(z, \phi) = w(E) \left| \frac{dH(z, \phi)}{dz} \right|^{-1} \delta(z \pm |H^{-1}(E, \phi)|) \quad (5.5)$$

At lowest order in a semi-classical expansion, these two trajectories correspond to two degenerate eigenstates, while at higher order the degeneracy is lifted[40] with splitting exponentially decreasing with $|J|$. Since this splitting is exponentially small, we will ignore it and assume all measurements occur before its dynamics are realized ($t < T_t \approx e^{|J|}$).

For $E \neq 1$, the eigenstate observables will be smooth in energy because, the difference between two neighboring eigenstate trajectories decreases to 0 as $|J|$ is increased. While for $E = 1$, the self trapping trajectories meet the free oscillating ones, a discontinuity emerges, and non analytic behavior of the eigenstate observables is expected. The behavior of the eigenstate observables has been identified previously[41, 8] and we confirm for J_x in Fig. 5.1.

Thus, we find that away from $E = 1$ and for large enough $|J|$, the assumptions of ETH hold, and we expect the LTOs to be described by a micro-canonical ensemble. While for eigenstates with energy $E \approx 1$, assumption A1) of ETH does not hold, and additional consideration is required to understand the long time behavior.

Numerical Analysis of the Diagonal Ensemble: From the analysis of the previous section we expect initial coherent states with z' and ϕ' away from the separatrix to show thermal behavior at long times. Using exact diagonalization, we confirm that memory of the initial state is lost for $E \neq 1$. This is shown in Fig. 5.2 for initial states in the free oscillation limit ($E = 0.5$), and it is shown in the SM for initial states in the self trapping limit. We also confirm that a micro-canonical ensemble, and a characteristic eigenstate describe the LTOs. This is shown in Fig. 5.1 for J_x and in the SM for other observables.

Close the $E = 1$, the micro-canonical ensemble and the characteristic eigenstate no longer match LTOs. Failure of the initial states at $E = 1$ to thermalize is further demonstrated in the right column of Fig. 5.2, which shows a dramatic dependence of the LTOs on the initial phase, ϕ' . This does not invalidate ETH because assumption A1) of ETH does not hold for these eigenstates.

Semi-Classical Analysis of the Breakdown of Thermalization: To better understand this breakdown of thermalization we investigate, using the semi-classical analysis, how the $E \approx 1$ eigenstates affect the LTO of the initial coherent states with $E \approx 1$. We begin by calculating the diagonal ensemble and its expectation values for the initial coherent states used above. Semi-classically[12] this diagonal ensemble is given as:

$$\rho_{diag} = \frac{1}{4\pi} \int_{-1}^1 \int_{-\pi}^{\pi} dz d\phi W_c(z, \phi, z', \phi') \rho_{E,s}(z, \phi) \quad (5.6)$$

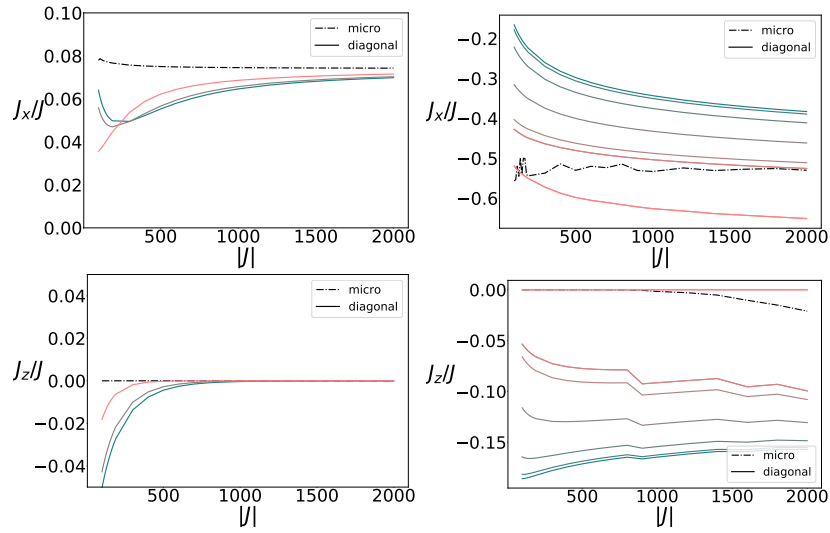


Figure 5.2: (color online) Micro-canonical and Diagonal Ensemble Expectation Values as a function of $|J|$ and ϕ' for $E = 0.5$ (1st column) and $E = 1$ (second column). The color indicates the initial phase ϕ' where in the second column it ranges from 0(dark blue) to π (bright pink). For $E = 0.5$: when $|J|$ increases the energy level spacing decreases, the assumptions A2) and A3) of ETH become more valid, and the dependence of the LTOs on the initial phase is lost. While for $E = 1$, memory of the initial state is maintained. These calculations were done with $\Lambda = 10$

where W_c is the initial coherent state Gaussian distribution centered around z' and ϕ' with variance $\sim \frac{1}{J}$, and the EWF, $\rho_{E,\pm}$, is given by Eq. 5.5. This integral can be computed when $(z', \phi') \neq (0, \pi)$ since the Jacobian $\left| \frac{dH(z, \phi)}{dz} \right|^{-1}$ is approximately constant in the vicinity of z' and ϕ' . Performing the Dirac delta and Gaussian integrations yields:

$$\rho_{diag}(\phi', z', E, s) \sim e^{-\frac{E-H(\phi', z')}{2\sigma^2(\phi', z')} + \ln(w(E))} \quad (5.7)$$

where $w(E)$ is the eigenstate normalization, and the energy variance $\sigma(\phi', z')$ scales with $|J|$ as $\sim \frac{1}{\sqrt{|J|}}$ with proportionality dependent on ϕ' and z' .

To calculate the LTOs, one must convolve the diagonal ensemble with the eigenstate expectation values:

$$O_{diag}(\phi', z') = \int_{-1}^{\Lambda/2} dE \sum_s \rho_{diag}(\phi', z', E, s) O(E, s) \quad (5.8)$$

where the sum over s is the sum over self trapping states when $E > 1$ and a fixed $s = 0$ for $E < 1$, and $O(E, s)$ is the eigenstate expectation value calculated using Eq. 5.4 with $W(z, \phi) = \rho_{E,s}(z, \phi)$.

Understanding this integral, and consequently why the LTOs encode information about the initial phase ϕ' , requires understanding the structure of the eigenstates and their EWFs. While an EWF is constrained to an equal energy surface, the shape of the energy surface affects how the EWF is distributed within the energy surface. This is captured by the Jacobian, $\left| \frac{dH(z, \phi)}{dz} \right|$, which appears in Eq. 5.5 due to the transformation of the energy delta function to phase space coordinates. Take the $s = 1$ self trapping eigenstate for example. If one integrates out z using the delta function, the Jacobian $\left| \frac{dH}{dz} \right|(E, \phi) = \left| \frac{d\phi}{dt} \right|(E, \phi)$ weighs the EWF. Therefore, the EWF will have more weight in regions where ϕ is changing slower in time.

On the separatrix, $E = 1$, the classical spin comes to a complete stop on the unstable fixed point; the Jacobian limits to 0, $\lim_{E \rightarrow 1} \lim_{\phi \rightarrow \pi} \left| \frac{dH}{dz} \right| (E, \phi) = 0$; and the EWFs with $E \rightarrow 1$ become localized on the unstable fixed point: $\rho_{E \rightarrow 1}(z, \phi) \approx \delta(z) \delta(\phi - \pi)$. The singularity of this localization result in the non-analytic behavior of the eigenstate expectation values near $E = 1$ (see for example J_x in Fig. 5.1).

This singular localization also produces a non-analyticity in the eigenstate overlaps for the set of initial coherent states with $E \approx 1$, but $\phi' \neq \pi$. Since these initial states have Wigner functions localized around ϕ' and $z' = H^{-1}(E = 1, \phi')$ and the EWFs for $E \approx 1$ are localized around $\phi = \pi \neq \phi'$ and $z = 0 \neq z'$, their overlap integrals in Eq. 5.8 will vanish.

These two non-analyticities are integrated over in Eq. 5.8 and result in the memory effects depicted in Fig. 5.2. In one limit, an initial coherent state with $\phi' \approx \pi$ will overlap the unstable fixed point eigenstate at $E = 1$, and the LTOs will closely match the observables of that same eigenstate ($J_z = 0$ and $J_x = -1$). In the other limit, when the initial ϕ' is away from π , the initial coherent state will have negligible overlap with the $E = 1$ eigenstate, the LTOs will depart from the observables of the $E = 1$ eigenstate. This is depicted in Fig. 5.2, in which the closer ϕ' is to π , the closer $j_z = J_z/J$ and $j_x = J_x/J$ approach 0 and -1 respectively.

To capture this behavior analytically, we perform a saddle point expansion for the integral Eq. 5.8, and evaluate the integrand at the peaks of ρ_{diag} , given in Eq. 5.7. To calculate the integrands that give the eigenstate normalization, $w(E)$, and the eigenstate observables, $O(E, s)$, we perform an expansion of the trajectories around the unstable fixed point to second order in (z, ϕ) . The phase, ϕ' , and size, $|J|$, dependence of diagonal ensemble

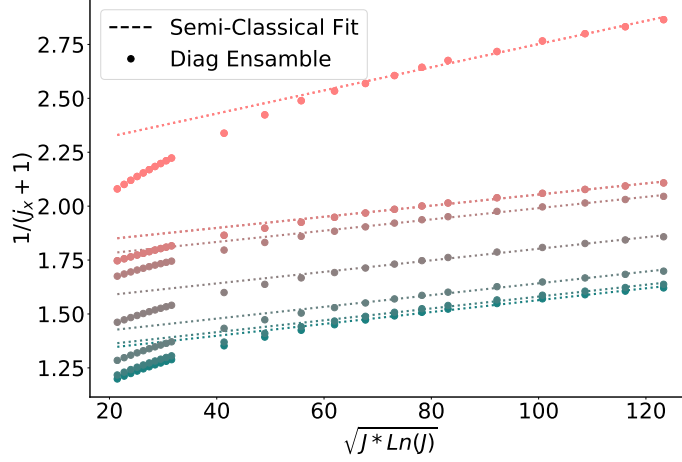


Figure 5.3: (Color Online) Classical fit to exact numerical calculations of diagonal ensemble. This plot shows the $\sqrt{|J| \ln |J|}$ scaling of $j_x = J_x/J$ for the diagonal ensemble of a set of initial states with energy $E = 1$ and different ϕ' and $|J|$. The dots are computed using exact diagonalization and the color indicates the initial ϕ' as in Fig. 5.2. Eq. 5.9 predicts $\sqrt{|J| \ln |J|}$ and the linear dashed lines are given by Eq. 5.9 with $F(\phi')$ fit to match the exact calculations for $|J| > 500$.

observables are then derived as¹:

$$j_{z,diag}(|J|, E = 1, \phi') = \frac{4\pi\sqrt{(\Lambda - 1)}}{3\Lambda \ln[F(\phi')|J| \ln[|J|]]} \quad (5.9)$$

$$j_{x,diag}(|J|, E = 1, \phi') = -1 + \frac{1}{\sqrt{F(\phi')|J| \ln[|J|]}} \frac{3 + \Lambda}{3(\Lambda - 1)}$$

where the factor $F(\phi') = [2\sigma(z', \phi')^2 |J|]^{-1}$, $j_{x(z)} = J_{x(z)}/J$, and z' is fixed by energy $z' = H^{-1}(E = 1, \phi')$. The factor $F(\phi')$ is constant in $|J|$ but has a non-trivial dependence on the initial phase ϕ' via $\sigma(z', \phi')$, the energy variance of the coherent state. This non-trivial dependence in ϕ' describes the memory effects shown in Fig. 5.2 for the initial states with $\phi' \neq \pi$. For the initial states with $\phi' \approx \pi$ the approximation for ρ_{diag} given in Eq. 5.7 breaks down, and the results in Eq. 5.9 become invalid. For these states, a different approximation is required and results in LTO closer to the unstable fixed point[12, 30].

While the exact diagonal ensemble for J_z becomes numerically unstable for large $|J|$, we

¹See SM for full derivation

can still compare exact results for J_x with Eq. 5.9. This comparison is shown in Fig. 5.3, where the $\sqrt{|J| \ln[|J|]}$ scaling is confirmed.

Discussion and Possible Experimental Realizations: Above we discussed how, for the large non-linear spin with energy $E \neq 1$, the assumptions of ETH hold and the spin thermalizes, while for $E = 1$ the spin does not thermalize. This lack of thermalization is particularly interesting because the remembered quantity, ϕ , is not a conserved quantity of the integrable classical dynamics. It is therefore a novel form of quantum memory, which is lost in the classical limit $J \rightarrow \infty$ (See Eq. 5.9).

The appearance of unstable fixed points in semi-classical dynamics is ubiquitous, and we expect this mechanism for the breakdown of thermalization to be general. While here we discussed a classically two-dimensional, integrable system, the Berry Conjecture[9, 13] suggests that the correspondence of eigenstates to trajectories, generalizes to a correspondence to micro-canonical ensembles in higher dimensional chaotic systems. Since the micro-canonical ensemble is also described by a delta function in energy, the Jacobian produced when transforming to the phase space coordinates would again reveal localization due to slow classical dynamics. One might again expect singularities due to a localized eigenstate and for them to produce memory effects following similar arguments as discussed above. This time, rather than the phase along a separatrix, it would be the distance to the unstable fixed point on the energy surface that is remembered. This is an exciting possibility which requires further investigation.

This mechanism for the breakdown of thermalization may be observable in ultra cold BECs[47, 34, 34] in which the bosons can be condensed into one of two modes such

as two different hyperfine states. A spin boson mapping then yields the non-linear spin Hamiltonian, where the parameter Λ is a ratio between the bosonic interaction energy and the energy associated with the tunneling between the two modes. Previous work has suggested that the other bosonic modes do not affect the dynamics on experimental time scales[27, 22]. Future work may find it interesting to investigate the effect of additional modes and may find connection with other forms of novel long time dynamics[26].

Acknowledgments: This work was supported in part by the NSF under Grant No. DMR-1411345, S. P. K. acknowledges financial support from the UC Office of the President through the UC Laboratory Fees Research Program, Award Number LGF-17-476883. The research of E. T. in the work presented in this manuscript was supported by the Laboratory Directed Research and Development program of Los Alamos National Laboratory under project number 20180045DR.

5.3 Supplemental Material

5.3.1 Large-J Scalling At Different Energies and for Different Observables

Thermalization in the Self-Trapping Limit

In Fig. 5.4, we demonstrate the validity of the ETH for $E=3$.

Ensemble Averages v.s. Energy

In this section we repeat a similar analysis done in Fig.1 in the main text for the observables J_z , J_x^2 , J_y^2 and J_z^2 . The results are shown in Figure 5.5. Each observable

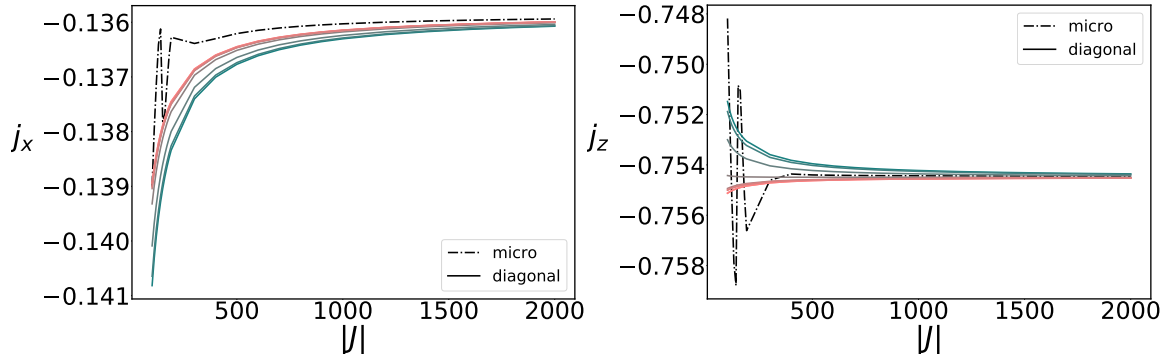


Figure 5.4: (Color Online) These plots demonstrate the validity of ETH in the self trapping limit for a fixed energy of $E = 3$. The different colors corresponds to different values of ϕ : blue (darker) $\phi = 0$, pink (lighter) $\phi = \pi$. The dashed line is the for the micro-canonical ensemble.

shows a non analyticity in the eigenstate observable as a function of energy. J_z shows a discontinuity while, the square observables show a cusp approaching the fixed point value.

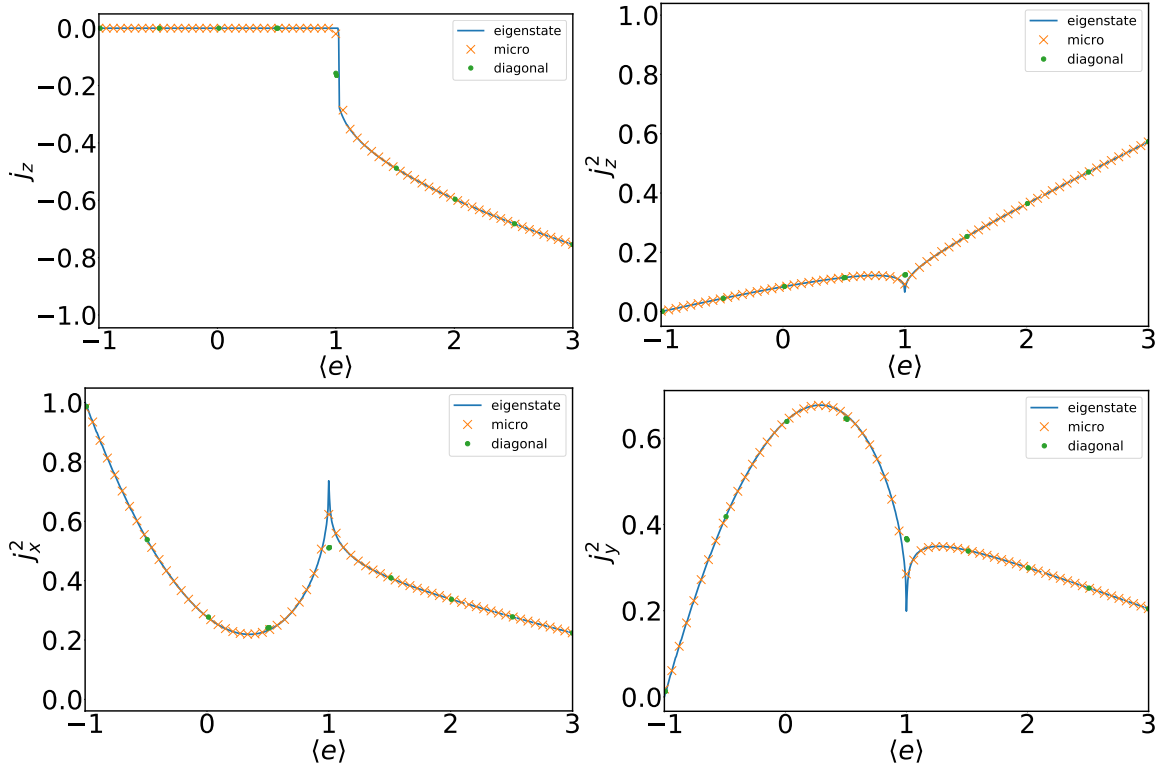


Figure 5.5: (Color Online) These plots demonstrate the validity of ETH in the self trapping and free oscillating limit, but it fails on the separatrix ($E=1$).

5.3.2 Numerical Details of Exact Construction of Micro-Canonical Ensembles

In the main text we discuss the use of exact diagonalization to construct the diagonal ensemble and micro-canonical ensemble. We use standard algorithms BLAS and LAPACK algorithms. The one subtlety is the identification of the two degenerate self trapping trajectories. We find that these algorithms naturally find a basis in which there is no tunneling between the two self trapping eigenstates. We then identify $s = \pm 1$ by the sign of $\langle J_z \rangle$ of the produced eigenstate. To confirm a lack of tunneling in the produced degenerate basis, we compute the overlap $\sum_{s j_z > 0} |\langle s | j_z \rangle|^2$. If the overlap is close to 1 then

we know there is very little tunneling between the two self-trapping trajectories. Note for the diagonal ensemble $\sum_n \rho_n |n\rangle \langle n|$, we use the non-tunneling degenerate basis, and thus treat the sign of J_z as a quasi-conserved integral of motion.

5.3.3 ETH for Off-Diagonal Elements and Equal Time Observables Without Time Averaging

In the main text, we used the eigenstate hypothesis for the diagonal matrix elements of the observables to argue about the thermalization of long-time-averaged observables. The full version of ETH hypothesizes a random structure for the off-diagonal elements, and, among other things, can be used to argue that time averaging is not required to see thermalization. One check of this part of the hypothesis is by checking if the level spacing follows Wigner-Dyson statistics. For the non-linear spin model studied here, the level spacing can be analytically expressed by a semi-classical analysis[22] and we do not expect the hypothesis to hold for the off-diagonal matrix elements of observables.

Therefore, ETH can not argue that equal-time observables will match their infinite-time-average counterparts at long times. In other words, without further analysis we can not show that an experiment will require time averaging to see thermalization. To find out if this is the case, we compute $J_z(t)$ and $J_x(t)$ for the initial states discussed in the paper with $|J| = 1000$. The results are presented in Fig. 5.6 and show that for $E \neq 1$, $J_x(t)$ and $J_z(t)$ equilibrate to their micro-canonical expectation value. For $E = 1$, small temporal fluctuations remain, but at any given time, the initial phase ϕ still determines how close J_x and J_z are equal to the fixed-point value ($J_x = -1$ and $J_z = 0$).

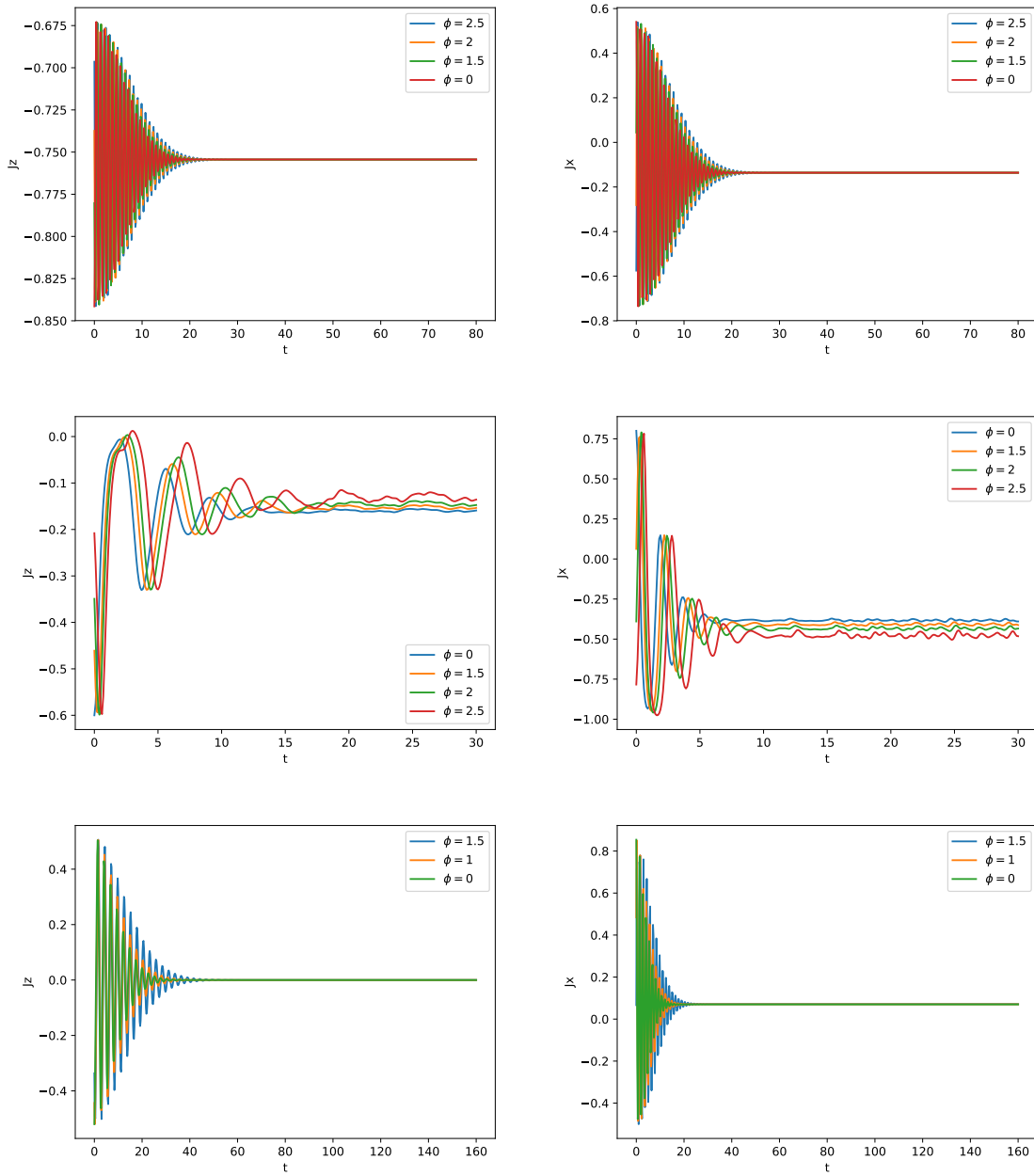


Figure 5.6: (Color Online) Dynamics of J_x and J_z for different values of ϕ at energies $E = 3$ (top), $E = 1$ (Middle) and $E = 0.5$ (Bottom).

5.3.4 Semi-Classical Eigenstates and Eigenstate normalization

. In the main text we defined the semi-classical eigenstate Wigner function (EWF) as:

$$\rho_E(z, \phi) = \omega(E)\delta(H(z, \phi) - E) \quad (5.10)$$

where the Hamiltonian is given as:

$$H = \frac{\Lambda z^2}{2} - \sqrt{1 - z^2} \cos(\phi), \quad (5.11)$$

and the normalization $\omega(E)$ is given as:

$$\omega(E)^{-1} = \int \int dz d\phi \delta(E - H(z, \phi)). \quad (5.12)$$

To compute this integral, we focus on the energy close to the separatrix, $E = 1 \pm |\delta|$, and expand the Hamiltonian around $E = 1$:

$$H - 1 = \frac{\Lambda - 1}{2} z^2 - \frac{(\phi - \pi)^2}{2} \quad (5.13)$$

Close to the unstable fixed point the trajectories trace out a hyperbola:

$$\begin{aligned} z &= \pm \sqrt{\frac{2}{\Lambda - 1}} \sqrt{\frac{\phi^2}{2} + (E - 1)} \\ \phi &= \sqrt{2(1 - E) + (\Lambda - 1)z^2} \end{aligned} \quad (5.14)$$

The Jacobian for both these trajectories are:

$$\begin{aligned} \left| \frac{dH}{dz} \right| &= (\Lambda - 1)z = \sqrt{(\Lambda - 1)} \sqrt{2(E - 1) + \phi^2} \\ \left| \frac{dH}{d\phi} \right| &= \phi = \sqrt{(\Lambda - 1)} \sqrt{\frac{2(1 - E)}{(\Lambda - 1)} + z^2}. \end{aligned} \quad (5.15)$$

Since the the inverse Jacobians, $\left|\frac{dH}{d\phi}\right|^{-1}$ and $\left|\frac{dH}{dz}\right|^{-1}$, contribute the most near the unstable fixed point and we can expand the integrand for $\omega(E)^{-1}$ near them and write:

$$\begin{aligned}\omega(1 + |\delta|)^{-1} &= \int_{-r_+}^{r_+} \left|\frac{dH}{dz}\right|^{-1}(\phi, \delta) + C_+ \\ \omega(1 - |\delta|)^{-1} &= \int_{-r_-}^{r_-} \left|\frac{dH}{d\phi}\right|^{-1}(z, \delta) + C_-\end{aligned}\tag{5.16}$$

where r_{\pm} denotes the limits where the hyperbolic expansion is valid and C_{\pm} are small and approximately constant for δ small. Defining a as:

$$\begin{aligned}a_+ &= 2(E - 1) \\ a_- &= \frac{2(1 - E)}{\Lambda - 1},\end{aligned}\tag{5.17}$$

these integrals can be expressed as:

$$\frac{1}{\sqrt{a(\Lambda - 1)}} \int_{-r}^r \frac{1}{\sqrt{1 - a^{-1}x^2}} dx = \frac{1}{\sqrt{(\Lambda - 1)}} \left[\sinh^{-1} \left(\frac{r}{\sqrt{a}} \right) \right]\tag{5.18}$$

and for $E \approx 1$, this approximates to as:

$$\begin{aligned}\omega(1 + |\delta|)^{-1} &= -\frac{Ln(|\delta|)}{2\sqrt{(\Lambda - 1)}} \\ \omega(1 - |\delta|)^{-1} &= -\frac{Ln(|\delta|)}{\sqrt{(\Lambda - 1)}}\end{aligned}\tag{5.19}$$

5.3.5 Eigenstate Overlaps and Saddle Point Approximation

To approximate the eigenstate overlap for initial states on the separatrix but away from the fixed points, we expand the energy to linear order in z and ϕ :

$$H = \kappa_1\phi + \gamma_1z + E_0\tag{5.20}$$

We first write the coherent state with initial imbalance z' and phase ϕ' as:

$$\rho(N, z', \phi', z, \phi) = \frac{\alpha_z(N, z')\alpha_\phi(N, z')}{\pi} \text{Exp} \left[-\alpha_z(N, z')(z - z')^2 - \alpha_\phi(N, z')(\phi - \phi')^2 \right]\tag{5.21}$$

where the inverse variances are:

$$\begin{aligned}\alpha_\phi(J, z') &= \frac{1}{2}J(1 - z^2) \\ \alpha_z(J, z') &= \frac{2J}{1 - z^2}\end{aligned}\tag{5.22}$$

The eigenstate overlap is then given as:

$$\rho_{diag}(z', \phi', E, s) = \frac{\omega(E)}{\gamma_1} \int d\phi \rho \left(N, z', \phi', \frac{\delta_0 - \kappa_1 \phi}{\gamma}, \phi \right),\tag{5.23}$$

where $\delta_0 = E - E_0$. This integrates by parts as:

$$\frac{\omega(E)}{\gamma_1} \frac{\sqrt{\alpha_z(N, z')\alpha_\phi(N, z')}}{\sqrt{\pi}\sqrt{\alpha_\phi + \frac{\kappa_1^2 \alpha_z}{\gamma_1^2}}} \exp\left(-\frac{\delta_0^2 \alpha_\phi \alpha_z}{\gamma_1^2 \alpha_\phi + \kappa_1^2 \alpha_z}\right)\tag{5.24}$$

Here we note that the energy uncertainty depends on the coherent state via the uncertainties α_z and α_ϕ . To find long term expectation values, we compute the diagonal ensemble average,

$$O = \int \rho_{diag}(E) O(E),\tag{5.25}$$

by performing a saddle point integration in the function ρ_{diag} .

Saddles

Analytic solutions for the saddle point only exist if $E_0 = 1$ so we focus on coherent states on this line. To find the saddle points we rewrite ρ_{diag} as:

$$\rho_{diag}(E = 1 \pm |\delta|) = \frac{K_\pm}{(1 - G_\pm \text{Ln}[\delta])} \text{Exp}[-2JF\delta^2]\tag{5.26}$$

where K_\pm and G_\pm are constants in δ , depend on C_\pm , and with \pm depending on the sign of δ . This function has a saddle at:

$$|\delta| = \frac{i}{\sqrt{(2JF)W_{-1}\left(-\frac{e^{-2/G_\pm}}{F2J}\right)}}\tag{5.27}$$

Where the product log, $W_{-1}(X)$, is the inverse of $e^x x$: $W_{-1}(e^x x) = x$ and the $_{-1}$ says to take the negative branch. For small x we get:

$$\lim_{x \rightarrow 0^-} \frac{W_{-1}(x)}{\text{Ln}(x)} = 1 \quad (5.28)$$

and we know $W_{-1}(x) \approx \text{Ln}(-x) - \text{Ln}(-\text{Ln}(-x)) + \dots$. We can then write this as:

$$|\delta| = \frac{i}{\sqrt{2JF \text{Ln}\left(\frac{e^{-2/G \pm}}{F2J}\right)}} \quad (5.29)$$

Which in the large- J limit goes as:

$$\frac{1}{\sqrt{2JF \text{Ln}(J)}} \quad (5.30)$$

and

$$2JF = \frac{\alpha_\phi \alpha_z}{\gamma_1^2 \alpha_\phi + \kappa_1^2 \alpha_z} \quad (5.31)$$

Thus the difference in initial states on the separatrix again shows up in the scaling to the large J limit. Also note G comes from $W(E)$ which depends on which side of the separatrix we are on (sign of δ). In the large- J limit the points become symmetric as indicated by the lack of dependence on G .

Eigenstate observables close to the separatrix

Next we compute the eigenstate observables, $O(E)$, which are given as

$$W(E) \int O(z, \phi) \delta[H(z, \phi) - E]. \quad (5.32)$$

J_z for Λ large has a amazingly simple solution. For $E < 1$, $J_z(E) = 0$ for $E > 1$ we integrate:

$$\int dz \delta[H(z, \phi) - E] = \int_{-\pi}^{\pi} d\phi z(\phi) \left| \frac{dH}{dz} \right|^{-1} \quad (5.33)$$

and for $\Lambda \gg 1$, $\left|\frac{dH}{dz}\right|^{-1} \approx \Lambda z$, the z 's cancel and we get

$$J_z(E) = \frac{W(E)2\pi}{\Lambda}. \quad (5.34)$$

J_x is more involved. We will take the same approach as the integral for $\omega(E)$. We assume the integral is dominated by the contribution near the unstable fixed point. Doing so allows us to expand J_x near the unstable fixed point: $J_x \approx -1 + \phi^2/2$. Solving for ϕ , we find that it is written as: $J_x \approx \frac{\Lambda-1}{2}z^2 - E$.

$$\begin{aligned} J_x(1 + |\delta|)^{-1} &= \omega(E)(\Lambda - 1) \int_{-r_+}^{r_+} \left(-\frac{E}{\Lambda - 1} + z^2/2\right) \left|\frac{dH}{dz}\right|^{-1} (\phi, \delta) + K_+ \\ J_x(1 - |\delta|)^{-1} &= \omega(E) \int_{-r_-}^{r_-} (-1 + \phi^2/2) \left|\frac{dH}{d\phi}\right|^{-1} (z, \delta) + K_- \end{aligned} \quad (5.35)$$

Similar to the integral for $\omega(E)$, these can be computed and in the limit of small δ we get:

$$\begin{aligned} J_x(1 + |\delta|)^{-1} &= -1 + \omega(|\delta|) \left(K_+ - \frac{|\delta| \text{Ln}(|\delta|)}{(\Lambda - 1)^{3/2}}\right) \\ J_x(1 - |\delta|)^{-1} &= -1 + \omega(|\delta|) \left(K_- - \frac{|\delta| \text{Ln}(|\delta|)}{\sqrt{\Lambda - 1}}\right) \end{aligned} \quad (5.36)$$

$\omega(|\delta|)$ goes to 0 faster than $\omega(|\delta|) |\delta| \text{Ln}(|\delta|)$ and we get:

$$\begin{aligned} J_x(1 + |\delta|)^{-1} &= -1 - \omega(|\delta|) \frac{|\delta| \text{Ln}(|\delta|)}{(\Lambda - 1)^{3/2}} \\ J_x(1 - |\delta|)^{-1} &= -1 - \omega(|\delta|) \frac{|\delta| \text{Ln}(|\delta|)}{\sqrt{\Lambda - 1}} \end{aligned} \quad (5.37)$$

Substituting ω :

$$\begin{aligned} J_x(1 + |\delta|)^{-1} &= -1 + \frac{2|\delta|}{\Lambda - 1} \\ J_x(1 - |\delta|)^{-1} &= -1 + |\delta| \\ J_z(1 + |\delta|) &= \frac{4\pi\sqrt{(\Lambda - 1)}}{\Lambda \text{Ln}(|\delta|)} \\ J_z(1 - |\delta|) &= 0 \end{aligned} \quad (5.38)$$

5.3.6 Semi-Classical Equilibrium Observables

Using the saddle point values to evaluate the diagonal ensemble observables we get:

$$O_{diag}(z', \phi') = \int \rho_{diag}(E, z', \phi') O(E) = \frac{1}{3} [2O(1 + |\delta|) + O(1 - |\delta|)] \quad (5.39)$$

There is a factor of 2 for $+|\delta|$ because $\rho_{diag}(E, z', \phi')$ in the small $|\delta|$ limit is twice as large on the self trapping side (The integral in $\omega(E)$ only integrates over one of the hyperbole on one side of the fixed point while it integrates both sides in the free oscillating limit). This gives the diagonal ensemble observables as:

$$\begin{aligned} J_z(z', \phi') &= -\frac{8\pi\sqrt{(\Lambda-1)}}{3\Lambda L n[|\delta|(z', \phi')]} \\ J_x(z', \phi') &= -1 + |\delta| \frac{3 + \Lambda}{3(\Lambda - 1)}. \end{aligned} \quad (5.40)$$

By substituting the saddle point location, we get the expressions given in the main text:

$$\begin{aligned} J_z(z', \phi') &= \frac{4\pi\sqrt{(\Lambda-1)}}{3\Lambda L n[F(z_0, \phi_0)JLn[J]]} \\ J_x(z', \phi') &= -1 + \frac{1}{\sqrt{F(z_0, \phi_0)JLn[J]}} \frac{3 + \Lambda}{3(\Lambda - 1)}. \end{aligned} \quad (5.41)$$

Bibliography

- [1] Dmitry A. Abanin, Ehud Altman, Immanuel Bloch, and Maksym Serbyn. Colloquium: Many-body localization, thermalization, and entanglement. *Rev. Mod. Phys.*, 91(2):021001, May 2019.
- [2] Michael Albiez, Rudolf Gati, Jonas Fölling, Stefan Hunsmann, Matteo Cristiani, and Markus K. Oberthaler. Direct observation of tunneling and nonlinear self-trapping in a single bosonic josephson junction. *Physical Review Letters*, 95(1):010402–010402, June 2005.
- [3] Geva Arwas and Doron Cohen. Chaos and two-level dynamics of the atomtronic quantum interference device. *New J. Phys.*, 18(1):015007, January 2016.
- [4] Geva Arwas and Doron Cohen. Chaos, metastability and ergodicity in Bose-Hubbard superfluid circuits. *AIP Conference Proceedings*, 1912(1):020001, December 2017.
- [5] Geva Arwas and Doron Cohen. Monodromy and chaos for condensed bosons in optical lattices. *Phys. Rev. A*, 99(2):023625, February 2019.
- [6] Geva Arwas, Amichay Vardi, and Doron Cohen. Superfluidity and Chaos in low dimensional circuits. *Scientific Reports*, 5:13433, August 2015.
- [7] Murray T. Batchelor and Angela Foerster. Yang–Baxter integrable models in experiments: From condensed matter to ultracold atoms. *J. Phys. A: Math. Theor.*, 49(17):173001, March 2016.
- [8] S. F. Caballero Benitez, V. Romero-Rochin, and R. Paredes. Delocalization to self-trapping transition of a Bose fluid confined in a double well potential. An analysis via one- and two-body correlation properties. *Journal of Physics B: Atomic, Molecular and Optical Physics*, 43(11):115301–115301, September 2009.
- [9] M V Berry. Regular and irregular semiclassical wavefunctions. *Journal of Physics A: Mathematical and General*, 10(12):2083–2091, dec 1977.
- [10] Immanuel Bloch, Jean Dalibard, and Wilhelm Zwerger. Many-body physics with ultracold gases. *Rev. Mod. Phys.*, 80(3):885–964, July 2008.

- [11] Amy C. Cassidy, Charles W. Clark, and Marcos Rigol. Generalized Thermalization in an Integrable Lattice System. *Phys. Rev. Lett.*, 106(14):140405, April 2011.
- [12] Maya Chuchem, Katrina Smith-Mannschott, Moritz Hiller, Tsampikos Kottos, Amichay Vardi, and Doron Cohen. Quantum dynamics in the bosonic Josephson junction. *Physical Review A*, 82(5):053617, November 2010.
- [13] Luca D'Alessio, Yariv Kafri, Anatoli Polkovnikov, and Marcos Rigol. From quantum chaos and eigenstate thermalization to statistical mechanics and thermodynamics. *Advances in Physics*, 65(3):239–362, May 2016.
- [14] J. M. Deutsch. Quantum statistical mechanics in a closed system. *Phys. Rev. A*, 43(4):2046–2049, February 1991.
- [15] Joshua M. Deutsch. Eigenstate Thermalization Hypothesis. *Rep. Prog. Phys.*, 81(8):082001, August 2018.
- [16] Martin C. Gutzwiller. Periodic Orbits and Classical Quantization Conditions. *J. of Math. Phys.*, 12(3):343–358, mar 1971.
- [17] Holger Hennig, Dirk Witthaut, and David K. Campbell. Global phase space of coherence and entanglement in a double-well bose-einstein condensate. *Phys. Rev. A*, 86:051604, Nov 2012.
- [18] Yixiao Huang, Wei Zhong, Zhe Sun, and Xiaoguang Wang. Fisher-information manifestation of dynamical stability and transition to self-trapping for bose-einstein condensates. *Phys. Rev. A*, 86:012320, Jul 2012.
- [19] John Z. Imbrie, Valentina Ros, and Antonello Scardicchio. Local integrals of motion in many-body localized systems. *Annalen der Physik*, 529(7):1600278, 2017.
- [20] R. V. Jensen and R. Shankar. Statistical Behavior in Deterministic Quantum Systems with Few Degrees of Freedom. *Phys. Rev. Lett.*, 54(17):1879–1882, April 1985.
- [21] Shane P. Kelly, Eddy Timmermans, and S.-W. Tsai. Detecting macroscopic indefiniteness of cat states in bosonic interferometers. *Phys. Rev. A*, 100:032117, Sep 2019.
- [22] Christine Khripkov, Doron Cohen, and Amichay Vardi. Temporal fluctuations in the bosonic Josephson junction as a probe for phase space tomography. *J. Phys. A: Math. Theor.*, 46(16):165304, April 2013.
- [23] Christine Khripkov, Doron Cohen, and Amichay Vardi. Thermalization of Bipartite Bose–Hubbard Models. *J. Phys. Chem. A*, 120(19):3136–3141, May 2016.
- [24] Christine Khripkov, Amichay Vardi, and Doron Cohen. Semiclassical theory of strong localization for quantum thermalization. *Phys. Rev. E*, 97(2):022127, February 2018.
- [25] M. Lapert, G. Ferrini, and D. Sugny. Optimal control of quantum superpositions in a bosonic Josephson junction. *Phys. Rev. A*, 85(2):023611, 2012.

- [26] Alessio Lerose, Jamir Marino, Bojan Žunkovič, Andrea Gambassi, and Alessandro Silva. Chaotic Dynamical Ferromagnetic Phase Induced by Nonequilibrium Quantum Fluctuations. *Phys. Rev. Lett.*, 120(13):130603, March 2018.
- [27] Izabella Lovas, József Fortágh, Eugene Demler, and Gergely Zaránd. Entanglement and entropy production in coupled single-mode Bose-Einstein condensates. *Phys. Rev. A*, 96(2):023615, August 2017.
- [28] Andrew D. Ludlow, Martin M. Boyd, Jun Ye, E. Peik, and P. O. Schmidt. Optical atomic clocks. *Rev. Mod. Phys.*, 87(2):637–701, June 2015.
- [29] Khan W. Mahmud, Heidi Perry, and William P. Reinhardt. Quantum phase-space picture of Bose-Einstein condensates in a double well. *Phys. Rev. A*, 71(2):023615, feb 2005.
- [30] R. Mathew and E. Tiesinga. Phase-space mixing in dynamically unstable, integrable few-mode quantum systems. *Phys. Rev. A*, 96(1):013604, July 2017.
- [31] A. Micheli, D. Jaksch, J. I. Cirac, and P. Zoller. Many-particle entanglement in two-component Bose-Einstein condensates. *Phys. Rev. A*, 67(1):013607, jan 2003.
- [32] Takashi Mori. Classical ergodicity and quantum eigenstate thermalization: Analysis in fully connected ising ferromagnets. *Phys. Rev. E*, 96:012134, Jul 2017.
- [33] Takashi Mori, Tatsuhiko N Ikeda, Eriko Kaminishi, and Masahito Ueda. Thermalization and prethermalization in isolated quantum systems: a theoretical overview. *Journal of Physics B: Atomic, Molecular and Optical Physics*, 51(11):112001, may 2018.
- [34] W. Muessel, H. Strobel, D. Linnemann, T. Zibold, B. Juliá-Díaz, and M. K. Oberthaler. Twist-and-turn spin squeezing in Bose-Einstein condensates. *Phys. Rev. A*, 92(2):023603, August 2015.
- [35] Rahul Nandkishore and David A. Huse. Many-Body Localization and Thermalization in Quantum Statistical Mechanics. *Annual Review of Condensed Matter Physics*, 6(1):15–38, 2015.
- [36] Andrea Pizzi, Fabrizio Dolcini, and Karyn Le Hur. Quench-induced dynamical phase transitions and π -synchronization in the bose-hubbard model. *Phys. Rev. B*, 99:094301, Mar 2019.
- [37] Andrea Pizzi, Johannes Knolle, and Andreas Nunnenkamp. Period- n discrete time crystals and quasicrystals with ultracold bosons. *Phys. Rev. Lett.*, 123:150601, Oct 2019.
- [38] Anatoli Polkovnikov. Phase space representation of quantum dynamics. pages 1–92, 2009.

- [39] Anatoli Polkovnikov, Krishnendu Sengupta, Alessandro Silva, and Mukund Vengalattore. Colloquium: Nonequilibrium dynamics of closed interacting quantum systems. *Rev. Mod. Phys.*, 83(3):863–883, August 2011.
- [40] Tadeusz Pudlik, Holger Hennig, Dirk Witthaut, and David K. Campbell. Tunneling in the self-trapped regime of a two-well bose-einstein condensate. *Phys. Rev. A*, 90:053610, Nov 2014.
- [41] S. Raghavan, A. Smerzi, S. Fantoni, and S. R. Shenoy. Coherent oscillations between two weakly coupled Bose-Einstein condensates: Josephson effects, oscillations, and macroscopic quantum self-trapping. *Phys. Rev. A*, 59(1):620–633, jan 1999.
- [42] Marcos Rigol, Vanja Dunjko, and Maxim Olshanii. Thermalization and its mechanism for generic isolated quantum systems. *Nature*, 452(7189):854–858, April 2008.
- [43] J. P. Shaffer, S. T. Rittenhouse, and H. R. Sadeghpour. Ultracold Rydberg molecules. *Nature Communications*, 9(1):1965, May 2018.
- [44] Mark Srednicki. Chaos and quantum thermalization. *Phys. Rev. E*, 50(2):888–901, August 1994.
- [45] Helmut Strobel, Wolfgang Muessel, Daniel Linnemann, Tilman Zibold, David B. Hume, Luca Pezzé, Augusto Smerzi, and Markus K. Oberthaler. Fisher information and entanglement of non-Gaussian spin states. *Science*, 345(6195):424–427, 2014.
- [46] Igor Tikhonenkov, Amichay Vardi, James R. Anglin, and Doron Cohen. Minimal Fokker-Planck Theory for the Thermalization of Mesoscopic Subsystems. *Phys. Rev. Lett.*, 110(5):050401, January 2013.
- [47] Tilman Zibold, Eike Nicklas, Christian Gross, and Markus K. Oberthaler. Classical Bifurcation at the Transition from Rabi to Josephson Dynamics. *Phys. Rev. Lett.*, 105(20):204101, nov 2010.

Chapter 6

Period- n Persistent Oscillations in the Kicked LMG Model

6.1 Abstract

In this chapter we study the quantum and classical dynamics of the LMG model with a periodically kicked interaction strength. In this model classical chaos appears similar to the standard map, in which chaos first appears near the separatrix and islands of stability emerge and remain for large kick strengths. The islands of stability contain new periodic trajectories not smoothly connected to the trajectories of the LMG hamiltonian. We find that these trajectories occur when the kick period is an arbitrary integer fraction, $1/n$, of the period of some LMG trajectory. Studying the effect of these trajectories on the quantum dynamics, we find that the islands of stability prevent dephasing and result in discrete time

translation symmetry breaking at long times. The period of the persistent oscillations that break discrete time translation symmetry is n times the kick period.

6.2 Introduction

Recently, the discovery of Many Body Localization[22, 1] has vitalized interest in systems with avoid Thermalization. Less recently, scientists spent centuries trying to create perpetual motion machines: a classical system which would avoid thermalization by oscillating for long times without an energy source. These past failed efforts have now morphed into the search for quantum time crystals, a quantum phase of matter which breaks time translation symmetry and exhibits a stable oscillation for long times[11, 8, 30]. The most distinctive form of this phenomena occurs in a many body localized spin chain in which all the spins are flipped at periodic intervals. After this system finds a dynamical equilibrium, energy is no longer exchanged with the periodic drive, and the local magnetization oscillates with a period twice the period of the flips. To call this long time behaviour a crystal or an emergent phase of matter, it should be stable with respect to small local perturbations. In this model, the stability is provided by the set of quasi-local integrals of motion which are characteristic of MBL phases.

A similar phenomena occurs in the kicked LMG model[28], which recently has found wide use in modeling boson tunneling experiments and as a mechanism for generating metrological useful entanglement[23, 21, 29, 31, 26, 2, 12, 14, 3, 5, 27, 10, 21, 5, 27, 10]. It has the following simple form:

$$H = -J_x + \frac{\Lambda}{2|J|} J_z^2 \tag{6.1}$$

where J_α are spin operators of size $|J|$, and it has been a significant source of insight into semi-classical methods[25, 19, 17, 24, 9, 15, 16, 18, 20, 13]. When $\Lambda < -1$, ferromagnetic symmetry breaking occurs in the ground state, while when $\Lambda > 1$ symmetry breaking occurs in the top of the spectrum. In the classical limit, these states are associated with “self trapping” trajectories which oscillate without changing sign of J_z , while the paramagnetic states are associated with “free oscillating” trajectories which oscillate around $J_z = 0$. Russomanno et. al [28] found that, when the spins are initialized in a ferromagnetic ground state and are flipped at periodic intervals, the spins would oscillate at a period twice the period of the intervals. This discrete time symmetry breaking mimics that which occurs in an MBL system, but now the ferromagnetic states stabilize the oscillations instead of the MBL integrals of motion.

In both these systems, the periodic dynamics are split into two parts: one part associated with the natural dynamics of the system and a spin flip part. The emergent periodicity of the discrete time translation symmetry breaking occurs because the spin flip part is completing half a period of a full spin rotation, while the stability emerges from the natural dynamics. In this chapter we report a discrete time translation symmetry breaking phenomena where the emergent periodicity is due to the natural dynamics completing an integer fraction of its natural period, and the stability emerge due to the cooperative effects of both parts of the dynamics.

We study dynamics similar to that done by Russomanno et. al.[28], but we replace the π spin rotation around the x axis (spin flip) with an arbitrary rotation around the x axis by a phase t_2 . We focus on the limit where t_2 is much smaller than the duration, t_1 , the LMG

hamiltonian is evolved for after each rotation. When both t_2 and t_1 are small, the Baker-Campbell-Hausdorff formula is valid and we can easily derive an effective time-invariant hamiltonian to model the kicked dynamics. In this limit, the model is classically integrable, the quantum wave function spread out across the integrable tori at times later than the Ehrenfest time, and similar to the model discussed in Chapter 5 long time observables equilibrate to a value described by a micro-canonical ensemble. When t_2 and t_1 increases, chaos and island of stability emerge similar to the standard map[7].

We find that the discrete time translation symmetry breaks due to the islands of stability. When, t_2 is small, these islands occur when t_1 is an integer fraction $1/n$ of a natural period of the LMG hamiltonian. At this resonance, n stable fixed points, and n unstable fixed points emerge, with integrable tori wrapping around the stable fixed points. Classically, the kicked dynamics hops between these n stable fixed points, moving within the integrable tori. Quantum mechanically, the stable fixed points prevent the spreading of the wave function around the LMG tori and also hops between the stable fixed points. For large enough spin sizes, the wave function can not spread between the stable fixed points even at long times and the n -period oscillations from the hopping between stable fixed points persists indefinitely.

We demonstrate the n -period oscillations using exact quantum dynamics and present the results in Section 6.5. By analyzing the Floquet spectrum, we show that these dynamics do not extract energy from the kicked unitary and present these results in the same section. The classical analysis explaining why these islands of stability emerge is given in Section 6.5, and the perturbative limit when $t_2 < t_1 < 1/\Lambda$ is discussed in Section 6.4. We

conclude in Section 6.6 with a discussion on the possibility of creating a true many body time crystal out of these persistent oscillations and there relationship to recent proposals for similar time crystal behavior.

6.3 Model and Classical Approximations

In this chapter we imagine an experiment where the interaction strength Λ of the LMG hamiltonian can be periodically turned on or off. This can be accomplished by pulsing the transverse field strength to much larger values or **using Feshbach resonances to turn off interactions between the spins**. The dynamics after m kicks will then be described by the following unitary:

$$U^m = (U_1 U_2)^m \tag{6.2}$$

$$U_i = e^{-iH_i t_i}$$

where

$$H_1 = -J_x + \frac{\Lambda}{2J} J_z^2 \tag{6.3}$$

$$H_2 = -J_x,$$

t_1 is the portion of time in which interactions are turned on and t_2 is the portion of time in which they are turned off. In the following sections we will systematically study the dynamics of this unitary in the “kicked” limit when $t_2 > t_1$. The solution to this classical dynamics is discussed both in Chapters 3 and 5. Through out this Chapter, we will work with $\Lambda = 10$.

6.3.1 Classical Dynamics

In the classical limit, a large spin is described by its z projection, z and azimuthal angle ϕ . In this mapping the spin variables become

$$J_z \rightarrow z \tag{6.4}$$

$$J_x \rightarrow \sqrt{1 - z^2} \cos(\phi)$$

$$J_y \rightarrow \sqrt{1 - z^2} \sin(\phi)$$

$$|J| \rightarrow 1,$$

the hamiltonian becomes

$$H_1(z, \phi) = -\sqrt{1 - z^2} \cos(\phi) + \frac{\Lambda}{2} z^2 \tag{6.5}$$

$$H_2(z, \phi) = -\sqrt{1 - z^2} \cos(\phi)$$

which has dynamics:

$$\frac{dz}{dt} = -\sqrt{1 - z^2} \sin(\phi) \tag{6.6}$$

$$\frac{d\phi}{dt} = \frac{z \cos(\phi)}{\sqrt{1 - z^2}} + \Lambda z$$

The classical approximation of the unitary $U = U_1 U_2$ is computed by the classical evolution by these equations of motion for a time t_1 followed by the classical equations of motion for H_2 (with $\Lambda = 0$) for a time t_2 .

6.4 Perturbative Limit

In the perturbative limit, we work with $t_1 < 2/\Lambda$ and $t_2 < t_1$. In this limit, the LMG dynamics still dominate, but the operator in the exponential is small and a BCH approximation can be applied. Defining, $U_1 U_2 \approx e^{-iH_{eff}T}$, and applying this approximation to second order we find:

$$-iTH_{eff} = -it_1 H_1 - it_2 H_2 + i\frac{t_1 t_2 \Lambda}{4J} \{J_z, J_y\} + i\tilde{H}^3 \quad (6.7)$$

where

$$\begin{aligned} i\tilde{H}^3 &= \frac{i}{12} (t_1^2 t_2 [H_1, [H_1, H_2]] - t_2^2 t_1 [H_2, [H_1, H_2]]) \\ &= \frac{-\Lambda}{24J} (t_1^2 t_2 [H_1, \{J_y, J_z\}] - t_2^2 t_1 [H_2, \{J_y, J_z\}]) \\ &= \frac{-\Lambda}{24J} \left(t_1^2 t_2 \left[\frac{\Lambda}{2J} J_z^2, \{J_y, J_z\} \right] - (t_1^2 t_2 - t_2^2 t_1) [J_x, \{J_y, J_z\}] \right) \\ &= \frac{-\Lambda}{24J} \left(t_1^2 t_2 \frac{\Lambda}{2J} (-i\{J_z, \{J_z, J_x\}\}) + (t_1^2 t_2 - t_2^2 t_1) (2i(J_y^2 - J_z^2)) \right) \\ &= i\frac{\Lambda}{24J} \left(t_1^2 t_2 \frac{\Lambda}{2J} (\{J_z, \{J_z, J_x\}\}) - 2(t_1^2 t_2 - t_2^2 t_1) (J_y^2 - J_z^2) \right) \end{aligned} \quad (6.8)$$

At zeroth level in this approximation the effective hamiltonian is simply a shift from H_1 toward a J_x dominated LMG. Setting $T = t_1 + t_2$, the effective hamiltonian has LMG form:

$$H_{eff}^{(0)} = -J_x + \frac{\Lambda}{2J(1 + t_2/t_1)} J_z^2. \quad (6.9)$$

This effective hamiltonian is equivalent to the LMG hamiltonian with rescaled Λ given as:

$$\Lambda \rightarrow \Lambda' = \frac{\Lambda}{1 + \frac{t_2}{t_1}} \quad (6.10)$$

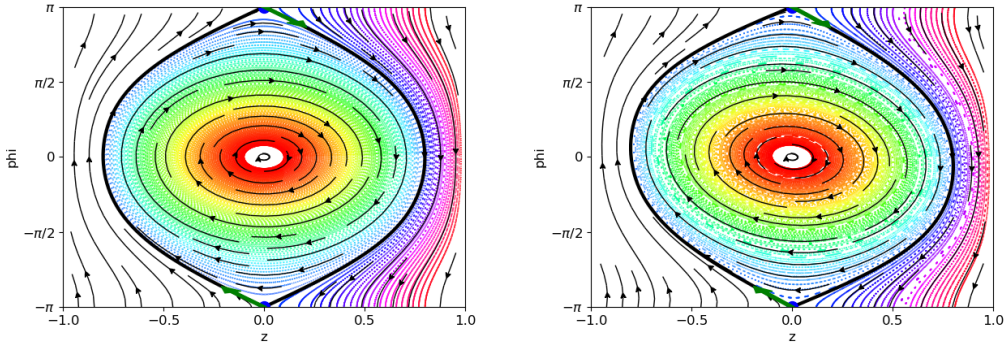


Figure 6.1: Classical Poincaré plots for $\Lambda = 10$ and $t_1 = t_2 = 0.01$ (left) and 0.25 (right). The black lines in the background are the classical trajectories determined by hamiltonian $H_{eff}^{(1)}$ and the color corresponds to the initial z used to generate the Poincaré plot. The initial ϕ was 0 . The solid black line depicts the separatrix for the deformed models

The primary effect from this rescaling is to enlarge the free oscillating region of the phase diagram. In this limit, the unstable fixed point remains unstable, and the self trapping dynamics still exist as long as $\frac{\Lambda}{1+\frac{t_2}{t_1}} > 1$.

At the next level in the approximation, the effective hamiltonian picks up a new term which more seriously deforms the LMG trajectories:

$$H_{eff}^{(1)} = H_{eff}^{(0)} + \frac{t_1 t_2 \Lambda}{4J(t_1 + t_2)} \{J_z, J_y\} \quad (6.11)$$

The classical form of this operator is:

$$\frac{t_2 \Lambda'}{2} z \sqrt{1 - z^2} \sin(\phi) \quad (6.12)$$

which modifies the classical equations of motion with the following terms:

$$\begin{aligned} \delta \frac{dz}{dt} &= -\frac{t_2 \Lambda'}{2} z \sqrt{1 - z^2} \cos(\phi) \\ \delta \frac{d\phi}{dt} &= \frac{t_2 \Lambda'}{2} \left(\sqrt{1 - z^2} \sin(\phi) - \frac{z^2 \sin(\phi)}{\sqrt{1 - z^2}} \right) \end{aligned} \quad (6.13)$$

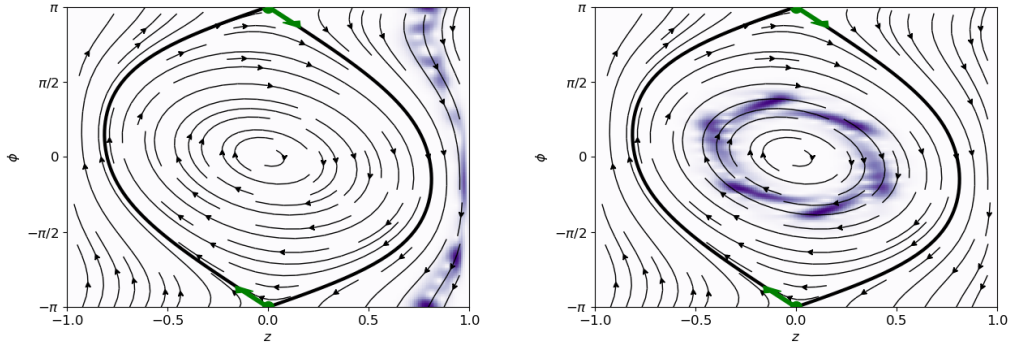


Figure 6.2: Long time Q functions of quantum dynamics for two different initial states $z =$ (left) and $z =$ (right), and for $\Lambda = 10$ and $t_1 = t_2 = 0.25$. This demonstrates that at long times, the dynamics of the kicked LMG model are constrained to the integrable tori defined by the effective hamiltonian H_{eff}

The qualitative picture of the LMG hamiltonian is not changed by these contributions, and the integrable tori of the LMG hamiltonian are simply deformed. These deformed tori are depicted in Fig 6.1.

Similarly, the quantum dynamics are not dramatically changed from what was discussed in chapters 3 and 5: the long time dynamics still has the quantum wave function spread across the now deformed tori; Cat states can still be created; and there will be long time memory for initial states starting on the now deformed separatrix. As a quick example, we plot in fig 6.2 the long time Q functions are shown to cover these tori.

The separatrix depicted in Fig 6.1 can be obtained by identifying the unstable fixed point, and the separatrix still occurs at $E = 1$ Using this we can construct an equation for the deformed separatrix:

$$H_{eff}(z, \phi) = 1 \tag{6.14}$$

which can be solved by numerical inversion.

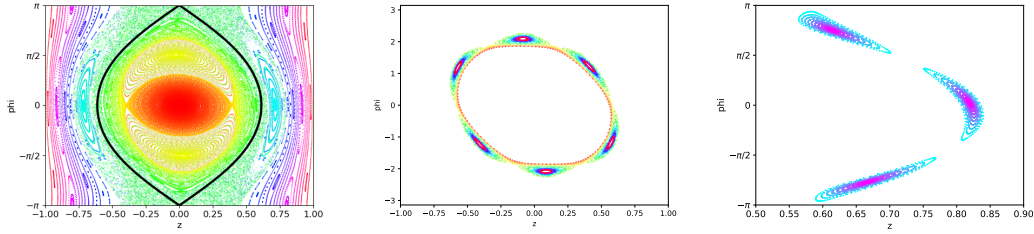


Figure 6.3: These are the classical Poincaré sections for the dynamics given by: $(t_1, t_2) = (1.1, 0.05)$ Left, $(0.35, 0.2)$ Middle, and $(0.3, 0.1)$ Right. In all three cases t_2 is sufficiently large, ensuring that the non-trivial trajectories are large. The non trivial trajectories occur when period of a near by trajectory is close to an integer multiple of t_1 : $\tau_{LMG}(z_0, \phi_0) \approx nt_1$ For the left figure, the non-trivial trajectory in the free oscillating region is an example of an $n = 2$, and the one in the self trapping region is an $n = 1$. This trajectory is particularly impressive, because the trivial trajectories surrounding have become chaotic while these non-trivial trajectories remain integrable. The middle and right plots show $n = 6$ and $n = 3$ non-trivial trajectories.

6.5 Islands of Stability and Persistent Oscillations

As we increase t_1 , or t_2 the following departures from the deformed trajectories occur: 1) new non-trivial “integrable tori” appear and 2) chaos emerges around the separatrix. The non-trivial tori are parts of phase space where integrable trajectories appear that are not topologically deformable into the LMG trajectories. A few examples of these non-trivial tori are shown in Fig 6.3. These non-trivial tori also appear in the standard map[7] and are often referred to as islands of stability because they can persist even in the chaotic limit when the bare tori are destroyed. In this section we will focus on the non-trivial integrable tori.

To explain these non-trivial integrable tori, we focus on the limit when $t_1 > \sqrt{2/\Lambda} \gg t_2$. We work in this limit, because here the LMG dynamics serve as a good reference point for discussing the dynamics of the kicked model. In fact, in Fig 6.3, the tra-

jectories around the stable fixed points of the LMG hamiltonian are roughly unperturbed. In this limit, we find the non-trivial tori occur when a period of the LMG hamiltonian, τ , is in resonance with t_1 : $\tau = nt_1$. This gives us a hint of why they occur more generally.

We therefore turn our attention to Fig. 6.4 where $t_2 < 0.01$, and we have plotted only a set of non-trivial tori in both the self trapping and self oscillating limit. There we have also plotted the resonant ($n = 1$) LMG trajectory in black. In the classical approximation, the dynamics of U_1 , bring initial states on this trajectory back to themselves. Semi-classically, we can approximate $U_1(t_1)$ as the identity. Similarly, when initial states start on an LMG trajectory with period slightly less than t_1 , they appear to move forward along the trajectory by a time $t_1 - \tau$. If t_1 is much less than the Ehrenfest time, then we can approximate $U_1(t_1) \approx U_1(t_1 - \tau)$ when U_1 acts in this region of phase space. Similarly when $t_1 < \tau$, the state appears to move backwards by a time $\tau - t_1$ and we can approximate $U_1(t_1) \approx U_1^\dagger(\tau - t_1)$. This inspires us to label the trajectories with $\tau < t_1$ as backward trajectories and the trajectories with $\tau > t_1$ as forward trajectories. Note a similar phenomena also occurs when video taping a propeller oscillating close to the frame rate of the camera.

By investigating the non-trivial trajectories in Fig. 6.4, we find that their dynamics short cut the LMG trajectories by changing between the forward and backward trajectories. This is occurring because the kick U_2 is kicking the spin between the two types trajectories when the spin approaches the turning points (i.e. when the spin crosses the resonant trajectory). This is explained visually in Fig. 6.4. For small t_2 , these non-trivial tori are neighbored by the LMG tori. The boundary between the trivial and nontrivial tori is determined by the kick strength t_2 . When t_2 is increased, the number of forward (backward)

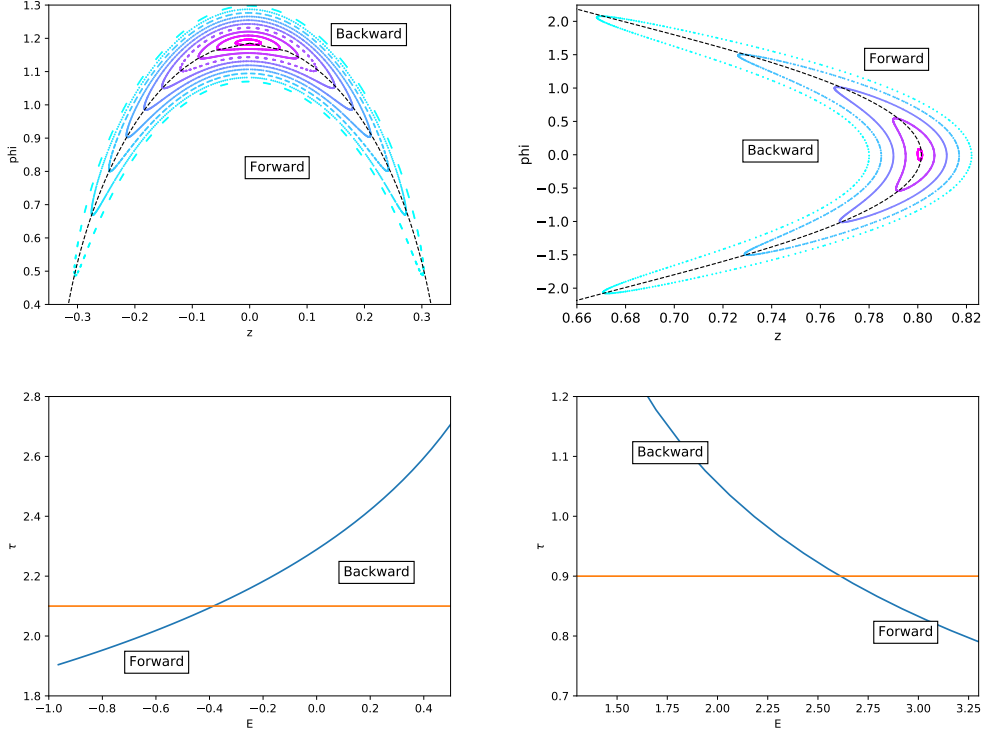


Figure 6.4: The top to figures show two example of $n = 1$ non-trivial trajectories for $(t_1, t_2) = (2.1, 0.005)$ Left and $(0.9, 0.004)$ Right. The black lines in each show the trivial trajectory which exists when $t_2 = 0$. The bottom two plots show $\tau_{LMG}(E)$ in blue for the LMG model corresponding to the U_1 dynamics in the top plots ($\Lambda = 10$). The orange line is t_1 , when $t_1 > \tau(E)$, U_1 moves the spin forward along the trajectory by a time $t_1 - \tau(E)$, while if $t_1 < \tau(E)$, U_1 moves the spin backwards along the trajectory by a time $\tau(E) - t_1$. U_2 kicks connects the forward and backward trajectories by. This is done differently in the two regions of phase space. For the left plot, U_2 always kicks z in the positive direction keeping ϕ constant. While in the right plot, U_2 kicks z in the $\pm z$ direction depending on whether $sign(\phi) = \pm 1$

trajectories that can be kicked into backward (forward) increases and the number of non-trivial tori increases. The stable fixed point at the center of the non-trivial tori is a point on the resonant trajectory where the action of U_2 also acts like the identity. It is interesting to note that these non-trivial tori often survive inside the chaotic limit of the model. One example of this is clearly highlighted in Fig 6.3. In this way these non-trivial tori get the name: islands of stability.

When the resonance condition occurs for $n > 1$ a similar description holds up to a few subtleties. First, U_1 only completes a fraction ($1/n$) of a trajectory. Therefore, we should define the forward and backward trajectories based off the classical trajectories of the unitary, $U'_1 = (U_1U_2)^{n-1}U_1$. In a perturbative limit, the classical periods and trajectories of U'_1 will only be slightly shifted from the LMG trajectories, and we can follow similar arguments as above. The dynamics defined by $(U'_1U_2)^m$ will then have a similar fixed point structure and trajectories as shown in Fig. 6.4, but will only capture the dynamics when looking every n steps of U_1U_2 . Looking every step, we see that U_1U_2 will shift the tori around the fixed point defined by U'_1U_2 to n different points in phase space. This shows that, at the resonances, there must be n fixed points of the U'_1U_2 dynamics, and this is confirmed in Fig. 6.3. Since these are fixed points of the U'_1U_2 dynamics, the U_1U_2 dynamics display an period n oscillation due to U_1 moving the spin between the different fixed points.

The fact the U'_1U_2 dynamics has n fixed points around the U'_1 trajectories also constrains the size of the non-trivial tori further then what is limited by the strength of the kick. This is because the tori around each of the fixed points can not intersect each other.

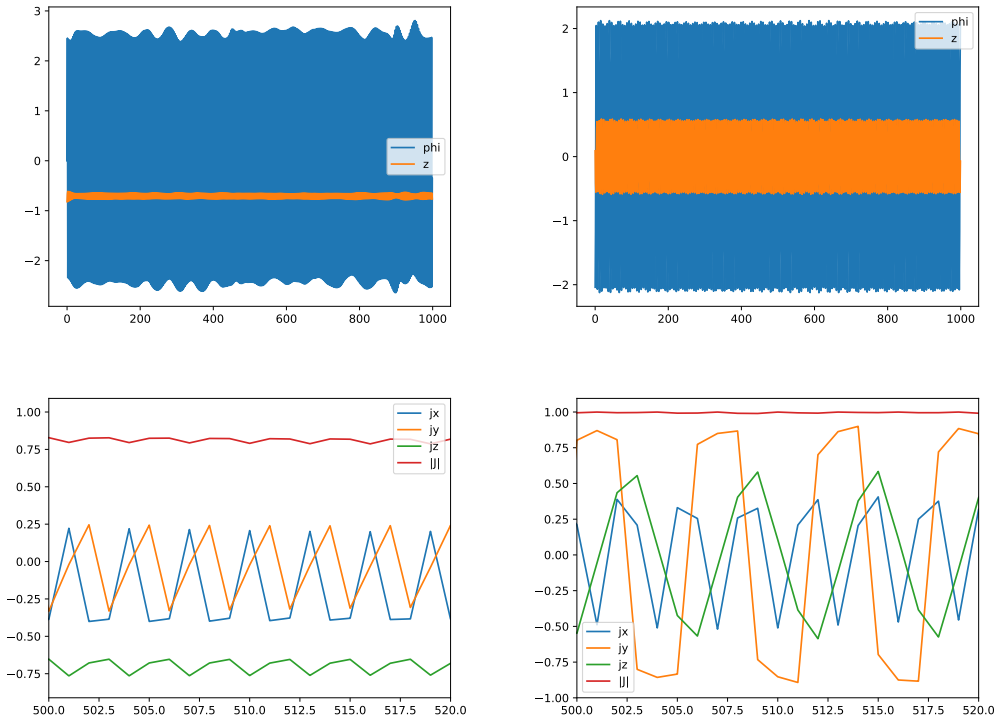


Figure 6.5: Period $n = 3$ (Left) and $n = 6$ (Right) Persistent Oscillations. The top panel shows these oscillations last indefinitely, while the bottom shows the shape of the oscillation in more detail.

Otherwise, the tori could not be defined. Therefore, the largest tori just barely meet at n unstable fixed points of the $U_1'U_2$ dynamics.

In the quantum dynamics of integrable classical systems, wave functions spread out across integrable tori generically leading to long time equilibrium. This is also true for the $n = 1$ resonances, but if n is greater than 1, then the wave function has no way of spreading between the n islands of stability. It therefore spreads out within one island of instability, and the period n oscillations persist at all times. This is shown in Fig. 6.5 where the exact quantum dynamics were computed for a spin of size $|J| = 500$. The fact the

wave function can only spread out within each island is captured by the dynamics of the observed magnitude $|J|^2 = \sum_{\alpha} \langle J_{\alpha} \rangle^2$. For classical states $|J| = 1$, while for states spread out along a classical trajectory, $|J| \rightarrow 0$. Thus, the non-trivial fixed points stabilize the persistent oscillations by stabilizing the classicality of the states evolving. This is the same mechanism for stabilizing persistent oscillations discussed in [28], but now the unstable fixed points emerge from the interplay of the kick and the LMG dynamics, rather than the LMG dynamics alone.

Systems displaying discrete time translation symmetry breaking have a portion of the spectrum which has very uniform level spacing. This uniform level spacing is at frequencies $\frac{1}{T}$ where T is the period of the oscillation which breaks discrete time translation symmetry. We can identify these Floquet eigenstates by using the expectation value of $\langle H_{LMG} \rangle$. This is because, following a WKB approximation procedure, one would expect the set of oscillatory eigenstates to overlap the non-trivial trajectories. Since these trajectories oscillate around a set of fixed points that emerge on the resonant LMG trajectory, phase space averages over them should yield energies close to that of the resonant LMG trajectory. Therefore the oscillatory Floquet eigenstates should all have $\langle H_{LMG} \rangle$ close to the energy of the resonant LMG trajectory. We have confirmed this in Fig. 6.6, in which the Floquet eigenstate phase ϕ_n is plotted versus $\tau(\langle H_{LMG} \rangle)/t_1$. This figure also confirms the $\frac{1}{T}$ level spacing required to yield long time oscillations. Furthermore, since the eigenstates which are responsible for the persistent oscillation all have the same energy $\langle H_{LMG} \rangle$, when these oscillations equilibrate, they do not exchange energy with the drive (the U_2 kicks).

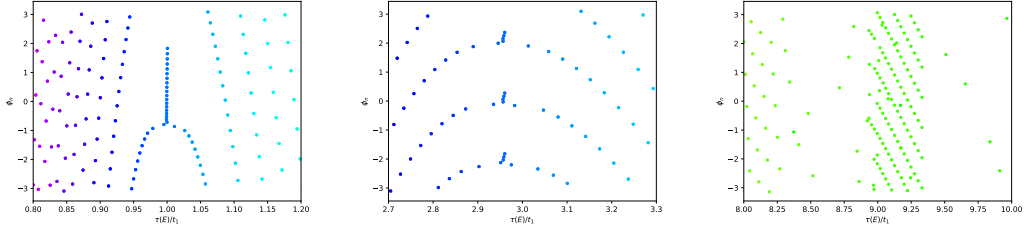


Figure 6.6: Floquet phases ϕ_n as a function of $\tau(E)$ where $E = \langle n | H_{LMG} | n \rangle$. The left plot corresponds to $(t_1, t_2) = (0.9, 0.004)$ with classical trajectories shown in Fig. 6.4, the middle plot is for $(t_1, t_2) = (0.3, 0.1)$ and has trajectories shown in Fig. 6.3 and quantum dynamics shown in Fig. 6.5, and the right plot is for $(t_1, t_2) = (0.35, 0.2)$ and has trajectories shown in Fig. 6.3 and quantum dynamics shown in Fig. 6.5. The middle and right plot corresponding to $n = 3$ and $n = 6$ and show a level spacing $= 2\pi/n$. For the $n = 3$ case, the perturbed trajectories for U'_1 are close to the those of the LMG trajectory so the they all have E close to that the $n = 3$ trajectory. For the $n = 6$ case, U'_1 is much more deformed from the LMG trajectoires and therefore these eigen states with $2\pi/n$ spacing are more spread out in energy E and further from the $\tau(E) = 6t_1$ “bare” resonance.

6.6 Conclusion

In this chapter we have discussed how period- n oscillations emerge in the kicked LMG model due to resonances with the kick frequency, t_1 . By analyzing exact eigenstates and dynamics, we showed that these oscillations will persist forever evading thermalization akin to a time crystal. We have opted not to call this a time crystal because, while the model is used for many body quantum gases, the two mode approximation reduces the Hilbert space to that of a single large spin. Therefore, the persistent oscillations do not have to compete with many body dephasing and these dynamics don’t yet deserve the label of a phase of matter such as a crystal.

It will be interesting for future works to investigate the effects of the other spatial modes in the BEC on these oscillations, and to find out if the stability of the fixed points can stabilize many body dephasing and diffusion in addition to quantum diffusion. These

possibility can also be investigated in long range spin models and there experimental realizations. Two types of experiments can realize these types of models: Rydberg atoms and cavity QED. For Rydberg atoms, long range dipolar interactions can, at first order be approximated as an all to all interaction [6]. This approximation yields the same model we described above. It will be interesting to study corrections to this model due to the finite range nature of the interactions. In cavity QED experiments, the long range nature of the spin-spin interaction is not in question, but the coupling can display inhomogeneities based on how the atoms in the cavity are organized[4]. These inhomogeneities are another interesting way to introduce a many-body aspect to the dynamics discussed in this paper.

Bibliography

- [1] Dmitry A. Abanin, Ehud Altman, Immanuel Bloch, and Maksym Serbyn. Colloquium: Many-body localization, thermalization, and entanglement. *Rev. Mod. Phys.*, 91(2):021001, May 2019.
- [2] Michael Albiez, Rudolf Gati, Jonas Fölling, Stefan Hunsmann, Matteo Cristiani, and Markus K. Oberthaler. Direct observation of tunneling and nonlinear self-trapping in a single bosonic josephson junction. *Phys. Rev. Lett.*, 95:010402, Jun 2005.
- [3] K. Baumann, R. Mottl, F. Brennecke, and T. Esslinger. Exploring symmetry breaking at the Dicke quantum phase transition. *Phys. Rev. Lett.*, 107(14):140402, 2011.
- [4] Gregory Bentsen, Tomohiro Hashizume, Anton S. Buyskikh, Emily J. Davis, Andrew J. Daley, Steven S. Gubser, and Monika Schleier-Smith. Treelike interactions and fast scrambling with cold atoms. *Phys. Rev. Lett.*, 123:130601, Sep 2019.
- [5] P. Berg, S. Abend, G. Tackmann, C. Schubert, E. Giese, W. P. Schleich, F. A. Narducci, W. Ertmer, and E. M. Rasel. Composite-Light-Pulse Technique for High-Precision Atom Interferometry. *Phys. Rev. Lett.*, 114(6):063002, feb 2015.
- [6] V. Borish, O. Marković, J. A. Hines, S. V. Rajagopal, and M. Schleier-Smith. Transverse-field ising dynamics in a rydberg-dressed atomic gas. *Phys. Rev. Lett.*, 124:063601, Feb 2020.
- [7] Boris V Chirikov. A universal instability of many-dimensional oscillator systems. *Physics Reports*, 52(5):263 – 379, 1979.
- [8] Soonwon Choi, Joonhee Choi, Renate Landig, Georg Kucsko, Hengyun Zhou, Junichi Isoya, Fedor Jelezko, Shinobu Onoda, Hitoshi Sumiya, Vedika Khemani, Curt von Keyserlingk, Norman Y. Yao, Eugene Demler, and Mikhail D. Lukin. Observation of discrete time-crystalline order in a disordered dipolar many-body system. *Nature*, 543(7644):221–225, Mar 2017. Letter.
- [9] Maya Chuchem, Katrina Smith-Mannschott, Moritz Hiller, Tsampikos Kottos, Amichay Vardi, and Doron Cohen. Quantum dynamics in the bosonic Josephson junction. *Physical Review A*, 82(5):053617, November 2010.

- [10] J. E. Debs, P. A. Altin, T. H. Barter, D. Döring, G. R. Dennis, G. McDonald, R. P. Anderson, J. D. Close, and N. P. Robins. Cold-atom gravimetry with a Bose-Einstein condensate. *Phys. Rev. A*, 84(3):033610, sep 2011.
- [11] Dominic V. Else, Bela Bauer, and Chetan Nayak. Floquet time crystals. *Phys. Rev. Lett.*, 117:090402, Aug 2016.
- [12] R. Gati, J. Esteve, B. Hemmerling, T. B. Ottenstein, J. Appmeier, A. Weller, and M. K. Oberthaler. A primary noise thermometer for ultracold Bose gases. *New J. Phys.*, 8:189–189, 2006.
- [13] Holger Hennig, Dirk Witthaut, and David K. Campbell. Global phase space of coherence and entanglement in a double-well bose-einstein condensate. *Phys. Rev. A*, 86:051604, Nov 2012.
- [14] B. Juliá-Díaz, T. Zibold, M. K. Oberthaler, M. Melé-Messeguer, J. Martorell, and A. Polls. Dynamic generation of spin-squeezed states in bosonic Josephson junctions. *Phys. Rev. A*, 86(2):023615, aug 2012.
- [15] Christine Khripkov, Doron Cohen, and Amichay Vardi. Temporal fluctuations in the bosonic Josephson junction as a probe for phase space tomography. *J. Phys. A: Math. Theor.*, 46(16):165304, April 2013.
- [16] Izabella Lovas, József Fortágh, Eugene Demler, and Gergely Zaránd. Entanglement and entropy production in coupled single-mode Bose-Einstein condensates. *Phys. Rev. A*, 96(2):023615, August 2017.
- [17] Khan W. Mahmud, Heidi Perry, and William P. Reinhardt. Quantum phase-space picture of Bose-Einstein condensates in a double well. *Phys. Rev. A*, 71(2):023615, feb 2005.
- [18] R. Mathew and E. Tiesinga. Phase-space mixing in dynamically unstable, integrable few-mode quantum systems. *Phys. Rev. A*, 96(1):013604, July 2017.
- [19] A. Micheli, D. Jaksch, J. I. Cirac, and P. Zoller. Many-particle entanglement in two-component Bose-Einstein condensates. *Phys. Rev. A*, 67(1):013607, jan 2003.
- [20] Takashi Mori. Classical ergodicity and quantum eigenstate thermalization: Analysis in fully connected ising ferromagnets. *Phys. Rev. E*, 96:012134, Jul 2017.
- [21] W. Muessel, H. Strobel, D. Linnemann, D. B. Hume, and M. K. Oberthaler. Scalable Spin Squeezing for Quantum-Enhanced Magnetometry with Bose-Einstein Condensates. *Phys. Rev. Lett.*, 113(10):103004, sep 2014.
- [22] Rahul Nandkishore and David A. Huse. Many-Body Localization and Thermalization in Quantum Statistical Mechanics. *Annual Review of Condensed Matter Physics*, 6(1):15–38, 2015.

- [23] Luca Pezzè, Augusto Smerzi, Markus K. Oberthaler, Roman Schmied, and Philipp Treutlein. Quantum metrology with nonclassical states of atomic ensembles. *Rev. Mod. Phys.*, 90:035005, Sep 2018.
- [24] Anatoli Polkovnikov. Phase space representation of quantum dynamics. pages 1–92, 2009.
- [25] S. Raghavan, A. Smerzi, S. Fantoni, and S. R. Shenoy. Coherent oscillations between two weakly coupled Bose-Einstein condensates: Josephson effects, oscillations, and macroscopic quantum self-trapping. *Phys. Rev. A*, 59(1):620–633, jan 1999.
- [26] Max F Riedel, Pascal Böhi, Yun Li, Theodor W. Hänsch, Alice Sinatra, and Philipp Treutlein. Atom-chip-based generation of entanglement for quantum metrology. *Nature*, 464(7292):1170–1173, 2010.
- [27] G. Rosi, L. Cacciapuoti, F. Sorrentino, M. Menchetti, M. Prevedelli, and G. M. Tino. Measurement of the Gravity-Field Curvature by Atom Interferometry. *Phys. Rev. Lett.*, 114(1):013001, jan 2015.
- [28] Angelo Russomanno, Fernando Iemini, Marcello Dalmonte, and Rosario Fazio. Floquet time crystal in the Lipkin-Meshkov-Glick model. *Phys. Rev. B*, 95(21):214307, June 2017.
- [29] Helmut Strobel, Wolfgang Muessel, Daniel Linnemann, Tilman Zibold, David B. Hume, Luca Pezzè, Augusto Smerzi, and Markus K. Oberthaler. Fisher information and entanglement of non-Gaussian spin states. *Science*, 345(6195):424–427, 2014.
- [30] J. Zhang, P. W. Hess, A. Kyprianidis, P. Becker, A. Lee, J. Smith, G. Pagano, I.-D. Potirniche, A. C. Potter, A. Vishwanath, N. Y. Yao, and C. Monroe. Observation of a discrete time crystal. *Nature*, 543(7644):217–220, Mar 2017. Letter.
- [31] Tilman Zibold, Eike Nicklas, Christian Gross, and Markus K. Oberthaler. Classical Bifurcation at the Transition from Rabi to Josephson Dynamics. *Phys. Rev. Lett.*, 105(20):204101, nov 2010.

Chapter 7

Exploring many-body localization in quantum systems coupled to an environment via Wegner-Wilson flows

7.1 Abstract

Inspired by recent experiments on many-body localized systems coupled to an environment, we apply a Flow Equation method to study the problem of a disorder chain of spinless fermions, coupled via density-density interactions to a second clean chain of spinless fermions. In particular, we focus on the conditions for the onset of a many-body localized phase in the clean sector of our model by proximity to the dirty one. We find that a many-

body localization proximity effect in the clean component is established when the density of dirty fermions exceeds a threshold value. From the flow equation method we find that, similar to many-body localization in a single chain, the many-body localization proximity effect is also described by an extensive set of local integrals of motion. Furthermore, by tuning the geometry of the inter-chain couplings, we show that the dynamics of the model is ruled, on intermediate time scales, by an emergent set of quasi-conserved charges. emergent integrals of motion.

7.2 Introduction

The advent of cold gas experiments [6] has revitalized interest in fundamental questions of quantum thermodynamics in isolated many-body systems. One of the most intriguing avenues of research is the quest for non-ergodic phases of quantum matter. Examples range from integrable models [13, 8] to quantum scars [57] and include the prominent example of ergodicity breaking by strong disorder: many-body localization (MBL) [40, 1]

MBL has been the subject of intense research activity in the last ten years; seminal works have studied the problem both in a perturbation treatment [2, 5, 21] and with numerical methods [42, 65, 41], establishing that a localized phase, which exhibits absence of diffusion on long time scales, can survive the presence of many body interactions. Interest in many-body localisation results from its rich phenomenology: unusual dynamical responses [29, 18], a novel pattern of quantum entanglement [4, 17, 28, 63, 15], the possibility to host new types of order without equilibrium counterpart [23, 45, 60, 59], and connections to the notion of quantum integrability [4, 53, 22, 49, 9, 16, 43]. MBL systems

possess an extensive set of quasi-local integrals of motion, conserved by the unitary dynamics, and preventing full thermalization. Such local degrees of freedom (called localized bits or l-bits) can be constructed via a sequence of local unitary transformations starting from a free Anderson insulator, and represents a form of quantum integrability robust to perturbations. This property is at the basis of a mathematical proof of the existence of the MBL phase for one-dimensional spin lattice systems with short-range interactions [25].

MBL is nowadays investigated in experiments with cold gases [52, 7, 10, 48] and superconducting qubits [50]. The advent of MBL in experimental platforms poses naturally the question of its robustness to the coupling with an external environment [39, 38]. A bath is expected to provide sufficient energy and phase-space to facilitate the hopping in an otherwise localized system [19, 3, 14, 30, 35, 11, 32, 46, 31]. On the other hand, a recent experiment [33] suggests that the clean 'environment' needs to reach a comparatively large density of particles with respect to the dirty MBL system in order to act as a thermodynamic environment and induce ergodic behavior. In order to render the problem treatable, the coupling between a quantum many body system and a bath is usually assumed weak. The complementary regime, however, presents an even more interesting scenario: when the back-action on the bath is strong, and the bath and system are of comparable size, the 'clean' bath could localize by proximity to the dirty system – a phenomenon called 'MBL proximity effect' [37, 24, 34].

Previous work has substantiated the existence of the 'MBL' proximity effect' via perturbative treatments [37, 34] and exact numerics on small system sizes [24], while to the best of our knowledge there has been no attempt at constructing integrals-of-motion,

or an *l-bit* Hamiltonian, for 'MBL proximity' induced phases. Therefore, in this work we investigate the possibility of such a construction by use of the Wegner-Wilson flow equation method [26]. Similar to renormalization group approaches to the MBL problem[61, 47, 12, 55, 64, 20], the Wegner-Wilson flow equation method[26] constructs a set flow equations implementing infinitesimal stepwise diagonalization of the many-body Hamiltonian. When both the clean and dirty components of the system localize, these equations describe a unitary transformation, in both clean and dirty components, to an *l-bit* Hamiltonian which is diagonal in an extensive set of local conserved charges. By focusing on this regime, one can make an ansatz of the *l-bit* Hamiltonian that only includes a few relevant many-body terms. Thus, in addition to being able to study regimes of strong system-bath coupling, the flow equation method is also able to access system's sizes beyond those treatable in exact diagonalization, when disorder is sufficiently strong.

This approach allows us to establish the existence of the MBL proximity effect, and its consistency with a diagonal *l-bit* Hamiltonian of local conserved charges, in a wide range of parameters. Of particular note, we identify a regime for the MBL proximity effect complementary to the one explored in the experiment of Ref. [33]: above a certain critical density the dirty system acts effectively as a source of disorder and induces an MBL phase into the clean component. We also focus on novel physical regimes occurring when the geometry of the system-bath coupling is modified. Specifically, we consider the case of a dirty chain of fermions, coupled every $\delta > 1$ sites, to the clean one (see Fig. 7.6); the dirty chain acts as a distribution of impurities placed every δ sites, cutting the clean chain into a sequence of emergent integrals of motions. These conserved charges lead to non-

ergodic dynamics on intermediate time scales but are destroyed when interactions between conserved charges becomes effective. At these longer time scales, instead, the dynamics cross over from non-ergodic behavior to thermal behavior.

7.2.1 Structure of the paper

We begin in section 7.3 with a review of the Wegner-Wilson flow Equation technique for a single chain and discuss how such a technique provides access to local conserved charges and an *l-bit* Hamiltonian. Then, in section 7.4, we generalize the approach for the two-chain problem and detail how to identify the parameter space where the MBL proximity effect is reliably described by an *l-bit* Hamiltonian. In section 7.5, we present the numerical solution to the flow equations in the case of two chains of equal length. Here, we demonstrate the stability of the MBL proximity effect, construct a qualitative phase diagram and present the numerically computed *l-bit* couplings. In section 7.6, we describe in greater detail the truncations made by the two-chain *l-bit* ansatz and sketch the derivation of the differential equations defining the FE unitary transformation. In section 7.7, we apply the method developed in the first sections to a novel geometry for the system-bath coupling, and discuss a novel relaxation process. We conclude with a quick overview on relevant experiments and possible future directions in section 7.8.

7.3 Flow Equation Approach For a Single Chain

The key idea of the FE approach is to introduce a family of unitary transformations, $U(l)$, parameterised by a 'renormalization group' scale, l , and generated by the

anti-hermitian operator, $\eta(l)$, via the relation, $U(l) = T_l \exp(\int \eta(l) dl)$. The fixed point of the FE procedure in the $l \rightarrow \infty$ limit, is a diagonal Hamiltonian with dressed couplings. Operators, $O(l)$, flow according to the equation $\frac{dO}{dl} = [\eta(l), O(l)]$. A customary procedure for constructing $\eta(l)$ is to first separate the Hamiltonian into its diagonal, $H_0(l)$, and off-diagonal, $V(l)$ parts. Then, the generator is constructed as $\eta(l) \equiv [H_0(l), V(l)]$ which guarantees vanishing off-diagonal terms at the fixed point, $l \rightarrow \infty$ [62]. Typically, the solution of an interacting quantum many-body system via the FE approach would require a broad set of variational parameters keeping track of the nested hierarchies of multi-particles correlations.

However, in the case of MBL systems, a guiding insight in fixing the variational ansatz for the flow equations comes from the l-bit picture [44, 56], which provides a method to numerically solve the flow in an efficient way: only the first leading terms describing pairwise interactions between the *l-bits* are retained, while higher order effects are truncated and discarded. This represents an excellent description as long as the system is strongly localized. Given this ansatz for $H(l)$, the flow of the couplings is readily given by the solution of $\frac{dH}{dl} = [\eta(l), H(l)]$. In other words, the flow brings the Hamiltonian of a single disordered fermionic wire (for instance, H_d in Eq. (7.2)) into an effectively diagonal one at the fixed point

$$\mathcal{H}(\infty) = \sum_i h_i(\infty) n_i + \sum_{i,j} \Delta_{ij}(\infty) n_i n_j. \quad (7.1)$$

This, in turn, shows that the FE method effectively brings the Hamiltonian into an l-bit basis, with couplings between the integrals-of-motion that decay in space as $\Delta_{ij}(\infty)_{ij} \propto \exp(-|i-j|/\xi)$. The values of $h_i(\infty)$ and $\Delta_{ij}(\infty)$ depend on the specific disorder realization.

Therefore, to consider disorder averaged quantities, the flow equations must be computed independently for each disorder realization.

In addition to extracting the conserved charges and l-bit Hamiltonian in Eq. 7.1, the FE method can be used to approximate a crossover region from the MBL phase to a delocalized phase [56]. This region is identified with the parameter space where truncation error proliferates. These errors indicate the departure from an MBL phase because they indicate that the true unitary transformation must contain correlations between local degrees of freedom that are not captured by the ansatz. Since the growth of correlation between local degrees of freedom is suggestive of delocalization, the proliferation of truncation error is also indicative of a breakdown of the MBL phase. In order to measure the truncation error, one calculates the so-called 'second invariant' [56, 36], a quantity conserved by the exact unitary transformation. Since the truncation breaks the unitarity of the flow, the truncation error is controlled by changes in second invariant.

By setting a small threshold for the change in the second invariant, a tight bound on the MBL phase region can be identified with the parameter space where the truncation yields error within the threshold. Such analysis performed on the single chain led gives a phase boundary consistent with exact diagonalization [56]. We discuss the second invariant in detail as it pertains to the MBL proximity effect in section 7.4.3.

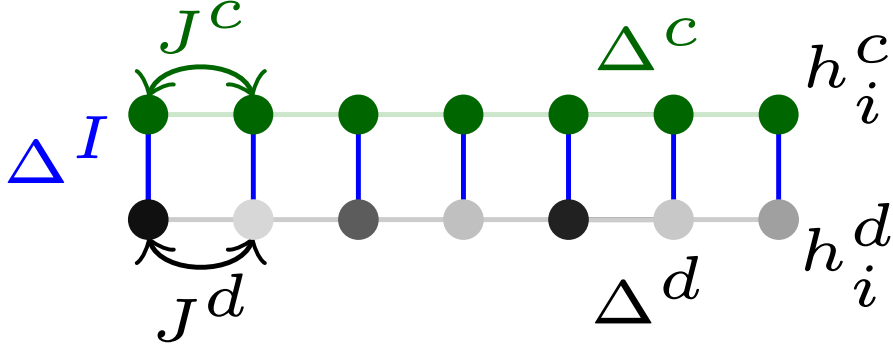


Figure 7.1: Cartoon of the model described by the Hamiltonian (7.2). The MBL sector (bottom wire) acts as a source of disorder to induce localization in the clean component (green sites). The two systems are coupled site by site via inter-chain couplings (blue lines) of strength Δ^I .

7.4 Flow Equation Approach For Two Chains

7.4.1 The model

In this section we extend the flow equation method to the system depicted in Fig. 7.1. We consider a system composed of two wires of interacting spinless fermions coupled via an inter-chain density-density interaction of strength Δ^I . The Hamiltonian of the system reads (cf. Fig. 7.1)

$$\begin{aligned}
 H &= H^c + H^d + H^I & (7.2) \\
 H^c &= \sum_{ij} J_{ij}^c c_i^\dagger c_j + \sum_{ij} \Delta_{ij}^c n_i^c n_j^c \\
 H^d &= \sum_{ij} J_{ij}^d d_i^\dagger d_j + \sum_{ij} \Delta_{ij}^d n_i^d n_j^d + \sum_k h_i n_i^d \\
 H^I &= \sum_{ij} \Delta_{ij}^I n_i^c n_j^d
 \end{aligned}$$

where the sums run over N_s dirty sites in the Hamiltonian H^d and over $\delta \times N_s$ clean sites (with $\delta \geq 1$) in the Hamiltonian H^c . The fields, h_i , are drawn from a uniform box

distribution of variance W , i.e. $h_i \in [-W, W]$; for sufficiently large W , the chain of fermions, d_i , will be in the MBL phase, and will act on the clean fermionic component, c_i , as a source of disorder. Even though we study a microscopic model that contains inhomogeneities only in the on-site fields, h_i , we write couplings in Eq. (7.2) with a generic dependence on spatial indices to emphasize that, already at the first steps of integration of the flow equations, couplings can inherit an explicit spatial dependence from the disordered fields.

7.4.2 Two Chain Ansatz

Similar to the FE method for single chain MBL phase, the FE method for the two-chain problem aims to construct a unitary transformation, $U(l) = T_l \exp(\int \eta(l) dl)$, that diagonalizes the Hamiltonian Eq. 7.2. In both cases, an exact calculation would require keeping track of $O(2^{N_s^2})$ matrix elements and is therefore numerically unfeasible. As for the MBL phase in the single chain problem, the local nature of the MBL proximity effect allows one to circumvent this issue via an ansatz for the Hamiltonian, $H(l) = U^\dagger(l) H U(l)$ at scale l of the unitary transform. The ansatz we use for the two-chain problem is $H(l) = H_0(l) + V(l)$ where

$$\begin{aligned}
H_0(l) &= H^c(l) + H^d(l) + H^I(l) & (7.3) \\
H^c(l) &= \sum_{ij} \Delta_{ij}^c(l) : n_i^c n_j^c : + \sum_k \bar{h}_k^c(l) : n_k^c : \\
H^d(l) &= \sum_{ij} \Delta_{ij}^d(l) : n_i^d n_j^d : + \sum_k \bar{h}_k^d(l) : n_k^d : \\
H^I(l) &= \sum_{ij} \Delta_{ij}^I(l) : n_i^c n_j^d : \\
V(l) &= \sum_{ij} J_{ij}^c(l) : c_i^\dagger c_j : + \sum_{ij} J_{ij}^d(l) : d_i^\dagger d_j,
\end{aligned}$$

: A : denotes Wick Ordering [26], the fields $\bar{h}^{c(d)}$ are given below in Eqs. (7.4), and we will use the convention that the first index in Δ_{ij}^I refers to the clean chain. In the limit $l \rightarrow \infty$, $V(l) \rightarrow 0$, the fixed-point Hamiltonian, $H(l \rightarrow \infty)$, is diagonal in an extensive set of l-bits localized on both the clean and dirty sites.

As customary for flow equation methods [56, 26], we use Wick-ordered operators, : A :, with respect to a reference state ρ . Wick ordering reduces errors in the truncated Hamiltonian $H(l)$ for the Hilbert space spanned by few particle excitations on top of the reference state ρ [26]. As done by Thomson *et al.* in [56], we choose a reference state with zero entanglement between local degrees of freedom. This extreme locality condition serves a starting point for the FE unitary transformation to capture the entanglement of the MBL proximity effect. The state ρ employed is a Boltzmann distribution, $\rho = \frac{1}{Z} e^{-\Theta H_w}$, with inverse temperature Θ , chemical potentials fixing particle densities $\langle n^d \rangle$ and $\langle n^c \rangle$, and Hamiltonian $H_w = \sum_i (h_i^d - \mu^d) n_i^d - \mu^c n_i^c$. The choice of this state allows to easily control energy density, Θ , and particle density distribution, $\langle n^d \rangle$.

By Wick-ordering the Hamiltonian at flow time $l = 0$, the clean and dirty chains pick up effective fields, given by

$$\begin{aligned}\bar{h}_i^d &= h_i^d + 2 \sum_j \Delta_{ij}^d \langle n_j^d \rangle + \sum_j \Delta_{ji}^I \langle n_j^c \rangle, \\ \bar{h}_i^c &= 2 \sum_j \Delta_{ij}^c \langle n_j^c \rangle + \sum_j \Delta_{ij}^I \langle n_j^d \rangle;\end{aligned}\tag{7.4}$$

where their distribution depends on the dirty chain density, $\langle n^d \rangle$, the inter-chain coupling Δ^I , and the disorder, W , in the dirty chain. From the expressions of the fields in Eq. (7.4), it is natural to observe that, if the dirty chain is sufficiently disordered and the inter-chain

couplings are sizable, the clean chain will localize as result of the effective disordered field, \bar{h}_i^c .

Note, the ansatz in (7.3) has the notational symmetry

$$\begin{aligned} c &\leftrightarrow d \\ \Delta_{ij}^I &\leftrightarrow \Delta_{ji}^I. \end{aligned} \tag{7.5}$$

By exploiting this symmetry, it is easy to derive flow equations for operators of the dirty chain from those of the clean one, and vice-versa. We will refer to terms (or equations) produced by such symmetry transformations using the notion $C \leftrightarrow D$ in the following.

7.4.3 Second Invariant and Phase Boundary Analysis

From the ansatz in Eq. 7.3, we can derive the FE generator $\eta(l) = [H_0(l), V(l)]$. Then, by matching the truncated terms in the Heisenberg equation of motion, $dH(l)/dl = [\eta(l), H(l)]$, the *truncated flow equations*, a set of first order differential equations for the couplings,

$$\Gamma = \{\Delta_{ij}(l)^{c(d,I)}, J_{ij}^{c(d)}(l), \bar{h}_k^{c(d)}(l)\}, \tag{7.6}$$

can be derived

$$\frac{d\Gamma}{dl} = \beta(\Gamma), \tag{7.7}$$

where the β functions are order three polynomials in the couplings Γ and their forms discussed in detail in section 7.6. An l -bit Hamiltonian, $H(l \rightarrow \infty)$, is retrieved by numerically evolving Eq. 7.7 with initial conditions given by the bare physical couplings, evolved for large l . Deep in the MBL proximity effect phase, these differential equations describe a

unitary transform to a diagonal Hamiltonian $H(l \rightarrow \infty)$, and the unitary transformation described by $\eta(l)$, along with the Hamiltonian $H(\infty)$, can be used to predict dynamics of relevant observables [56, 26, 58].

When either chain delocalizes, the *l-bit Hamiltonian* ansatz will be an insufficient representation of the effective Hamiltonian, and the couplings $\eta(l)$ and $H(\infty)$ cannot be used to make predictions. To detect the breakdown of the MBL proximity effect ansatz, we monitor the extent that the truncated flow equations, Eq. 7.7, break unitarity. For this goal, we employ a quantity known as the second invariant, see, for instance, previous work in Refs. [56, 36]. The second invariant is the $p = 2$ case of a class of many invariants of the FE unitary transformation given by $\text{Tr}[H(l)^p]$. It is particularly easy to calculate for the spin systems and is given by:

$$\text{Tr} [H(l)^2] = \sum_{ij,r=c,d} (J_{ij}^r)^2 + (\Delta_{ij}^r)^2 + \Delta_{ij}^I + \sum_{k,r=c,d} (\bar{h}_k^r)^2. \quad (7.8)$$

We can then quantify the error made by a given ansatz by computing the change in the second invariant:

$$\delta I = 2 \frac{\text{Tr} [H(l = \infty)^2] - \text{Tr} [H(l = 0)^2]}{\text{Tr} [H(l = \infty)^2] + \text{Tr} [H(l = 0)^2]}. \quad (7.9)$$

If δI is small, then the MBL proximity effect ansatz in Eq. 7.3, and the approximations discussed above, represent a reliable description and can be used to compute dynamics and the local conserved l-bits. On the other hand, when δI is large, we have an indication that the ansatz fails and that we cannot use the generator $\eta(l)$ nor the l-bit Hamiltonian $H(\infty)$ to make predictions.

By identifying a threshold for δI , we can find a tight bound on the phase boundary for the MBL proximity effect. While the choice of threshold is arbitrary, by making it

stringently small, one can ensure that below that threshold the MBL proximity effect is properly captured. On the other hand, if it is above that threshold, we must conclude that 1) the system is delocalized or, 2) it is localized in an operator basis not captured by the ansatz. If 2) is the case, then, the operator basis must contain either non-local operators or operators capturing stronger correlations. In either case, a reasonably chosen threshold should yield an approximate boundary for the MBL proximity effect.

7.5 Numerical Results For Equal Length Chains

7.5.1 MBL Proximity Effect

In this section, we present numerical results, for system sizes unattainable with exact diagonalization, that establish the validity of using an l-bit Hamiltonian to describe the MBL proximity effect. . We study the model introduced in section 7.4.1 for two equal length chains of length $N_s = 24$ (48 total sites), and numerically solve the differential flow equations, Eq. 7.7. For this model, the initial couplings are given as:

$$\begin{aligned}
\Gamma(l=0) &= & (7.10) \\
\left\{ \begin{aligned}
\Delta_{ij}^{c(d)}(l=0) &= \Delta^{c(d)}(\delta_{i,j+1} + \delta_{j,i+1}), \\
\Delta_{ij}^I(l=0) &= \Delta^I \delta_{ij}, \\
J_{ij}^{c(d)}(l=0) &= J^{c(d)}(\delta_{i,j+1} + \delta_{j,i+1}), \\
\bar{h}_i^d(l=0) &= h_i^d + 2 \sum_j \Delta_{ij}^d(l=0) \langle n_j^d \rangle + \sum_j \Delta_{ji}^I(l=0) \langle n_j^c \rangle, \\
\bar{h}_i^c(l=0) &= 2 \sum_j \Delta_{ij}^c(l=0) \langle n_j^c \rangle + \sum_j \Delta_{ij}^I(l=0) \langle n_j^d \rangle \}
\end{aligned} \right.
\end{aligned}$$

where h_i^d is drawn from a box distribution in the interval, $[-W, W]$, and clean and dirty number densities are computed with respect to the Wick ordering reference state, $\langle n_k^{c(d)} \rangle = \text{Tr}[\rho n_k^{c(d)}]$. We focus on the limit in which the disordered system would be strongly localized and vary the inter-chain coupling, clean chain hopping strength and reference state parameters. Therefore, we set $W = 60$, $\Delta^d = J^d = 0.1$, and vary the parameters Δ^I , J^c , $\langle n^d \rangle(\mu^d)$ and Θ . By setting $\Delta^c = 0.1$, we also focus our attention to the limit in which the clean intra-chain coupling is weak.

The exact form of the truncated flow-equations are given in 7.9.3 and discussed in section 7.6. For a fixed configuration of h_i^d , the truncated flow equations are numerically evolved for a sufficiently long flow-time such that 1) the hoppings, $J_{ij}^{c(d)}(l)$, have become sufficiently small, and 2) there is no appreciable change in the flow of any other coupling. The evolution is repeated for different random instances of h_i^d , and we present the disorder average of the asymptotic ($l \rightarrow \infty$) couplings.

In analogy to a single disordered chain, we define an effective disorder parameter as $W^c = \Delta^I/2J^c$ and work in a limit in which the clean chain is expected to be strongly localized: $\Delta^I = 45$, $J^c = 0.1$, $\Theta = 0.3$ and $\langle n^d \rangle = 0.5$ (i.e. $W^c = 225$). We choose such a strong effective disorder to benchmark the method and isolate the effects of varying different parameters. Solving the numerical flow equations (see 7.9.4 for details on numerical implementation), we find that the density-density couplings, $\Delta_{ij}^{c(d)}$, are exponentially suppressed in $|i - j|$, as it occurs in the applications of the Wegner flow to single disordered chains[44, 56]. In Fig. 7.2a, we show the decay in space of the disorder-averaged, asymptotic, density-density couplings, $\Delta_{ij}^c(l \rightarrow \infty)$, on a logarithmic scale, and they illustrate the

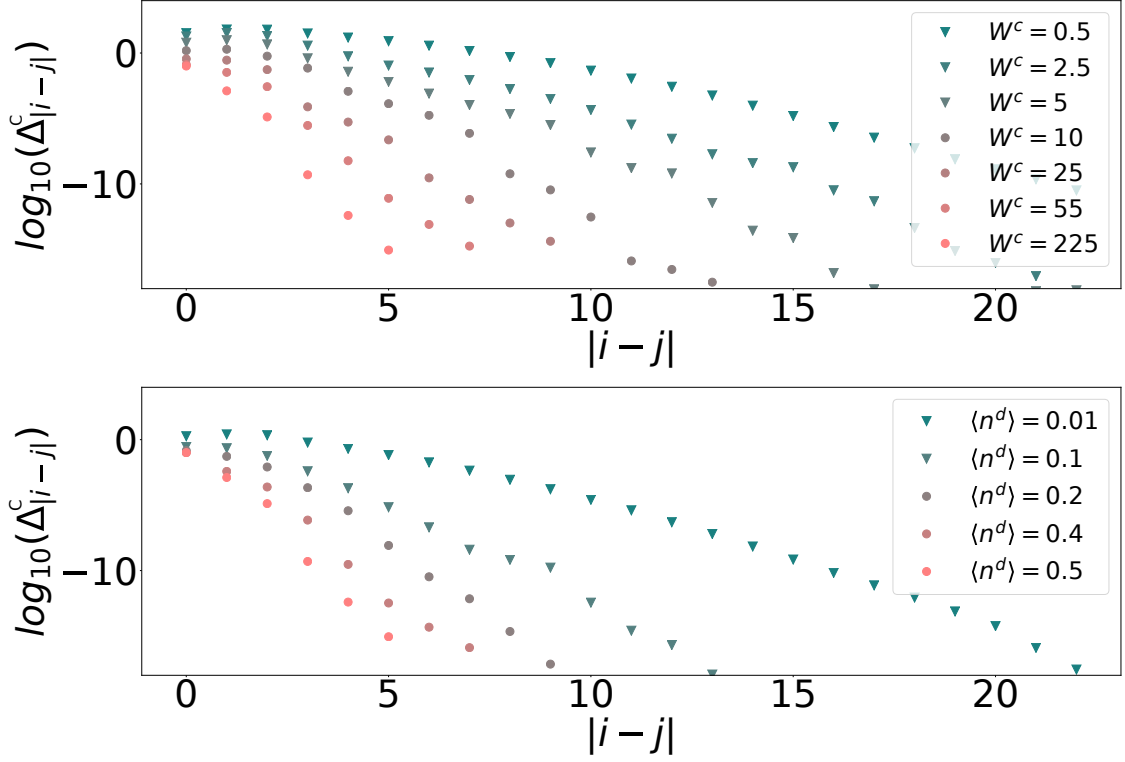


Figure 7.2: Instances of the MBL proximity effect: the plots show, in logarithmic scale, the spatial decay of the couplings between integrals of motion in the clean sector of the system. We display results for parameters which yield both a large and small change in the second invariant, and distinguish them using triangle and circle markers respectively. The results for parameters that yielded a large change in the second invariant (marked with triangles) do not reflect the true l-bit coupling but are displayed to depict how the MBL proximity effect ansatz breaks down. The final clean-chain density-density couplings $\Delta_{|i-j|}^c$ depicted here are averaged over 256 disorder realizations. In the top panel, we plot how the final density-density couplings depend on $W^c = \Delta^I/2J^c$ (J^c fixed) while in the bottom panel we plot their dependence on $\langle n^d \rangle$. In the top panel $\langle n^d \rangle = 0.5$ while in the bottom panel $W^c = 225$ ($\Delta^I = 45$ and $J^c = 0.1$). The remaining Hamiltonian parameters are $W = 60$, $J^d = \Delta^d = 0.1$, $\Delta^c = J^c = 0.1$, $\Theta = 0.3$, and $\langle n^c \rangle = 0.1$. These results are not affected by $\langle n^c \rangle$ since they are uniformly distributed in the reference state ρ and do not have an impact on the disorder of the effective fields.

onset of an MBL phase in the clean chain. As discussed below, the change in the second invariant for these parameters is small for the majority of disorder realizations and thus confirms the validity of the MBL proximity effect ansatz employed in this ansatz.

The top panel of Fig. 7.2 shows that by decreasing the inter-chain coupling, the final density-density couplings between the l -bits present a slower decay in space suggesting a departure from the MBL proximity phase. The effective disorder parameter, $W^c = \Delta^I/2J^c$, can be used to compare with the disordered Heisenberg chain (a prototype of MBL), which shows a transition at $W/J = 4$. By considering the second-invariant, we find that the truncation produces minimal error for $W^c \gtrsim 10$ and the MBL proximity is well-established. Note that while we benchmark the method with $W^c = 225$, we found the MBL proximity effect to be consistent with a l -bit ansatz for a reasonable effective disorder strength of $W^c > 10$. While for $W^c \lesssim 10$, the error grows with decreasing W^c and suggests that somewhere in the range $W^c \lesssim 10$ the system undergoes a transition to a delocalized phase. In this limit, we have found that the final density-density couplings for the dirty-chain, $\tilde{\Delta}_{ij}^d$, are still strongly localized while those for the clean-chain are not. This suggests that the source of truncation error is due to the clean-chain becoming delocalized.

The bottom panel of Fig. 7.2b is one of the most interesting results of our analysis. Here, different curves correspond to different fermionic densities of the dirty component in Hamiltonian (7.2), with fixed total fermionic density, $\langle n_{tot} \rangle \equiv \langle n^d \rangle + \langle n^c \rangle = 0.5$. This variation of $\langle n^d \rangle$ follows a similar logic to the experiment in Ref. [51], where a complementary situation has been considered (the melting of an MBL phase by coupling to a clean bath). There, the delocalizing effect of the clean component on the dirty component has been experimentally observed in a mixture of collisionally coupled ultra-cold bosons in a two-dimensional optical lattice. Above a certain critical density of bosons, the clean component acts as an ergodic bath and destroys the features of the MBL phase in the dirty sector.

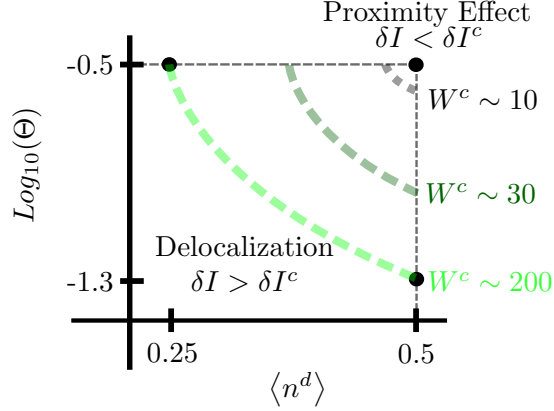


Figure 7.3: Regions of parameter space where the MBL proximity effect is established. We focus on an instance of a strongly localized dirty chain ($W = 60$, $\Delta^d = J^d = 0.1$), and on a clean chain with $\Delta^c = J^c = 0.1$. The thin, dashed, black lines delimit a square where the parameters Θ and $\langle n^d \rangle$ have been varied in our numerical trials. The region of parameters space in which the MBL Proximity Effect is established is determined by the region where the second invariant is below a specified threshold $\delta I < \delta I^c = 0.1$. In the figure, we draw three different thick, curved, dashed lines, corresponding to the values of the parameter $W^c = 10$ (gray), 30 (dark green), 200 (bright green). These lines mark the values of Θ and $\langle n^d \rangle$ where we expect the second invariant to equal the threshold value $\delta I(W^c, \langle n^d \rangle, \Theta) = \delta I^c$, and above which we expect $\delta I(W^c, \langle n^d \rangle, \Theta) < \delta I^c$. This analysis demonstrates that the MBL Proximity Effect can be observed for the smaller $\langle n^d \rangle$ and Θ when W^c is larger.

Complementary, we find that a critical density of dirty fermions is required in order for the MBL systems to be sufficiently large to entail localization in the clean component. The analysis of the second invariant identifies that the MBL proximity effect is well-established for $\langle n^d \rangle > 0.25$, and suggests that for some value of $\langle n^d \rangle$ less than 0.25 , the clean chain goes through a delocalization transition. It is important to note that we are unable to identify with accuracy the point of transition since our ansatz fails close to it (see also Ref. [56]).

We have also studied the effect of increasing the clean-chain hopping, J^c and the energy density parameterised by the inverse temperature, Θ of the reference state ρ . We found that the l-bit ansatz, Eq. 7.3, becomes inefficient for large clean chain hopping, $J^c >$

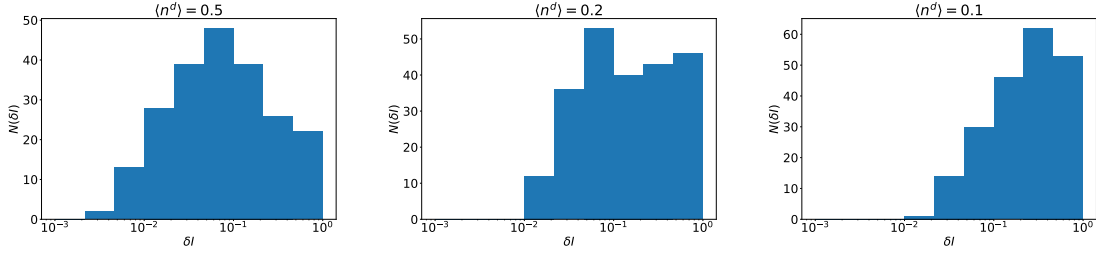


Figure 7.4: Histograms of the change in the second invariant as $\langle n^d \rangle$ is varied across the transition ($W = 60$, $J^d = \Delta^d = 0.1$, $\Delta^c = J^c = 0.1$, $\Theta = 0.3$, and $\langle n^c \rangle = 0.1$).

0.5, and at large energy densities, $\Theta < 0.05$. In these limits, the clean chain couplings, Δ_{ij}^c , begin to delocalize while the dirty chain couplings, Δ_{ij}^d , are unaffected. This dependence of localization on the hopping strength is similar to a standard MBL system (the system delocalizes at strong hopping), while the dependence on the energy density of the dirty chain is novel. At low energy density, the dirty chain charge distribution in the reference state, $\langle n_k^d \rangle$, and, correspondingly, the effective clean disorder fields, \bar{h}_k^c , are strongly disordered, and the clean chain localizes. While for high energy density, the reference state has no disorder in the dirty chain densities, and the clean chain delocalizes. Extrapolating these results, we expect that the localization of the clean chain depends on the disorder of the dirty chain charge distribution.

We summarize our results in the portrait of Fig. 7.3, which shows the region of the Θ - $\langle n^d \rangle$ plane where the change in the second invariant is expected to be smaller than our chosen threshold $\delta I^c = 0.1$. In addition to depicting the trends just discussed, it shows that the dirty chain densities of the reference state must be strongly disorder to compensate for a weaker inter-chain coupling Δ^I (W^c), in order to induce MBL in the clean sector.

7.5.2 Second Invariant

Above we used the second invariant, δI , to identify when the truncated flow equations preserve the unitarity of the exact Wegner-Wilson flow and to justify the MBL-proximity effect ansatz, Eq. 7.3. Because the flow equation transformation depends on the disorder realization, δI varies from sample-to-sample. The left panel of Fig. 7.4 shows the distribution of δI for a disorder strength where the MBL-proximity effect ansatz is valid for the majority of disorder realizations, while the right panel shows the distribution for a system where the same ansatz fails for the majority of disorder realizations. In order to distinguish between these two situations, we can compute the median of δI (we don't use the mean because it is artificially biased by the few trials with large second invariant weight). As shown in Fig. 7.5, the median δI shows that the MBL proximity effect ansatz becomes worse for decreasing Δ^I and $\langle n^D \rangle$. Here we see that for $W^c > 10$ and for $\langle n^d \rangle > 0.25$, the median second invariant is small and relatively unaffected by changes in W^c and $\langle n^d \rangle$, demonstrating the validity of the MBL proximity effect ansatz. While for small $W^c < 10$ and small $\langle n^d \rangle < 0.25$, the error made by truncation is large and suggestive of a transition to delocalization somewhere below these values. The large sample-to-sample variation of the second invariant suggests the presence of regions not captured by the MBL proximity effect ansatz, and future work may attempt to reduce the second invariant for these disorder realizations by improving the ansatz.

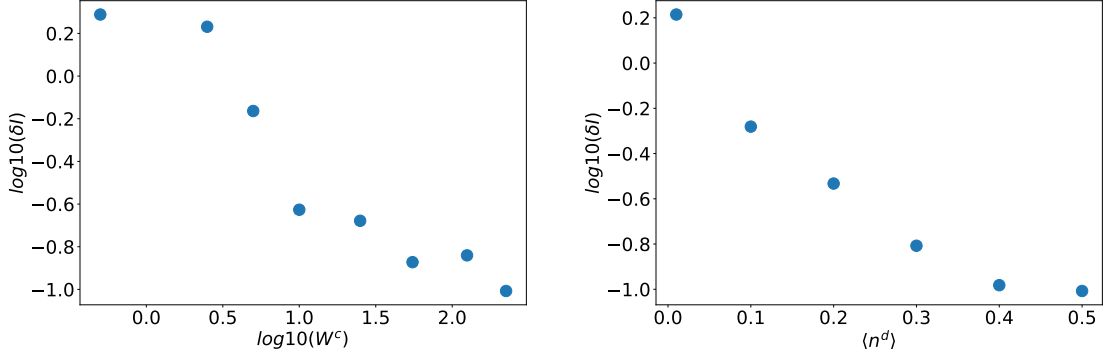


Figure 7.5: Median change in the second invariant as a function of $\langle n^d \rangle$ (right) and of W^c (left). W^c is plotted on a log scale since it varies over two orders of magnitude. The remaining Hamiltonian parameters are $\Delta^I = 45$ ($W^c = 225$), $J^d = \Delta^d = 0.1$, $\Delta^c = J^c = 0.1$, $\Theta = 0.3$, and $\langle n^c \rangle = 0.1$. In the left panel $\langle n^d \rangle = 0.5$, while, on the right panel, $W^c = 225$ ($\Delta^I = 45$).

7.6 Truncated Flow Equations and Truncation Error

7.6.1 Truncation Error for the MBL Proximity Effect Ansatz

In the previous section we have shown that the *l-bit ansatz*, Eq. 7.3, accurately describes the MBL proximity effect phase and that the truncated flow equations, Eq. 7.7, imply a small error in approximating the exact flow equation unitary transformation, $U(l)$. In this section, we analyze the approximations made by the truncation in Eq. 7.3, and we discuss, in section 7.6.2, the physics of the terms contributing to the truncated flow equations. The first type of operators dropped are the $n > 2$ body terms such as the three body scattering, $: c_i^\dagger c_j^\dagger c_k^\dagger c_i c_j c_k :.$ As long as the integrals of motion do not contain $n > 3$ body operators with significant weight, then truncating these terms will not produce significant error in the integrals of motion, FE unitary transformation, or *l-bit* Hamiltonian. This is confirmed by the small second invariant presented in the previous section. It is important to note that, despite dropping these n -body scattering operators, the ansatz

does not ignore all n -body correlations: while at scale l the few body terms are not $n > 3$ body correlated in the transformed basis, they do contain $n > 3$ correlations in the physical basis (i.e. $U(l) : c_i^\dagger(l)c_j(l) : U^\dagger(l)$ contains n -body operators).

In addition to dropping $n > 3$ body scattering operators from the *l-bit ansatz*, we drop the off-diagonal terms $: n_k^c c_i^\dagger c_j :$ and $: c_k^\dagger c_l c_i^\dagger c_j :$, which we will call correlated hopping and full two-body scattering (F.S) respectively. Including these terms requires keeping track of $O(N_s^3)$ ($O(N_s^4)$ for F.S.) number of couplings and significantly increases the computational resources required. To identify the error produced by dropping these terms we highlight how they are produced as the flow evolves.

We identify 7 distinct operators by the 7 sums shown in Eq 7.3:

$$\begin{aligned}
H^c(l) &= \hat{\Delta}^c + \hat{h}^c & (7.11) \\
H^d(l) &= \hat{\Delta}^d + \hat{h}^d, \\
H^I(l) &= \hat{\Delta}^I \\
V(l) &= \hat{J}^c + \hat{J}^d
\end{aligned}$$

where, $\hat{h}^c = \sum_k \bar{h}_k^c : n_k^c :$, $\hat{J}^c = \sum_{ij} J_{ij}^c(l) : c_i^\dagger c_j :$, etc. (see 7.9.1 for explicit forms for the remaining operators). We then classify contributions to the generator by the type of off-diagonal operator appearing in the commutator: $\eta = [H_0, J] = \eta_h + \eta_\Delta + \eta_I$ where:

$$\begin{aligned}
\eta_h &= [\hat{J}^c, \hat{h}^c] + [\hat{J}^d, \hat{h}^d] & (7.12) \\
\eta_\Delta &= [\hat{J}^c, \hat{\Delta}^c] + [\hat{J}^d, \hat{\Delta}^d] \\
\eta_I &= [\hat{J}^c + \hat{J}^d, \hat{\Delta}^I].
\end{aligned}$$

These commutators are computed using rules for Wick ordering [26] and yield:

$$\begin{aligned}
\eta_h &= \sum_{ij} F_{ij} : c_i^\dagger c_j : + C \leftrightarrow D \\
\eta_\Delta &= \sum_{ijk} \Gamma_{ij|k}^c : n_k^c c_i^\dagger c_j : + F_{ij}^\Delta : c_i^\dagger c_j : + C \leftrightarrow D \\
\eta_I &= \sum_{ijk} \Gamma_{ij|k}^I : n_k^d c_i^\dagger c_j : + C \leftrightarrow D \\
&,
\end{aligned} \tag{7.13}$$

where the coefficients Γ and F are given in 7.9.2. The form of the generators are either a hopping operator, $: c_j^\dagger c_i :$, a correlated hopping (C.H) operator, $: n_k^c c_i^\dagger c_j :$ or an inter-chain correlated hopping (C.H.I) operator $: n_k^c c_i^\dagger c_j :$. It will be important for quantifying the error implied by our truncation to notice that each of the generators is proportional to J_{ij}^c or J_{ij}^d . In addition, the η_Δ generator is also proportional to $\Delta_{ij}^{c(d)}$.

Taking the commutator $[\eta(l), H_0(l) + V(l)]$ yields contributions contained both inside and outside the ansatz, $H(l)$, and are summarized in Table. 7.1. The operators outside the ansatz are dropped and produce errors proportional to their coefficients. We expect the majority of these coefficients to be small because we study the MBL proximity effect in a limit that the couplings $\Delta_{ij}^{c(d)}$ and $J_{ij}^{c(d)}$ are initialized as small. For example, operators appearing in the second row and second and third column appear with coefficients that are proportional to the square of these couplings, and since they are initialized with $\Delta^{c(d)} = J^{c(d)} = 0.1$ the error made is $O(0.01)$.

Besides these operators, there are still a few that appear linear in a small coupling and could produce larger error. For example, $[\eta^I, \hat{h}^c]$ produces an inter-chain correlated hopping operator, $n_k c_i^\dagger c_j$, which has a coefficient proportional to $J^c(\Delta^I)^2$. While this off-diagonal operator is not small, it is initialized to zero and only affects the diagonal

	$\hat{h}^{c(d)}$	$\hat{j}^{c(d)}$	$\hat{\Delta}^{c(d)}$	$\hat{\Delta}^I$
η_h	$J_{ij}^{c(d)}$	$J_{ij}^{c(d)}, h_i^{c(d)}$	C.H. $J_{ij}^{c(d)}$	C.H.I
η_Δ	C.H.	$\Delta_{i,j}^{c(d)}, \text{C.H.}, \text{F.S.}$ $J_{ij}^{c(d)}, h_i^{c(d)}$	3P C.H. $J_{ij}^{c(d)}$	3P C.H.I
η_I	C.H.I	$\Delta_{i,j}^I, \text{C.H.I.}, \text{F.S.I}$ $J_{ij}^{d(c)}, h_i^{d(c)}$	3P C.H.	3P C.H.I $J_{ij}^{c(d)}$

Table 7.1: This table lists which terms in the commutator $[\eta, H]$ contribute to the beta function $\beta(\Gamma)$ (highlighted in blue) and which are dropped by our ansatz (not highlighted). The rows are labeled by the terms in the sum for the generator $\eta = \eta_h + \eta_\Delta + \eta_I$, and the columns are labeled by the terms in the sum for the Hamiltonian, Eq. 7.11. The notation for the dropped terms is as follows: correlated hopping (C.H.) have a form $n_k^c c_i^\dagger c_j$, inter-chain correlated hopping operators C.H.I. have a form $n_k^d c_i^\dagger c_j$, full scattering terms F.S. have a form $c_i^\dagger c_j^\dagger c_k c_l$, and 3P terms describing three-body and higher particle scattering. The justification for dropping the contributions to $J_{ij}^{c(d)}$ in the third and forth column is discussed in section 7.6.2.

Hamiltonian after commuting with a generator that is also proportional to J^c . Therefore, its effect on the diagonal Hamiltonian will remain small as long as J^c remains small. This is confirmed by the small change in the second invariant presented above.

This completes our analysis of the error produced by the truncation in the Ansatz, Eq. 7.3. In summary, we have discussed how we expect that a small error will be produced in our truncation scheme, as long as $\Delta^{c(d)}$ and $J^{c(d)}$ are initialized to small values. We then referenced results in section 7.5, which demonstrate small truncation error via a small change in the second invariant, to confirm such expectations.

7.6.2 Truncated Flow Equations

In the previous section, we have sketched the derivation of the FE Heisenberg equation of motion, $\frac{dH}{dt} = [\eta(l), H(l)]$, and discussed the error produced by the truncation of the ansatz. In this section we focus on operators in $[\eta(l), H(l)]$ that contribute to the ansatz and truncated flow equations (Eq. 7.7). We first focus on the contribution in first row, first column of table 7.1. For the clean chain it produces a term:

$$[\eta_h, \hat{h}] = \left[[\hat{J}^c, \hat{h}^c], \hat{h}^c \right] + \dots = \quad (7.14)$$

$$-J_{ij}^c (\bar{h}_i^c - \bar{h}_j^c)^2 : c_i^\dagger c_j + \dots$$

and therefore contributes to the evolution of J_{ij}^c :

$$\frac{dJ_{ij}^c}{dl} = -J_{ij}^c (\bar{h}_i^c - \bar{h}_j^c)^2 + \dots \quad (7.15)$$

This is the primary contribution evolving the off diagonal terms to 0, and is responsible for the intuitive physics discussed above. If we ignore the other contributions to dJ_{ij}^c/dl then the evolution of J_{ij} is:

$$J_{ij}^c(l) = J_{ij}^c(l=0)e^{-(\bar{h}_i^c - \bar{h}_j^c)^2 l}. \quad (7.16)$$

Thus, the stronger the disorder in the effective fields \bar{h}_i^c , the faster the off diagonal terms decay.

In addition to producing terms in the β functions that removes the off diagonal couplings J_{ij}^c , the generator η_h renormalizes $\hat{h}^{c(d)}$ and generates off diagonal hoppings $J_{ij}^{c(d)}$ at intermediate scales l of the FE evolution. These terms come from the first row, second column of table. 7.1 and have a characteristic contribution, $[\eta_h, \hat{J}^c] = \left[[\hat{J}^c, \hat{h}^c], \hat{J}^c \right] + \dots$,

which produces contributions to the truncated flow equations as:

$$\begin{aligned}\frac{d\bar{h}_k^c}{dl} &= \sum_i 2(J_{ik}^c)^2(\bar{h}_k^c - \bar{h}_i^c) + \dots \\ \frac{dJ_{ij}^c}{dl} &= -\sum_k J_{ik}^c J_{kj}^c (2\bar{h}_k^c - \bar{h}_i^c - \bar{h}_j^c) + \dots\end{aligned}\tag{7.17}$$

Together with Eq. 7.15, Eq. 7.17 highlights the physics contained in the unitary transformation generated by η_h : The generator η_h is constructed to remove hoppings $J_{ij}^{c(d)}$ that change the energy of the diagonal Hamiltonian, H_0 , due to the effective fields $\bar{h}_k^{c(d)}$. Eq. 7.15 shows that the contribution from the commutator $[\eta_h, \hat{h}^c]$ removes off diagonal couplings, while Eq. 7.17 captures new terms produced by the rotation by η_h .

Similar physics occurs for the generators η_Δ and η_I , which are constructed to remove hoppings that change energy via the density-density interaction. In a strong interacting limit, the exact unitaries produced by these generators will generate a Hamiltonian describing doublon and domain wall propagation[54]. If disorder is also strong, these quasi-particle excitation may also localize, realizing a novel MBL of correlated quasi-particles. Unfortunately, in order to capture these effects, one needs to keep track of computationally demanding correlated hopping operators [54] dropped by our ansatz.

While such considerations offer promising prospects for future work, they also have direct consequences for the contributions we include in the truncated flow equations. Since the generators η_Δ and η_I transform the hopping operators, $\hat{J}^{c(d)}$, into a set of correlated hopping operators that commute with density-density interactions [54], the truncation above yields a transformation which simply removes the hopping operators without producing the correlated hopping operators they transform into. If these correlated hopping operators are responsible for delocalization, then removing them would produce an artificial localiza-

tion. To avoid this false localization, we remove the contribution to $\frac{d}{dl} J_{ij}^{c(d)}$ coming from $[\eta_\Delta, \Delta]$ and $[\eta_I, \Delta^I]$ (respectively, second row, third column; and third row, fourth column; of table 7.1). Ignoring these contributions only produces small error for the same reason dropping the correlated hopping operators produces small error: the error in J_{ij} is proportional to $J_{ij}^{c(d)}$ but its contribution to the l -bit Hamiltonian is $(J_{ij}^{c(d)})^2$. The small error is numerically confirmed by a small second invariant as discussed above.

The remaining contributions from η_Δ and η_I are the ones in the second column of table 7.1 and describe delocalization processes produced by density-density interactions. A characteristic contribution is:

$$[[\hat{J}^c, \hat{\Delta}^c], \hat{J}^c], \quad (7.18)$$

which produce a contribution to the evolution of Δ_{ij}^c as:

$$\frac{d\Delta_{ij}^c}{dl} = 2 \sum_{k \neq i, j, l=i, j} J_{lk}^2 (\Delta_{ij}^c - \Delta_{kl}^c). \quad (7.19)$$

This contribution captures how the truncated flow equations break the unitary character of the FE transform in a delocalized limit. When disorder is small, J_{ij} remains finite longer during the flow equation evolution and Δ_{ij}^c has a longer time to grow according to the contribution in Eq. 7.19. This growth produces larger truncation error because, as discussed in the previous section, truncation error is only small when Δ_{ij}^c is small. This concludes our analysis of the physical content of the contributions to the truncated flow equations. The full set of truncated flow equations used in our numerics are reported in 7.9.3.

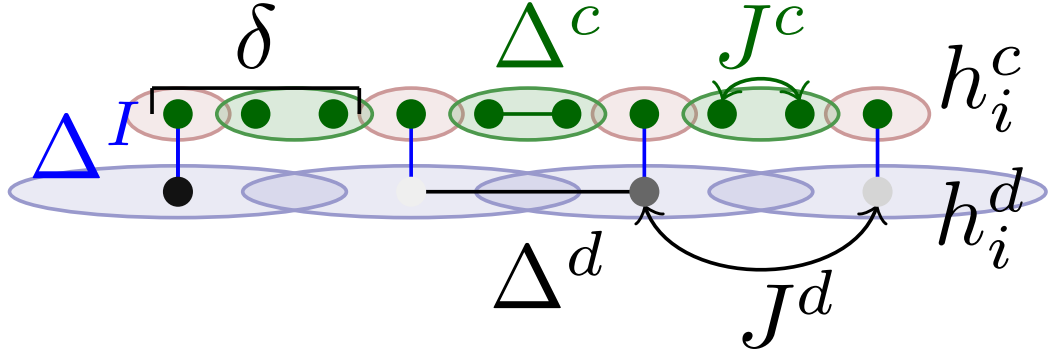


Figure 7.6: The dirty chain couples to the clean chain every $\delta = 3$ sites. The emergent integrals of motion are illustrated with different colors: n_k^d (blue), $n_{f,r=0}^c$ (red) and N_f (green).

7.7 Engineering the geometry of the inter-chain couplings

We now discuss novel effects arising by tuning the coupling geometry. In the geometry of Fig. 7.6 each fermion of the dirty chain is coupled, every δ sites, to a fermion of the clean chain. This new geometry can still be studied using analogous flow equations to those employed above. Since the clean chain is δ times longer than the dirty chain, we can label the dirty chain with $f = 0 \dots N_s - 1$, and conveniently reference the sites of the clean chain ($k = 0 \dots N_s \delta - 1$) with r , using $k = f\delta + r$. f labels the dirty sites, and $r = 0 \dots \delta - 1$ is the number of sites away from the coupled site. We can now explicitly write the initial inter-chain coupling as $\Delta_{f,r,f'} = \Delta^I \delta_{f,f'} \delta_{r,0}$. This leads to an initial clean-chain effective field of $\bar{h}_{f,r}^c = \Delta^I \langle n_f^d \rangle \delta_{r,0}$.

With this important modifications, we can straightforwardly evolve the couplings using the same truncated flow equations discussed in the previous sections. We show evolution of few of them in Fig. 7.7. The right panel of Fig. 7.7 shows the suppression of the

hopping between a coupled site $f, r = 0$ and an uncoupled site $f, r = 1$, while the left panel of Fig. 7.7 shows the hopping between two uncoupled sites, $f, r = 1$ and $f' = f, r = 2$, remaining constant. This is consistent with the expectations given by Eq. 7.16: for a particle to hop on to a coupled site its energy must change by $(\bar{h}_i^c - \bar{h}_j^c) \approx \Delta^I \langle n^d \rangle$, while such a change of energy is not required for a particle hopping between two uncoupled sites.

With the hopping between uncoupled sites remaining constant, Eq. 7.19 predicts the divergence of the associated density-density couplings. This is depicted in the left panel of Fig. 7.7 and explains the failure of the MBL proximity effect ansatz. Instead of modifying the ansatz, we propose to modify the generator, $\eta(l)$ of the unitary transformation. We define a modified generator $\eta' = [H_0, V']$, where we choose V' to only include hoppings to coupled sites:

$$V'(l) = \sum_{f,f'} J_{f,f'}^d d_f^\dagger d_{f'} + \sum_f J_{f,0,f,1}^c (c_{f,0}^\dagger c_{f,1} + h.c.) + J_{f,0,f-1,\delta-1}^c (c_{f,0}^\dagger c_{f-1,\delta-1} + h.c.) \quad (7.20)$$

Using such a generator, one can employ the same ansatz as above, but the transformation now results in a novel fixed point Hamiltonian describing transport between uncoupled sites and conserved charges on coupled and dirty sites ($n_{f,r=0}^c$ and n_f^d respectively). In addition, the new generator produces a next-nearest neighbor hopping across the coupled site (i.e $J_{f,r=\delta-1,f'=f+1,r=1}$). In the proceeding section we derive this hopping rate as $\frac{1}{\tau_n} = [J^c(l=0)]^2 / \bar{h}^c(l=0)$, which in the limit of strong inter-chain coupling, Δ^I , is smaller than the other timescales in the system. In this limit, relaxation occurs in two steps: first, on times scales shorter then τ_n , transport is blocked by the coupled sites, and second, on times scales longer then τ_n , charge is allowed to diffuse across the coupled sites.

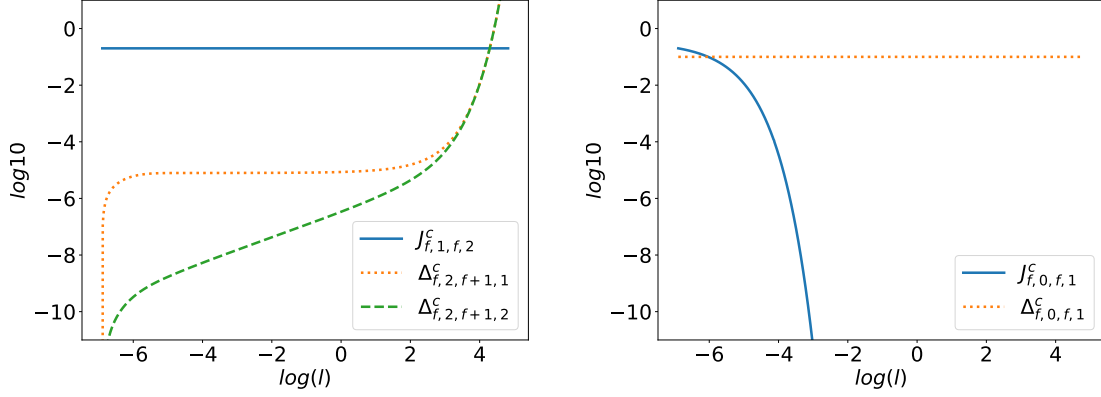


Figure 7.7: The flow of J_{ij}^c and Δ_{ij}^c for the geometry depicted in Fig. 7.6. The left panel shows the flow of couplings on the clean-chain sites that are not coupled to the dirty chain. It shows an unsuppressed hopping and diverging density-density coupling at long flow time l . The right panel shows the flow of couplings on the clean chain sites that involve a site coupled to the dirty chain. It shows that the hopping onto the coupled site, $r = 0$ (for any f), are suppressed and the density-density coupling involving a coupled site, remains constant instead. This calculation has been performed using an unmodified generator $\eta = [H_0, V]$; in order to remove the divergences in $\Delta_{f,r,f',r'}^c$, we modify the generator to $\eta = [H_0, V']$, with V' given in Eq. 7.20.

In the first step, when $\tau \lesssim \tau_n$, the system relaxes to a state in which the charge on the bunches of uncoupled sites, $N_f = \sum_{r=1}^{\delta} n_{f,r}^c$, is conserved. While on longer times, charge on the uncoupled sites can fully relax via unconstrained transport. In the following two sections, we further investigate this novel behavior by first, in section 7.7.1, deriving the time, τ_n , separating the two relaxation steps, and second, in section 7.7.2, investigating and deriving the Hamiltonian that governs short time relaxation.

7.7.1 Separation of Time Scales

To derive an estimate of the next-nearest neighbor hopping rate, we first assume $\Delta \ll W$. This guarantees that the flow of the dirty chain reaches a steady state before

there are significant changes in the clean one. We can then treat the clean chain as a single chain with an effective field $\bar{h}_{f,r}$. We write the new generator as

$$\eta' = \sum_f \eta_f \quad (7.21)$$

where

$$\eta_f = -J\bar{h}_{f,0}(c_{f-1,\delta-1}^\dagger c_{f,0} - h.c) + J\bar{h}_{f,0}(c_{f,0}^\dagger c_{f,1} - h.c), \quad (7.22)$$

with J the strength of the hopping on to the coupled site. The first term in η_f will suppress hopping between the coupled site and its left neighbor, while the second term will enforce the same on the right neighbor. Since $[\eta_f, \eta_{f'}] = 0$ for $\delta > 2$, we can focus on a single coupled site and its neighbor.

We will label the coupled site with 0 and its left and right neighbor sites with -1 and $+1$. The hopping and effective field couplings will then flow as

$$\begin{aligned} \frac{d\bar{h}_{\pm 1}}{dl} &= -2J^2\bar{h}_0, \\ \frac{d\bar{h}_0}{dl} &= 2J^2\bar{h}_{+1} + 2J^2\bar{h}_{-1}, \\ \frac{dJ}{dl} &= -J\bar{h}_0^2, \\ \frac{dJ_2}{dl} &= 2J^2\bar{h}_0, \end{aligned} \quad (7.23)$$

where J_2 is the magnitude of the next-nearest neighbor hopping, $J_2(l) = J_{f,r=\delta-1,f'=f+1,r=1}(l)$.

The flow of these couplings do not depend on the flow of the density-density coupling and can thus be solved independently. We use the assumption that $J \ll \bar{h}$ and note that the flow of J is much faster than the flow of the other couplings. Thus, assuming \bar{h} constant, we can approximate the flow of $J(l)$ as

$$J(l) = J(l=0)e^{-\bar{h}_0^2 l}. \quad (7.24)$$

Approximating \bar{h}_0 as constant, we find

$$J_2(l) = -\frac{J^2}{\bar{h}_0}(1 - e^{-2\bar{h}_0^2 l}). \quad (7.25)$$

Thus, $\tau_n = \frac{\bar{h}_0}{J^2}$ is the characteristic time when relaxation crosses over to full transport and eventually to thermalization. A meaningful separation of time scales therefore requires $\bar{h}_0 \gg J^2$. In the following section we will discuss the form of the effective Hamiltonian describing the first stage of relaxation.

7.7.2 Effective Hamiltonian at intermediate times: $\tau \lesssim \tau_n$

As discussed above, relaxation in the novel geometry with large inter-chain coupling, occurs in two stages: first, during intermediate times, the model relaxes to a state in which the clean-charge distribution on the uncoupled clusters is approximately conserved, while, on longer times, the clean-charge relaxes to a homogeneous distribution. The Hamiltonian describing the first relaxation process is obtained by dropping the next nearest neighbor hoppings from the Hamiltonian, $H(l \rightarrow \infty)$. This Hamiltonian, has 3 types of conserved charges as depicted in Fig. 7.6: the first type, n_k^d , are the conserved charges on the dirty chain, the second type $n_{f,r=0}^c$ are the conserved charge on the coupled site and $N_f = \sum_{r=1}^{\delta} n_{f,r}^c$ is the total conserved charge on an uncoupled cluster. For $\delta > 2$ these charges do not determine the dynamics of the charge distribution within an uncoupled cluster, and we must consider the interplay between the intra-cluster tunneling and inter-cluster density-density coupling.

There are two possibilities for such interplay: the density-density coupling between two neighboring sets of uncoupled sites is smaller than J_2 , or it is larger:

- In the first case, the density-density coupling can be accurately dropped from the intermediate time effective Hamiltonian. This leads to each set of uncoupled sites, labeled by f , evolving completely independently on intermediate times. The dynamics can be described as the evolution of an effective spin, $\vec{L}_f = \{L_x, L_y, L_z\}$, of size

$$|\vec{L}_f| = \frac{1}{2} \binom{\delta - 1}{N_f} + \frac{1}{2}. \quad (7.26)$$

The local map between the N_f fermions on $\delta - 1$ sites and the spin can be performed by identifying the basis states labeled by the eigenvalues of $n_{f,r \neq 0}^c$ with the basis states labeled by the eigenvalues of L_f^z . Operators that are polynomial in the densities will then be mapped to operators that are polynomial in L_z . The remaining terms in the Hamiltonian describe tunneling within a set of uncoupled sites with all the same f . They describe transition between the L_f^z basis states and are thus described by polynomials in L_f^x and L_f^y .

- In the second case, when the density-density interaction between the uncoupled cluster is relevant, the local emergent spins will be coupled. Since the hopping operators at a site f commute with those at a site f' , a Jordan-Wigner string is not required to correctly reproduce spin statistics, and the coupled Hamiltonian can be written as:

$$H(\{\bar{n}_f^d\}, \{\bar{n}_{f,r=0}^c\}, \{\bar{N}_f\}) = \sum_{ff'} F(L_f^z, L_{f'}^z) + \sum_f R_f(L_f^x, L_f^z, L_f^y), \quad (7.27)$$

where the function F depends on the intra-chain coupling, Δ^c , and the function R depends on $h_k^c, J_{ij}^c, \Delta_{ij}^I$, and Δ_{ij}^c . In general, if the dirty chain or coupled sites have

a disordered distribution of charges, the local operators, R_f , in the Hamiltonian will be disordered too. The issue of whether the system is fully localized on intermediate times, will then depend on any integrability present in this intermediate time Hamiltonian, or on the impact of disorder on R_f .

In the first case, the intermediate time Hamiltonian can be diagonalized by independently diagonalizing the Hamiltonian of effective spins L_f . In the second case, when the spins are coupled, further analysis is required to explore the dynamics at intermediate times and will be the subject of Sec. 7.7.4.

7.7.3 Density-Density interactions between uncoupled clusters

To determine if the effective spins \vec{L}_f are coupled or not, we compute the magnitude of the density-density interaction between two uncoupled clusters. We focus again on one coupled site, labeled by $r = 0$, and its neighboring sites, labeled by $r = \pm 1$ (for any f). The flow equation equations for the density-density couplings then becomes

$$\begin{aligned}\frac{d\Delta_{-1,1}^c}{dl} &= 2J^2(\Delta_{-1,1}^c - \Delta_{0,1}^c) + 2J^2(\Delta_{-1,1}^c - \Delta_{0,-1}^c), \\ \frac{d\Delta_{0,1}^c}{dl} &= -2J^2(\Delta_{-1,1}^c - \Delta_{0,1}^c), \\ \frac{d\Delta_{-1,0}^c}{dl} &= -2J^2(\Delta_{-1,1}^c - \Delta_{0,-1}^c).\end{aligned}\tag{7.28}$$

These coupled differential equations describe a rotation in a three-dimensional space at an instantaneous rate $2J(l)^2$. Given that $\Delta_{-1,1}^c(l=0) = 0$, the system (7.28) can be solved and yields

$$\Delta_{-1,1}^c(l) = \Delta_{0,1}^c(l=0) \left[1 - e^{\int_0^l dl' 2J^2(l')} \right],\tag{7.29}$$

where:

$$\int_0^l dl' 2J^2(l') = \frac{J^2(l=0)}{\bar{h}_0^2(l=0)}(1 - e^{-2h_0^2 l}). \quad (7.30)$$

Therefore, the amplitude of the rotation in such three-dimensional parameter space is small in J^2/\bar{h}_0^2 .

We are now in place to discuss which of the two possibilities discussed in the previous section is realized. If $J_2(l = \infty) \ll \Delta_{-1,1}(l = \infty)$, then an interacting Hamiltonian describes the intermediate time dynamics while, if the inequality is not satisfied, a non-interacting spin chain will describes the intermediate time dynamics. Given the assumption $J \ll h$, this inequality simplifies to $h \ll \Delta$. Thus, for the approximation made in ansatz Hamiltonian above, we must choose $h > \Delta$ and conclude that the intermediate time Hamiltonian describes a set of independently evolving spins.

Alternatively, we could assume the bare Hamiltonian has a next-nearest neighbor coupling of the order $\Delta_{-1,1}(l = 0) \approx \Delta_{0,1} < h$. In this case the rotation in Δ_{ij}^c space, described by Eq. 7.28, would still be of a small angle, but away from an initial vector with $\Delta_{-1,1}(l = 0)$ already greater than $J_2(l = \infty)$. Intermediate time dynamics would then be described by a set of coupled emergent spins of size $|\vec{L}_f|$.

7.7.4 Explicit form of the Hamiltonian for $\delta = 3$

As an example, we now can consider the $\delta = 3$ case in which there are two uncoupled sites for each dirty site f , and discuss the effective Hamiltonian governing the intermediate time dynamics. The local Hilbert space for these two sites is 4 dimensional

and the basis vectors can be labeled by the different ways in which 2 sites may be occupied with particles (the label '1' indicates an occupied site)

$$\left\{ |00\rangle, |01\rangle, |10\rangle, |11\rangle \right\}, \quad (7.31)$$

The local Hamiltonian on these sites reflects the block diagonal structure enforced by the conserved charges:

$$\begin{bmatrix} 0 & 0 & 0 & 0 \\ 0 & \tilde{\Delta}^L & J_{f2,f1}^c(l) & 0 \\ 0 & J_{f1,f2}^c(l) & \tilde{\Delta}^R & 0 \\ 0 & 0 & 0 & \tilde{\Delta}^{R+L} \end{bmatrix}, \quad (7.32)$$

where $\tilde{\Delta}^L, \tilde{\Delta}^R$, and $\tilde{\Delta}^{R+L}$ are functions linear in the operators n_i^d and $n_{f' \neq f}^c$ and depend on the intra and inter-chain couplings, and fields h^c , at the flow time $l = \infty$. For $\delta = 3$ the conserved charge N_f has eigenvalues 0, 1, and 2 that correspond to the three blocks in Eq. 7.32. This block structure can be represented by two trivial spin-zero subspaces and one spin-half subspace.

We consider the case that $N_f = 1$ for each f , so that the local Hilbert space for the block of interest will be spin-half. The mapping to spin-halves can be performed via

$$\begin{aligned} L_f^z &= \frac{\hat{n}_{f,1} - \hat{n}_{f,2}}{2} \\ L_f^x &= \frac{c_{f,1}^\dagger c_{f,2} + h.c.}{2}, \end{aligned} \quad (7.33)$$

and the constraint $\frac{1}{2} = \frac{\hat{n}_{f,1} + \hat{n}_{f,2}}{2}$.

We write down the Hamiltonian at the flow time $l = \infty$ as follows:

$$\begin{aligned}
H &= \sum H_f + \sum_{f,f'} \sum_{r,r'=1,2} \Delta_{f,r,f',r'}^c n_{f,r}^c n_{f',r'}^c \\
H_f &= \sum_i \xi_{f,i} n_{f,i} + J_f^{un}(l) [c_{f,1}^\dagger c_{f,2} + c_{f,2}^\dagger c_{f,1}] \\
&\quad + \Delta_{f,1,f,2}^c n_{f,2}^c n_{f,1}^c,
\end{aligned} \tag{7.34}$$

where $\xi_{f,i}$ is an effective field that depends on the bare fields at flow time l , the couplings Δ_{ij}^c and Δ_{ij}^I , and the eigenvalues of the conserved charges, \bar{n}_f^d and $\bar{n}_{f,r=0}^c$:

$$\xi_{f,i} = \bar{h}_{f,i}^c(l) + \sum_f \Delta_{f,i,f'}^I(l) \bar{n}_{f'}^d + \sum_f \Delta_{f,i,f',0}^c(l) \bar{n}_{f',0}^c.$$

Applying the mapping (7.33) we get the spin Hamiltonian:

$$H = \sum_f h_f^z L_f^z + h_f^x L_f^x + \sum_{ff'} \Omega_{f,f'} L_f^z L_{f'}^z + C \tag{7.35}$$

with

$$\begin{aligned}
h_f^x &= 2J_f^{un}(l) \\
h_f^z &= \xi_{f,1} - \xi_{f,2} \\
\Omega_{f,f'} &= \Delta_{f,1,f',1}^C + \Delta_{f,2,f',2}^C - \Delta_{f,1,f',2}^C - \Delta_{f,2,f',1}^C.
\end{aligned} \tag{7.36}$$

Here, we explicitly see how the spins are coupled by the next-nearest neighbor density-density couplings. Thus, if the local spins are coupled at a strength less than the next-nearest neighbor hopping, $|\Omega_{f,f'}| < J_2$, the intermediate time dynamics describes independent spins rotating around an axis in the $x-z$ plane. While, if $|\Omega_{f,f'}| > J_2$, we have to consider the interacting spin problem to understand the intermediate time dynamics.

If there is no disorder in the dirty and coupled site charge distributions, the z component of the local field, h_f^z will be null and the translationally-invariant emergent spin-model will be a transverse field Ising model. This Hamiltonian is integrable via the Jordan-Wigner transformation:

$$\begin{aligned} L_f^x &\rightarrow n_f^a - 1/2 \\ L_f^z L_{f+1}^z &\rightarrow (a_f^\dagger - a_f)(a_{f+1} + a_{f+1}^\dagger), \end{aligned} \quad (7.37)$$

which produces an exactly solvable single particle Hamiltonian in Jordan-Wigner fermions. Taking $\Omega_{f,f'} = \Omega\delta_{f',f+1}$, this single particle Hamiltonian is given as

$$\sum_f h^x n_f^a + \Omega(a_f^\dagger a_{f+1} + h.c.) + \Omega(a_f^\dagger a_{f+1}^\dagger + h.c.), \quad (7.38)$$

which can be brought in diagonal form $\sum_q \omega_q n_q$ in momentum space via a Bogolyubov rotation, where n_q is the occupation of the mode q and $\omega_q = \sqrt{1 + 2\frac{\Omega}{h} \cos(q) + \frac{\Omega^2}{h^2}}$. We therefore, in addition to the local conserved charges, $n_{f,0}^c$, n_f^d , N_F , have the conserved momentum space modes n_q . The non ergodic behavior during intermediate times after the initial relaxation period and before τ_n will display a mixture of local conserved charges, and extended conserved charges, n_q .

If there is disorder in the dirty and coupled site charge distributions, the z -components of the local field, h_z , given in Eq. 7.36 will be finite. The Jordan-Wigner transformation of L_f^z will introduce a many body operator via the Jordan-Wigner string, $L_f^z = a_f^\dagger e^{i\pi \sum_{f'} N_{f'}} + h.c.$, and the new fermion Hamiltonian will no longer be diagonalizable via a single particle transformation. In this case, n_q will no longer be conserved and, if h^z is weak compared to the transverse field h_f^x , only the local conserved charges, $n_{f,0}^c$, n_f^d ,

and N_F , will survive after the first relaxation period. If the disorder field, h_f^z , dominates over the transverse field, h_f^x , the effective Hamiltonian, Eq. 7.35, will many body localize and develop a set of local conserved charges L_f^z . We have confirmed these expectations via exact diagonalization of the intermediate time Hamiltonian and by studying the level spacing statistics for $N_s = 8$ and $\delta N_s = 24$ ($\delta = 3$).

7.8 Conclusions

A natural direction we are currently scrutinizing consists in extending the FE method to capture physics akin to the one reported in the experiment of Ref. [51]. However, in order to have a quantitative understanding of the delocalizing impact of the clean environment on the disordered chain, one should assume that the clean chain is delocalized, and therefore extend the ansatz employed here to treat Hamiltonian diagonal in momentum space. It could also be of interest to employ the FE method to study a broader variety of MBL proximity effects. An appealing direction consists in studying a point-like, local coupling, between an MBL segment of interacting, disordered fermions and a clean one. This would pave way to understand the effect of the 'intrusion' of the localized system into the clean one, or viceversa, explore how an MBL system can act as an 'insulator' with respect to the clean segment. Analysis in this direction is ongoing [27].

Acknowledgments

S. P. K. and J. M. are indebted with S. J. Thomson and M. Schiro for helpful and clarifying discussions and exchanges on the flow equation method for MBL systems.

We thank I. Bloch for inspiring discussions. JM is supported by the European Union’s Horizon 2020 research and innovation programme under the Marie Skłodowska-Curie grant agreement No 745608 (QUAKE4PRELIMAT). This research was supported in part by the National Science Foundation under Grant No. NSF PHY-1748958.

This work is based upon work supported in part (RN, JM) by the Air Force office of Scientific Research under award number FA 9550-17-1-0183.

S. P. K. acknowledges financial support from the UC Office of the President through the UC Laboratory Fees Research Program, Award Number LGF-17- 476883

Los Alamos National Laboratory is managed by Triad National Security, LLC, for the National Nuclear Security Administration of the U.S. Department of Energy under Contract No. 89233218CNA000001

7.9 Appendix

7.9.1 Notation

We define the onsite fields before Wick ordering as $h_k^{c(d)}$, and after Wick ordering, the effective fields are defined with a bar: $\bar{h}_k^{c(d)}$. We define the couplings with unaccented variables with subscripts indexing sites: $\Delta_{ij}^I, \Delta_{ij}^{c(d)}, J_{ij}^{c(d)}$. The dependence on the scale l of the flow equations is often made implicit in expressions: $\Delta_{ij}^I(l) \rightarrow \Delta_{ij}^I$. For Δ_{ij}^I the first index i labels the clean chain sites and the second the dirty chain sites. The spatial dependence of the couplings defines geometry and the magnitude is set by the parameters $\Delta^{I(c,d)}, J^{c(d)}$. In addition to these parameters, the dirty chain fields are randomly selected from a box

distribution, $[-W, W]$, and the Wick ordered reference state is set by: $\langle n^d \rangle = \frac{1}{N_s} \sum_k \langle n_k^d \rangle$

and temperature Θ , where $\langle n_k^d \rangle = \text{Tr}[\rho n_k^d]$

We work with a set of unaccented operators: $U, H, H_0, V, H^c, H^d, H^I, \eta_h, \eta_\Delta, \eta_I, c_k, d_k, n_k^c, n_k^d$ and $\vec{L}_f = \{L_f^x, L_f^y, L_f^z\}$. We also define a set of operators accented with a hat as:

$$\begin{aligned}
\hat{J}^c &= \sum_{ij} J_{ij}^c : c_i^\dagger c_j : \\
\hat{J}^d &= \sum_{ij} J_{ij}^d : d_i^\dagger d_j : \\
\hat{\Delta}^c &= \sum_{ij} \Delta_{ij}^c : n_i^c n_j^c : \\
\hat{\Delta}^d &= \sum_{ij} \Delta_{ij}^d : n_i^d n_j^d : \\
\hat{\Delta}^I &= \sum_{ij} \Delta_{ij}^I : n_i^c n_j^d : \\
\hat{h}^c &= \sum_k \bar{h}_k^c : n_k^c : \\
\hat{h}^d &= \sum_k \bar{h}_k^d : n_k^d : .
\end{aligned} \tag{7.39}$$

Finally, we also defined a symmetry operation, $C \leftrightarrow D$, that swaps the superscripts c and d of the couplings and operators and swaps the site indices of the inter-chain coupling:

$$\begin{aligned}
c &\leftrightarrow d \\
\Delta_{ij}^I &\leftrightarrow \Delta_{ji}^I
\end{aligned} \tag{7.40}$$

7.9.2 Flow Equation Generators

In the main text we defined 3 different generators the commutator: $\eta = [H_0, J] = \eta_h + \eta_\Delta + \eta_I$ where:

$$\eta_h = [\hat{J}^c, \hat{h}^c] + [\hat{J}^d, \hat{h}^d] \quad (7.41)$$

$$\eta_\Delta = [\hat{J}^c, \hat{\Delta}^c] + [\hat{J}^d, \hat{\Delta}^d]$$

$$\eta_I = [\hat{J}^c + \hat{J}^d, \hat{\Delta}^I].$$

and presented their form as:

$$\eta_h = \sum_{ij} F_{ij}^c : c_i^\dagger c_j : + C \leftrightarrow D \quad (7.42)$$

$$\eta_\Delta = \sum_{ijk} \Gamma_{ij|k}^c : n_k^c c_i^\dagger c_j : + F_{ij}^{\Delta^c} : c_i^\dagger c_j : + C \leftrightarrow D$$

$$\eta_I = \sum_{ijk} \Gamma_{ij|k}^I : n_k^d c_i^\dagger c_j : + C \leftrightarrow D.$$

The coefficients F and Γ are given as:

$$F_{ij}^c = J_{ij}^c (\bar{h}_i^c - \bar{h}_j^c) \quad (7.43)$$

$$F_{ij}^{\Delta^c} = 2J_{ij}^c \Delta_{ij}^c (n_i - n_j)$$

and

$$\Gamma_{ijk}^c = 2J_{ij}^c (\Delta_{ik}^c - \Delta_{jk}^c) \quad (7.44)$$

$$\Gamma_{ijk}^I = J_{ij}^c (\Delta_{ik}^I - \Delta_{jk}^I).$$

While the coefficient for the dirty chain can be obtained from the symmetry operation $C \leftrightarrow D$.

7.9.3 The Flow Equations.

The full set of flow equations used in the numerics discussed in the main text is given as:

$$\begin{aligned}
\frac{d\bar{h}_k^c}{dl} &= \sum_i 2(J_{ik}^c)^2 [(\bar{h}_k^c - \bar{h}_i^c) + 2\Delta_{ik}^c(n_k^c - n_i^c)] \\
&\quad + 2 \sum_{ij} (J_{ij}^c)^2 (\Delta_{kj}^c - \Delta_{ki}^c)(n_j^c - n_i^c) + \sum_{ij} (J_{ij}^d)^2 (\Delta_{kj}^I - \Delta_{ki}^I)(n_j^d - n_i^d) \\
\frac{dJ_{ij}^c}{dl} &= -J_{ij}^c(\bar{h}_i^c - \bar{h}_j^c)^2 - 2J_{ij}^c \Delta_{ij}^c (n_i^c - n_j^c)(\bar{h}_i^c - \bar{h}_j^c) - \sum_k J_{ik}^c J_{kj}^c (2\bar{h}_k^c - \bar{h}_i^c - \bar{h}_j^c) \\
&\quad - 2 \sum_k J_{ik}^c J_{kj}^c [\Delta_{ij}^c (n_i^c + n_j^c - 2n_k^c) + 2\Delta_{ki}^c (n_k^c - n_i^c) + 2\Delta_{kj}^c (n_k^c - n_j^c)] \\
&\quad - J_{ij}^c (\bar{h}_i^c - \bar{h}_j^c)(n_i^c - n_j^c)(\Delta_{ij}^c + \Delta_{ji}^c) \\
\frac{d\Delta_{ij}^c}{dl} &= 2 \sum_{k \neq i, j, l=i, j} (J_{lk}^c)^2 (\Delta_{ij}^c - \Delta_{kl}^c) \\
\frac{d\Delta_{ij}^I}{dl} &= 2 \sum_k (J_{jk}^d)^2 (\Delta_{ij}^I - \Delta_{ik}^I) + 2 \sum_k (J_{ik}^c)^2 (\Delta_{ij}^I - \Delta_{kj}^I)
\end{aligned} \tag{7.45}$$

where $n_k^{c(d)} = \langle n_k^{c(d)} \rangle$ are the densities of the Wick ordered reference state, and the flow for the dirty couplings can be found using the symmetry operation $C \leftrightarrow D$.

7.9.4 Numerical Details

The flow equations are numerically solved using an adaptive step 4^{th} order Runge-Kutta. We work with a clean chain length of 24 sites $\delta N_s = 24$ for a total of 48 sites (32 sites when $\delta = 3$). We control the adaptive step by attempting around 800 discrete Runge-Kutta

steps on a log scale from $l = 10^{-3}$ to $l = 10^2$. The adaptive step usually requires additional steps to reach the desired accuracy result in an average number of steps of around 3000.

Since our results requires an accuracy for the couplings on a scale absolute scale 10^{-15} , we devoted careful attention to numerical errors. We found that numerical errors were due to floating-point errors for numbers close to 0 during both the first step and at latter steps. Numerical errors in the first step of a Runge-Kutta approximation are well-known, while the ones at later steps are due to the form of the flow equations. These long time error are due to contributions like $\sum_k J_{ik}J_{kj}(h_i + h_j - h_k)$ that could easily flip sign and cause numerical noise at longer times during the flow.

To manage these errors, we initialized the hoppings J_{ij} for $i \neq j \pm 1$ to ϵ_1 and treated a hopping with $|J_{ij}| < \epsilon_2$ as exactly 0. Choosing $\epsilon_2 > 10^{-15}$ and $\epsilon_1 > \epsilon_2$ was sufficient to reduce floating-point errors to the desired accuracy 10^{-15} . We tested the validity of these numerical approximations by varying ϵ_1 and ϵ_2 and observing no change in the flow.

Bibliography

- [1] D. Abanin, E. Altman, I. Bloch, and M. Serbyn. *arXiv:1804.11065*, 2018.
- [2] Boris L. Altshuler, Yuval Gefen, Alex Kamenev, and Leonid S. Levitov. Quasiparticle lifetime in a finite system: A non-perturbative approach. *Phys. Rev. Lett.*, 78:2803–2806, Apr 1997.
- [3] Sumilan Banerjee and Ehud Altman. Variable-range hopping through marginally localized phonons. *Phys. Rev. Lett.*, 116:116601, Mar 2016.
- [4] Jens H. Bardarson, Frank Pollmann, and Joel E. Moore. Unbounded growth of entanglement in models of many-body localization. *Phys. Rev. Lett.*, 109:017202, Jul 2012.
- [5] D.M. Basko, I.L. Aleiner, and B.L. Altshuler. Metal–insulator transition in a weakly interacting many-electron system with localized single-particle states. *Annals of Physics*, 321(5):1126 – 1205, 2006.
- [6] Immanuel Bloch, Jean Dalibard, and Wilhelm Zwerger. Many-body physics with ultracold gases. *Rev. Mod. Phys.*, 80:885–964, Jul 2008.
- [7] Pranjal Bordia, Henrik P. Lüschen, Sean S. Hodgman, Michael Schreiber, Immanuel Bloch, and Ulrich Schneider. Coupling identical one-dimensional many-body localized systems. *Phys. Rev. Lett.*, 116:140401, Apr 2016.
- [8] P. Calabrese and J. Cardy. Quantum quenches in 1+1 dimensional conformal field theories. *J. Stat. Mech.* 064003, 2016.
- [9] A. Chandran, A. Pal, C. R. Laumann, and A. Scardicchio. *ArXiv e-prints: 1605.00655*, 2016.
- [10] J. Choi, S. Hild, J. Zeiher, P. Schauss, A. Rubio-Abadal, T. Yefsah, V. Khemani, D. A. Huse, I. Bloch, and C. Gross. Exploring the many-body localization transition in two dimensions. *Science*, 352(6293):1547–1552, June 2016.
- [11] W. De Roeck and F. Huveneers. *arXiv 1608.01815*, 2016.

- [12] Philipp T. Dumitrescu, Romain Vasseur, and Andrew C. Potter. Scaling theory of entanglement at the many-body localization transition. *Phys. Rev. Lett.*, 119:110604, Sep 2017.
- [13] Fabian H L Essler and Maurizio Fagotti. Quench dynamics and relaxation in isolated integrable quantum spin chains. *J. Stat. Mech.*, 2016(6):064002, 2016.
- [14] Mark H Fischer, Mykola Maksymenko, and Ehud Altman. Dynamics of a many-body-localized system coupled to a bath. *Phys. Rev. Lett.*, 116:160401, Apr 2016.
- [15] S D Geraedts, N Regnault, and R M Nandkishore. Characterizing the many-body localization transition using the entanglement spectrum. *New Journal of Physics*, 19(11):113021, 2017.
- [16] Scott D. Geraedts, R. N. Bhatt, and Rahul Nandkishore. Emergent local integrals of motion without a complete set of localized eigenstates. *Phys. Rev. B*, 95:064204, Feb 2017.
- [17] Scott D. Geraedts, Rahul Nandkishore, and Nicolas Regnault. Many-body localization and thermalization: Insights from the entanglement spectrum. *Phys. Rev. B*, 93:174202, May 2016.
- [18] Sarang Gopalakrishnan, Markus Müller, Vedika Khemani, Michael Knap, Eugene Demler, and David A. Huse. Low-frequency conductivity in many-body localized systems. *Phys. Rev. B*, 92:104202, Sep 2015.
- [19] Sarang Gopalakrishnan and Rahul Nandkishore. Mean-field theory of nearly many-body localized metals. *Phys. Rev. B*, 90:224203, Dec 2014.
- [20] Anna Goremykina, Romain Vasseur, and Maksym Serbyn. Analytically solvable renormalization group for the many-body localization transition. *Phys. Rev. Lett.*, 122:040601, Jan 2019.
- [21] I. V. Gornyi, A. D. Mirlin, and D. G. Polyakov. Electron transport in a disordered luttinger liquid. *Phys. Rev. B*, 75:085421, Feb 2007.
- [22] David A. Huse, Rahul Nandkishore, and Vadim Oganesyan. Phenomenology of fully many-body-localized systems. *Phys. Rev. B*, 90:174202, Nov 2014.
- [23] David A. Huse, Rahul Nandkishore, Vadim Oganesyan, Arijeet Pal, and S. L. Sondhi. Localization-protected quantum order. *Phys. Rev. B*, 88:014206, Jul 2013.
- [24] Katharine Hyatt, James R. Garrison, Andrew C. Potter, and Bela Bauer. Many-body localization in the presence of a small bath. *Physical Review B*, 95, 01 2016.
- [25] John Z. Imbrie. Diagonalization and many-body localization for a disordered quantum spin chain. *Phys. Rev. Lett.*, 117:027201, Jul 2016.
- [26] S. Kehrein. *The flow equation approach to many-particle systems*. Springer, 2007.

- [27] Shane Kelly and et al. *in preparation*, 2019.
- [28] Vedika Khemani, S. P. Lim, D. N. Sheng, and David A. Huse. Critical properties of the many-body localization transition. *Phys. Rev. X*, 7:021013, Apr 2017.
- [29] Vedika Khemani, Rahul Nandkishore, and S. L. Sondhi. Nonlocal adiabatic response of a localized system to local manipulations. *Nat Phys*, 11(7):560–565, 07 2015.
- [30] Emanuele Levi, Markus Heyl, Igor Lesanovsky, and Juan P. Garrahan. Robustness of many-body localization in the presence of dissipation. *Phys. Rev. Lett.*, 116:237203, Jun 2016.
- [31] S. Lorenzo, T. Apollaro, G. M. Palma, R. Nandkishore, A. Silva, and J. Marino. Remnants of anderson localization in prethermalization induced by white noise. *Phys. Rev. B*, 98:054302, Aug 2018.
- [32] D. J. Luitz, F. Huveneers, and W. De Roeck. How a small quantum bath can thermalize long localized chains. *Phys. Rev. Lett.*, 119:150602, Oct 2017.
- [33] H. P. Lüschen, P. Bordia, S. S. Hodgman, M. Schreiber, S. Sarkar, A. J. Daley, M. H. Fischer, E. Altman, I. Bloch, and U. Schneider. Signatures of many-body localization in a controlled open quantum system. *Phys. Rev. X*, 7:011034, Mar 2017.
- [34] J. Marino and R. M. Nandkishore. Many-body localization proximity effects in platforms of coupled spins and bosons. *Phys. Rev. B*, 97:054201, Feb 2018.
- [35] M. Medvedyeva, T. Prosen, and M. Znidaric. Influence of dephasing on many-body localization. *Phys. Rev. B*, 93:094205, Mar 2016.
- [36] Cécile Monthus. Flow towards diagonalization for many-body-localization models: adaptation of the toda matrix differential flow to random quantum spin chains. *Journal of Physics A: Mathematical and Theoretical*, 49(30):305002, jun 2016.
- [37] Rahul Nandkishore. Many-body localization proximity effect. *Phys. Rev. B*, 92:245141, Dec 2015.
- [38] Rahul Nandkishore and Sarang Gopalakrishnan. Many body localized systems weakly coupled to baths. *Annalen der Physik*, pages 1521–3889, 2016.
- [39] Rahul Nandkishore, Sarang Gopalakrishnan, and David A. Huse. Spectral features of a many-body-localized system weakly coupled to a bath. *Phys. Rev. B*, 90:064203, Aug 2014.
- [40] Rahul Nandkishore and David A. Huse. Many-body localization and thermalization in quantum statistical mechanics. *Annual Review of Condensed Matter Physics*, 6(1):15–38, 2015.
- [41] Vadim Oganesyan and David A. Huse. Localization of interacting fermions at high temperature. *Phys. Rev. B*, 75:155111, Apr 2007.

- [42] Arijeet Pal and David A. Huse. Many-body localization phase transition. *Phys. Rev. B*, 82:174411, Nov 2010.
- [43] S. A. Parameswaran and S. Gopalakrishnan. Non-Fermi glasses: fractionalizing electrons at finite energy density. *ArXiv e-prints*, August 2016.
- [44] David Pekker, Bryan K. Clark, Vadim Oganesyan, and Gil Refael. Fixed points of wegner-wilson flows and many-body localization. *Phys. Rev. Lett.*, 119:075701, Aug 2017.
- [45] David Pekker, Gil Refael, Ehud Altman, Eugene Demler, and Vadim Oganesyan. Hilbert-glass transition: New universality of temperature-tuned many-body dynamical quantum criticality. *Phys. Rev. X*, 4:011052, Mar 2014.
- [46] P. Ponte, C. Laumann, D. Huse, and A. Chandran. Thermal inclusions: how one spin can destroy a many-body localized phase. *Philosophical Transactions A*, 2017.
- [47] Andrew C. Potter, Romain Vasseur, and S. A. Parameswaran. Universal properties of many-body delocalization transitions. *Phys. Rev. X*, 5:031033, Sep 2015.
- [48] M. Rispoli, A. Lukin, R. Schittko, S. Kim, M. E. Tai, J. Leonard, and M. Greiner. *arXiv:1812.06959*, 2018.
- [49] V. Ros, M. Mller, and A. Scardicchio. Integrals of motion in the many-body localized phase. *Nuclear Physics B*, 891:420 – 465, 2015.
- [50] P. Roushan, C. Neill, J. Tangpanitanon, V. M. Bastidas, A. Megrant, R. Barends, Y. Chen, Z. Chen, B. Chiaro, A. Dunsworth, and et al. *Science* 358, 1175-1179, 2017.
- [51] A. Rubio-Abadal, J. Choi, J. Zeiher, S. Hollerith, J. Rui, I. Bloch, and C. Gross. *arXiv:1805.00056*, 2018.
- [52] M. Schreiber, S. S. Hodgman, P. Bordia, H. P. Luschen, M. H. Fischer, R. Vosk, E. Altman, U. Schneider, and I. Bloch. Observation of many-body localization of interacting fermions in a quasi-random optical lattice. *Science*, 349(6250):842–845, jul 2015.
- [53] Maksym Serbyn, Z. Papić, and Dmitry A. Abanin. Local conservation laws and the structure of the many-body localized states. *Phys. Rev. Lett.*, 111:127201, Sep 2013.
- [54] Jürgen Stein. Flow equations and the strong-coupling expansion for the hubbard model. *Journal of Statistical Physics*, 88(1):487–511, Jul 1997.
- [55] Thimothée Thiery, Francois Huveneers, Markus Müller, and Wojciech De Roeck. Many-body delocalization as a quantum avalanche. *Phys. Rev. Lett.*, 121:140601, Oct 2018.
- [56] S. Thomson and M. Schiro. *arXiv:cond-mat*, pages Phys. Rev. B 97, 060201, 2018.
- [57] C. J. Turner, A. A. Michailidis, D. A. Abanin, M. Serbyn, and Z. Papić. *Nature Physics*, 14, 7, 745-749, 2016.

- [58] Vipin Kerala Varma, Abhishek Raj, Sarang Gopalakrishnan, Vadim Oganesyan, and David Pekker. Length scales in the many-body localized phase and their spectral signatures. *arXiv:1901.02902 [cond-mat, physics:quant-ph]*, January 2019. arXiv:1901.02902.
- [59] Ronen Vosk and Ehud Altman. Many-body localization in one dimension as a dynamical renormalization group fixed point. *Phys. Rev. Lett.*, 110:067204, Feb 2013.
- [60] Ronen Vosk and Ehud Altman. Dynamical quantum phase transitions in random spin chains. *Phys. Rev. Lett.*, 112:217204, May 2014.
- [61] Ronen Vosk, David A. Huse, and Ehud Altman. Theory of the many-body localization transition in one-dimensional systems. *Phys. Rev. X*, 5:031032, Sep 2015.
- [62] Franz Wegner. Flow-equations for hamiltonians. *Annalen der Physik*, 506(2):77–91, 1994.
- [63] Z.-C. Yang, A. Hama, S. M. Giampaolo, E. R. Mucciolo, and C. Chamon. Entanglement Complexity in Quantum Many-Body Dynamics, Thermalization and Localization. *ArXiv e-prints*, March 2017.
- [64] Shi-Xin Zhang and Hong Yao. Universal properties of many-body localization transitions in quasiperiodic systems. *Phys. Rev. Lett.*, 121:206601, Nov 2018.
- [65] M. Znidaric, T. Prosen, and P. Prelovsek. Many-body localization in the heisenberg xxz magnet in a random field. *Phys. Rev. B*, 77:064426, Feb 2008.

Chapter 8

Conclusion

In this Dissertation, I have proposed five ultra cold atoms experiments that make use of quantum effects to produce novel macroscopic phenomena. Chapter 2 investigated the possibility to produce a p-wave fermionic condensate in a unique cold atom set up . Chapters 3, 5 and 6, discussed 3 different novel phenomena that can occur when ultra cold BECs are allowed to condense into one of two modes. The issue of thermalization and known results were presented in Chapter 4, and Chapters 5, 6 and 7 discussed 3 mechanisms for which thermalization can be avoided.

The primary result of chapter 2 was that p-wave superconductivity may be accessible in ultra cold atom systems if low enough temperatures can be reached. P-wave pairing requires p-wave attractive scattering to develop between the quasi-particles, and on a lattice this requires at least interactions between neighboring sites. In this chapter we showed it is possible to create such an effective interaction using a second lighter particle as a mediator of the interaction. Inspired by novel trapping set up in ultra cold atom experiments, we

assume the p-wave fermions live in two dimensions, while the meditating particles live in 3 dimensions. We showed first that by tuning the density and on site interaction strength, the p-wave and s-wave scatterings can be tuned to give rise to p-wave pairing. We confirm this prediction using a non-perturbative technique known as functional Renormalization Group.

In chapters 3, 5, and 6, we discussed a set of possible experiments that can take place when a Bose-Einstein condensate is allowed to condense into one of two different modes. These two modes can be two spatially separated modes, like the arms of a bosonic interferometer or the wells of a double well. Or they can be the two hyperfine states of the internal energy levels of the bosonic atoms. In these chapters we apply the two-mode approximation which assumes the bosons occupy only these two modes, and the additional spacial models are ignored. Doing so allows the dynamics of the atoms to be described by a single large spin of size $|J| = N/2$ where N is the number of particles.

In all three chapters, interesting states are produced by a non-linear spin hamiltonian:

$$H = -J_x + \frac{\Lambda}{2} J_z^2 \tag{8.1}$$

where J_x models the single particle tunneling between the two modes and J_z^2 models interactions between the particles. When there are a macroscopic number of particles, the dynamics of the spin can be described by a semi-classical approximation. The classical approximation of H is integrable and results in two types of topologically distinct trajectories: free oscillating: where the spin oscillates around $J_x = 1$ and describes the particles oscillating evenly between the two modes, and self trapping: where the spin oscillates around one of two different fixed points close to $J_z = \pm 1$ and describes a situation where the par-

ticles are stuck in one of the two modes, never fully completing an oscillation to the other. Separating the two behaviors is a separatrix which passes through an unstable fixed point.

Chapter 3 is a paper which studies the detection of cat states created by the dynamics of the hamiltonian H evolving classical states initialized on the separatrix. In this work we develop a method to investigate the indefiniteness of these cat states using currently available cold atom technology. The method we propose uses the observation of a statistical distribution to demonstrate the macroscopic distinction between dead and alive states, and uses the determination of the interferometric sensitivity (Fisher information) to detect the indefiniteness of the cats vital status. We show how combining the two observations can provide information about the structure of the quantum state without the need for full quantum state tomography, and propose a measure of the indefiniteness based on this structure. Numerically simulating our proposed method, we show that as the temperature of this initial state is increased, the produced state undergoes a quantum to classical crossover where the indefiniteness of the cats vital status is lost, while the macroscopic distinction between dead and alive states of the cat is maintained.

Chapter 5 is a paper which focuses on the long time dynamics of the Hamiltonian H . In particular, we ask if the long time averages of observables equilibrate to values predicted by a micro-canonical ensemble. We find that states initialized on the self-trapping or free oscillating trajectories do equilibrate to values predicted by a micro-canonical ensemble. While for state initialized on the separatrix, the long time observables do not equilibrate to values described by a micro-canonical ensemble. Instead, the long time values of observables retain information about where on the separatrix the dynamics of the spin began. We

showed that this long time memory is due to the unstable fixed point producing a set of localized eigenstates. This then allowed us to derive how the equilibrium value of observables encodes information about the initial state.

Then in chapter 6, we investigate the dynamics of bosons obeying the hamiltonian H , but with a periodic kick of the form $U = e^{-it_2 J_x}$ applied periodically at intervals t_1 . We first showed how, for small values of t_1 and t_2 , classical integrability is still present and can be computed via perturbation theory. We then focused our attention to a set of resonances that occur before the onset of complete chaos. These resonance occur when t_1 is a fractional integer, $1/n$, of a period of one of the trajectories of the hamiltonian, H . We show and explain how these resonances produce n stable fixed points that the system hops between before every kick. We find that since the stable fixed points prevent quantum diffusion, the hopping between the different fixed points lasts forever. These persistent oscillations are then compared to those in time crystals.

Then in the final chapter 7, I present a paper that studies another system in which thermalization is avoided. This system, is of two chains of interacting fermions, one of which contains strong disorder and the other which is clean. When the chains do not interact, the clean chain thermalizes, while the dirty one ends up stuck in a many body localized phase. We then study which physics wins when the chains are allowed to interact via density-density interactions every δ sites (see Figure 7.6). When $\delta = 1$, we find that the many body localized phase can spread to the clean chain when 1) the density of fermions in the dirty chain is sufficiently high, 2) interactions between the chain is sufficiently large and 3) the energy density of the dirty chain fermions is sufficiently low. When $\delta > 1$, and

some of the clean chain sites are not coupled, we find novel behavior occurring in the clean chain, where on short time scales transport is allowed within the clusters of uncoupled sites but not between the clusters. Thus on short time scales, the clusters act as large spins which can thermalize or not depending on the emergent interactions between them. Then on longer times, transport is allowed between the cluster and the whole system comes to thermal equilibrium.

Each of these projects leave room for new research. In chapter 2, we assumed the mediating particles moved infinitely faster than the pairing particles. This approximation leaves out the possibility that the mediating particles become entangled with the pairing particles and produce novel states of matter. Similar “adiabatic” approximations occur in cavity QED systems where the photon is assumed to be much faster. In both these systems the non-adiabatic limit offers new possibilities for entanglement and phases of matter.

In chapter 3, we ignored the primary mechanism in which superpositions of dead and alive cats decohere and the uncertainty becomes classical: environmental decoherence. In this system there are two mechanism for decoherence: particle loss and excitation of other spatial modes. Future projects could model these effects to identify the feasibility of creating the cat states investigated in that chapter. Similarly the effect of the other spacial modes may dramatically affect the results in chapters 5 and 6.

The variety in the projects I investigated during my PhD and the variety in the possible future research directions reflects the breath of field which ultra-cold atom physics and generically quantum many body physics covers. In addition to the topics covered in this dissertation, the large fields of quantum computing and topological states of matter offer an

even wider range of possibility for ultra-cold atom physics. I am excited for these possibilities and grateful to my advisers Shan-Wen Tsai and Eddy Timmermans for providing me the opportunity to study such a wonderful range of physics.

Appendix A

Many Body Quantum Mechanics: an Overview

A.1 General Quantum Mechanics

In quantum mechanics we model states with vectors, $|\psi(t)\rangle$ in a complex hilbert space. Measurements are model with observables O , which are hermitian operators. They are broken in to there eigenvalues and vectors: $O = \sum_o o |o\rangle \langle o|$. Expectation value of an obserrvables is given by the inner product: $\langle O \rangle$. And the probability of an observable taking a particular value is: $|\langle o|\psi(t)\rangle|^2$ If we are uncertain about the state we can use density matrices $\rho = \sum_i p_i |i\rangle \langle i|$, where i labels the states we are uncertain about and p_i are the probabilities associated to those states. Its important that multiple ensemblbes i can

give the same density matrix ρ . Where expectation values and probabilities are given as:

$$\langle O \rangle = Tr[\rho O] \tag{A.1}$$

$$P(o) = \langle o | \rho | o \rangle$$

A.1.1 Unitary Dynamics

Dynamics are described by completely positive trace preserving maps which take an initial state ρ_0 to a evolved state $L(\rho_0, t)$. This map must keep the trace of the density matrix $tr[\rho] = 1$ and all of its eigen values positive. This way we can continue to think of that operator as a representation of uncertainty about a set of states.

The simplest dynamics are unitary where $L(\rho, t) = U(t)\rho U(t)^\dagger$. where $U(t)$ is defined by a hamiltonian H via:

$$U(t) = e^{-iHt/\hbar} = \sum_n e^{iE_n t/\hbar} |n\rangle \langle n| \tag{A.2}$$

This unitary can be derived from the schrodinger equation:

$$i\hbar\partial_t |\psi(t)\rangle = H |\psi(t)\rangle \tag{A.3}$$

If the hamiltonian has time dependence, the unitary is given as:

$$U(t) = T e^{-\frac{i}{\hbar} \int_0^t H(t) dt} = \lim_{N \rightarrow \infty} \prod_{n=1}^N e^{\frac{itn}{N\hbar} H(tn/N)} \tag{A.4}$$

The T reminds us that the true expression is the time order products of a bunch of infinitesimal unitaries.

A.1.2 Heisenberg Picture, simple BCH

In the Heisenberg Picture, operators evolve as:

$$\begin{aligned} O &\rightarrow O(t) = U^\dagger(t)OU(t) \\ \rho &\rightarrow \rho \end{aligned} \tag{A.5}$$

with a first order differential equation as:

$$\partial_t O(t) = \frac{i}{\hbar} [H, O(t)] \tag{A.6}$$

The solution of this equation can be written using the BCH formula:

$$e^{xA} B e^{-xA} = \sum_n \frac{1}{n!} Ad_A^n(B) x^n \tag{A.7}$$

where

$$\begin{aligned} Ad_A^0(B) &= B \\ Ad_A^1(B) &= [A, B] \\ Ad_A^n &= [Ad_A^{n-1}, B] \end{aligned} \tag{A.8}$$

For unitary dynamics, B is some observable, $A = H$ and $x = it/\hbar$. Two common situations are when $[H, O_c] = ic$ and when $[H, O_b] = bO_b$, and in these situations the sum can be computed and yields:

$$\begin{aligned} O_c(t) &= O_c + icx = O_c - tc/\hbar \\ O_b(t) &= O_b e^{xb} = O_b e^{ibt/\hbar} \end{aligned} \tag{A.9}$$

A.1.3 Interaction Picture

The interaction picture breaks the unitary $U(t)$ into two by using the identity: $U_0 U_0^\dagger = 1$. There are in fact two interaction pictures depending on where you insert this identity in an expectation value. It will determine whether you perform perturbation theory on the wave function or operators. The standard (state interaction):

$$\langle O \rangle(t) = \langle \psi(t) | U_0 U_0^\dagger O U_0 U_0^\dagger | \psi(t) \rangle \quad (\text{A.10})$$

In this picture one can derive:

$$O_I(t) = U_0^\dagger O U_0 \quad (\text{A.11})$$

$$i\hbar \partial_t |\psi(t)_I\rangle = V_I(t) |\psi(t)_I\rangle$$

In the operator interaction picture:

$$\langle O \rangle(t) = \langle \psi | U_0^\dagger U_0 U^\dagger O U U_0^\dagger U_0 | \psi \rangle \quad (\text{A.12})$$

In this picture:

$$|\psi_I(t)\rangle = U_0 |\psi\rangle \quad (\text{A.13})$$

$$V_I(t) = U_0 V U_0^\dagger$$

$$\partial_t O(t) = \frac{i}{\hbar} [V_I(t), O(t)]$$

A.1.4 Correlations, Generating Functions, Greens Functions

In the Schrödinger and Heisenberg picture one studies either states or operators and then takes averages at the end to obtain correlation functions. It can be convenient to track

correlations directly and this can be done with generating functions. For unitary evolution we construct express any unequal time correlation functions using the hisenberg picture:

$$\left\langle \prod_i O_i(t_i) \right\rangle = \left\langle \prod_i U(t_i)^\dagger O_i U(t_i) \right\rangle$$

If I remove the observables from this expression, the set of unitaries describe evolution of a set along a path in time, first evolving the state to t_0 , then t_1 and so on. The path through time can go forward and backward depending on the order of times in the operators and the end of the evolution, the unitaries must bring the state back to the initial state. This evolution can be condensed into a single operator:

$$U_P(t) = P e^{\frac{-i}{\hbar} \oint dt H(t)}$$

Now instaed of time ordering, P orders along the path required to visit all the times of the operators in order. The \oint intergral is then an integral along this path. If we add source fields to the hamilonian:

$$\sum_i A(t)_i O_i$$

then we can define a correlation generating function via:

$$\mathcal{G}(A_i(t)) = \langle U_P(t) \rangle = \left\langle P e^{\frac{-i}{\hbar} \oint dt (H(t) + \sum_i A(t)_i O_i)} \right\rangle$$

Where t can take a value anywhere on the path P . By taking derivitives with respect to $A_i(t)$ we can reconstruct the correlation functions above:

$$(i\hbar)^N \left[\prod_i^N \partial_{A_i(t_i)} \mathcal{G}(\{A(t)\}) \right]_{A=0} = \left\langle P \prod_i O_i(t_i) \right\rangle \quad (\text{A.14})$$

This is the same as a correlation generating function for probability distributions:

$$\left\langle e^{\sum_i x_i O_i} \right\rangle$$

except now we allow for time evolution. If we want a cumulant generating function, we take the log:

$$\mathcal{W}(A_i(t)) = \ln [\mathcal{G}(A_i(t))]$$

If we perform a Legendre transform, we get a function of the expectation values $\langle O_i(t) \rangle$. This new function $\Gamma(O_i(t))$, when minimized, yields the expectation values $\langle O_i(t) \rangle$ defined by $\mathcal{G}(A_i(t))$. Since these are equal time correlation functions, the minimization procedure yields an evolution equation for the observables $\langle O_i(t) \rangle$. One can therefore think of this as an effective action for the classical variables $\langle O_i(t) \rangle$.

A.1.5 Two time correlations

Lets focus on properties of two time correlations. In a gaussian theory they determine every other correlation, and since we are often building off fluctuations of Gaussian theory, then two time correlations will be the building blocks of the full theory. They also play an important role in identifying quantum effects like Leggett Garg violation and quantum fisher information.

For an observable A at time t_1 and observable b at time t_2 the correlators:

$$\langle a(t_1)b(t_2) \rangle$$

$$\langle b(t_2)a(t_1) \rangle$$

are non hermitian and therefore not necessarily real. In fact, if a and b are unitaries then they represent an overlap between two states. Both of these amplitudes can be generated

from the generating function: $\mathcal{G}(A(t))$ when the path is a single closed path, with a forward branch labeled by $+$ and a backwards branch labeled by $-$. With a forward and backward branch, there are 4 possible ways to generate an amplitude with a and b and time t_1 and t_2 :

$$\begin{aligned}
G_{++} &= \frac{d^2}{A(t_1, +)B(t_2, +)} \mathcal{G}(A(t)) = -\frac{1}{\hbar^2} \langle Tb(t_2)a(t_1) \rangle \\
G_{+-} &= \frac{d^2}{A(t_1, +)B(t_2, -)} \mathcal{G}(A(t)) = -\frac{1}{\hbar^2} \langle b(t_2)a(t_1) \rangle \\
G_{-+} &= \frac{d^2}{A(t_1, -)B(t_2, +)} \mathcal{G}(A(t)) = -\frac{1}{\hbar^2} \langle a(t_1)b(t_2) \rangle \\
G_{--} &= \frac{d^2}{A(t_1, -)B(t_2, -)} \mathcal{G}(A(t)) = -\frac{1}{\hbar^2} \langle \tilde{T}b(t_2)a(t_1) \rangle
\end{aligned}$$

where T and \tilde{T} are time ordering. The correlations G_{++} and G_{--} are both linearly dependent on G_{+-} and G_{-+} . This redundancy in the generating function can be partially removed once we represent it with a path integral.

When $[a(t_1), b(t_2)]$ don't compute, the above correlations are non-hermitian. Their real and imaginary parts produce two hermitian operators:

$$\begin{aligned}
G_A &= -\frac{i}{\hbar} \theta(t_1 - t_2) \langle [a(t_1), b(t_2)] \rangle \\
G_R &= \frac{i}{\hbar} \theta(t_2 - t_1) \langle [a(t_1), b(t_2)] \rangle \\
G_K &= \langle \{a(t_1), b(t_2)\} \rangle
\end{aligned}$$

where G_R is the response of b at time t_2 due to a perturbation by a at time t_1 . and G_K described fluctuations.

A.1.6 The thermal state and the KMS relation

For a quantum system, which has equilibrated to a thermal bath, the equilibrium state is determined by the gibbs state:

$$\rho_\beta = \frac{e^{-\beta H}}{Z} \quad (\text{A.15})$$

where Z ensure normalization of ρ . The correlation generating function for the dynamics of this system is given by:

$$\mathcal{G}_\beta(A_i(t)) = \langle U_P(t) \rangle = Tr \left\langle P e^{\frac{-i}{\hbar} \int dt (H(t) + \sum_i A(t)_i O_i)} \frac{e^{-\beta H}}{Z} \right\rangle$$

Noting that $-i\hbar \int_{i\beta\hbar}^0 dt = -\beta H$, we can extend the path P to start at an imaginary time $i\beta\hbar$ and move to the complex origin, before generating the full path. This gives us a generalized “imaginary time correlation function”. When studying the thermal state, it is often easiest to only consider a Path that moves in imaginary time:

$$\mathcal{G}_T(A_i(t)) = Tr \left\langle P e^{-\int_0^\beta d\tau (H(\tau) + \sum_i A(\tau)_i O_i)} \right\rangle$$

this function generates the correlations:

$$(-1)^N \left[\prod_i^N \partial_{A_i(\tau_i)} \mathcal{G}_T(\{A(\tau)\}) \right]_{A=0} = Tr \left\langle T \prod_i O_i(\tau_i) \right\rangle \quad (\text{A.16})$$

with:

$$O_i(\tau_i) = e^{\tau_i H} O_i e^{-\tau_i H} \quad (\text{A.17})$$

These types of correlations show up in perturbative calculations of thermal states and there free energies.

KMS relation

The real time correlations of a thermal state satisfy a useful relation called the KMS relation. Writing explicitly a two time correlation:

$$\begin{aligned}
 Tr \left\langle O_1(t_1) O_2(t_2) e^{-\beta H} \right\rangle &= Tr \left\langle e^{it'_1 H} O_1 e^{-it'_1 H} e^{it'_2 H} O_2 e^{-it'_2 H} e^{-\beta H} \right\rangle = & (A.18) \\
 &= Tr \left\langle e^{it'_2 H} O_2 e^{-it'_2 H} e^{-\beta H} e^{it'_1 H} O_1 e^{-it'_1 H} \right\rangle = \\
 &= Tr \left\langle e^{i(t'_2 - i\beta) H} O_2 e^{-i(t'_2 - i\beta) H} e^{it'_1 H} O_1 e^{-it'_1 H} e^{-\beta H} \right\rangle = \\
 Tr \left\langle O_2(t_2 - i\beta) O_1(t_1) e^{-\beta H} \right\rangle &= Tr \left\langle O_2(t_2) O_1(t_1 + i\beta) e^{-\beta H} \right\rangle
 \end{aligned}$$

In the equilibrium state, there is time translation symmetry and we can set $t_2 = 0$ and $t_1 = \tau = t_1 - t - 2$ yielding:

$$Tr \left\langle O_1(\tau) O_2 e^{-\beta H} \right\rangle = Tr \left\langle O_2 O_1(\tau + i\beta) e^{-\beta H} \right\rangle \quad (A.19)$$

or:

$$G_{+-}(\tau) = G_{-+}(\tau + i\beta) \quad (A.20)$$

Fourier transforming we get:

$$G_{-+}(\omega) = G_{+-}(\omega) e^{\omega\beta} \quad (A.21)$$

Which gives the relationship:

$$G_K = i\hbar \coth(\beta\omega/2) (G_R - G_A) \quad (A.22)$$

A.2 Quantum Components

A.2.1 Spins: Operators

Spin observables are defined to have the following commutation relations:

$$[S^i, S^j] = i\epsilon_{ijk}\hbar S^k \quad (\text{A.23})$$

and the ladder operators are defined as:

$$\alpha S^\pm = S^x \pm iS^y \quad (\text{A.24})$$

where $\alpha = 1$ or $\alpha = \hbar$ depending on convention. Their commutation relations with S^z are:

$$[S^z, S^\pm] = \pm\hbar S^\pm \quad (\text{A.25})$$

and with themselves:

$$[S^+, S^-] = 2\hbar/\alpha^2 S^z$$

their product is:

$$S^+ S^- = \frac{S^{x2} + S^{y2} + \hbar S^z}{\alpha^2} \quad (\text{A.26})$$

Finally, their evolution is given by:

$$e^{-i\phi S^z} S^\pm e^{i\phi S^z} = S^\pm e^{\mp i\hbar\phi} \quad (\text{A.27})$$

spin-half

The spin half are written in terms of Pauli matrices: Which are diagonal in the S^z basis, and correspond to \vec{S} when $\hbar = 2$

$$\begin{aligned} S_z &= \frac{\hbar}{2}\sigma^z = \frac{\hbar}{2} \begin{bmatrix} 1 & 0 \\ 0 & -1 \end{bmatrix} \\ S_x &= \frac{\hbar}{2}\sigma^x = \frac{\hbar}{2} \begin{bmatrix} 0 & 1 \\ 1 & 0 \end{bmatrix} \\ S_y &= \frac{\hbar}{2}\sigma^y = \frac{\hbar}{2} \begin{bmatrix} 0 & -i \\ i & 0 \end{bmatrix} \end{aligned} \tag{A.28}$$

For spin half

$$S^+S^- = \frac{\hbar^2/2 + \hbar S^z}{\alpha^2} \tag{A.29}$$

A.2.2 Spins: Wave Functions

A spin-half Hamiltonian has the form:

$$H = \vec{B} \cdot \vec{S} \tag{A.30}$$

The magnitude of B sets the overall energy scale. Since the vector \vec{B} has 3 components, $\vec{B}/|B|$ lives on the unit sphere. Therefore all spin-half Hamiltonian live on the sphere. Furthermore, all spin-half states also live on the sphere. Thus, understanding the coordinate systems of a sphere is very useful for describing spin-half states. Furthermore, since a sphere is closed, there is no single map from the space of Hamiltonian to eigenstates which

is continuous and differential everywhere. It is therefore important to know where the singularities are in any coordinate system we use. For spherical coordinates, there are two coordinate singularities: the north and south pole: Here the azimuthal angle becomes undefined. Writing \vec{B} in spherical coordinates:

$$\vec{B} = (\cos(\beta), \sin(\beta) \cos(\alpha), \sin(\beta) \sin(\alpha)) \quad (\text{A.31})$$

The eigenstates, in the z basis are derived as:

$$\begin{aligned} |+\rangle &= \cos\left(\frac{\beta}{2}\right) |0\rangle + \sin\left(\frac{\beta}{2}\right) e^{i\alpha} |1\rangle \\ |-\rangle &= \sin\left(\frac{\beta}{2}\right) |0\rangle + \cos\left(\frac{\beta}{2}\right) e^{-i\alpha} |1\rangle \end{aligned} \quad (\text{A.32})$$

with ± 1 eigen values. Thus the map between spheres is:

$$\beta' = \beta/2 \quad (\text{A.33})$$

$$\alpha' = \alpha$$

Notice that if I go around the state sphere once, I go around the Hamiltonian sphere twice.

This is because in this coordinate system, the overall phase of the wave function is undefined.

This can cause singularities in functions of the hamiltonian at the poles $\beta = 0, \pi$.

Stereographic Projection

The stereographic coordinate system is another option. It maps the sphere to a plane by projecting it through one of the poles. Given the unit spheres x, y, z coordinates,

the projection through the north pole is given by:

$$\begin{aligned} X &= \frac{x}{1-z} \\ Y &= \frac{y}{1-z} \end{aligned} \tag{A.34}$$

and the projection through the south pole is given by:

$$\begin{aligned} X' &= \frac{x}{1+z} \\ Y' &= \frac{-y}{1+z} \end{aligned} \tag{A.35}$$

It only has one coordinate singularity at the north pole: $z = 1$. One can map this to a complex manifold using:

$$W = X + iY \tag{A.36}$$

or

$$Z = X' + iY' \tag{A.37}$$

with a map between them $W = 1/Z$. In these coordinates the eigenvector equations can be written as:

$$\begin{aligned} W\psi_{u+} &= \psi_{d+} \\ -\psi_{u-} &= W\psi_{d-} \end{aligned} \tag{A.38}$$

or:

$$\begin{aligned}\psi_{u+} &= Z\psi_{d+} \\ -Z\psi_{u-} &= \psi_{d-}\end{aligned}\tag{A.39}$$

The phase of Z or W defines the phase difference of the eigenstates while its magnitude determines the magnitude. Except when Z or W diverge at the south or north pole. The eigenstates of linear higher-spins can be found using bosonic operators and is described below.

A.2.3 Bosons: Operators

For bosonic systems the observables are x and p , and there commutation relation is:

$$[x, p] = i\hbar\tag{A.40}$$

It is natural to form the boson creation, annihilation and number operators:

$$\begin{aligned}\alpha b &= (x + ip) \\ n &= b^\dagger b = \frac{1}{\alpha^2}(x^2 + p^2 + \hbar)\end{aligned}\tag{A.41}$$

which gives:

$$\begin{aligned}[b, b^\dagger] &= (2\hbar/\alpha^2) \\ [n, b] &= -(2\hbar/\alpha^2)b \\ [n, b^\dagger] &= (2\hbar/\alpha^2)b^\dagger\end{aligned}\tag{A.42}$$

It is important that $(2\hbar/\alpha^2) = 1$ so the number operator has integer eigen values, and this fixes $\alpha = \sqrt{2\hbar}$. a simple choice is to take $\alpha = \hbar = 2$. There are two types of transformation usefull to know for boson operators:

$$U_n(t) = e^{-i\omega t n} \quad (\text{A.43})$$

$$U_\Delta(t) = e^{-i\Delta_x p/\hbar} e^{i\Delta_p x/\hbar}$$

which gives:

$$U_n(t)^\dagger b U_n(t) = b e^{-i\omega t \frac{2\hbar}{\alpha^2}} \quad (\text{A.44})$$

and

$$U_\Delta(t)^\dagger x U_\Delta(t) = x + \Delta_x \quad (\text{A.45})$$

$$U_\Delta(t)^\dagger p U_\Delta(t) = p + \Delta_p$$

I remember signs by the following:

- keep i with t
- schrodinger equation should have a sign so its $i\partial_t$
- unitary, $U(t)$ is solution to the schrodinger equation so it has a $-i\Delta t$ and shifts t by Δt
- the boson creation operator is always in the ket state so it has a sign like $U(t) e^{-it}$
- x gets shifted like t , so the unitary should be $-\Delta_x p$ so $x \rightarrow x + \Delta x$
- p gets oppocite sites from x

- the signs in the commutator for x and p are natural because x is more important so it comes first.
- the sign for the commutator of n and b comes from the fact that b has to decrease the number of particles.
- alternatively, it should be $[b, b^\dagger] = 1$ because b is more natural than b^\dagger

A.2.4 Bosons: Wave Functions

Basis States

Basis states are constructed from the eigen states of operators. For bosons, these operators are x, p, b, n . and the basis states will be written as $|x(p, \alpha, n)\rangle$. What is useful is being able to transform between basis states. The transformation between x and p is given by the fourier transform:

$$\begin{aligned} |p\rangle &= \frac{1}{\beta\sqrt{\hbar}} \int_{-\infty}^{\infty} e^{ipx/\hbar} |x\rangle dx \\ |x\rangle &= \frac{1}{\alpha\sqrt{\hbar}} \int_{-\infty}^{\infty} e^{-ipx/\hbar} |p\rangle dp \end{aligned} \tag{A.46}$$

with the constraint that $\alpha\beta = 2\pi$. It's important to point out that, these are not states in the hilber space, because they are not square integrable. Instead we treat them as place holders to make meaning full the representation of any state $|\psi\rangle$ in the $x(p)$ 'basis': $\langle x(p)|\psi\rangle$

From this we can derive the action of p in position space:

$$\langle \psi | p | x \rangle = \frac{1}{\alpha\sqrt{\hbar}} p \int_{-\infty}^{\infty} e^{-ipx/\hbar} \langle \psi | p \rangle dp = i\hbar \partial_x \langle \psi | x \rangle \tag{A.47}$$

The eigenstates of b are given in terms of n as the coherent states:

$$|\alpha\rangle = e^{\psi b^\dagger} |0\rangle = \sum_n \frac{\psi^n}{\sqrt{n!}} |n\rangle \quad (\text{A.48})$$

which can be proved from the action of the creation and annihilation operators on the number eigen states:

$$\langle n' | b | n \rangle = \sqrt{n} \delta_{n, n'-1} \quad (\text{A.49})$$

Since a is not hermitian, the coherent state is only its right eigen state, the eigen values, ψ can be complex and the eigen states can be non orthonormal. In fact they aren't:

$$\langle \phi | \psi \rangle = e^{\phi^* \psi} \quad (\text{A.50})$$

which can be proved from Wicks theorem. Regardless they can be used to form a complete basis:

$$1 = \frac{1}{\pi} \int d\phi d\phi^* e^{-|\phi|^2} |\phi\rangle \langle \phi| \quad (\text{A.51})$$

where the double integral over ϕ and ϕ^* should be done over the real and imaginary parts.

A.2.5 Spin-Boson Mapping

Mapping spins to bosons can be done by:

$$\begin{aligned} J_z &= \frac{\hbar}{2}(n_1 - n_2) \\ J_x &= \frac{\hbar}{2}(a_1^\dagger a_2 + h.c) \\ J_y &= \frac{\hbar}{2i}(a_1^\dagger a_2 - h.c) \end{aligned} \quad (\text{A.52})$$

This will yield:

$$[J_x, J_y] = i\hbar J_z \quad (\text{A.53})$$

and

$$J^2 = \frac{\hbar^2}{4} N^2 \quad (\text{A.54})$$

Using this representation, one can construct the eigen states of a linear spin:

$$H = -\vec{B} \cdot \vec{J} \quad (\text{A.55})$$

using fock states. The bosonic H can be diagonalized using the spin-half eigenstates:

$$\begin{aligned} b_+ &= \cos\left(\frac{\beta}{2}\right)a_1 + \sin\left(\frac{\beta}{2}\right)e^{i\alpha}a_2 \\ b_- &= \sin\left(\frac{\beta}{2}\right)a_1 + \cos\left(\frac{\beta}{2}\right)e^{-i\alpha}a_2 \end{aligned} \quad (\text{A.56})$$

yielding:

$$H = -|B| \frac{\hbar}{2} (n_+ - n_-) \quad (\text{A.57})$$

which has eigenstates:

$$\frac{b_+^m}{\sqrt{m!}} \frac{b_+^{N-m}}{\sqrt{(N-m)!}} |0, 0\rangle \quad (\text{A.58})$$

A.3 Composite Systems

A.3.1 Fermionic Systems

Fermions are inherently multi component systems because they arise from an anti symmetry restriction between components. Fermion operators are defined by anti-commutation:

$$\{c_i, c_j^\dagger\} = \delta_{ij} \quad (\text{A.59})$$

commutators with a quadratic operator behave the same as bosons though:

$$[c_i^\dagger c_k, c_j] = -c_k \delta_{ij} \quad (\text{A.60})$$

$$[c_k^\dagger c_i, c_j^\dagger] = c_k^\dagger \delta_{ij}$$

This implies the evolution of a creation operator is the same:

$$U_n(t) = e^{-i\omega t n} \quad (\text{A.61})$$

$$U_n(t)^\dagger c U_n(t) = c e^{-i\omega t}$$

A.3.2 Majorana Fermions

One can construct hermition operators similar to the boson x and p :

$$\alpha A_{2i} = c_i^\dagger + c_i \alpha A_{2i+1} = c_i^\dagger + c_i$$

They obey the following anti commutation relations:

$$A_i, A_j = \delta_{ij} \frac{2}{\alpha^2} \quad (\text{A.62})$$

Commutators with quadratic operators:

$$[A_i A_j, A_k] = \frac{2}{\alpha^2} (A_i \delta_{jk} - A_j \delta_{ik}) \quad (\text{A.63})$$

A.3.3 Representation Of Operators

Above we discussed the lie-algebra, group and representation structures which define some of the standard smallest components of a quantum system. Large quantum systems are constructed from the tensor products of the component vector spaces. If the representation of the component lie-algebras are d dimensional, and there are N components, then the composite space is d^N . Generically the set of all hermitian operators of this composite space form an $SU(d^N)$ algebra. Taking simple products of the component lie algebra elements does not produce all these operators if the d is larger than the minimal representation. Therefore, one needs to be careful with how the $2d^N - 1$ operators are organized. In other words, one needs to be careful to construct a proper operator basis for the $SU(d^N)$ algebra which describes all hermitian observables. For spin-halves, d is minimal, and this isn't an issue and strings of the $SU(2)$ operators form a proper basis. For larger spins, or bosons, this is an issue and can be resolved by wick ordering. In the next sections we will discuss the wick ordering representation and how to take commutators for it for bosons. Later we will do the same for fermions.

Wick Ordering

The trouble of creating a basis of operators is that order of the operators matter and you may create an over complete basis if you are not careful. Therefore, a basis should

specify a operator order. Wick ordering does this by three rules[26]:

$$\langle : A_1 A_2 \cdots A_n : \rangle = 0 \quad (\text{A.64})$$

$$d_{A_i} : A_1 A_2 \cdots A_n : = : A_1 \cdots A_{i-1} A_{i+1} \cdots A_n : \quad (\text{A.65})$$

$$: 1 : = 1 \quad (\text{A.66})$$

When the state used in the expectation value is gaussian, one can derive a nice recursion relation:

$$A_k : O := A_k O + \sum_l C_{kl} : \frac{dO}{dA_l} \quad (\text{A.67})$$

where $C_{kl} = \langle A_k A_l \rangle$. From this there are two usefull expressions for finding the wick ordered expression[26, 20]:

$$e^{-\sum_{kl} C_{kl} \partial_{A_k} \partial_{A_l} O} = : O : \quad (\text{A.68})$$

$$: O_1 :: O_2 : = e^{-\sum_{kl} C_{kl} \partial_{A_k} \partial_{A'_l}} : O_1(A) O_2(A') : \quad (\text{A.69})$$

From eq.A.69 we one can prove the orthogonality of the set of wick ordered operators[20].

For fermions, one has to treat the derivitives and operators as anti-commutiting objects when evaluating the above:

$$\partial_{A_i} A_j = \delta_{ij} - A_j \partial_{A_i} \quad (\text{A.70})$$

From this one see that fermions anti-commute with in the wick ordered symbol:

$$: A_i A_j := - : A_j A_i : \quad (\text{A.71})$$

which differs from bosons which commute:

$$: A_i A_j := : A_j A_i : \quad (\text{A.72})$$

In this way, the operators with in the wick ordered symbol act as (anti-)commuting numbers. This symmetry means that the basis operators must be specified with a fixed order with in the wick ordered expression. To allow for all orderings one can also take the basis states as equal superpositons of each ordering:

$$\begin{aligned} : a_i a_j : + : a_j a_i : & \quad \text{for bosons} \\ : a_i a_j : - : a_j a_i : & \quad \text{for fermions} \end{aligned} \tag{A.73}$$

This is usually my choice. This symmetry does not need to be taken between creation and annihilation operators since they are already distinguished and will be in the coefficients of the basis. If the basis only of hermitian operators, then the symmetric and imaginary anti symmetric combinations can be taken as the basis operators.

One can also wick order polynomials using the same rules. In this case the expectation values should be taken with respect to a gaussian probability distribution.

Role of Symmetry in the Representation of Operators

As noted above, the symmetries play an important role in representing operators in some operator basis. To do so, we will apply a super operator F to the single particle operators A . And then assist the new multiparticle operator is equal to the original. As an example lets take a 4-particle operator:

$$V = \sum_{ijkl} V_{ijkl} : A_i A_j A_k A_l : \tag{A.74}$$

If we insist this operator conserves number conservation, we apply the $U(1)$ phase rotation:

$$F(\phi) [a_i] = e^{i\phi} a_i \quad (\text{A.75})$$

Applying this operator to the single particle operators in V , we find that only operators with equal number and creation operators conserved total number of particles. We can therefore write V as:

$$V = \sum_{ijkl} V_{ijkl} : a_i^\dagger a_j^\dagger a_k a_l : \quad (\text{A.76})$$

We can also use the exchange symmetry to constraint V :

$$V = \sum_{ijkl} V_{ijkl} : a_i^\dagger a_j^\dagger a_k a_l := \pm \sum_{ijkl} V_{ijkl} : a_j^\dagger a_i^\dagger a_k a_l := - \sum_{ijkl} V_{ijkl} : a_i^\dagger a_j^\dagger a_l a_k := \sum_{ijkl} V_{ijkl} : a_j^\dagger a_i^\dagger a_l a_k \quad (\text{A.77})$$

which yields:

$$V_{ijkl} = \pm V_{ijlk} = \pm V_{jikl} = V_{jilk} \quad (\text{A.78})$$

Similarly with Hermitian conjugation we get

$$V_{ijkl} = V_{klij} \quad (\text{A.79})$$

If we add a spin index: $V_{i\sigma_i, j\sigma_j; k\sigma_k, l\sigma_l}$ and insist invariance in a specified spin direction $e^{i\phi\sigma^z}$ then we get conservation of spin-z quantum number:

$$\sum_i (a_{i\sigma}^\dagger \partial_{a_{i\sigma}^\dagger} - a_{i\sigma} \partial_{a_{i\sigma}}) V \quad (\text{A.80})$$

which yields:

$$V = \sum_{ijkl, \sigma_i \sigma_j} U_{\sigma_i \sigma_j}(i, j; k, l) a_{i\sigma_i}^\dagger a_{j\sigma_j}^\dagger a_{k\sigma_k} a_{l\sigma_l} + W_{\sigma_i \sigma_j}(i, j; k, l) a_{i\sigma_i}^\dagger a_{j\sigma_j}^\dagger a_{k\sigma_k} a_{l\sigma_i} \quad (\text{A.81})$$

Writing $U = T + S$ and $W = T - S$ then I can write:

$$V_{i\sigma_i, j\sigma_j; k\sigma_k, l\sigma_l} = S_{\sigma_i\sigma_j}(i, j; k, l)(\delta_{\sigma_i\sigma_k}\delta_{\sigma_j\sigma_l} - \delta_{\sigma_i\sigma_l}\delta_{\sigma_j\sigma_k}) + T_{\sigma_i\sigma_j}(i, j; k, l)(\delta_{\sigma_i\sigma_k}\delta_{\sigma_j\sigma_l} + \delta_{\sigma_i\sigma_l}\delta_{\sigma_j\sigma_k}) \quad (\text{A.82})$$

Then from exchange symmetry I get the symmetry constrains:

$$S_{\sigma_i\sigma_j}(i, j; k, l) = \mp S_{\sigma_i\sigma_j}(i, j; l, k) \quad (\text{A.83})$$

$$T_{\sigma_i\sigma_j}(i, j; k, l) = \pm T_{\sigma_i\sigma_j}(i, j; l, k)$$

Since the S forces the spins to have oppocite spin, we will considerate the singlet coupling while T the tripplet coupling.

These same type of symmetry arguments can apply to the vertex expansion of functions[20].

Commutators for wick ordering

For a commutator $[: O_1(A) :, : O_2(A') :]$, we must apply wicks second theorem twice:

$$\begin{aligned} &[: O_1(A) :, : O_2(A') :] = \quad (\text{A.84}) \\ &: exp(\sum_{kl} C_{k,l}) \frac{\partial^2}{\partial A'_l \partial A_k} O_1(A) O_2(A') : - : exp(\sum_{kl} C_{k,l}) \frac{\partial^2}{\partial A_l \partial A'_k} O_2(A') O_1(A) : \end{aligned}$$

For a given contraction, the contractions swap creation and annihilation operators between the first and second terms in the commutator: $C \leftrightarrow C^T$ The only other difference between the first and second term is for fermions the sign might change. Two factors effect the change in sign: the contraction and the number of exchanges required to make the operators not contracted in the first and second term the same.

For the first factor: This sign depends on the total number of creation and annihilation operators in O_1 , n and the number in O_2 , m . For a single contraction, we first assume the sign for the first term is $(-1)^{r_1}$. In the second term, the r_2 operators between the two in the contraction end up on the outside of the two operators. Thus the number of terms between the two operators for the second term is $r_2 = m + n - r_1 - 2$. Thus the sign difference between the first and second term due to one contraction is $(-1)^{m+n}$. Since subsequent contractions involve $m + n - 2l$ total operators, the sign difference due to a contraction only depends on $m + n$. If $m + n$ is even, there will be no sign change due to the contractions. If $m + n$ is odd, there will be a sign change for every contraction, with an overall $(-1)^{(m+n)l}$, where l is the number of contractions.

For the second factor: After l contractions one must commute $m - l$ terms through $n - l$ terms to match the operator in the first term. This produces an additional sign of $(-1)^{(m-l)(n-l)}$.

Overall, we are left with an additional sign of $-1^{(n+m)l+(m-l)(n-l)}$ between the first and second term of the commutator. For particle whole symmetric operators, $n\%2 = m\%2 = 0$, thus the overall sign difference is $(-1)^l$.

Thus we can commute commutators summing over all contractions like:

$$[: A_a A_b \cdots \overbrace{A_1 \cdots A_i A_j \cdots A_2} :] \quad (\text{A.85})$$

With the following rules,

- first compute the contraction for the first term in the commutator
- For bosons: subtract the same term with $C \leftrightarrow C^T$

- For fermions: subtract the same term with $C \leftrightarrow C^T$ with an additional $(-1)^{l(n+m)+(m-l)(n-l)}$ sign in the second term.

In effect we are commuting the contractions with $C \leftrightarrow C^T$ for bosons. While for fermions we are either anti commuting or commuting depending on the parity of $l(n+m) + (m-l)(n-l)$. For particle whole symmetric operators, we anitcommute if l is odd and commute if l is even.

Appendix B

Path Integrals and Classical Approximations

B.1 Semi-Classical Analysis

A classical dynamical system of quantum model can be constructed in multiple ways. A list of the ways are as follows:

1. Wigner Function Representation of state + $1/N$ or $1/\hbar$ approximation
2. Path integral minimization
3. inverse of canonical quantization: $[\cdot, \cdot]_{\frac{1}{i\hbar}} \rightarrow \{, \}$
4. Variational method for state
5. Variational method for operator
6. Cumulants

The first and second ways can be equivalent as long as the resolution of the identity in each are nicely related. I'm not sure when they might fall apart. The third way is equivalent to the first or second way as long as one is in the classical limit. Otherwise, the third way is not unique. For the 4th-6th methods, one is not guaranteed to get a symplectic structure. As it is the simplest, we will start with the inverse of canonical quantization.

B.1.1 Inverse of Canonical Quantization

Bosons

In canonical quantization one replaces the poisson bracket with the commutator. One can do the opposite map to produce a classical hamiltonian and dynamics from a quantum Hamiltonian. For boson position and momentum:

$$[x, p]/(i\hbar) = 1 \rightarrow \{x, p\} = 1 \quad (\text{B.1})$$

For bosons creation and annihilation operators the procedure is:

$$[b, b^\dagger]/(i\hbar) = \frac{1}{i\hbar} \rightarrow \{b, b^*\} = \frac{1}{i\hbar} \quad (\text{B.2})$$

The factor of i is because b and b^\dagger are not hermitian operators. To find the time derivatives of b we use:

$$\partial_t b = \{b, H\} = \frac{i}{2\hbar} \frac{dH}{db^*} \quad (\text{B.3})$$

We can also work with densities and phases:

$$\begin{aligned}
 b &= \sqrt{\rho} e^{i\phi} \\
 b^* &= \sqrt{\rho} e^{-i\phi} \\
 \rho &= b^* b \\
 \phi &= \frac{2}{i} (\log(b) - \log(b^*))
 \end{aligned}
 \tag{B.4}$$

We can show ρ and ϕ are conjugate coordinates by computing their variation and time derivatives:

$$\begin{aligned}
 d\rho &= b db^* + b^* db \\
 d\phi &= \frac{2}{i} \left(\frac{db}{b} - \frac{db^*}{b^*} \right) \\
 \frac{d\rho}{dt} &= -\frac{ib}{2\hbar} \frac{dH}{db^*} + \frac{ib^*}{2\hbar} \frac{dH}{db} = -\frac{1}{\hbar} \frac{dH}{d\phi} \\
 \frac{d\phi}{dt} &= \left(\frac{1}{\hbar b} \frac{dH}{db^*} + \frac{1}{\hbar b^*} \frac{dH}{db} \right) = \frac{1}{\hbar} \frac{dH}{d\rho}
 \end{aligned}
 \tag{B.5}$$

If we define $\phi' = \hbar\phi$ or $\rho' = \hbar\rho$ then we have:

$$\begin{aligned}
 \{\phi', \rho\} &= 1 \\
 \{\phi, \rho'\} &= 1
 \end{aligned}
 \tag{B.6}$$

Spins

Using the spin to boson mapping, we can find a prescription to describe equations of motion for spins.

$$\begin{aligned} J_z &= \frac{\hbar}{2}(n_1 - n_2) = \frac{\rho'_1 - \rho'_2}{2} \\ J_x &= \frac{\hbar}{2}(a_1^\dagger a_2 + h.c) = \frac{\sqrt{\rho'_1 \rho'_2}}{2} \cos(\phi_1 - \phi_2) \\ J_y &= \frac{\hbar}{2i}(a_1^\dagger a_2 - h.c) = \frac{\sqrt{\rho'_1 \rho'_2}}{2} \sin(\phi_1 - \phi_2) \end{aligned} \tag{B.7}$$

For fixed spins size is convenient to choose $\hbar = 1/N$ and define

$$\begin{aligned} z &= \frac{\rho_1 - \rho_2}{2N} \\ \phi &= \phi_1 - \phi_2 \end{aligned} \tag{B.8}$$

such that the classical mapping is:

$$\begin{aligned} J_z &= z \\ J_x &= \sqrt{1 - z^2} \cos(\phi) \\ J_y &= \sqrt{1 - z^2} \sin(\phi) \\ |J| &= 1 \end{aligned} \tag{B.9}$$

B.2 Path Integrals

A solutions for general quantum problems rely on obtaining the matrix elements of an exponential operator. For thermal states the exponential operator is $\rho_\beta = e^{-\beta H}$, for unitary evolution it is $U(t)$, and for lindblad evolution it is $e^{-t\mathcal{L}}$ which acts on the space of

density matrices (a tensor product of two Hilbert spaces). The path integral offers a way of constructing matrix elements of exponential operators from the knowledge of the matrix elements of H without having to perform exact diagonalization. We will therefore focus on exponential operators of the form:

$$e^{-xH} \tag{B.10}$$

This is done by noting that for small x the exponential can be expanded:

$$\langle n | e^{-xH} | m \rangle \approx \langle n | 1 - xH | m \rangle \approx e^{-xH_{nm}} \tag{B.11}$$

For which the matrix elements are easily computed from those of H . Thus, for large x , we can break the exponential operator into N products of the operator with an effective $\tilde{x} = x/N$:

$$e^{-xH} = \prod_{n=1}^N e^{-\frac{x}{N}H} \tag{B.12}$$

Next we insert n resolutions of the identity in some basis l_n :

$$\langle L_N | e^{-xH} | L_0 \rangle = \langle L_N | \prod_{n=1}^N I_n e^{-\frac{x}{N}H} | L_0 \rangle = \prod_{n=1}^N \sum_{l_n} W(l_n) \langle l_n | e^{-\frac{x}{N}H} | l_{n-1} \rangle \delta_{l_n, L_N} \tag{B.13}$$

and with $l_0 = L_0$ and $W(l_n)$ is the normalization of the l_n state. Different types of path integrals can be created by using different resolutions of the identity. These resolutions of the identity are often chosen so they contain eigenstates of the operators which make up H . In doing so the path integral becomes:

$$\sum_{l_n} W(l_n) e^{\sum_{n=1}^N \ln(\langle l_n | l_{n-1} \rangle) - \frac{x}{N} H(l_{n-1}, l_n)} \delta_{l_n, L_N} = \sum_{l_n} W(l_n) e^{S(l_n)} \tag{B.14}$$

There are multiple ways of evaluating this:

- Numerical Sum (monte carlo)
- Saddle point approximation (pick the best path): leads to classical solutions
- gaussian integration ontop of the saddle
- Controlled pertubation Series on top of gaussian fluxtuations
- resumatation of pertubation series
- resumatation recast as hubbard statonavich
- renormalization group

B.2.1 Bosonic Path integral

For bosons, the coherent state resolution of the identity in Eq.A.51 is the simplest for constructing a path integral:

$$\begin{aligned}
 |l_n\rangle &\rightarrow |\psi_n\rangle & (B.15) \\
 W(l_n) &\rightarrow e^{-|\psi_n|^2} \\
 \sum_{l_n} &\rightarrow \int \frac{d\psi_n^* d\psi_n}{\pi}
 \end{aligned}$$

To compute $\langle \psi_n | e^{-\frac{x}{N}H} | \psi_{n-1} \rangle$ we assume H is expressed in creation and annihilation operators and normal ordered so all creation operators are on the left. In this way, one can replace b^\dagger with ψ_n^* and b with ψ_{n-1} leading to

$$\langle \psi_n | e^{-\frac{x}{N}H} | \psi_{n-1} \rangle = e^{\psi_n^* \psi_{n-1} - \frac{x}{N}H(\psi_n^*, \psi_{n-1})} \quad (B.16)$$

We now have the path integral representation of an exponential operator as:

$$e^{-|\psi_N|^2} U(\psi_N, \psi_0) = \tag{B.17}$$

$$e^{-|\psi_N|^2} \langle \psi_N | e^{-xH} | \psi_0 \rangle = \left(\prod_{n=1}^{N-1} \int \frac{d\psi_n^* d\psi_n}{\pi} \right) e^{\sum_{n=1}^N (\psi_n^* \psi_{n-1} - |\psi_n|^2 - \frac{x}{N} H(\psi_n^*, \psi_{n-1}))}$$

The exponent, $-S(\psi(n))$ is a functional of the function from the discrete time index n to the field ψ and has a form of a discrete action. If one takes the N infinite limit now then one sees that exponent really is an action. But this is wrong. We must solve before taking a limit, otherwise we risk missing the boundary conditions ψ_N and ψ_0 . This can only be solved exactly if H is at most bilinear in the fields. The most general single boson hamiltonian of this form is:

$$xH = \int dx \omega(x) b^\dagger b + J(x) a^\dagger + J^*(x) a \tag{B.18}$$

the integral form allows for the coefficients to depend on the field so that:

$$H(\psi_n^*, \psi_{n-1}) = \omega(n) \psi_n^* \psi_{n-1} + J(n) \psi_n^* + J^*(n) \psi_{n-1} \tag{B.19}$$

For this type of single particle hamiltonian, the path integral corresponds to a product of gaussian integrals.

B.2.2 Fermionic Path Integrals

To construct a fermionic path integral, we need to find a resolution of the identity, and if we want to make use of gaussian integration methods, we will need the resolution of the identity to look something like the bosonic coherent state. This is accomplished by enlarging the hilbert space using a linear space over grassmann, anti-commuting numbers

instead of complex numbers. In this space, the fermion creation operator has a eigenstate given by:

$$e^{-\xi_i c_i^\dagger} |0\rangle. \quad (\text{B.20})$$

Using grassmann rules, one can compute an overlap between two fermionic coherent states:

$$\langle \xi | \xi' \rangle = e^{\xi^* \xi'}, \quad (\text{B.21})$$

and we can write the resolution of the identity as:

$$1 = \int \prod_i d\xi_i^* d\xi_i e^{-\sum_i \xi_i^* \xi_i} |\xi\rangle \langle \xi|. \quad (\text{B.22})$$

Playing the same game as before with bosons, we get the same representatin of an exponential operator, but with grassman fields instead of bosonic fields, and a different integration measure. These different have dramatic effects when performing the integration over fields.

If a hamiltonian is given in terms of majorana fermions, the technical procedure would first require a rotation to fermions, then use the coherent state identiy and then rotate the complex fermionic grassmann fields back to real majorana grassmann fields. Actually, this can usually be skipped and the majorana operators can be replaced by the real grassmann fields. Trouble only arizes if this replacement is done to an $A_i^2 = 1$ before this identiy is used, as the square of a grassmann number is 0 not 1.

B.2.3 Imaginary Time Correlations at the Gaussian Level

Now that we have a way of expressing exponential operators we can start solving for correlation functions. We will do this for the imaginary time generating function, Eq.

A.16, for a single mode non-interacting model and then discuss generalizations. Using Eq.B.19 for a hamiltonian $H = \omega n$, \mathcal{G}_T is written as:

$$\mathcal{G}_T(A_i(t)) = Tr \left\langle P e^{-\int_0^\beta d\tau (H(\tau) + \eta^*(\tau)a + \eta(\tau)a^\dagger)} \right\rangle = \int \frac{d\psi_N^* d\psi_N}{\pi} e^{-|\psi_N|^2} \langle \psi_N | e^{-\beta H} | \pm \psi_N \rangle = \left(\prod_{n=0}^N \int \frac{d\psi_n^* d\psi_n}{\pi} \right) e^{\sum_{n=1}^N (\psi_n^* \psi_{n-1} - |\psi_n|^2 - \frac{\beta}{N} H(\psi_n^*, \psi_{n-1}))} \delta(\psi_0 \mp \psi_N)$$

Where the + is for bosons and - for fermions. To compute this we need to know how to do gaussian integrals. For bosons:

$$\prod_i \int \frac{dRe\phi_i dIm\phi_i}{\pi} e^{-\sum_{ij} \phi_i^* H_{ij} \phi_j + \sum_i \eta_i^* \phi_i + \eta_i \phi_i^*} = \frac{1}{\det H} e^{\sum_{ij} \eta_i^* H_{ij}^{-1} \eta_j}, \quad (\text{B.23})$$

for fermionic:

$$\prod_i \int d\xi_i d\xi_i^* e^{-\sum_{ij} \xi_i^* H_{ij} \xi_j + \sum_i \eta_i^* \xi_i + \eta_i \xi_i^*} = \det H e^{\sum_{ij} \eta_i^* H_{ij}^{-1} \eta_j}, \quad (\text{B.24})$$

and for Majorana operators:

$$\prod_i \int dA_i e^{-\sum_{ij} A_i H_{ij} A_j + \sum_i \eta_i A_i} = \sqrt{\det H} e^{\sum_{ij} \eta_i \frac{H_{ij}^{-1}}{2} \eta_j} \quad (\text{B.25})$$

Therefore, we need to compute the determinant and inverse of the matrix in the exponent. This matrix has -1 on the diagonals, $1 - \beta/N\omega$, and a $\pm(1 - \beta/N)$ on a corner from the boundary condition. The determinant is easy to compute giving:

$$\det S = 1 \mp (1 - \beta/N\omega)^N \quad (\text{B.26})$$

which in the large N limit gives: $1 \mp e^{\beta\omega}$ The inverse is harder, but can be solved by fourier transform. Doing so, the action become:

$$S = \sum_{m=1}^N \left[e^{i\omega m} \left(1 - \frac{\omega\beta}{N} \right) - 1 \right] |\psi_{\omega m}|^2 \quad (\text{B.27})$$

where $\omega_m = \frac{(2m+1\mp 1)\pi}{N}$. We can evaluate the fourier transforming of the inverse:

$$\frac{1}{N} \sum_m e^{-i\omega_m(n+1-m)} \frac{1}{(1 - \omega\beta/N) - e^{-i\omega_m}} \quad (\text{B.28})$$

which has a pole at $i\omega_m = \omega' = \ln(1 - \omega\beta/N)$. Preforming the sum using the matsubara frequency integral (on wiki) one gets:

$$\begin{aligned} & -\frac{1}{N}(1 - \omega\beta/N)^{n+1-m} \frac{N}{1 \mp (1 - \omega\beta/N)^N} (1 - \omega\beta/N)^{-1} \text{for } n - m > 0 \\ & \frac{1}{N}(1 - \omega\beta/N)^{n+1-m} \frac{N}{1 \mp (1 - \omega\beta/N)^{-N}} (1 - \omega\beta/N)^{-1} \text{for } n - m < 0 \end{aligned} \quad (\text{B.29})$$

where the last, $(1 - \omega\beta/N)^{-1}$, comes from the derivitive of the denominator for complex pole, and the different cases depending on n and m are due to having to use different integration functions to capture the convergence of either the left or right side of the complex plaine. Defining $m = \tau_m N/\beta$ we can go to continous time by taking the large N limit. Doing so we get:

$$\begin{aligned} H^{-1}(\tau_n - \tau_m) &= e^{-\omega(\tau_n - \tau_m)} (1 \pm n_{\pm}(\omega)) \text{for } n - m > 0 \\ H^{-1}(\tau_n - \tau_m) &= e^{-\omega(\tau_n - \tau_m)} n_{\pm}(\omega) \text{for } n - m < 0 \end{aligned} \quad (\text{B.30})$$

where $n_{\pm}(\omega)$ is the boson or fermion density at inverse temperature β . Taking derivitves of the generating function with respect to η_m^* and η_n , we find the imaginary time two point corrrelation as $H^{-1}(\tau_n - \tau_m)$. An alternative way to find the two point correlation function is to use BCH for $e^{-\tau\omega n} a e^{-\tau\omega n}$, and one finds the same things after imaginary time path ordering.

Generalizations

Two ways in which this calculation becomes more complex are 1) by working with real time paths and 2) adding multiple modes. When adding multiple modes it is easier to first diagonalize the single particle hamiltonian and then treat each mode independently. In real time, the boundary conditions become more complicated, and for generic initial states might not be gaussian. In this case, it is often easier to find H^{-1} by using BCH for the correlation function. One can then construct a model action off of this continuous time H^{-1} , where the gaussian part is given by H . Since perturbative and renormalization group techniques use products of the path integrals “covariance”, H^{-1} , solving for H^{-1} in the path integral formalism isn’t required, unless a classical approximation is first applied.